CALT-68-1231
DOE RESEARCH AND
DEVELOPMENT REPORT

A STUDY OF THE IOTA IN RADIATIVE J/PSI DECAYS

Thesis by
Jeffrey David Richman

In Partial Fulfillment of the Requirements
for the Degree of
Doctor of Philosophy

California Institute of Technology
Pasadena, California

1985

(Submitted December 17, 1984)

Acknowledgements

I would like to express my deep appreciation to all the members of the Mark III collaboration for their advice and support.

My adviser, David Hitlin, provided valuable guidance and encouragement. I am especially grateful for the confidence implied by the independence he allowed me.

My fellow graduate students were extremely generous with their ideas and help. In particular, I am deeply indebted to Kevin Einsweiler and Tony Spadafora. This thesis would not have been possible without the assistance, instruction, and suggestions of Lutz Köpke, Jacques Perrier, Jimmy Roehrig, J. J. Russell, Michele Scarlatella, Terry Schalk, Abe Seiden, Jon Thaler, Walter Toki, Norbert Wermes, and Bill Wisniewski. Rich Partridge tackled the difficult job of implementing EGS in the Mark III Monte Carlo so that the spin analysis of $\iota \to K^+K^-\pi^0$ could be performed. The wisdom, curiosity, and friendship of Al Odian were a constant help. Rose Mary Baltrusaitis shared not only her expertise in physics, but also her indomitable spirit, sense of humor, and vast knowledge of wine. Her guidance in this last regard is especially appreciated.

Elliot Cheu and JoAnn Anderson spent many long hours courageously typing this thesis.

For their understanding, inspiration, generosity, and wisdom, I thank my parents. (I ignored their advice, however, and became a physicist anyway.)

This thesis is dedicated to Kate Metropolis, for her friendship, support, patience, and love. Without her I would never have made the remarkable discovery that physics is not the only thing—it is not even the most important thing.

Abstract

An analysis of the production, decay, and quantum numbers of the $\iota(1440)$ in radiative J/ψ decays is presented. The $\iota(1440)$, because of its large production in this OZI-suppressed channel, is considered a possible gluonic bound-state, or glueball. Such states appear to be a natural consequence of the non-Abelian structure of the SU(3) color gauge group of QCD. The data, 2.7×10^6 produced J/ψ's, were obtained using the Mark III detector at the SPEAR e^+e^- storage ring.

The spin-parity of the $\iota(1440)$ is independently determined to be 0^- using two decay modes, $\iota \to K^0_S K^{\pm}\pi^{\mp}$ and $\iota \to K^+K^-\pi^0$. The technique used is based on the three-body helicity formalism, which provides a means of studying the decay angular distributions in a manner independent of the structure of the Dalitz plot. This is particularly useful in the case of $\iota \to K\bar{K}\pi$, where the limited phase space makes it difficult to unambiguously identify the two-body modes. In addition, the measured angular distributions provide direct visual evidence supporting the spin-parity assignment. Measurements of the ι mass, width, and branching fractions are obtained using $\iota \to K^0_S K^{\pm}\pi^{\mp}$, $\iota \to K^+K^-\pi^0$, and $\iota \to K^0_S K^0_S \pi^0$. The relative branching fractions are consistent with the isospin 0 predictions. From a study of the $K\bar{K}\pi$ Dalitz plot, an upper limit for $\iota \to K^*\bar{K} + c.c.$ is obtained. These results are discussed in the context of the current experimental status of the $E(1420)$.

Upper limits are presented for $B(\iota \to \eta\pi\pi)$, $B(\iota \to \delta\pi \to \eta\pi\pi)$, $B(\iota \to K\bar{K}\pi\pi)$, and $B(\iota \to \rho\pi\pi)$. The limit on $B(\iota \to \delta\pi \to \eta\pi\pi)$ appears to be inconsistent with a large value of $B(\iota \to \delta\pi \to K\bar{K}\pi)$. However, the very uncertain status and properties of the $\delta(980)$ make it difficult to pinpoint the source of this inconsistency. Together, these upper limits provide evidence that,

apart from a possible $\iota \to \rho\rho$ signal, $K\bar{K}\pi$ is the dominant ι decay and that inclusive ι production is dominated by $J/\psi \to \gamma\iota$, $\iota \to K\bar{K}\pi$.

The double radiative channels $J/\psi \to \gamma X$, $X \to \gamma +$ Vector, where Vector $= \rho^0$, ϕ, ω are studied to probe the quark content of the object X. Many pseudoscalar mixing models predict that the ι acquires a large radiative width into $\gamma\rho^0$ through mixing with the η and η'. In the $\gamma(\gamma\rho^0)$ final state, a broad structure is observed in the 1.4 GeV region. Although the measured angular distributions are consistent with the pseudoscalar predictions, the central mass of this structure is below that found for the ι in the $K\bar{K}\pi$ channels. Thus, with the present limited statistics, it is unclear whether this structure should be identified with the ι. Upper limits are obtained for $\iota \to \gamma\phi$ and $\iota \to \gamma\omega$. Measurements are also obtained for $B(J/\psi \to \gamma\eta')$ and $B(J/\psi \to \gamma\eta)$ using the $\gamma(\gamma\pi^+\pi^-)$ final state. These results are compared with theoretical predictions.

Measurements of the hadronic decays $J/\psi \to \phi\eta$, $\omega\eta$, and $\omega\pi^0$, as well as the observation of the isospin-violating decay $J/\psi \to \rho^0\eta$, are presented.

Finally, the two- and three-body helicity formalisms are discussed in the Appendices.

Table of Contents

List of Tables

List of Figures

Chapter 1. Introduction

The discovery of charm in 1974 was a decisive step toward understanding the structure of matter. The observation of the J/ψ in both e^+e^- and pBe interactions (1), the subsequent observation of other states in the charmonium system, and finally the discovery of the explicitly charmed D-mesons, firmly established the existence of quarks – despite the fact that free quarks apparently cannot be produced. Remarkably, theoretical investigations (2) four years preceding the discovery showed that the existence of a fourth quark could explain the suppression of weak strangeness–changing neutral currents, which govern $K_L^0 \to \mu^+\mu^-$ and the $K_L^0 K_S^0$ mass difference. For $m_W \sim 80$ GeV, the predicted $K_L^0 K_S^0$ mass difference is far too large unless a fourth quark, with mass m_c, is introduced. Then one obtains $\Delta m/m_K \simeq (\frac{G_F}{2\pi} f_K m_c \cos\theta_C \sin\theta_C)^2$, which agrees with measured mass difference for $m_c \sim 1.5$ GeV. Similarly, $K_L^0 \to \mu^+\mu^-$ is suppressed by interference between diagrams in which the u- and c- quarks are interchanged.

Crucial to most of the experimental investigations were advances in instrumentation, in particular the development of the electron-positron storage ring. The annihilation of an e^+e^- pair into a virtual photon provides a means of producing and studying the $J^{PC} = 1^{--}$ states that couple to the photon. The success of e^+e^- rings can be seen from a plot of

$$R \equiv \sigma(e^+e^- \to \text{ hadrons})/\sigma(e^+e^- \to \mu^+\mu^-)$$

as a function of the center-of-mass energy (Fig. 1.1). In this plot, one observes peaks corresponding to the J/ψ (hereafter ψ) and its radial excitations and similar peaks for the Υ resonances, which are $b\bar{b}$ bound states. Step-function increases in R occur at thresholds for production of particles ($D\bar{D}$, $B\bar{B}$, etc.)

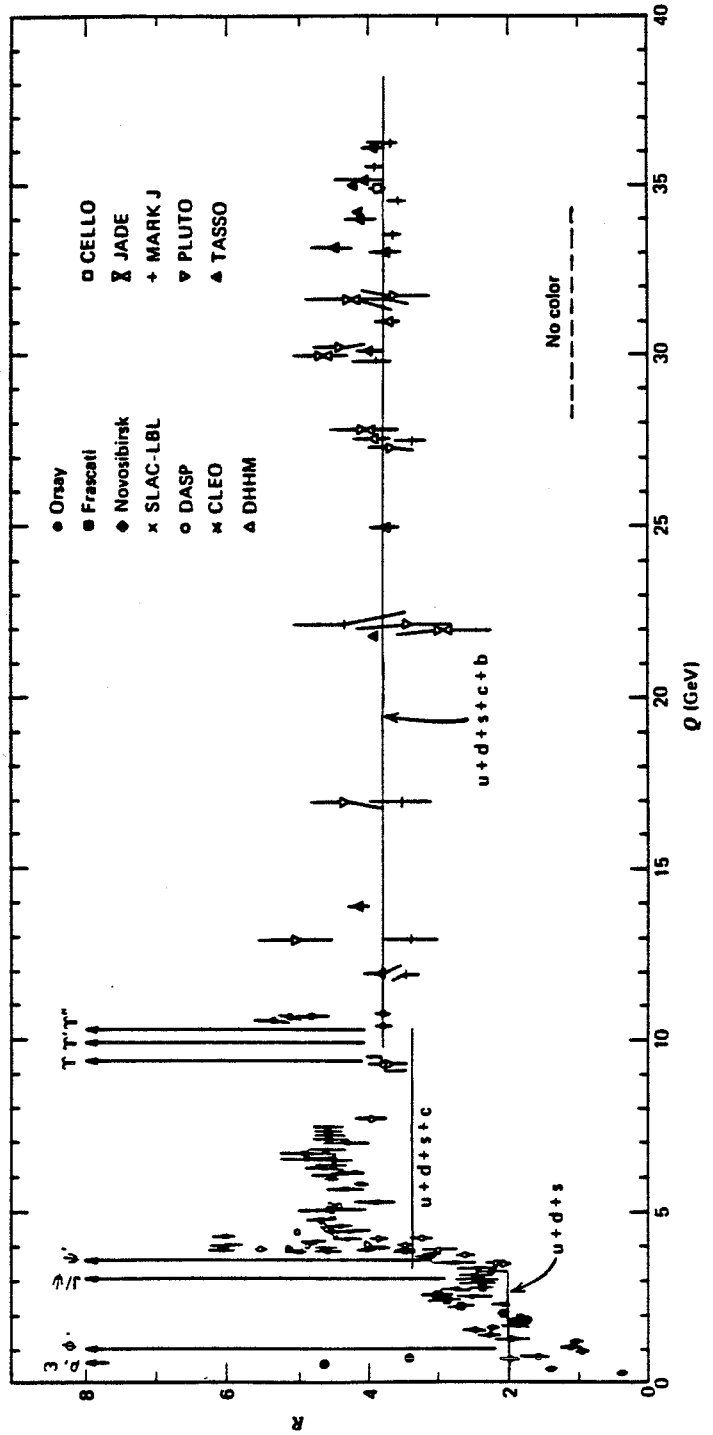

Figure 1.1. R as a function of the center-of-mass energy (3).

with non-zero quantum numbers for a new quark flavor. In fact, the onset of production of a new heavy lepton (e.g., the τ) also results in a step up in R, but these contributions are usually subtracted by convention.

At about the same time as the ψ discovery, a field-theoretic description of the strong interactions was reinstated with the invention of quantum chromodynamics (QCD) and the elucidation of its remarkable properties (4): the direct gluon-gluon coupling, asymptotic freedom, and the possibility of quark confinement. Understanding the decay properties of the ψ has proved to be a particularly interesting application of QCD. The line-width of the ψ, $\Gamma = (63 \pm 9)$ KeV, is only about one-thousandth of what one expects for a strongly decaying resonance of its mass. The unusually long ψ lifetime can be understood as the result of two effects. First, the ψ is not sufficiently massive to decay into a $D\bar{D}$ pair. Such a decay would ordinarily be the natural process to occur, because it requires only that the $c\bar{c}$ quarks separate and each combine with one member of a light quark pair created with the available energy. With this channel closed, the only strong decay of the ψ is the process whereby the $c\bar{c}$ quarks annihilate. In the framework of QCD, this results in the formation of gluons, which subsequently materialize into hadrons (Fig. 1.2a). The second reason the decay is suppressed is that the QCD coupling constant, α_s, is a decreasing function of the q^2 carried by the gluons and is substantially less than one at the ψ. In order to make a colorless state with odd charge conjugation, at least three gluons must be created; consequently the coupling enters as α_s^3 in the decay probability.

The lowest order diagrams for ψ decay are shown in Fig. 1.2. These diagrams represent a) hadronic decay; b) electromagnetic decay into a virtual photon, which then couples to leptons or quarks; c) radiative ψ decay with annihilation of the $c\bar{c}$ quarks into two gluons; and d) the M1 radiative transition of the ψ to

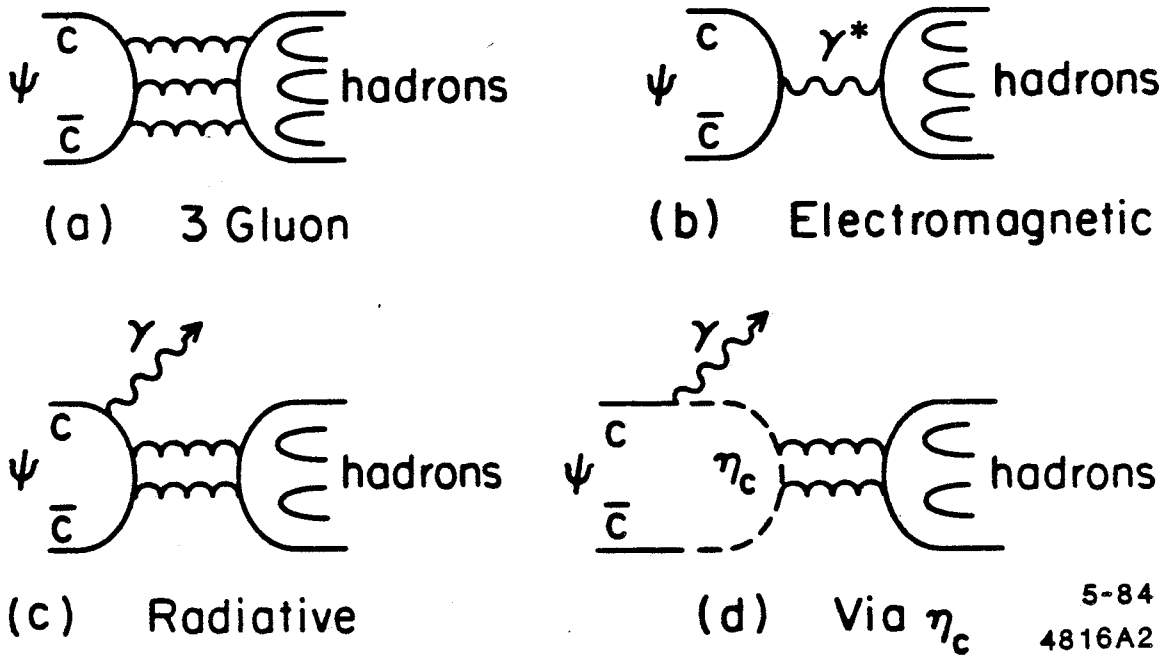

Figure 1.2. Lowest order diagrams for ψ decay. a) hadronic decay b) electromagnetic decay c) radiative decay into gluons d) radiative decay to the η_c.

the pseudoscalar charmonium state, the $\eta_c(2980)$. The calculation of the decay into three on-shell gluons gives (5)

$$\Gamma(\psi \to 3g) = \frac{16}{9\pi}(\pi^2 - 9)\frac{5}{18}\alpha_s^3 \frac{|\Psi(0)|^2}{M_\psi^2}, \tag{1.1}$$

where $\Psi(0)$ is the value of the radial wave function of the ψ at the origin. This result is identical to that obtained for the decay of $^3S_1$ positronium into three photons, with the replacement $\alpha^3 \to \frac{5\alpha_s^3}{18}$. If one assumes that the three-gluon system couples to hadrons with unit probability, then Eq. (1.1) gives the strong interaction contribution to the first-order parital width into hadrons.

Because the strong decays of the ψ are suppressed, the electromagnetic decays contribute substantially to the total width. For example,

$$\Gamma(\psi \to e^+e^-) = 4(Q_c\alpha)^2 \frac{|\Psi(0)|^2}{M_\psi^2}, \tag{1.2}$$

where $Q_c = \frac{2}{3}$ is the charge of the charmed quark. Experimentally, it is found that $\mathrm{B}(\psi \to e^+e^-) = (7.4 \pm 1.2)\%$ or $\Gamma(\psi \to e^+e^-) = (4.7 \pm 1.0)$ KeV. Hadron production can also occur through the annihilation of the $c\bar{c}$ system into a virtual photon. The partial width is

$$\Gamma(\psi \to \gamma^* \to \text{hadrons}) = \mathrm{R}(\text{off-resonance})\Gamma(\psi \to e^+e^-) \simeq 10.3 \text{ KeV}.$$

The partial width for the radiative decay into two on-shell gluons is (6)

$$\Gamma(\psi \to \gamma gg) = \frac{32}{9\pi}(\pi^2 - 9)\alpha_s^2 \alpha Q_c^2 \frac{|\Psi(0)|^2}{M_\psi^2}.$$

Using the known branching fraction to e^+e^-,

$$\frac{\Gamma(\psi \to e^+e^-)}{\Gamma(\psi \to \gamma^* \to e^+e^-, \mu^+\mu^-, \text{hadrons}) + \Gamma(\psi \to \gamma gg) + \Gamma(\psi \to ggg)} = 0.074$$

and the above formulas for the partial widths, one can extract $\alpha_s \simeq 0.18$. The small value of α_s provides some justification for the perturbative calculation.

The radiative decay of the ψ into two gluons has a substantial rate. The second-order calculation for the ratio of radiative to hadronic ψ decays predicts that (7)

$$\frac{\Gamma(\psi \to \gamma gg)}{\Gamma(\psi \to ggg)} = \frac{36}{5} Q_c^2 \left(\frac{\alpha}{\alpha_s}\right) \left[1 + \frac{2.2\alpha_s}{\pi} + \ldots\right] \simeq 14.6\%,$$

assuming $\alpha_s \simeq 0.18$. Using

$$\Gamma(\psi \to 3g) = \frac{5}{18\pi}(\pi^2 - 9)\frac{\alpha^3(M_\psi)}{\alpha^2}\Gamma(\psi \to e^+e^-) \simeq 39 \text{ KeV}$$

one obtains

$$\Gamma(\psi \to \gamma gg) = 5.7 \text{ KeV} \qquad B(\psi \to \gamma gg) \simeq 9.1\%,$$

which indicates that these decays should be a good source of hard gluons.

The interest in radiative ψ decays is due to the fact that lattice, bag, and potential models of QCD all strongly suggest the existence of gluonic bound states (glueballs) with masses comparable to those of ordinary mesons (8). The coupling between gluons is a consequence of the non-Abelian nature of the SU(3) color gauge group of QCD. In addition, the non-observation of free quarks provides empirical support for the notion that color is confined by a force that increases with distance. Thus, glueballs appear to be an entirely natural consequence of the properties of QCD, and as such, their observation would constitute one of the best possible tests of the theory. The lightest glueballs are expected to have masses ranging from 0.5–2.5 GeV (depending on the model), and to have spin-parity 0^{++}, 0^{-+}, or 2^{++}. Because this mass range is accessible in radiative ψ decays, and because these quantum numbers should predominate

in the two-gluon system produced when the $c\bar{c}$ annihilate, radiative ψ decays are considered to be a favorable channel in which to search for glueballs. (The description of the gluonic resonance as a two-gluon system, however, may not be very meaningful, as mixing is sometimes allowed between two- and three-gluon systems (9).)

The question of whether the two gluons resonate directly (a glueball) or first decay perturbatively into quarks, which then resonate as a meson or four-quark state, is one of detailed long-range QCD dynamics and cannot as yet be addressed by theory. In fact, there are several well-known examples of radiative decays into mesons: $\psi \rightarrow \gamma\eta, \gamma\eta', \gamma f$, and γf. Radiative decays to isovectors are strongly suppressed; they must occur through a process in which the photon is radiated by a light quark in the *final state*. Figure 1.3 shows some of the possible interactions of the two gluons. In addition to glueball and meson production, it is possible to form a hybrid state (10) consisting of $q\bar{q}g$. In fact, it appears unlikely that pure glueball states will remain unmixed with ordinary mesons; one expects the physical states to contain both gluonic and $q\bar{q}$ components.

It has proved extremely difficult to find properties that distinguish a glueball from an ordinary meson. A simple guide to (pure) glueball widths is based on the similarity between glueball decay into mesons and the OZI-suppressed decay of a meson, such as $\phi \rightarrow 3\pi$. In OZI-suppressed decays, the quarks annihilate to gluons, which couple again to quarks to produce the final state mesons. Glueball decay, however, requires only one transition from gluons to quarks. Consequently, if OZI- processes are suppressed by a factor $\Gamma_{OZI}/\Gamma_{hadron}$, where Γ_{hadron} is a typical hadronic width, then glueball decays should be suppressed by $\sqrt{\Gamma_{OZI}/\Gamma_{hadron}}$. An estimate for the glueball width is therefore

$$\sqrt{\Gamma_{OZI}/\Gamma_{hadron}} \times \Gamma_{hadron} = \sqrt{\Gamma_{OZI}\Gamma_{hadron}} = \mathcal{O}(1 - 10 \text{ MeV}).$$

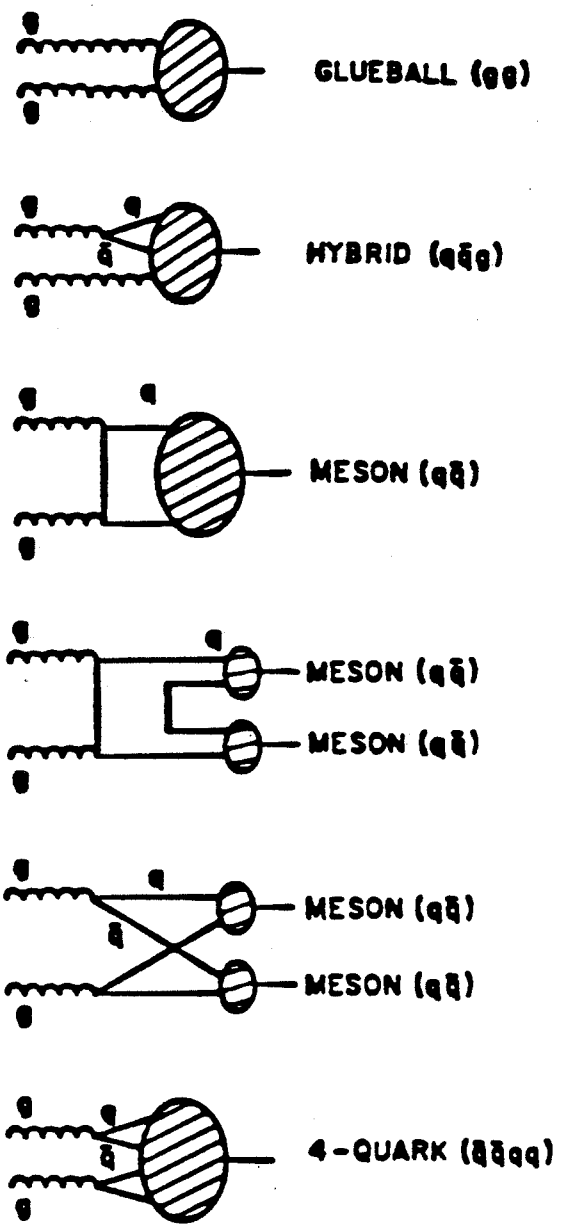

Figure 1.3. Some of the possible interactions of the two-gluon system produced in radiative ψ decays.

In spite of the heuristic appeal of this argument, it may not be reliable in many cases of interest, especially when there is $q\bar{q}$-glue mixing. The argument has also been challenged (9) on the grounds that the width of a two-gluon glueball should be larger than that of the η_c ($\Gamma \sim 12$ MeV). In η_c decays, the $c\bar{c}$ system annihilates into two gluons, which then hadronize with unit probability. Consequently, $\Gamma(\eta_c \rightarrow hadrons) \sim \alpha_s^2$. A glueball decay would not be suppressed by α_s^2 and would therefore have a width comparable to that of an ordinary meson.

A second idea is that glueballs, which are manifestly SU(3) flavor singlets, might be expected to have SU(3) symmetric decays (11). A sufficiently heavy C-even glueball would then decay into $\rho\rho$, $\phi\phi$, and $\omega\omega$, whereas a meson in an ideally mixed C-even nonet would decay into ($\rho\rho$, $\omega\omega$) *or* $\phi\phi$, depending on its quark content. The decay of a C-even glueball into $K\bar{K}^*$ is suppressed by G_V parity: the SU(3) singlet component of the $K\bar{K}_V^*$ system is odd under C. Similarly, the decays of a C-odd glueball into G_V-even final states, such as $K\bar{K}$ and $K_V^*\bar{K}_V^*$, are suppressed. Because the SU(3) octet component of the two strange-meson wave function does not have definite C, these selection rules do not apply to ideally mixed mesons.

There are various SU(3)-breaking mechanisms, however, that may favor certain channels. For $J = 0$ glueballs, helicity conservation could suppress decays into two spin-$\frac{1}{2}$ fermions, and could enhance $s\bar{s}$ production by a factor m_s^2/m_u^2. In the spherical cavity approximation to the bag model, it is found that TM gluon modes couple predominantly in the s-channel to strange quarks (12). Although it is difficult to determine whether these mechanisms are actually operating, multi-kaon final states are prominent in the decays of the ι, θ, and ξ.

The allowed quantum numbers of glueballs have been investigated in the context of the lattice, bag, and potential models of QCD (13). Although there

is some question as to whether the gluons should be considered massless, each model allows exotic quantum numbers that are not allowed for $q\bar{q}$ states. In lattice calculations, for example, the quantum numbers (ordered according to increasing glueball mass) are

$$J^{PC} = 0^{++}, 0^{-+}, 2^{++}, 1^{-+}, 0^{--},$$

where the possible excitations of each channel are omitted. Unfortunately, no states with exotic quantum numbers have been observed. The mass spectra predicted by these models are summarized in Ref. (13); beyond the expectation that typical glueball masses are in the $1 - 3$ GeV range, there is little reliable information. For example, all models predict that the scalar glueball is the lightest, but its mass remains very uncertain ($0.5 - 1.7$ GeV). The lattice calculations are presently limited by computing power. Quark loops are not included, so that mixing with ordinary mesons cannot yet be studied with this method.

At present, there is only one reliable criterion to determine whether a resonance with non-exotic quantum numbers is an ordinary meson. That is simply to ask whether all available slots in the meson nonets of the appropriate quantum numbers are occupied. The radially excited mesons must also be considered, because these states can lie in the 1-2 GeV mass range. Thus, the identification of a glueball or hybrid state can involve tracking down obscure results in the dark corners of meson spectroscopy (14). In addition, this method is extremely dependent on reliable spin-parity measurements, which are notoriously difficult to obtain. A central goal of this thesis is to provide an unambiguous spin-parity determination of the ι, one of the most interesting glueball candidates.

Table 1.1. Summary of Known Radiative ψ Decays.

$\psi \to \gamma + X$ $X =$	$B(\psi \to \gamma X)$ (in Units of 10^{-3})	Modes X Observed to Decay into (various expt.'s)	$J^P(X)$
π^0	$0.036 \pm 0.011 \pm 0.007$	$\gamma\gamma$	0^-
η	$0.88 \pm 0.08 \pm 0.11$	$\gamma\gamma, \gamma\pi^+\pi^-, 3\pi$	0^-
η'	$4.7 \pm 0.2 \pm 0.7$	$\eta\pi\pi, \gamma\rho^0, \gamma\omega, \gamma\gamma$	0^-
$f(1270)$			2^+
$\to \pi\pi$	$1.15 \pm 0.07 \pm 0.19$	$\pi^+\pi^-, \pi^0\pi^0$	
$f'(1515)$			2^+
$\to K\bar{K}$	$0.60 \pm 0.14 \pm 0.12$	$K^+K^-, K_S^0K_S^0$	
$\iota(1440)$			
$\to K\bar{K}\pi$	$5.0 \pm 0.3 \pm 0.7$	$K_S^0K^\pm\pi^\mp, K^+K^-\pi^0, K_S^0K_S^0\pi^0$	0^-
$\to \gamma\rho^0$ (probable)	$0.010 \pm 0.02 \pm 0.02$	$\gamma\rho^0$	0^- prob.
$X(1.2-2.0$ GeV)			?
$\to \eta\pi\pi$	3.0 ± 0.6	$\eta\pi^+\pi^-, \eta\pi^0\pi^0$	
$X(1.5-1.9$ GeV)			
$\to \rho\rho$	2.3 ± 0.9	$\rho^0\rho^0, \rho^+\rho^-$	$(\text{even})^-$
$\to \omega\omega$	$0.67 \pm 0.17 \pm 0.24$	$2(\pi^+\pi^-\pi^0)$	$(\text{even})^-$
$\theta(1700)$			
$\to K\bar{K}$	$0.96 \pm 0.12 \pm 0.18$	$K^+K^-, K_S^0K_S^0$	2^+
$\to \eta\eta$	0.38 ± 0.16	$\eta\eta$	
$\to \pi^+\pi^-$ (probable)	$0.16 \pm 0.04 \pm 0.03$		
$X(2.1$ GeV$) = h(2040)$?		$\pi^+\pi^-$	$(\text{even})^+$
$\to \pi^+\pi^-$	$0.30 \pm 0.05 \pm 0.06$		
$\xi(2220)$			
$\to K^+K^-$	$0.058 \pm 0.018 \pm 0.015$	K^+K^-	$(\text{even})^+$
$\eta_c(2980)$	12.7 ± 3.6	$\eta\pi\pi, \eta'\pi\pi, \eta'K\bar{K}, K\bar{K}\pi,$ $\rho\rho, \phi\phi, K^*\bar{K}^*$	0^-
$p\bar{p}$ inclusive	0.489 ± 0.049		
$\eta\eta'$ inclusive	< 0.84 (90% *C.L.*)		
$S^*(975)$			
$\to \pi\pi$	< 0.07 (90% *C.L.*)	$\pi^+\pi^-$	0^+

The present status (15) of radiative ψ decay measurements is summarized (16) in Table 1.1. All numbers quoted are from Mark III except for $\gamma\pi^0$,

$\gamma\eta$,$\gamma\theta(\eta\eta)$, $\gamma\eta_c$ (inclusive), and the $\gamma\eta\eta'$ upper limit, which are from the Crystal Ball. In addition to the ι, there are other interesting glueball candidates. The $\theta(1720)$, with $J^{PC} = 2^{++}$, is observed in K^+K^-, $K^0_SK^0_S$, $\eta\eta$, and probably also $\pi\pi$. The $\xi(2220)$, which is unusually narrow ($\Gamma < 40$ MeV at 90% C.L.), is observed (17) in K^+K^-. Its spin and parity are unknown, although they are restricted to the values (even)$^{++}$ because $C(K\bar{K}) = P(K\bar{K}) = (-1)^L$, and production in radiative ψ decay implies $C = +1$. Structure is also observed in the $\eta\pi\pi$, $\rho\rho$, and $\omega\omega$ channels in the 1-2 GeV region. Recent studies indicate that even spin and odd parity are dominant in the 1.5-1.7 GeV mass region in $\rho\rho$ and $\omega\omega$ (18). It has proved very difficult with the present statistics to untangle what are probably 2-3 resonances in the $\eta\pi\pi$ mass spectrum.

The radiative decays to exclusive final states (excluding the η_c) sum to a branching fraction of about 2%, only 22% of the theoretical prediction. The Mark II collaboration has made an inclusive measurement for values of $x = 2E_\gamma/M_\psi$ from 0.6 to 1.0. The branching fraction is (19)

$$B(\psi \to \gamma + X) = (4.1 \pm 0.8)\%,$$

which is in reasonable agreement with the QCD prediction of 5% for this range. The shape of the QCD photon energy spectrum, however, does not agree well with the data. The theoretical spectrum is governed largely by three-body phase space for massless particles and is peaked at high x, whereas the measured spectrum falls for $x > 0.6$. More sophisticated theoretical calculations will be described later.

In this thesis, analyses of the production, decay, and quantum numbers of the ι are presented in the context of both theoretical predictions and previous results on the ι and other isoscalar states in the 1.4 GeV mass region. After a description

of the Mark III detector, studies of the $\psi \to \gamma K^0_S K^{\pm}\pi^{\mp}$, $\gamma K^+K^-\pi^0$, and $\gamma K^0_S K^0_S \pi^0$ channels are presented. The spin-parity measurement is performed in both the $K^0_S K^{\pm}\pi^{\mp}$ and $K^+K^-\pi^0$ modes using a three-body analysis technique that is insensitive to which two-body decay modes are present in the $K\bar{K}\pi$ system. A study is also made of the decays $\psi \to \gamma X$; $X \to \gamma V$, where $V = \rho^0$, ϕ, and ω. This electromagnetic decay provides information about the quark content of the state X. Measurements of $B(\psi \to \gamma\eta')$ and $B(\psi \to \gamma\eta)$ are also made and compared with the results obtained for the ι. Upper limits for ι signals in the $\eta\pi\pi$, $K\bar{K}\pi\pi$, and $\rho\pi\pi$ channels are presented and compared with theoretical expectations. Evidence is also presented for a number of previously unobserved decays of the form $\psi \to$ Vector + Pseudoscalar, which were found as backgrounds to the channels listed above. Finally, detailed discussions of the two- and three-body helicity formalisms and their application to the calculation of the decay angular distributions are given in the two appendices.

Chapter 2. The Mark III Detector

2.1 Overview of the Mark III Detector

The design of the Mark III detector (20) evolved from that of previous magnetic detectors at SPEAR. The basic requirements for studying physics in the 3-4 GeV region (ψ, ψ', ψ'') follow from a few simple considerations (21):

1. The particle momenta are typically about 0.5 GeV/c; very few tracks have $p > 1$ GeV/c.

2. The mean multiplicity of both charged tracks and photons is about four. Events with more than eight charged tracks are rare.

3. Because of the presence of π^0's and η's in many decays, good photon detection efficiency in the 50-300 MeV range is extremely important.

There are several consequences of the low charged particle momenta. First, the momentum resolution is predominantly due to multiple scattering. It is therefore essential to minimize the amount of material encountered by the charged tracks. Second, for a path length of about 1 m, very good $\pi/K/p$ separation can be achieved by time-of-flight with a time resolution of about 200 psec. Finally, although a high magnetic field improves the momentum resolution, it also increases the transverse momentum required for a charged track to reach the time-of-flight counters. For a 1.15 m radius and a B-field of 4 kG, the cutoff in p_T is about 70 MeV/c.

Figure 2.1 shows the axial and transverse views of the Mark III detector. The main features of the detector, moving outward from the beam axis, will now be described. (The thickness in radiation lengths of various components is

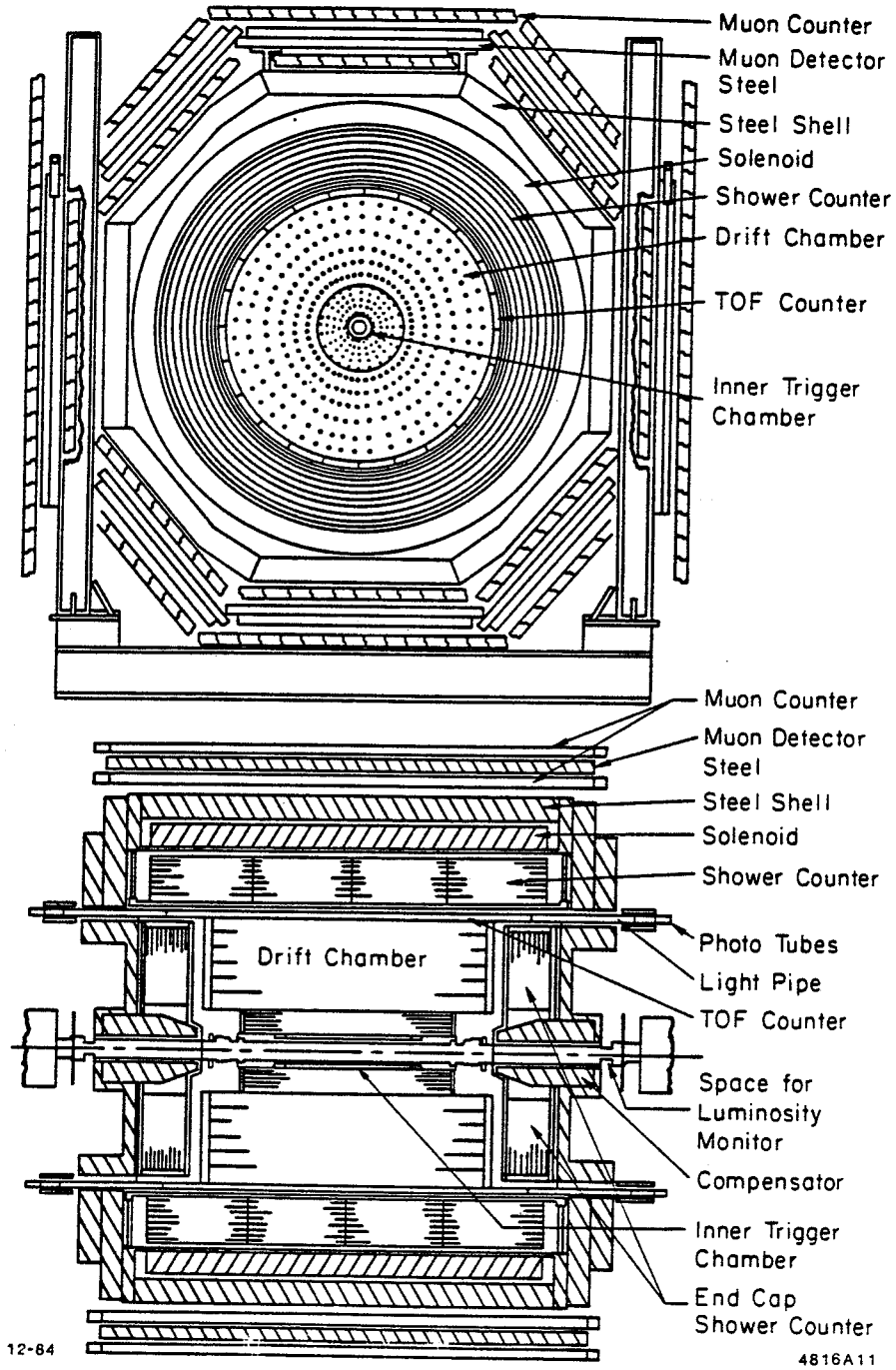

Figure 2.1. The Mark III detector viewed a) from along the beam axis and b) from the side (transverse view).

Table 2.1. Thickness in Radiation Lengths of Detector Materials.

Detector Component	Thickness (% r.l.)
Beam pipe (1.5 mm Thick Be)	0.400
Trigger drift chamber	
Gas	0.026
Wires	0.031
Cylinders (5)	0.610
Total	0.667
Main drift chamber	
Inner wall	0.160
Gas	0.754
Wires	0.154
Total	1.068
Time-of-Flight Scintillators	12.0
Aluminum spool	28.0

given in Table 2.1.) The beam pipe is made of beryllium to minimize multiple scattering. Surrounding the beam pipe at a radius of about 0.1 m is a small drift chamber that provides a timing signal for the trigger as well as four position measurements radially. The main drift chamber, which is 2.337 m long, has 30 sense wires arranged radially, and covers 85% of the solid angle. Just outside the main drift chamber, at a radius of 1.15 m, are the 48 time-of-flight scintillation counters. The electromagnetic calorimetry consists of a barrel shower counter and two endcaps, which together cover 94% of the solid angle. The barrel is inside the conventional solenoidal magnet in order to maximize the efficiency for low-energy photons. The magnet produces an axial field of about 4 kG. The steel flux return and the muon counters are outside the coil.

The following coordinate system is used to describe events. The x-axis points inward, towards the center of the ring; the y-axis is vertical, normal to the plane of the ring; and the z-axis points along the positron beam. Thus, the x-z plane coincides with the bend plane of the SPEAR dipole magnets.

2.2 THE TRIGGER DRIFT CHAMBER

The trigger drift chamber (layer 1) is a low-mass, cylindrical chamber immediately surrounding the beam pipe. Its primary purpose is to provide a timing signal, t_{event}, that can be compared to the beam crossing time t_{cross}. Events with large values of $|t_{event} - t_{cross}|$ are usually due to cosmic rays and are rejected by the trigger. In previous magnetic detectors at SPEAR this time measurement was performed by a set of scintillation counters surrounding the beam pipe. However, multiple scattering of charged tracks in such counters makes a substantial contribution to the momentum resolution at low momentum. Mark III chose to improve the momentum resolution at the expense of some time resolution. The trigger rate is still quite low, however.

The trigger drift chamber is composed of four concentric layers of drift cells separated by thin foam cylinders (Fig. 2.2a). The cylinders are covered on each side with aluminized mylar. Each layer contains 32 sense wires (38 μm stainless steel) maintained at about +2100 volts, alternating in ϕ with 32 guard wires (178 μm BeCu) maintained at about −200 volts. The z-coordinate is measured by charge division. The materials in layer 1, including the cylinders, wires, and gas (70% argon/30% ethane) account for 6.67×10^{-3} r.l.

The technique by which layer 1 is used to obtain a timing signal is illustrated in Fig. 2.2b. Near the interaction region, the x-y projection of most tracks is

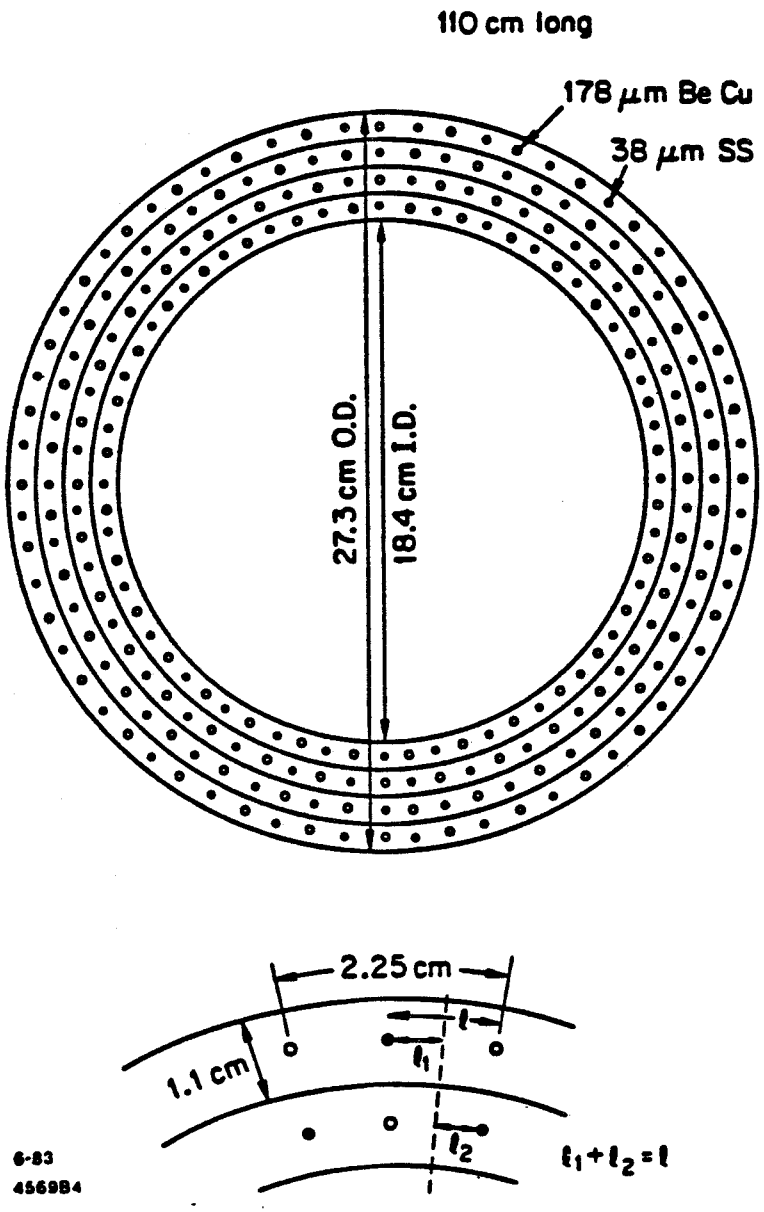

Figure 2.2. Trigger drift chamber electronic structure. a) Cell configuration as viewed along the beam axis. In each of the four sub-layers, the 32 sense wires (dark circles) alternate in ϕ with 32 field wires (open circles). b) Expanded view showing half-cell offset of wires in consecutive layers. The sum of the drift distances $l = l_1 + l_2$, and hence the sum of drift times, is approximately constant.

very nearly radial. As a result, the sum of the drift times,

$$t = t_1 + t_2 = \frac{l_1 + l_2}{v_d},$$

in two consecutive layers is essentially constant, regardless of the position of the track within the cell. To reduce time slewing, the signals from each end of a wire are OR'ed, and the resulting signals from two offset wires are fed into opposite ends of a tapped delay line (chronotron). The time at which the pulses overlap is approximately constant for true e^+e^- events.

In practice, it is required that the overlap take place within a 100 ns gate. This reduces the triggers from cosmic ray events by the ratio of the chronotron gate width to the time interval between beam crossings (781 ns), approximately 0.13. (Without the chronotron, the gate width would have to be extended to the maximum drift time (250 ns); the cosmic ray rejection would then be only $250/781 \approx 0.3$.) A rough estimate of the cosmic ray trigger rate is therefore

$$\nu_{cosmic} \sim (2 \times 10^2 m^{-2} s^{-1})(10^{-1} m^2)(\tfrac{1}{8}) \sim \mathcal{O}(1 \text{ Hz}).$$

Figure 2.3 shows the distribution of $t = t_1 + t_2$ for events satisfying the trigger requirements (and therefore have at least one track within the time gate). The hadronic events occur well within the 100 ns interval and peak at $t = 0$, whereas the cosmic ray events are distributed uniformly over the gate interval.

2.3 The Main Drift Chamber

The main drift chamber (22) provides momentum measurements of charged tracks over about 85% of the solid angle. The chamber incorporates a number of unusual features, including an inner layer of large cells for dE/dx measurements (layer 2) and six outer layers of small cells (layers 3-8) with a triplet sense wire

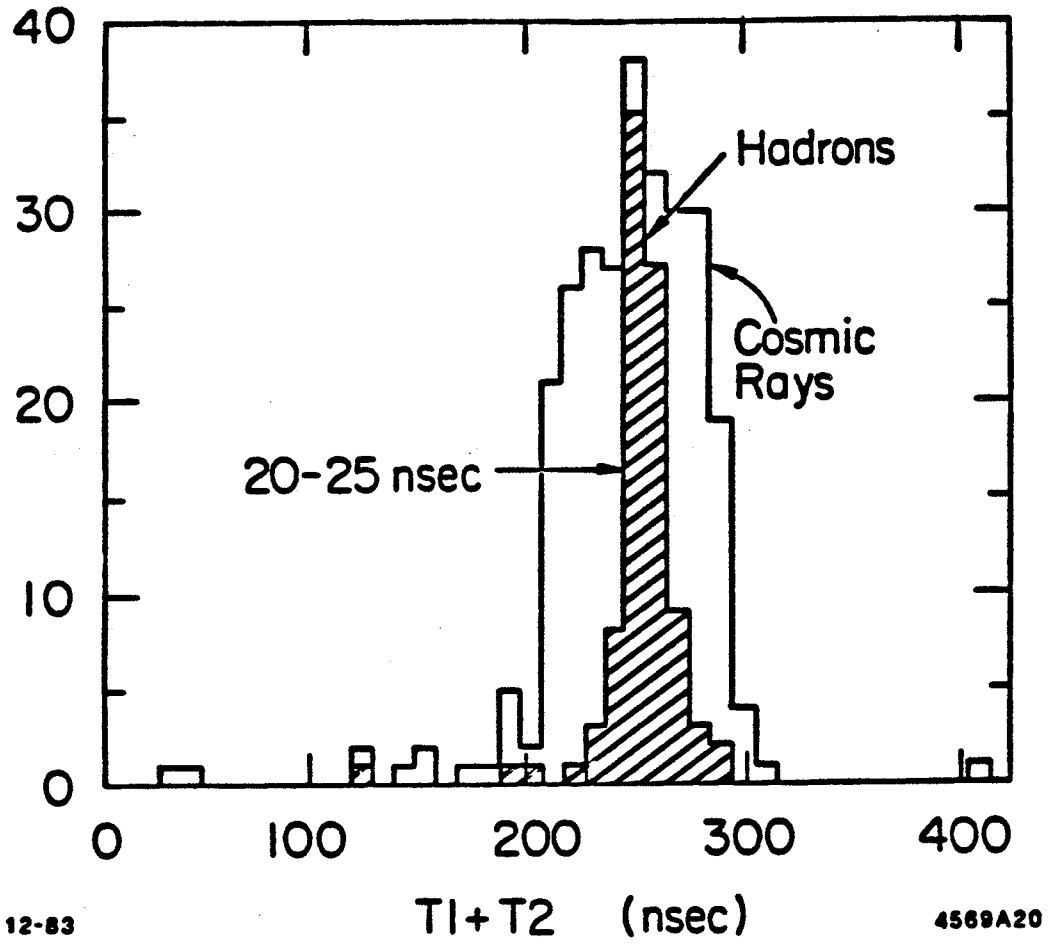

Figure 2.3. The distribution of the chronotron time sum $t = t_1 + t_2$ for events satisfying the trigger. Events from e^+e^- collisions peak at $t = 0$, whereas the distribution of cosmic ray events is uniform.

configuration. The middle wire of each triplet is offset by 800 μm in ϕ with respect to the other two sense wires, allowing immediate resolution of the left-right ambiguity. Together, layers 2-8 contain 1968 sense wires and provide up to 30 position measurements per track. The z-coordinates of the tracks are determined both by stereo angle layers (layers 4 and 6) and by charge division measurements (in layers 3, 5, and 7). The design, electronics, and performance of the drift chamber are summarized below.

Design

The main drift chamber is a cylindrical structure of inner radius 14.47 cm, outer radius 114.3 cm, and length 233.7 cm. Axial and transverse views of the drift chamber are shown in Fig. 2.4. The inner boundary of the chamber (1.7×10^{-3} r.l.) is a phenolic clad paper hexcell tube covered on both sides with mylar and 8 μm of aluminum. The aluminum surface inside the chamber is held at about -2kV. The outer surface of the drift chamber is a 6.25 mm thick curved aluminum plate that counteracts the pull of the wires on the endplates and provides a gas seal. The inner surface of these panels is also covered with an aluminized mylar skin that is held at about -2kV. The negative high voltage on the inner and outer cylindrical boundaries simulates the presence of neighboring layers. Without this high voltage, the electric field, and hence the gain, would drop in the inner and outer layers.

Figure 2.4 shows that layer 2 is shorter in the z-direction than the outer layers. This allows space for the compensating solenoids, which are positioned close to the drift chamber. The endplates for layer 2 are made of NEMA G-10; those for the outer layers are made by mounting 16 pie-shaped G-10 pieces on the outside of 7.62 cm thick aluminum hexcell. The wires are held in place by feedthroughs mounted in precision drilled holes in the G-10, and their positions

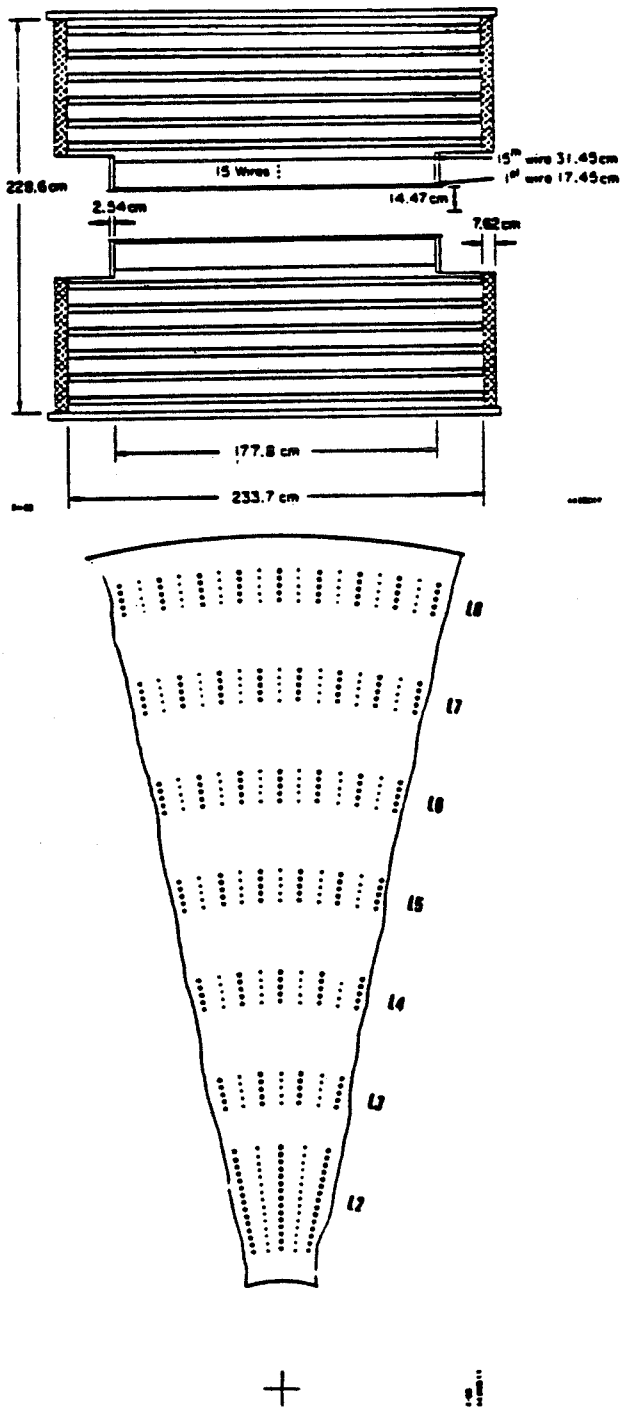

Figure 2.4. The main drift chamber a) transverse and b) axial views showing the cell configuration. Layers 2, 3, 5, 7, and 8 are axial; layers 4 and 6 are stereo.

in the outer layers are known to about 50 μm.

The cell arrangement is shown in Fig. 2.4b. In layer 2, there are 32 cells azimuthally, each of which contains 13 gold-plated tungsten sense wires (20 μm diameter) spaced 1 cm apart radially. The middle wire, however, is not read out. To resolve the left-right ambiguity, the sense wires are alternately offset by $\pm$150 μm with respect to the center of the cell. The wires are instrumented for dE/dx and provide a high density of measurements to improve the reconstruction efficiency for K_s^0's and decaying charged kaons. The dE/dx measurements have provided useful K/π separation at low momenta but were not used in the analysis discussed herein. The cells are bounded by a 57 μm stainless steel guard wire at the inner and outer radii and by fifteen 175 μm CuBe field wires in the ϕ direction. Because the cell half-width increases from 1.8 cm to 3.0 cm, the high voltage must be increased with radius to equalize the sense wire gain. For dE/dx measurements, the gain must also be kept low ($\sim 2 \times 10^4$) to prevent saturation.

The outer layers (layers 3-8) are composed of small cells, arranged so that layer N is at the radius $13.45 \times N$ cm and contains $16 \times N$ cells. Consequently, the dimensions of the cells are similar, 4 cm high and 5.28 cm wide (Fig. 2.5). The three gold-plated tungsten sense wires are at ground potential. The outer two sense wires are offset by $+400\mu$m in the ϕ direction, and the middle sense wire is offset by -400μm. The resistive stainless steel guard wires, also at ground, bound the cell at the inner and outer radii. They provide measurements of the z-coordinate by charge division in layers 3, 5, and 7. The pulse on the guard wire is induced by positive ions drifting away from the sense wire; its pulse height is about 15% of that on the neighboring signal wire. The two guard wires are not read out individually but are joined at the ends. More precise z measurements are provided by the wires in layers 4 and 6, which have $+7.7°$ and $-9.0°$ stereo

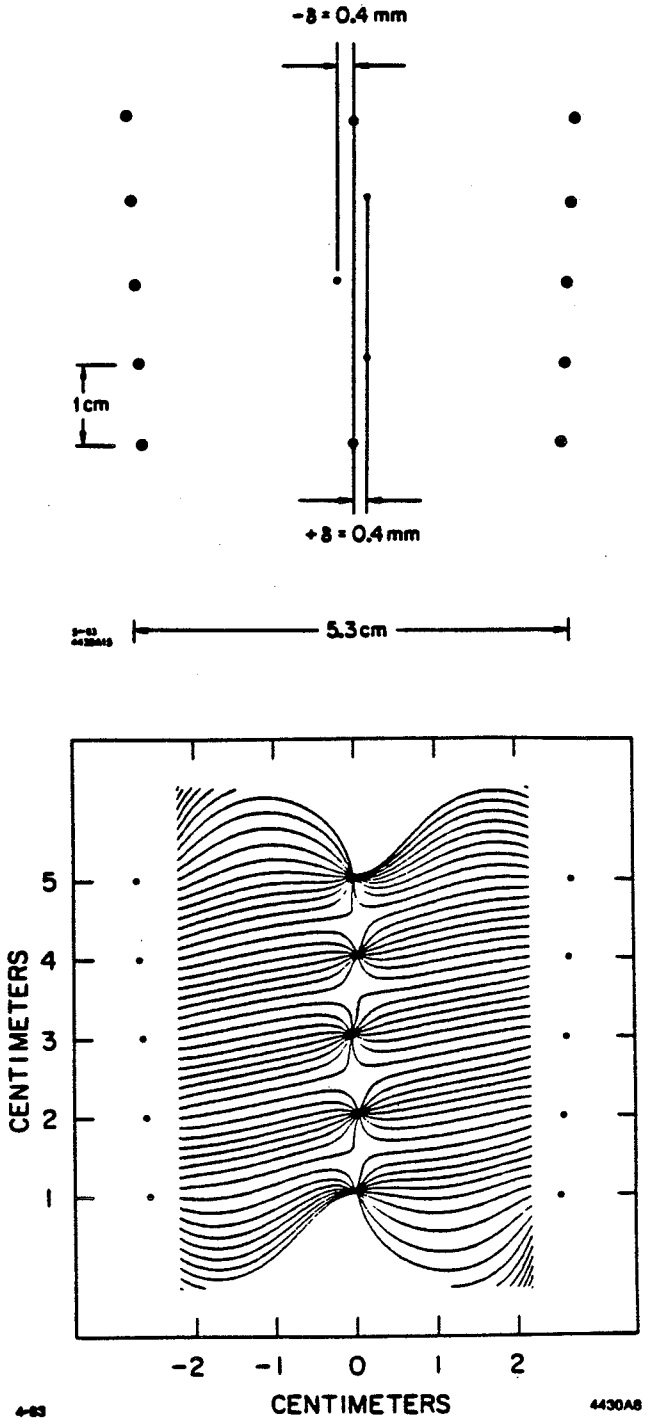

Figure 2.5. Main drift chamber electronic structure. a) Cell configuration in layers 3-8. The sense wires are offset by ± 400 μm with respect to the center of the cell. b) Electron drift trajectories.

angles, respectively. The diameters of the sense, guard, and field wires are 20 μm, 57 μm, and 175 μm, respectively, as in layer 2.

The voltages on the CuBe field wires increase radially within a cell from about 4200 volts to 4400 volts. This graded voltage sequence compensates for the increase in cell size and results in approximately equal gains ($\sim 2 \times 10^5$) for the sense wires in layers 3-8. The electron drift trajectories are shown in Fig. 2.5b. The electric field ($\sim$ 800 volts/cm) is fairly uniform over most of the drift region. The maximum drift time is 550 ns.

The gas mixture used is 89% argon, 10% CO_2, 1% CH_4, which is adequate but not optimal in terms of drift properties. The drift velocity as a function of E-field is shown in Fig. 2.6. This mixture does not have a tendency to grow "whiskers," which are potentially disastrous carbon filaments deposited on the wires. At the very high electric fields encountered at the surface of the field wires, high voltage breakdown appears to trigger the formation of such whiskers in many drift chamber gas mixtures commonly used.

Electronics

Block diagrams of the electronics for layer 2 and layers 3-8 are shown in Fig. 2.7. Because layer 2 is operated at low gain for dE/dx ($\sim 2 \times 10^4$), it was necessary to install preamplifiers on the face of the chamber. An additional difficulty was the presence of crosstalk between the neighboring sense wires within the cells of layer 2. The induced pulse on a sense wire has the opposite polarity from the direct pulse, and the resulting cancellation reduces the efficiency. Given the large fluctuations in pulse height, this can be a severe problem. To minimize this effect, resistors are placed between nearest and next-nearest radially neighboring sense wires. The values of the resistors are chosen so that the charge taken away from a hit wire to the neighboring wire approximately

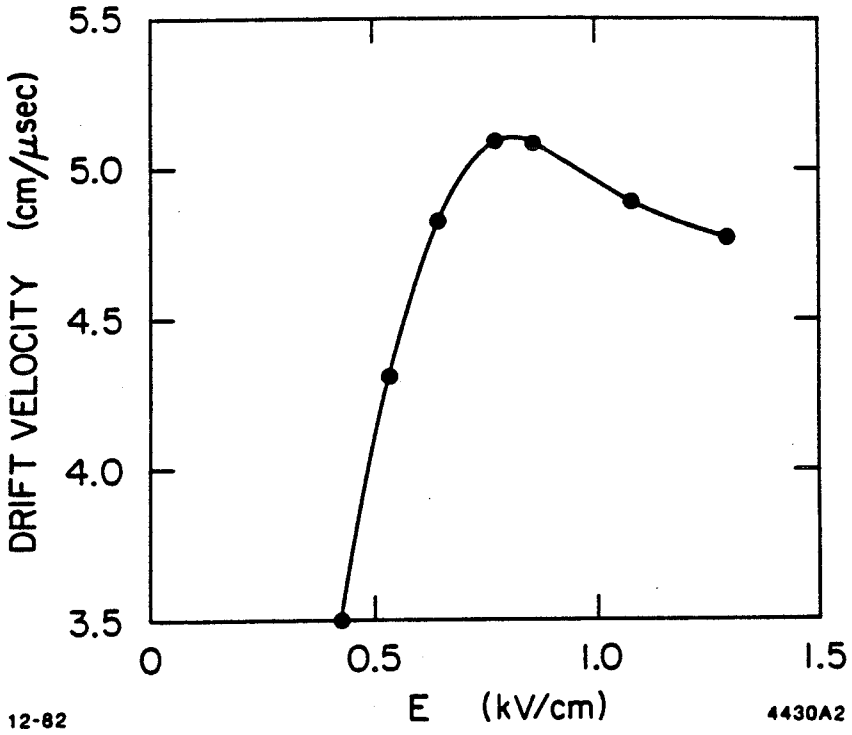

Figure 2.6. Drift velocity as a function of E-field for the 89% Ar, 10% CO_2, 1% CH_4 gas mixture used in the main drift chamber.

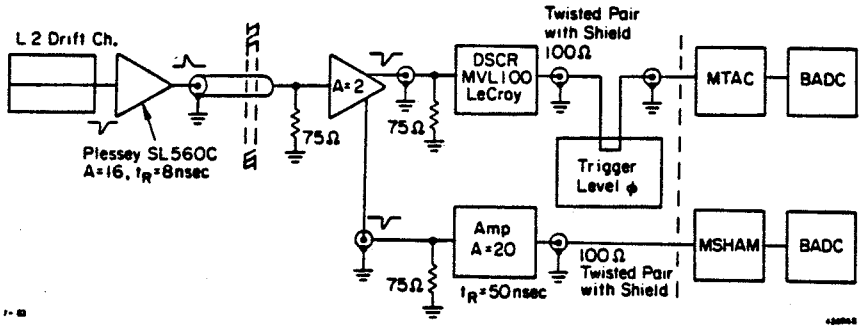

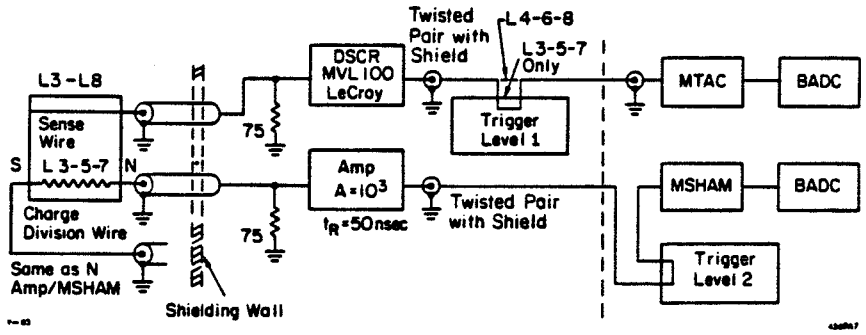

Figure 2.7. Block diagrams of the electronics in layer 2 and in layers 3-8.

cancels the induced pulse. The signals from the preamplifiers are then further amplified and discriminated by LeCroy MVL 100's. In layers 3-8, the signals from the sense wires go directly to the MVL 100's.

The discriminated signals from layers 2-8 are fed into multi-hit time to amplitude converters, or MTAC's (23). In each MTAC channel, the start up of a ramp is initiated by a signal derived from beam crossing. The ramp charges a set of four capacitors. When the discriminator pulses from a single wire arrive at the MTAC, they successively clock a bit through a shift register that decouples the corresponding capacitor from the ramp by opening a FET switch. The charge on a capacitor is therefore proportional to the drift time. In principle, up to 4 hits per wire can be measured, but in practice only the earliest hit is used.

The pulses from the charge division and dE/dx wires are first amplified and then fed into multi-hit sample and hold modules, or MSHAM's (24), which measure the total charge in the signal. The gate width is set to be the maximum possible drift time, although up to four possible time bins can be used. The slow fall-off of the drift chamber pulses, however, makes the use of one long time bin desirable.

As in all systems in Mark III, if the event satisfies the trigger requirements, all of the analog timing and pulse height information is digitized and corrected by a smart processor (BADC) and then transferred to the VAX 11/780 online computer.

Performance

A large number of detailed properties of the drift chamber must be understood to achieve optimum resolution. These include the wire positions; electrostatic deflection and gravitational sag; the drift velocity in different cell

regions and sides of the cell; the t_0's (offsets corresponding to the earliest possible drift time); and the Lorentz angle. A useful quantity for studying the resolution is

$$\Delta = V_{drift}\left[\tfrac{1}{2}(t_1 + t_3) - t_2\right], \tag{2.1}$$

where t_1 and t_3 are the drift times to the outer two sense wires and t_2 is the drift time to the middle sense wire. The sign of Δ gives the side of the cell on which the track passed, and the magnitude of Δ gives the stagger between the sense wires. Figure 2.8a shows the distribution of Δ for all cells in layer 5. There are two well-resolved peaks corresponding to tracks on the two sides of the cell. Because $\sigma_\Delta = \sqrt{3/2}\,\sigma_x$, where σ_x is the single wire resolution, the width of the peaks is a measure of the position resolution. For layers 3-8 the resolution is about 220 μm, and for layer 2 it is 250-300 μm. In addition to resolving the left-right ambiguity, the three sense wires measure the local tangent vector to the track. This vector aids considerably in pattern recognition.

The z-position is determined to about 0.15 cm from a stereo angle wire and to about 1.5 cm by charge division. The charge division information is used primarily in pattern recognition, predicting which stereo angle cells should be associated with a track consisting of cells from the axial layers. The charge division measurements are also used for steep tracks, which do not reach layer 4 and therefore have no stereo information.

These measurements lead to the following resolutions on the momentum p, azimuthal angle ϕ, and dip angle λ:

$$\sigma_p/p = 0.015\sqrt{1 + p^2(\mathrm{GeV})^2}$$

$$\sigma_\phi = 2 \text{ mrad}$$

$$\sigma_{\tan\lambda} = 0.011,$$

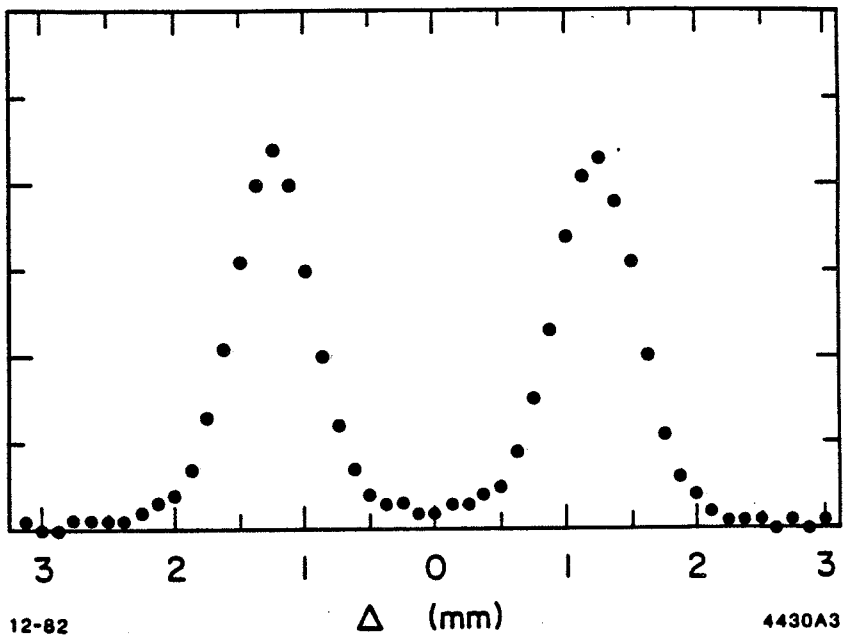

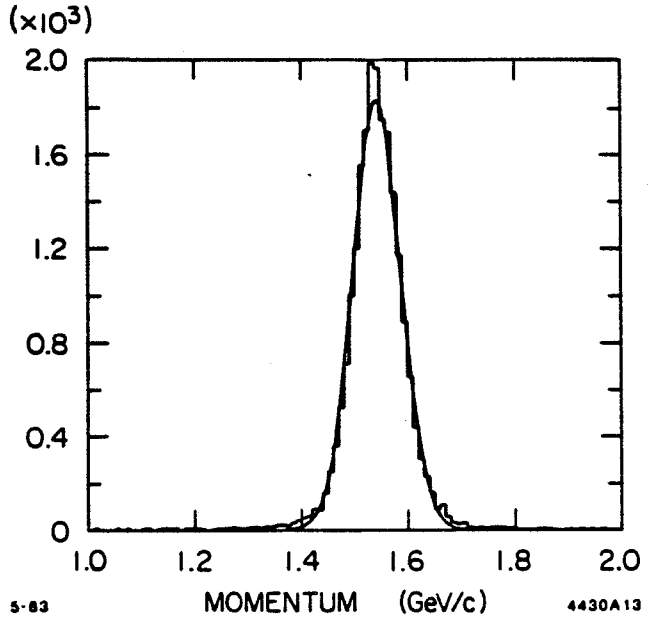

Figure 2.8. Main drift chamber performance. a) The distribution of Δ, which is the difference between the average drift distance to the outer two sense wires and the drift distance to the middle sense wire. The two peaks correspond to tracks on the two sides of the cell, and the width of the peak is a measure of the intrinsic resolution. b) Momentum spectrum for muons produced by the process $\psi \rightarrow \mu^+\mu^-$. The σ of the Gaussian curve is 45 MeV/c.

where the first term in the momentum error is due to multiple scattering. The momentum spectrum for muons produced by the process $\psi \rightarrow \mu^+\mu^-$ ($p = 1.545$ GeV/c) is shown in Fig. 2.8b. The σ of the Gaussian curve is 45 MeV/c.

2.4 THE TIME-OF-FLIGHT SYSTEM

Particle identification by time-of-flight is essential for removing backgrounds that cannot easily be rejected by kinematic fits. The time-of-flight system consists of 48 scintillation counters that cover about 80% of the solid angle and allow more than 2σ separation of charged kaons and pions up to 1.2 GeV/c. The main features of the time-of-flight system, including a brief description of the counters, the electronics, and the use of time-of-flight information in data analysis is given below. The system is discussed in greater detail in the references (25).

The Counters

The 48 Nuclear Enterprises Pilot-F scintillation counters are mounted lengthwise in a cylindrical configuration on the outside of the main drift chamber (Fig. 2.9) and are held in place by stainless steel bands about the circumference. The radius at the inner surface is 1.15 m. Because the time resolution is in general (26) proportional to $\sqrt{L/N_e}$, where N_e is the number of photoelectrons and L is the length of the counter, it is desirable to maximize the number of produced photons and hence the thickness of the counters. The scintillators are 5.1 cm thick (12% r.l.) trapezoids that are about 3.175 m long and 0.156 m wide over most of their length.

The light from each end of the scintillator is brought out through holes in the iron magnetic flux return by ultraviolet transmitting plexiglass light guides. The area of the light guides is decreased in two steps, first at the holes in the

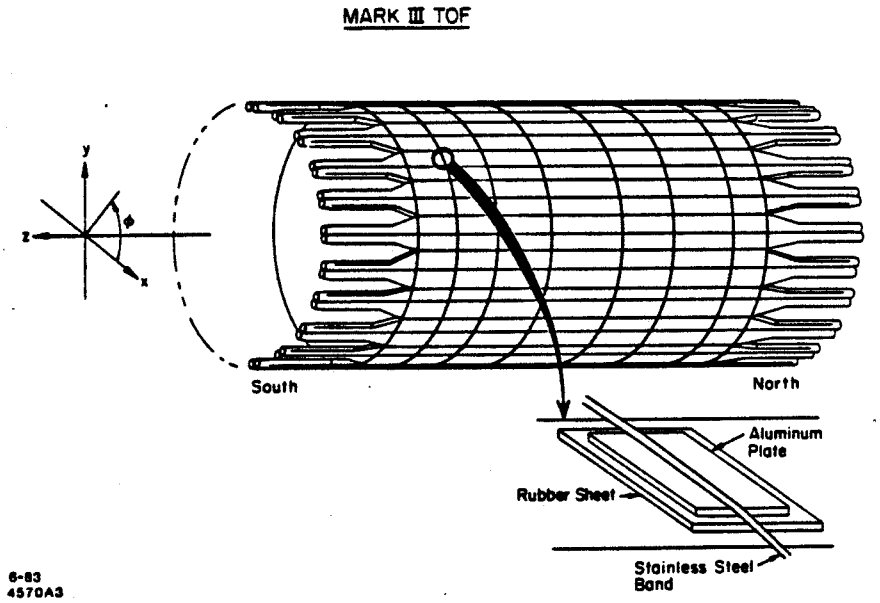

Figure 2.9. Configuration of the 48 scintillators that make up the time-of-flight system. The light is detected by phototubes at each end.

magnet yoke and then at the photomultiplier. The area of the light guide does not decrease in the intermediate region so that the time spread of the leading photons is minimized. The relative times of the signals from the two ends can be used to determine the rough z-position of the incident particle. In practice, the z-dependence of the signal arrival time is removed by using drift chamber information to calculate the projected z-position of the track at the scintillator.

The photomultipliers, Amperex XP2020, were chosen for their small transit time variation (0.25 ns) across the photocathode surface. Each photomultiplier is mounted outside the flux return in a cylinder made of mu-metal and iron, which reduces the magnetic field to about 0.1 G at the photocathode.

Electronics

The timing of the system is governed by a signal induced in a monitor in the SPEAR beam pipe by the incoming electron bunch. The signal is discriminated by a very fast discriminator that also compensates for pulse height variations; the resulting resolution on the beam-crossing time is a few picoseconds. (However, the spread of the bunches in the z-direction leads to an uncertainty in the collision time of about 90 psec.) When a pulse arrives from a photomultiplier, it initiates the discharge of a capacitor that normally rests at 5 volts. The discharge does not begin until the pulse-height exceeds a threshold set by the computer. The discharge is stopped by the delayed beam-crossing signal, leaving a residual charge that is used to determine the time-of-flight. The motivation for using the beam-crossing signal as a common stop, rather than as a common start, is that it allows one to hold the capacitors at their constant resting voltage for most of the time, avoiding the possibility of residual charge caused by polarization of the dielectric. The time at each of two thresholds is measured to provide additional pulse-shape information; in practice, the higher threshold time does not improve

the resolution beyond that achieved using the first time and correcting for time-walk as discussed below.

The total charge of the pulse is also measured, which allows time-walk variations to be removed. The time-walk is due to the fact that the rise time of the signal to threshold is a function of the total charge in the signal ($t_w \propto q^{-\frac{1}{2}}$). Both pieces of information are digitized by the BADC and transferred via CAMAC to the online VAX 11/780 computer if the event satisfies the trigger requirements.

Performance and Use in Data Analysis

Optimum performance of the time-of-flight system is achieved only after extensive online and offline calibration. The performance of the system is monitored online using a laser that sends light to the center of the scintillators via quartz fibers. Details of the calibration are discussed in Ref. (25). Particle identification by time-of-flight is based on the relations

$$M^2 = p^2 \left(\frac{1-\beta^2}{\beta^2} \right) \qquad \beta = L/cT, \tag{2.2}$$

where β is determined using the time-of-flight T and the path length L, which is measured in the drift chamber. Because L, P, and z are required, the tracking resolution of the drift chamber contributes to the overall time-of-flight resolution:

$$\sigma^2_{TOF} = \sigma^2_{SCINT} + \sigma^2_{DC}. \tag{2.3}$$

The σ^2_{DC} term is determined using the drift chamber track parameters and the associated error matrix. The intrinsic time-of-flight resolution, σ_{SCINT}, has some z-dependence, being somewhat worse near the centers of the counters. The average time resolution is $\sigma_{TOF} = 171$ psec for bhabhas

($e^+e^- \to e^+e^-$ or $e^+e^- \to \psi \to e^+e^-$), 175 psec for μ pairs ($e^+e^- \to \mu^+\mu^-$ or $e^+e^- \to \psi \to \mu^+\mu^-$), and 189 psec for pions from $\psi \to \rho\pi$ events (Fig. 2.10a). The reason for the somewhat poorer resolution for pions is not well understood.

To use the time-of-flight information quantitatively, one calculates the likelihood that the measured time would be found for a particular mass hypothesis and track parameters. If the measured time is T and the predicted time for mass hypothesis m_I is T_I, then the likelihood is

$$w_I = e^{-\frac{1}{2}\left(\frac{T-T_I}{\sigma_I}\right)^2}. \tag{2.4}$$

This quantity is used extensively in the data analysis discussed later.

The good $\pi/K/p$ separation is evident from scatterplots of mass squared vs. momentum (Fig. 2.10b) and β vs. momentum (Fig. 2.11). The events are selected from a sample of ψ decays in which the z-positions calculated from the drift chamber data and from the time-of-flight data agree. The resolution on the mass squared is

$$\sigma_{M^2} = \frac{\partial M^2}{\partial T}\sigma_T = 2\left(\frac{P^2}{\beta}\right)\frac{\sigma_T}{t_0} = 2PE\left(\frac{\sigma_T}{t_0}\right), \tag{2.5}$$

where $t_0 = L/c$ is in the range 4.0–5.6 nsec. At high momentum, the resolution on the mass squared is proportional to P^2, explaining the shape of the distributions in Fig. 2.10b. Using $\sigma = 189$ psec, one finds that $\sigma_{M^2}/M^2 \simeq 0.2$ for a kaon with $p = 800$ MeV/c.

2.5 The Shower Counter

The Mark III electromagnetic calorimetry consists of three components (Fig. 2.12): a cylindrical barrel shower counter (27) and two endcap shower counters (28) that extend the solid angle coverage to within about 11° of the

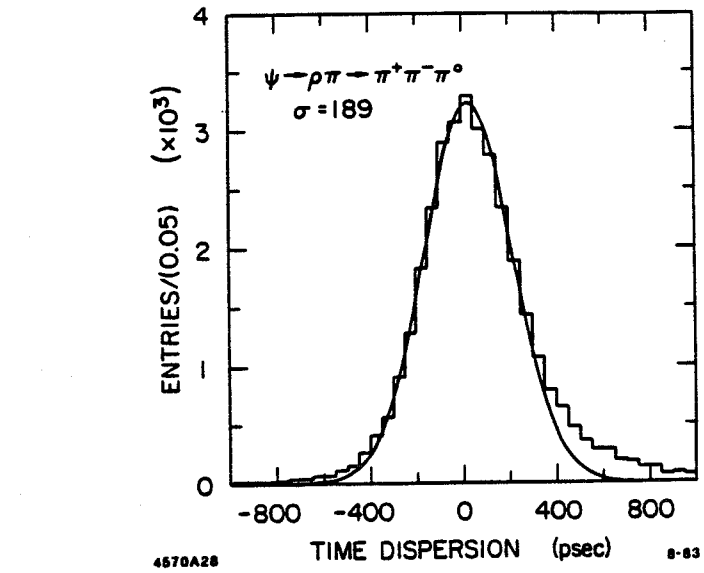

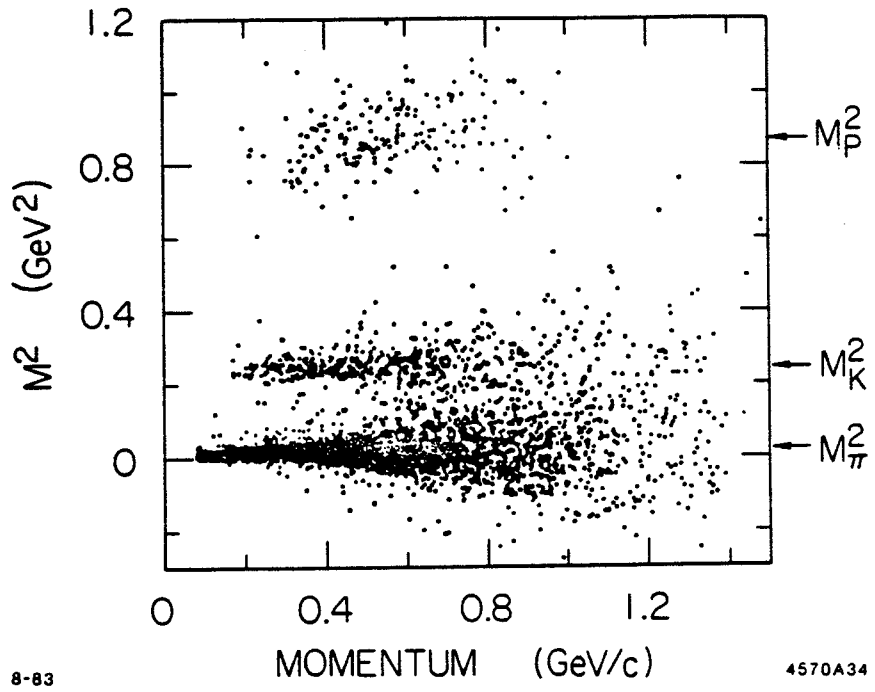

Figure 2.10. Time-of-flight system performance. a) Time resolution for pions from $\psi \rightarrow \rho\pi$: $\sigma = 189$ ps b) mass squared vs. momentum, showing π, K, p bands.

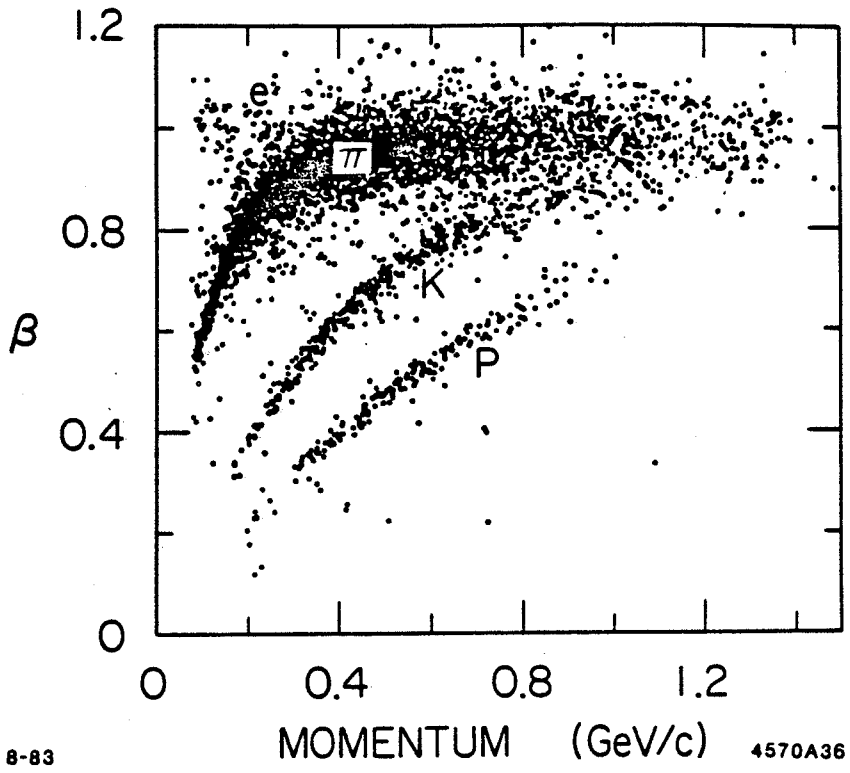

Figure 2.11. Time-of-flight system performance. β vs. momentum.

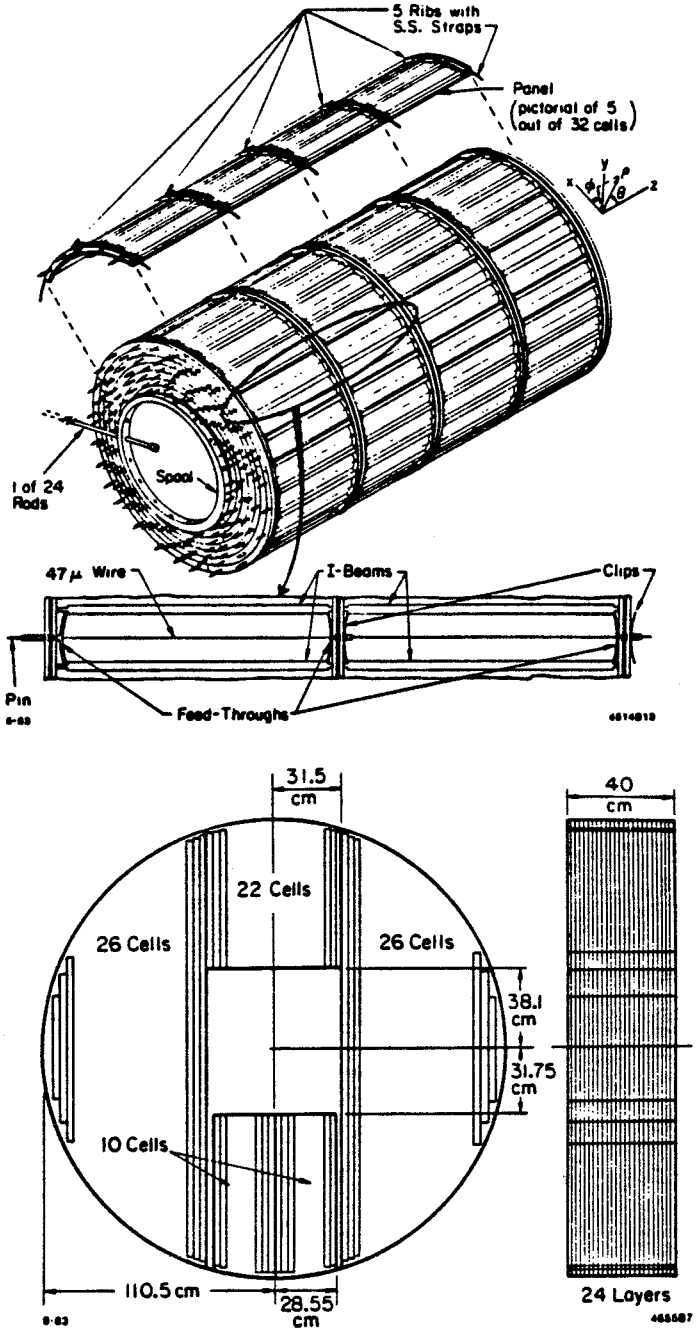

Figure 2.12. Electromagnetic calorimetry. a) Schematic drawing of the barrel shower counter (not to scale) and b) the endcap shower counters.

beam axis. The total solid angle coverage of these systems is 94% of 4π. Because many decay processes involve π^0's or η's, good efficiency for low-energy photons is essential for the reconstruction of exclusive final states. Good efficiency can also be important for spin-parity analyses, because the energy of a photon is often correlated with the angle at which it is emitted in the decay rest frame. The design, electronics, and performance of the shower counters are discussed briefly below.

Design

The barrel and endcaps have a similar design with 24 layers of rectangular proportional tubes alternating with 23 sheets of 0.5 r.l. thick lead-antimony alloy. In the barrel, the proportional tubes are formed from aluminum I-beams and lie along the beam direction (z); in the endcaps the tubes are aluminum extrusions and are mounted in the vertical (y) direction. Each tube contains a single 46 μm diameter stainless steel sense wire maintained at about 2kV. The coordinate of the shower counter along the wire is measured by charge division. Both systems use a gas mixture of 80% argon/20% methane.

To minimize the material traversed by photons before they are detected, the barrel shower counter was placed inside the magnet. As a consequence, the efficiency for low-energy photons is very good (see below). The placement of the barrel inside the magnet required a cylindrical structure that could be supported from the ends. This problem was solved with an aluminum spool of length 3.85 m, outer diameter 2.52 m, and thickness 23 ± 4 mm, on which the barrel is mounted. The structure is supported by radial stainless steel rods passing outward from flanges at each end of the spool. The spool and the scintillation counter plastic provide 0.4 r.l. of material before the first layer of proportional tubes.

An important feature of the shower counter is its high degree of segmentation. In the barrel, there are 320 cells arranged azimuthally in each layer, and in the endcaps there are 74 cells above the beam pipe and 72 below it. This segmentation gives good position resolution and pattern recognition capability. These are useful in resolving photons produced with a very small opening angle from symmetric decays of high-energy π^0's.

Electronics

In both the barrel and the endcaps the wires in the first six layers are read out individually, whereas the wires in the outer eighteen layers are grouped radially in six triplets. This reduces the number of electronics channels but preserves the full information from the inner layers, where the showers from low-energy photons are usually confined. The signal from each end of a wire or triplet of wires is fed into a module (29) consisting of an amplifier followed by a sample and hold circuit. Because of the high drift velocity of the argon-methane mixture, even at low fields, the maximum time for ionization collection is only about 0.2 μsec. The pulse, however, has a long tail, and the gate on the sample and hold circuit is 1 μsec. The charge deposited per cell by a minimum ionizing track is 1pC, compared with 5 fC noise for the 1 μsec gate. Over the full track length, this signal is equivalent to that of a photon with $E \sim 200$ MeV.

The capacitors at each end of the wire that decouple the high voltage from the read-out electronics can discharge into each other and reduce the charge asymmetry that gives the z-position. To reduce this effect, large (25 nf) capacitors were used.

Performance

The position and energy resolutions for the shower counters are given in

Table 2.2. Energy and Position Resolution of the Mark III Shower Counter

Measurement	Barrel	Endcaps
Energy resolution	$\sigma_E = 17.5\% \times \sqrt{E(GeV)}$	$\sigma_E = 17.0\% \times \sqrt{E(GeV)}$
Position resolution along the wire	$\sigma_z = 0.8\% \times$ (wirelength)	$\sigma_y = 1\% \times$ (wire length)
Position resolution transverse to the wire	$\sigma_\phi = 7$ mrad	$\sigma_x = 7$ mm

Table 2.2. The ϕ coordinate of a shower in the barrel is determined from a fit to the shower shape and has a resolution $\sigma_\phi \simeq 7$ mrad compared with the cell size of 20 mrad. The linearity of the shower counter has been checked using Bhabhas at $E_{cm} = 3.1$, 3.7, and 4.3 GeV. For lower energies, from 0–1 GeV, the linearity was checked using $\psi \rightarrow \rho\pi$ events. The true photon energies were determined from a kinematic fit using only the photon momentum directions, the charged track momenta, and the π^0 mass constraint. The average measured energy vs. the fitted energy is shown in Fig. 2.13a; it has a linear dependence.

Due to the small fraction of the shower sampled by the gas proportional tubes, the measured energy is subject to large statistical fluctuations. In addition, large Landau fluctuations further degrade the resolution. Figure 2.13b shows the energy for Bhabha-scattered electrons at $E_{beam} = \frac{1}{2}m_\psi$. The energy distribution is approximately Gaussian, and the resolution can be expressed as

$$\frac{\sigma_E}{E} = 0.175/\sqrt{E(GeV)}. \tag{2.6}$$

Although this resolution is not good enough to identify resonances from the inclusive photon spectrum, nearly all exclusive channels of interest can be studied using kinematic fitting. For example, in the process $\psi \rightarrow \gamma_1\eta'$;

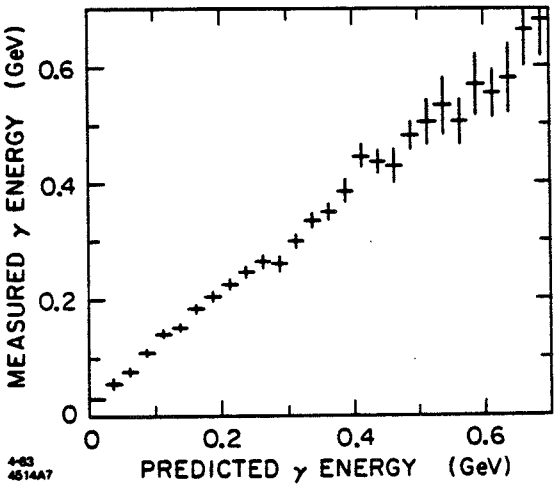

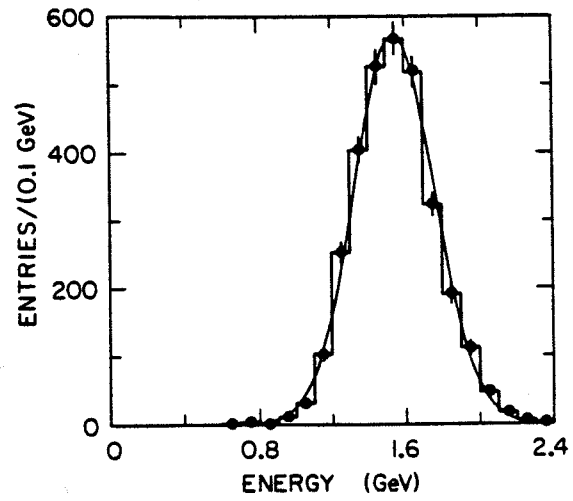

Figure 2.13. Shower counter performance. a) Average measured energy vs. the fitted (true) energy for photons from $\rho\pi$ events, showing a linear energy scale. b) Shower energy distribution for Bhabha-scattered electrons at the ψ.

$\eta' \to \gamma_2\rho^0$, the energy resolution on γ_1 is $\sigma_E \sim 3$ MeV after the four-constraint fit to energy and momentum conservation. Thus, the well-measured charged track momenta and photon directions are sufficient to determine the photon energies. The variable used in the kinematic fit is $\sqrt{E}$ rather than E, because it has been observed that $\sqrt{E}$ has a more Gaussian behavior at low energies and has a resolution independent of E:

$$\sigma_{\sqrt{E}} = \frac{dE^{\frac{1}{2}}}{dE}\sigma_E = 0.085(\sqrt{\text{GeV}}). \tag{2.7}$$

The photon detection efficiency for the barrel shower counter as a function of energy is shown in Fig. 2.14. The efficiency (not including geometrical factors) is determined using the approximately 7000 $\psi \to \rho^0\pi^0$ events in the data sample. Because the π^0 is essentially monochromatic and the photons are emitted isotropically in the π^0 rest frame, the photon energy spectrum in the lab frame should be uniform from about 4 MeV to 1.45 GeV. The deviation from that shape at low energies is therefore due to loss of efficiency. At 100 MeV, the efficiency is close to 100%; it falls to about 75% at 50 MeV.

An accurate measurement of the efficiency at low energies is complicated by the presence of spurious photons ("split-offs") due to secondary hadronic interactions of pions and kaons in the shower counter. At low momenta the cross section for such πN and KN interactions is quite high. As a consequence, about 40% of all $\rho\pi$ events have at least one fake gamma. It is sometimes difficult to distinguish such shower clusters from real low-energy ($\lesssim$100 MeV) photons. The spurious clusters, however, are usually highly concentrated around charged tracks. Figure 2.15 shows the distribution of the angle between the shower cluster position and the entry point of the nearest charged track in the shower counter for $\rho\pi$ events. The peak at $\cos\theta_{\gamma q} \simeq 1$ is due to spurious photons.

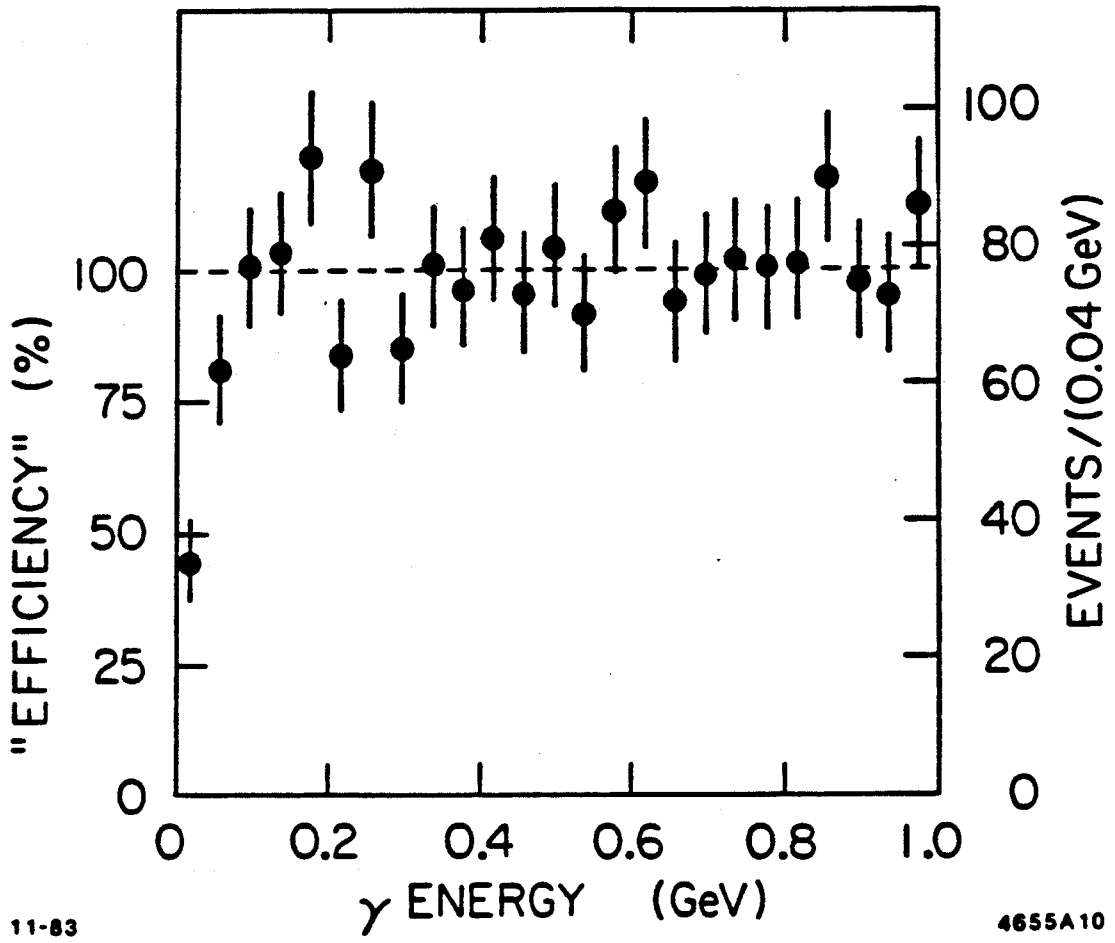

Figure 2.14. Photon detection efficiency as a function of energy determined from $\rho^0\pi^0$ events. The decay of the monochromatic π^0 results in a uniform energy distribution of photons in the lab frame.

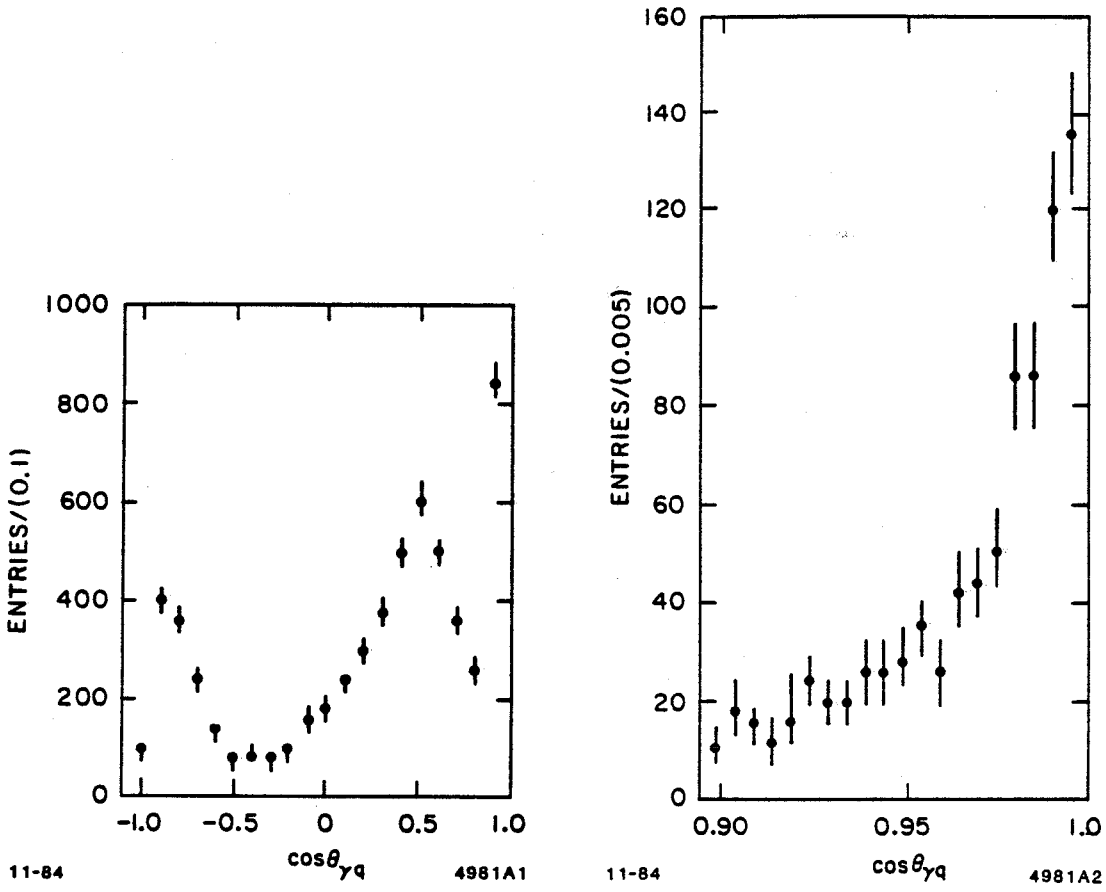

Figure 2.15. Study of fake photons. The figure shows the distribution of the angle between the shower cluster and the nearest charged track from $\rho\pi$ events. The peak at $\cos\theta_{\gamma q} = 1$ is due to split-offs from the pion interacting in the shower counter.

There are two common approaches to this problem. First, one can exclude all clusters with $\cos\theta_{\gamma q} > 0.95$ and model the loss of solid angle with the Monte Carlo. This procedure should be quite reliable if the angular distribution of the final state particles is known. A second approach that is often used in the analysis of exclusive channels is to try several kinematic fits to a given event using different subsets of the shower clusters as photon candidates. Thus, if one is studying the process $\gamma\pi^0K^+K^-$, events with up to six shower clusters might be fit using various subsets of the five highest energy clusters. The fit yielding the best χ^2 is chosen. Because split-offs tend to have energies below 100 MeV, it is usually the case that the highest energy shower clusters are due to real photons, whereas the lowest energy clusters, especially if they are near charged tracks, are spurious.

Reconstruction of Data

The pattern recognition problem in the shower counter is potentially very complicated, but in most cases a fairly simple algorithm isolates the correct clusters. We will take the case of the barrel shower counter as an example, but the procedure for the endcaps is quite similar. Because the position resolution in the ϕ-direction is much better than that in the z-direction, the first step in the search is to scan around the barrel in ϕ, ignoring the radial and z-coordinates. The algorithm groups together hits that have a small ($\leq$ 2 cell) separation in ϕ, and requires a minimum of two cells hit with consistent z information to form a cluster. The second step involves sorting the z-coordinates of the hits in each of the original ϕ-clusters. If there are distinguishable concentrations of hits clustered at different z-coordinates, the ϕ-cluster is split. The final step in pattern recognition is to examine the shower structure in the $r-\phi$ coordinates. If the cluster has two distinct prongs at the shower counter inner radius that

later merge, the shower is split. Such topologies are usually due to photons from high energy π^0's that decay symmetrically. The final shower clusters must have a minimum of two cells hit with consistent z-positions.

The starting positions of the shower clusters are determined by fitting a straight line to the shower shape. The position of this line at the minimum radius is taken to be the particle entry point. All clusters whose entry point is consistent with that of a charged track are removed from the list of photon clusters.

2.6 THE MAGNET

The 4 kG axial magnetic field is provided by a solenoid surrounding the barrel shower counter. With this arrangement, the number of windings can be increased without reducing the photon detection efficiency. In the Mark III design there are four layers of 5 cm by 5 cm cross-section aluminum conductor compared to only two layers in the previous SPEAR magnetic detectors. This results in a reduction in the power consumption from 2 MW to 1 MW. The magnet is cooled by water flowing through a 2.5 cm diameter hole in the conductor.

2.7 THE MUON SYSTEM

The muon system (30) consists of two layers of gas proportional tube modules mounted in an octagonal array outside the steel flux return of the magnet. The solid angle coverage of the system is 65% of 4π. Between the two layers is a 12.5 cm thick steel plate to absorb hadrons. Each layer consists of modules that contain two overlapping sub-layers of circular cross section gas proportional tubes. The z-coordinates are measured by charge division on the resistive

stainless steel wires. At $p = 1$ GeV, the pion punch through (including decays) is 5% for the inner layer and 3% for the outer layer.

The muon system does not play an important role in the analysis of most ψ decays because muon production is very limited, occurring only in $e^+e^- \to \gamma\mu^+\mu^-$, $\psi \to \mu^+\mu^-$, and K and π decays. The back-to-back dimuons, however, are important in studying the performance of other components of the detector.

2.8 THE TRIGGER

The trigger (31) is designed to minimize the detector dead time by rejecting uninteresting events (*e.g.*, cosmic rays and scattering of the beam by residual gas in the beam pipe) before the lengthy ($\sim$ 30 ms) process of digitization and data transfer to the online computer is begun. The primary trigger considerations arise from the 781 ns period between SPEAR beam crossings (1.28 MHz). To exploit this, the decision process is divided into two steps, the first of which is completed in less than the time interval between successive beam crossings. Events that fail this step do not contribute to the dead time. At present, the trigger uses information only from the drift chambers and the time-of-flight counters. Thus, an event with only photons in the final state will not be recorded, although a neutral trigger may be implemented in the future.

The first trigger step, referred to as level 0, is completed within 590 ns after beam crossing. This allows the various capacitors in the system that record times and pulse heights to be reset before the next beam crossing. Level 0 consists of two parts running in parallel, either of which will satisfy level 0 and lead to further consideration of the event by level 1. The first part is a single-track trigger that requires a hit from the inner drift chamber chronotron within a 100

ns gate *and* a hit from the time-of-flight chronotron within a 27 ns gate. The time-of-flight signal is obtained by feeding pulses from the last dynode at each end of a counter into a chronotron circuit. This reduces the timing ambiguity due to the z-position of the hit along the counter. The second part of level 0 is a two-track trigger that requires two chronotron hits from the inner drift chamber, but does not require time-of-flight information. If the level 0 trigger is satisfied by either test, the trigger performs the level 1 step and inhibits the reset of the electronics. At the ψ, the level 0 trigger rate is 2-3 kHz. These triggers are primarily due to beam gas scattering, as the cosmic ray trigger rate is only about 1 Hz.

The level 1 trigger also has parallel one-track and two-track tests but uses information from layers 3 and 5 of the main drift chamber in addition to the layer 1 chronotron signals. Because the maximum drift time in the main drift chamber is 550 ns, this information arrives too late to be used in the level 0 trigger. Level 1 uses programmable array logic to implement a rudimentary track-finding algorithm. The idea of the algorithm is illustrated in Fig. 2.16. Starting with each cell in layer 5, which covers 88% of 4π, the level 1 trigger looks for valid patterns of hit cells within a certain allowed region defined by a minimum transverse momentum cut (75 MeV). The patterns are found by forming triple coincidences of the hit cells, where a hit cell has signals from at least two out of three sense wires.

The level 1 one- and two-track triggers are continuations of their counterparts in level 0. Thus, an event may satisfy the two-track trigger without satisfying the one-track trigger because it lacks time-of-flight information. The outputs of the one and two track triggers are OR'ed, however, so that either one is sufficient to keep the event.

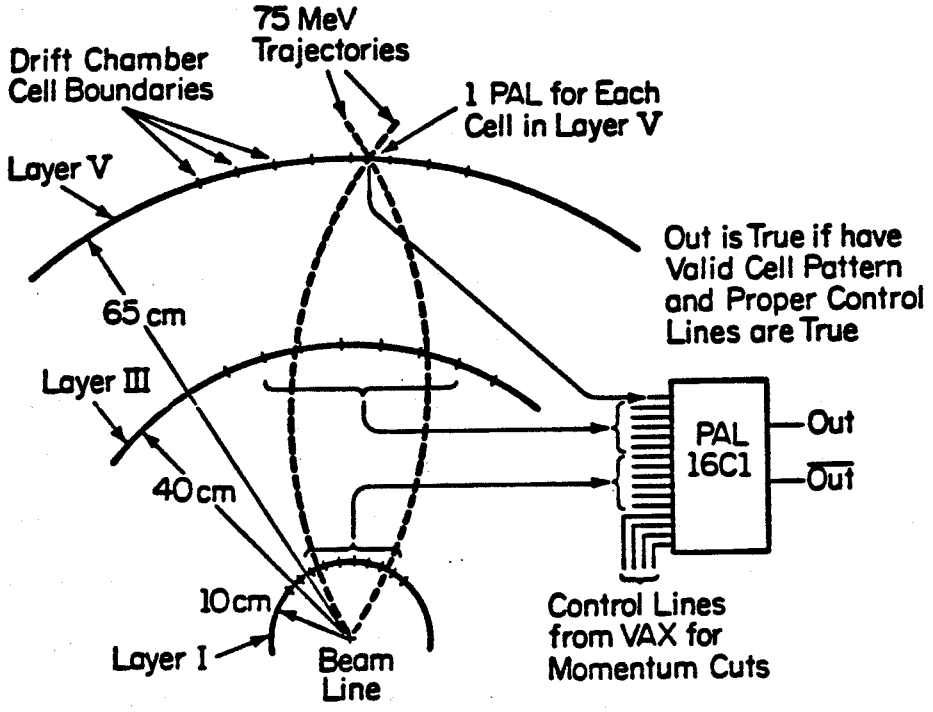

Figure 2.16. Illustration of the track-finding algorithm used in level 1 of the trigger. A track must have cells hit in layers 1, 3, and 5, limiting solid angle coverage to 88% of 4π.

Table 2.3. Mark III Run History

Year	Run	Data Collected
1981	Summer	Installation at SPEAR
	Fall	Checkout and Debugging
1982	Spring	ψ: $\sim$ 0.9 M produced
	Fall	ψ': $\sim$ 150 K hadronic events logged
		ψ'': $\sim$ 1800 nb^{-1}
1983	Spring	ψ: $\sim$ 1.8 M produced
		ψ'': 3800 nb^{-1}
	Fall	SPEAR problems
1984	Spring	ψ'': reached total of 8.9 pb^{-1}

At the typical luminosity of 4×10^{29} cm^{-2}s^{-1} at the ψ, the level 1 trigger rate is 2-3 Hz. About 1.1 Hz is from e^+e^- collisions, 1.4 Hz is from cosmic rays, and 0.5 Hz is from beam gas events. The dead time of the experiment is 8-12%, depending upon beam conditions. The primary contribution to trigger inefficiency is inefficiency in the inner drift chamber, which has single-wire cells. The overall efficiency per track is about 96% over the solid angle covered by layer 5. The overall trigger efficiency for ψ's is 93% (see following section).

2.9 Mark III Run History and Data Sample

The run history of Mark III is shown in Table 2.3. The detector was installed in the west interaction region of the SPEAR ring in the summer of 1981. The first useful ψ data, consisting of 0.9×10^6 produced ψ's, were taken in the spring of 1982, although some components of the detector were not fully operational. In particular, crosstalk compensating resistors and preamplifiers had not yet been installed on layer 2 of the drift chamber, and its efficiency was quite low. However, most other components were working reasonably well, and checks with

several well-known ψ decays indicate that there are no major problems with this data sample. The second ψ data sample, taken in the spring of 1983, consists of 1.8×10^6 produced ψ's. The detector was fully operational. Unfortunately, the experiment takes data for only half the time that SPEAR is operational; during the other half, SPEAR runs in a single-beam mode for the Stanford Synchrotron Radiation Laboratory (SSRL).

The number of events on tape from the two ψ runs is approximately 10^7. To minimize the computer time required for reconstruction (300 ms/event), it is desirable to remove beforehand the beam gas and cosmic ray backgrounds. A fast (~10 ms/event) analysis program, using a minimum of detector information, was used for this purpose (32). First, cosmic rays are removed by using both time-of-flight and muon counter information. Second, the number and energy of the shower clusters (which may be due to charged tracks) are used to identify Bhabhas and clear hadronic events. Finally, drift chamber hits (but not times) are used to count tracks and identify beam gas events. This filtering process reduces the event sample by about 70% and removes only about 0.5% of real hadronic events.

To determine the normalization for branching ratios, it is necessary to correct the number of observed ψ's for the detection efficiency. Efficiency losses are due primarily to events with all neutral particles and events in which all the charged tracks are close to the beam pipe. The detection efficiency can be measured using the process $\psi' \rightarrow \pi^+\pi^-\psi$. For this purpose, about 10^5 ψ' events were logged in the fall of 1982. Events with ψ's are tagged using only the four-vectors of the charged pions to calculate the missing mass. The pions are then excluded from consideration, and it is determined with software whether the detector would have triggered on the remaining particles. The ψ momentum is

sufficiently low that it does not bias the measurement. The efficiency determined from this procedure is 93%, and the fraction of zero-prong ψ decays is found to be $(3.5 \pm 0.5)\%$.

The 1983 data sample corresponds to $(1.79 \pm 0.11) \times 10^6$ produced ψ's. The size of the 1982 data sample was found by scaling the total number of events according to the number of $\mu^+\mu^-$ events relative to the 1983 data sample. The combined 1982 + 1983 data samples correspond to $(2.71 \pm 0.05 \pm 0.15) \times 10^6$ produced ψ's.

Chapter 3. Analysis of the Decay $\psi \to \gamma\iota;\ \iota \to K\bar{K}\pi$

3.1 INTRODUCTION

The ι was first observed in radiative ψ decay by Mark II in the process $\psi \to \gamma\iota;\ \iota \to K^0_S K^{\pm}\pi^{\mp}$ (33). The signal, which was originally assumed to be the $E(1420)$, contained about 30 events when the 1.2 GeV photon was identified and about 85 events when that requirement was relaxed (Fig. 3.1a, b). The ι was subsequently studied with greater statistics (174 ± 30 events) in the $K^+K^-\pi^0$ mode by the Crystal Ball (Fig. 3.1c), and a partial wave analysis of the $K^+K^-\pi^0$ system was performed (34). The results of the Mark II, Crystal Ball, Mark III, and DM2 analyses are summarized in Table 3.1.

The most intriguing of these results is the branching fraction: $\psi \to \gamma\iota$ is the largest of all radiative ψ decays that proceed via annihilation of the $c\bar{c}$ system into gluons. (The magnetic dipole transition $\psi \to \gamma\eta_c$, which has a branching fraction of $(1.27 \pm 0.36)\%$, does not require the quarks to annihilate.) The only comparable mode is $\psi \to \gamma\eta'$, whereas $f(1270)$ production is only about one-quarter of that for the ι. This large coupling of the ι to the gluonic intermediate state suggests that the ι wave function has a large $SU(3)$ flavor singlet component. A more interesting – but amazingly difficult to prove – conjecture is that the ι is a glueball.

3.2 THE E MESON

A continuing source of confusion is the existence in the same mass region of what is probably a different state, the $E(1420)$. This meson was first observed in the process $p\bar{p} \to E\pi\pi$, $E \to K\bar{K}\pi$ (36). In the original analysis, the quantum numbers $J^P = 0^-$ were preferred over $J^P = 1^+$; the same conclusion was

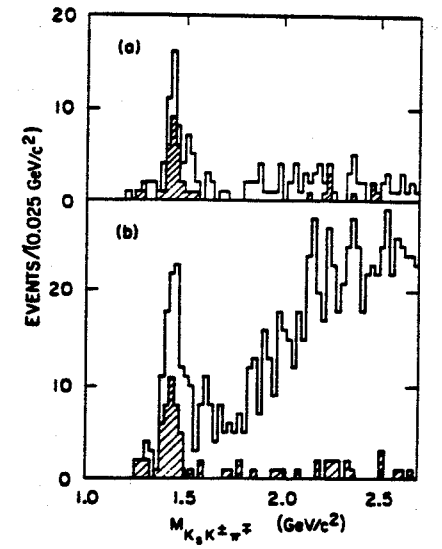

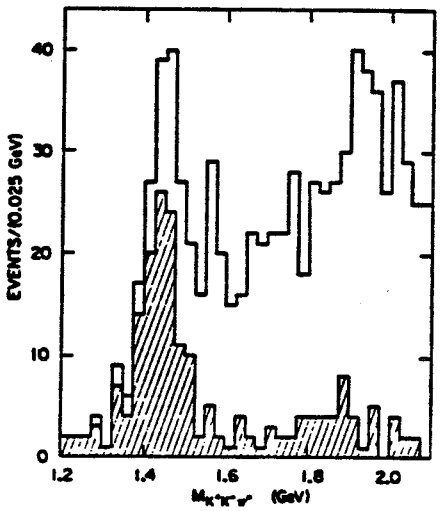

Figure 3.1. Observations of the ι by Mark II and Crystal Ball. a) Mark II, photon required b) Mark II photon not required. Events in shaded region have $M(K\bar{K}) < 1.05$ GeV. c) Crystal Ball, events in shaded region have $M(K\bar{K}) < 1.125$ GeV.

Table 3.1. Results on the ι From Radiative ψ Decay.

Measured Quantity	Mark II Ref. (33)	Crystal Ball Ref. (34)	Mark III	DM2 DCI Ref. (35)
Mass (GeV)	$1.44^{+0.01}_{-0.015}$	$1.44^{+0.020}_{-0.015}$	$1.456 \pm 0.005 \pm 0.006$	1.474 ± 0.015
Width (GeV)	$0.05^{+0.03}_{-0.02}$	$0.055^{+0.020}_{-0.030}$	$0.095 \pm 0.010 \pm 0.015$	0.076 ± 0.016
$B(\psi \to \gamma\iota)\times$ $B(\iota \to K\bar{K}\pi)$	(4.3 ± 1.7) $\times 10^{-3}$	$(4.0 \pm 0.7 \pm 1.0)$ $\times 10^{-3}$	$(5.0 \pm 0.3 \pm 0.7)$ $\times 10^{-3}$	--
J^P	--	0^-	0^-	--
# events observed in signal	~ 85 in $K^0_S K^\pm \pi^\mp$	174 ± 30 in $K^+K^-\pi^0$	~ 360 in $K^0_S K^\pm \pi^\mp$ ~ 400 in $K^+K^-\pi^0$ ~ 50 in $K^0_S K^0_S \pi^0$	$60 - 100$ in $K^0_S K^\pm \pi^\mp$
Decay Mode	low-mass $K\bar{K}$	$\frac{B(K^*K)}{B(K^*K+\delta\pi)} < 0.25$ (90% *C.L.*)	$\frac{B(K^*K)}{B(KK\pi)} < 0.35$ (90% *C.L.*)	--

reached in a later reanalysis of the data (37). The $K\bar{K}\pi$ Dalitz plot was found to contain $(50 \pm 10)\%$ $K\bar{K}^* + c.c$ and $(50 \pm 10)\%$ $(K\bar{K})_{res}\pi$, where $(K\bar{K})_{res}$ is a resonance with M=1.0 GeV and $\Gamma = 0.07$ GeV.

A signal at the same mass was observed in the process $\pi^- p \to (K\bar{K}\pi)n$ (38). Here, the partial wave analysis favored $J^P = 1^+$ over $J^P = 0^-$, and it became more or less accepted that the $E(1420)$ was an axial vector meson decaying predominantly into $K\bar{K}^* + c.c.$

Recently, two high statistics experiments have reported contradictory results on the E. The WA76 experiment (39), with about 1000 events, finds that $J^P(E) = 1^+$ and $\frac{B(E\to K^*\bar{K})}{B(E\to K\bar{K}\pi)} \simeq 100\%$, whereas MPS 771 (40), with about 1200 events, has reported a complicated structure in the 1.4 GeV region. This structure is associated with the 0^- partial wave; no resonant 1^+ is found. Both $K^*\bar{K}$ and $\delta\pi$ appear to be present. This confusing state of affairs is summarized

Table 3.2. Results on the E Meson (Hadronic Production)

Measurement	81 cm HBC (CERN) Ref. (36)	2 m HBC (CERN) Ref. (38)	WA76 (CERN) Ref. (39)	MPS Expt. 771 (AGS) Ref. (40) **PRELIMINARY**
Production process	$p\bar{p}$ (at rest) $\rightarrow (K\bar{K}\pi)\pi\pi$	π^-p$\rightarrow K^0_S K^{\pm}\pi^{\mp} n$ $p(\pi^-) = 3.95$ GeV/c	π^+p$\rightarrow \pi^+(K^0_S K^{\pm}\pi^{\mp})$p pp$\rightarrow$p$(K^0_S K^{\pm}\pi^{\mp})$p $p = 85$ GeV/c	$\pi^- p \rightarrow K_S K^+ \pi^- n$
Mass (GeV)	1.425 ± 0.007	1.426 ± 0.006	1.425 ± 0.002	1.421 ± 0.002
Width (GeV)	0.080 ± 0.010	0.040 ± 0.015	0.062 ± 0.005	0.060 ± 0.010
J^P	0^{-+}	1^{++}	1^{++}	complicated structure in 1.4 GeV region: resonant 0^{-+}; no evidence for resonant 1^{++}
# events observed	~ 890 in three channels	152 ± 25	~ 1000	~ 1200
Decay Mode	$\frac{B(K^*\bar{K})}{B(K^*\bar{K}+(K\bar{K})_{,es^x})} = 0.5 \pm 0.1$	$\frac{B(K^*\bar{K})}{B(K^*\bar{K}+\delta\pi)} = = 0.86 \pm 0.12$ $(\delta \rightarrow K\bar{K})$	$\frac{B(K^*\bar{K})}{B(K\bar{K}\pi)} = 1$	resonance has substantial K^*K and $\delta\pi$ coupling

in Table 3.2.

It is difficult to interpret the discrepancies among these experiments. One possibility is that the state observed in the $p\bar{p}$ experiment is the same as that observed in radiative ψ decays and is distinct from the state observed in $\pi^- p$ interactions. This hypothesis does not explain the contradictory results of WA76 and MPS 771, however, and it appears more likely that there are systematic errors in at least one experiment that are not fully understood. It is clear that partial wave analyses in the presence of large backgrounds and multiple resonances–even with a large number of events–are quite difficult to perform.

Although a definitive spin-parity measurement of the E would be valuable, the different masses and widths of the E and the ι provide reasonably convincing

evidence that these resonances are distinct. The E signal observed by WA76 (accompanied by a $D(1285)$ signal) is shown in Fig. 3.2a. The E is clearly at a lower mass and appears to be narrower than the ι.

The measurements of $B(E \to K^*\bar{K})/B(E \to K\bar{K}\pi)$ differ substantially, as seen from Table 3.2. (The decay $E \to \eta\pi\pi$ has not been unambiguously observed.) The result from Dionisi, *et al.* (38), is sometimes inaccurately stated as

$$B(E \to K^*\bar{K})/B(E \to K^*\bar{K} + \delta\pi) = 0.86 \pm 0.12,$$

without the additional condition that $B(\delta \to K\bar{K}) = 1$ is assumed. In any case, the Dalitz plots obtained for the E mass region appear to show clear evidence for K^* bands without the appropriate node structure for spin 0 (Fig. 3.2b), although it is not always clear from these plots how much is due to background.

3.3 Review of the Mark II and Crystal Ball Analyses

Before presenting the Mark III data, it is useful for comparison to discuss certain aspects of the Mark II and Crystal Ball analyses. Figure 3.3 shows the Dalitz plots and the $K\bar{K}$ mass distributions obtained by the two experiments. The events were required to have $M(K\bar{K}\pi)$ in the range 1.375-1.500 GeV (Mark II) or 1.400-1.500 GeV (Crystal Ball). The $K\bar{K}$ mass distributions peak at threshold and fall to essentially zero at about 1.3 GeV. The inequality $M(K\bar{K}) \leq M(K\bar{K}\pi) - M(\pi)$ must be satisfied, of course, so for the preceding $K\bar{K}\pi$ mass cuts one has $M(K\bar{K}) \leq 1.36$ GeV. The peak at threshold, however, is not just the projection of three-body phase space, which peaks closer to 1.14 GeV. (See the dashed curves in Fig. 3.3.)

For events with $M(K\bar{K}\pi) > 1.5$ GeV it is found that the $K\bar{K}$ mass is

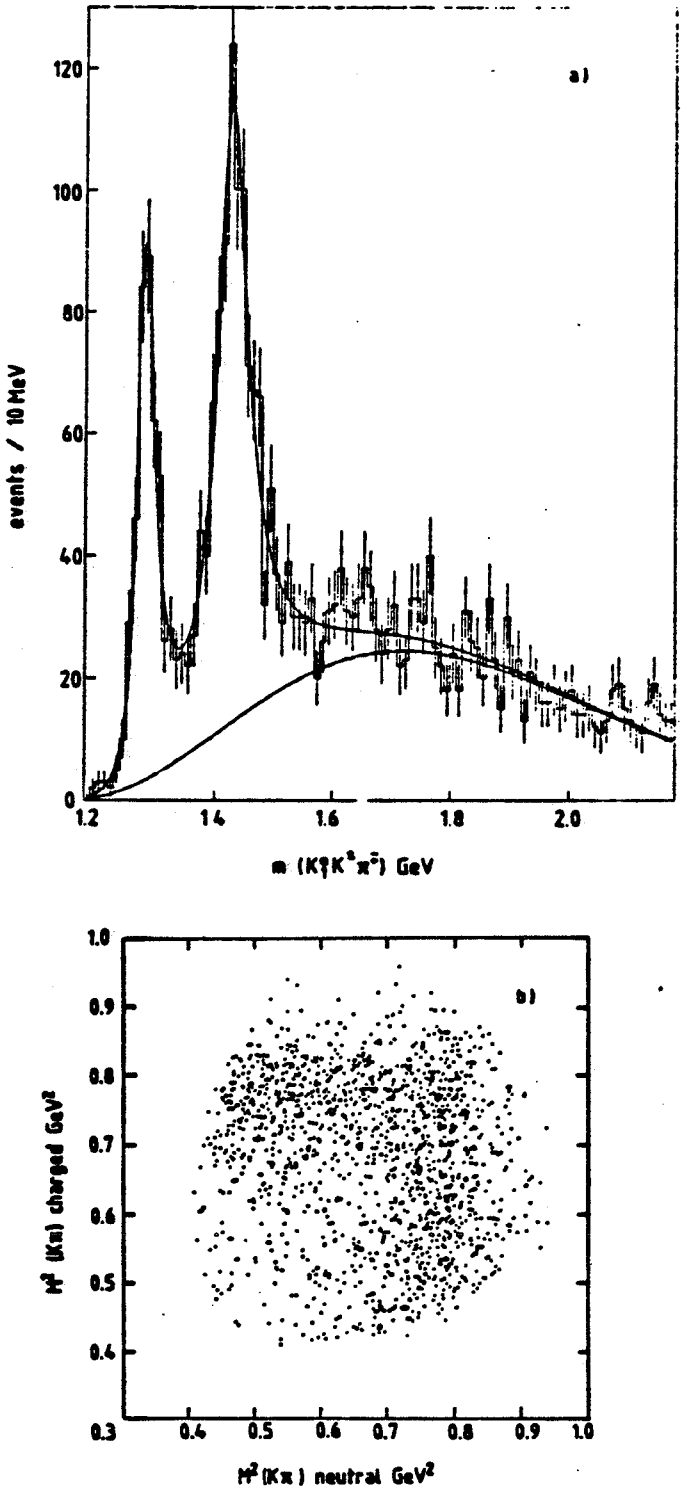

Figure 3.2. Results on the $E(1420)$ meson from WA76. a) $D(1285)$ and $E(1420)$ signals b) Dalitz plot for the E mass region.

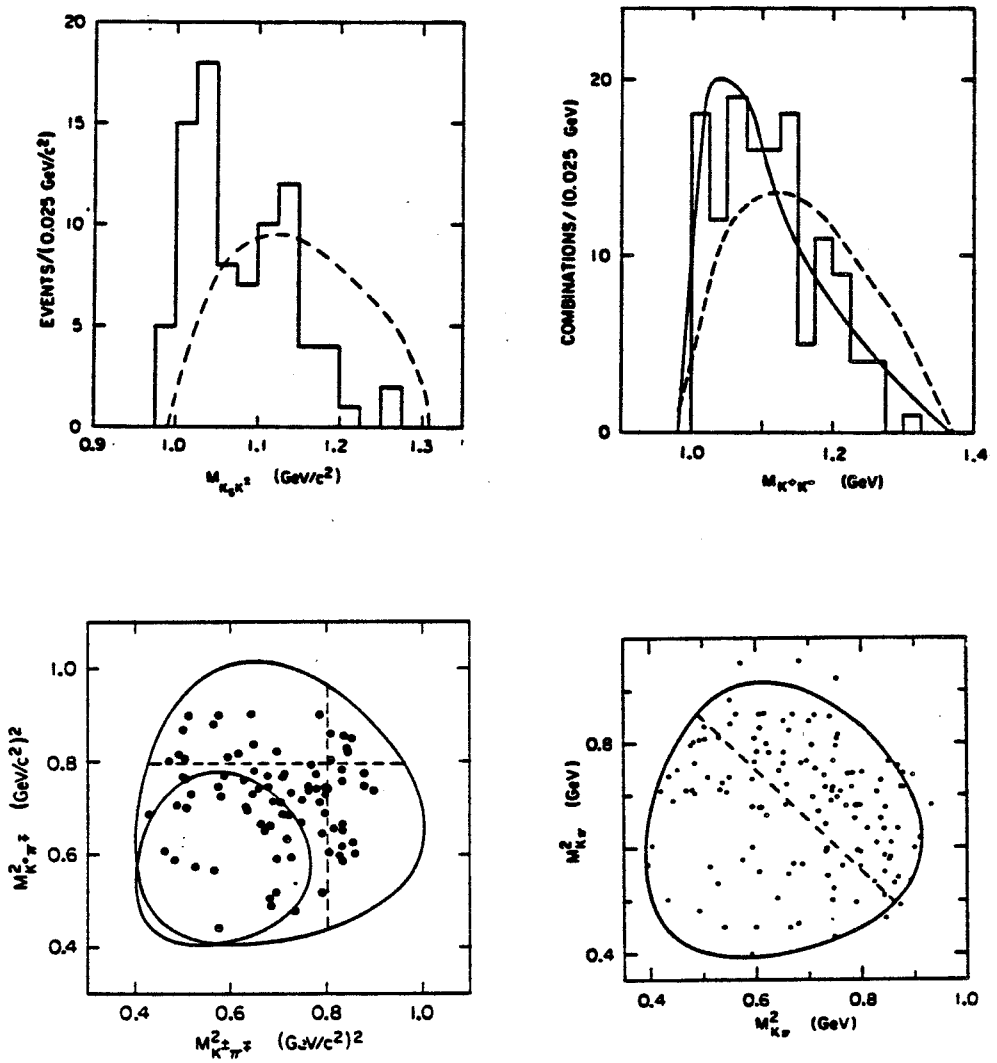

Figure 3.3. Mark II and Crystal Ball ι analyses. The Dalitz plots and $K\bar{K}$ mass distributions for the ι mass region do not show evidence for K^* bands.

typically much higher. One contribution to the background is from

$$\psi \rightarrow K^*(890)\bar{K}^*(1430) + c.c.$$

where each K^* decays into $K\pi$ or $\bar{K}\pi$. Because the kaons are heavy compared to the pions, they tend to remain in the same back-to-back configuration as their parent K^*'s and consequently have a high effective mass. Thus, it is sometimes useful to make a $K\bar{K}$ mass cut. The effect of the cuts $M(K\bar{K}) < 1.05$ GeV (Mark II) and $M(K\bar{K}) < 1.125$ GeV (Crystal Ball) is also shown in Fig. 3.3. Although these experiments find that the Breit-Wigner fit parameters of the ι are insensitive to the $K\bar{K}$ mass cut, this is not the case in the Mark III data. The requirement $M(K\bar{K}) < 1.125$ GeV causes a downward shift in the ι mass of about 20 MeV.

One possible explanation for the concentration of events at low $K\bar{K}$ mass is the decay

$$\iota \rightarrow \delta\pi; \qquad \delta \rightarrow K\bar{K}.$$

The $\delta(980)$ is a poorly understood isovector state with $J^P = 0^{++}$. According to some phenomenological analyses (41) its true width may be as large as 300 MeV, and it may not actually be a resonance. The main difficulty in understanding this state is that its mass is below $K\bar{K}$ threshold; in fact, one explanation of the δ is that it is a four-quark $K\bar{K}$ bound state (42).

The δ appears to decay into $\eta\pi$ as well as into $K\bar{K}$. Therefore if $\iota \rightarrow \delta\pi$, one should observe $\iota \rightarrow \delta\pi \rightarrow \eta\pi\pi$. Unfortunately, the ratio of the branching fraction to $\eta\pi$ relative to $K\bar{K}$ is poorly measured (43):

$$\frac{B(\delta \rightarrow \eta\pi)}{B(\delta \rightarrow K\bar{K})} = 0.25 - 1.3.$$

Any value within the above range, however, leads to an observable $\iota \rightarrow \eta\pi\pi$ signal with the present Mark III data sample. It will be shown in a later chapter that no signal is observed at this level. Thus, there is some doubt as to whether the δ is really present in ι decays.

Obtaining a description of the δ line-shape in the $K\bar{K}$ channel is not at all trivial. It certainly cannot be described by a symmetric Breit-Wigner because its mass is below threshold. The rapidly varying phase space and presence of the $\eta\pi$ channel appear to require a coupled channel parameterization of the line-shape. The observed narrow signal in $\eta\pi$ is then explained in the following way: As the $\eta\pi$ mass exceeds $K\bar{K}$ threshold, that channel opens up, and due to unitarity the $\eta\pi$ cross section suddenly falls. There is an additional effect due to analyticity: the opening of the $K\bar{K}$ channel also produces a drop in the $\eta\pi$ cross section below the δ peak. The result is a cusp whose width is considerably narrower than the "underlying" width of the state. The parametrization of the δ most commonly used is (41)

$$\frac{d\sigma_x}{dm} = C\left|\frac{m_R\sqrt{\Gamma_0\Gamma_x}}{m_R^2 - m^2 - im_R(\Gamma_{\pi\eta} + \Gamma_{K\bar{K}})}\right|^2$$

$$\Gamma_{\pi\eta} = g_\eta q_\eta$$

$$\Gamma_{K\bar{K}} = \begin{cases} g_K\sqrt{(\frac{1}{4})m^2 - m_K^2} & \text{above threshold} \\ ig_K\sqrt{m_K^2 - (\frac{1}{4})m^2} & \text{below threshold,} \end{cases}$$

where the subscript x refers to either $\pi\eta$ or $K\bar{K}$; q_η is the decay momentum at mass m into the $\pi\eta$ system; m_R is the mass of the resonance; and g_η and g_K are the squares of the coupling constants for the resonance couplings to the $\pi\eta$ and $K\bar{K}$ channels.

In addition to $\iota \rightarrow \delta\pi$ (or some isovector threshold enhancement in the $K\bar{K}$ system), there are two other decay channels available: $\iota \rightarrow K^*\bar{K}$ and the

decay into three-body phase space. (After the K^* the lightest strange mesons are the $Q(1280)$ with $J^P = 1^+$ and the $\kappa(1350)$ with $J^P = 0^+$.) Examination of the Dalitz plot shows that the phase space is quite limited and that the position of the K^* bands would coincide to a large extent with the δ region. For $M(K\bar{K}\pi) = 1.45$ GeV, the K^* bands overlap at $M(K\bar{K}) \approx 1.05$ GeV. Thus, it is difficult to determine the relative contributions of the $K^*\bar{K}$ and $\delta\pi$ by a simple inspection of the Dalitz plot.

The Crystal Ball partial wave analysis (34) includes the following contributions:

$\iota \to K\bar{K}\pi$	angular distributions uniform
$\to \delta\pi$	$J^P = 0^-$
$\to \delta\pi$	$J^P = 1^+$
$\to K^*\bar{K} + c.c.$	$J^P = 0^-$
$\to K^*\bar{K} + c.c.$	$J^P = 1^+$

The last four processes are allowed to interfere with arbitrary phases. The total amplitude includes the Breit-Wigners for the resonances and the appropriate angular distributions with unknown helicity amplitudes where required. For the fit, the signal region (1.3-1.8 GeV) is divided into five mass bins, and the relative contributions of the partial waves to each bin are determined. Figure 3.4 shows that the dominant contributions are $K\bar{K}\pi$ with all angular distributions uniform and $\delta\pi$ with $J^P = 0^-$. There are some events in the $K^*\bar{K}$ $J^P = 1^+$ partial wave, but these are distributed uniformly.

3.4 Theoretical Predictions for $\psi \to \gamma$ + Pseudoscalar

Since the discovery of the ι, there has been a proliferation of papers dealing with the question: Is it a glueball? Because of the well-known difficulties in

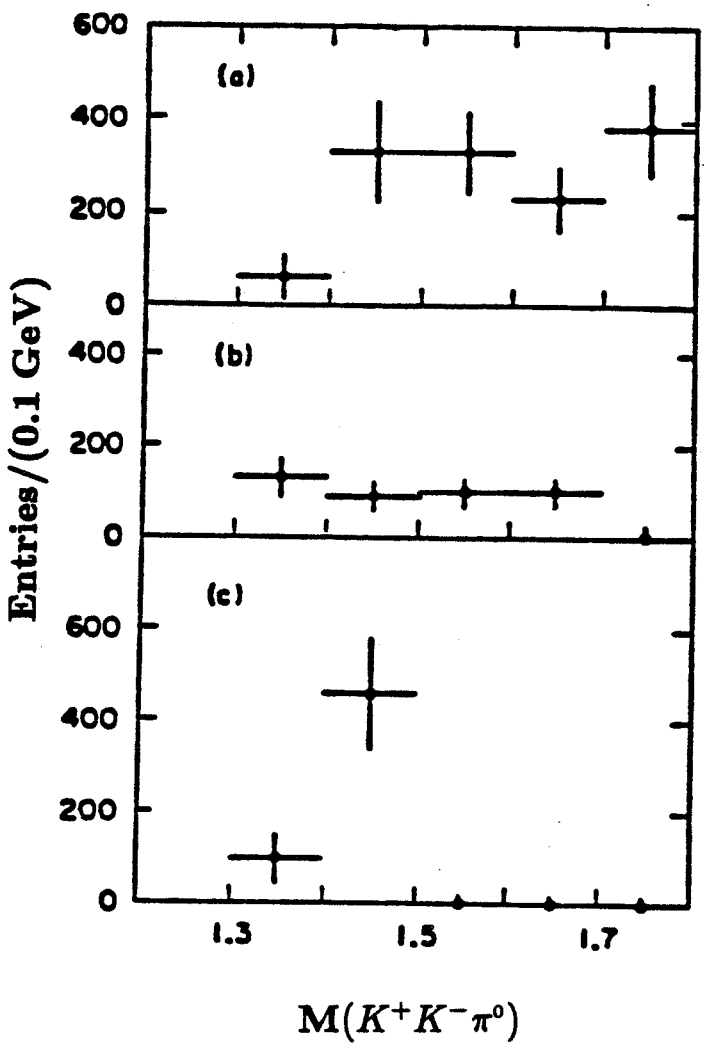

Figure 3.4. Results from the Crystal Ball partial wave analysis. The histograms show the partial wave contributions as a function of $K\bar{K}\pi$ mass for a) $K\bar{K}\pi$ with all angular distributions uniform. b) $K^*\bar{K} + c.c.$, $J^P = 1^+$ c) $\delta\pi$, $J^P = 0^-$.

calculating observable quantities in QCD, however, relatively few of these papers have made any quantitative predictions. In spite of the discouraging absence of reliable theoretical results, we present here a list of questions that have been addressed by theorists and discuss some of the progress that has been made on them.

1. How reliable is the perturbative picture of radiative ψ decays? Even if the radiative decay of the ψ into gluons can be calculated, what about the coupling of the gluons to light mesons? Is a non-relativistic description of these mesons adequate for such a calculation?

2. Assuming that the perturbative approximation is reliable, what are the branching fractions for $\psi \to \gamma P$, where $P = \eta$, η', or a pseudoscalar glueball? Can one calculate the rate for $\psi \to \gamma P'$, where P' is a radially excited pseudoscalar? What does $B(\psi \to \gamma\iota) > B(\psi \to \gamma\eta')$, imply about the quark content of the ι?

3. A frequently made argument is that spin-one states are not likely to be found in radiative ψ decays because Yang's theorem states that two massless vector particles do not couple to spin one. To what extent can the gluons be regarded as massless? Should one expect there to be substantial $E(1420)$ signal (assuming that it is an axial vector meson!) under the ι? Is there any hope for discovering a hybrid state with the exotic quantum numbers $J^{PC} = 1^{-+}$ in radiative ψ decays?

An interesting approach to studying the two-gluon system in the lowest order radiative diagram is to calculate its spin-parity content as a function of mass. This type of analysis has been done by Billoire, et al., (44) assuming the gluons to be massless. This assumption immediately forbids $J^P = 1^+$ and $(\text{odd})^-$.

The cross section for each spin-parity channel as a function of the mass of the two-gluon system is shown in Fig. 3.5a. The $J^P = 0^-$ and 0^+ contributions are identical and fairly large, but the 2^+ contribution is dominant. There is a $J^P = 4^+$ contribution at low mass, but because high spin mesons are relatively heavy there will not be any significant hadron production.

The more recent analysis of Körner, et al., (45) has examined the first-order perturbative diagram in greater detail. To calculate the production of specific mesons, it is assumed that they can be approximated as non-relativistic, weakly bound $q\bar{q}$ systems. Although this assumption is probably adequate to describe the annihilation of the $c\bar{c}$ quarks into gluons, it is not clear how reliable it is for the subsequent coupling of the gluons to light mesons. In this approximation the values of the meson wave functions at the origin are the only unknown quantities and can be obtained from $\Gamma(\psi \to e^+e^-)$, $\Gamma(\eta' \to \gamma\gamma)$, etc. Beyond this, the first order perturbative diagram is calculated exactly (including the loop integral) so that there is no assumption that the gluons are on-shell. For the case of pseudoscalar production the radiative partial width is found to be

$$\Gamma(\psi \to {}^1S_0 + \gamma) = \tfrac{1}{6}(\tfrac{2}{3})^2 \alpha_s^4 \alpha Q_c^2 \frac{1}{M_\psi^3} \left(\frac{4R_\psi(0)}{\sqrt{4\pi M_\psi}}\right)^2 \left(\frac{4R_{PS}(0)}{\sqrt{4\pi m}}\right)^2 \times \left[x|\hat{H}^{PS}(x)|^2\right], \tag{3.1}$$

where

$R_\psi(0) =$ wave function of the ψ at the origin

$R_{PS}(0) =$ wave function of the pseudoscalar at the origin

$m =$ mass of the pseudoscalar

$x = 1 - (\frac{m}{M_\psi})^2 = \frac{2p}{M_\psi} \Rightarrow m = M_\psi(1-x)^{\frac{1}{2}}$

$\hat{H}^{PS}(x) =$ reduced pseudoscalar helicity amplitude

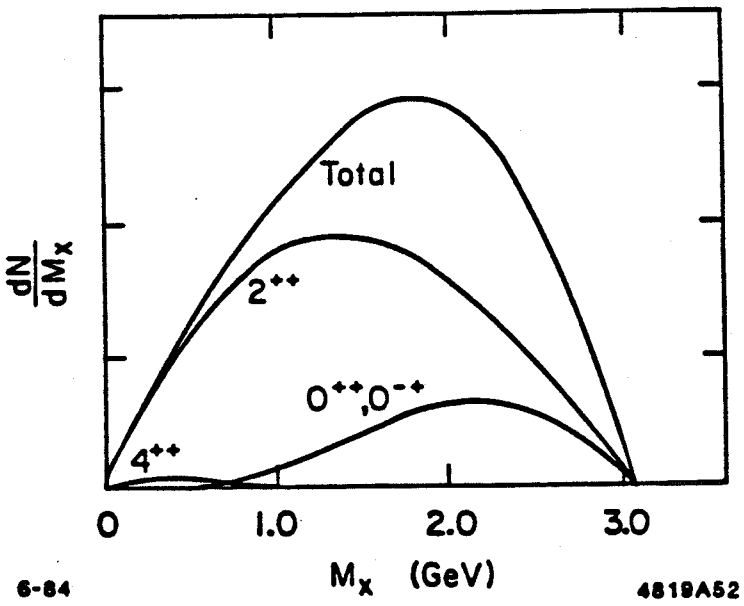

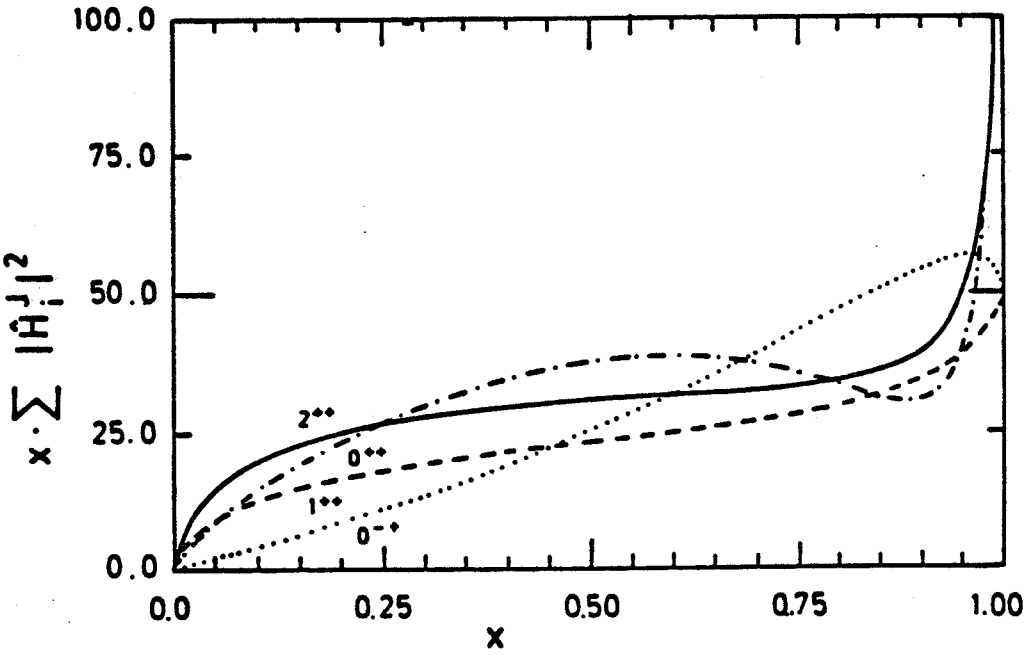

Figure 3.5. Perturbative calculations of radiative ψ decay. a) Spin-parity content of the two-gluon system as a function of mass (27). b) Summed squares of the reduced helicity amplitudes for various J^P values (28).

The amplitude $\hat{H}^{PS}(x)$ is obtained from the loop integral calculation and has an interesting behavior. In the limit $x \to 1$ $(m/M_\psi \to 0)$, the amplitude is dominated by the contribution from off-shell gluons. This contribution is not included in the calculation of Billoire, et al.

The decay rates for $J^P = 0^{++}$, 1^{++}, and 2^{++} are also calculated, but for $J > 0$ there are additional helicity amplitudes. Figure 3.5b compares the summed squares of the reduced helicity amplitudes for different J^P values. It is found that $J^P = 1^+$ is not suppressed compared to the other channels and that $J^P = 2^+$ does not dominate over the other contributions. Thus, the argument that the ι could not have spin one that is based on the assumption that the gluons are quasi-real is not supported by this analysis.

To evaluate the partial width for $\psi \to \gamma\eta'$, the ψ and η' wave functions at the origin must be known. These are obtained using $\Gamma(\psi \to e^+e^-) = 4.7$ keV and $\Gamma(\eta' \to \gamma\gamma) = 5$ keV, and by assuming that a non-relativistic description of these states is adequate. The value for α_s at the η' mass is found to be 0.31 from the first-order formula for the running coupling constant with $\Lambda = 100$ MeV. Finally, the width from Eq. (3.1) is multiplied by the SU(3) factor $3\cos^2\theta_{PS}$ $(\theta_{PS} = -11°)$. The result is $\Gamma(\psi \to \gamma\eta') = 188$ eV or

$$B(\psi \to \gamma\eta')_{theory} = 3 \times 10^{-3}.$$

The Mark III value for this branching ratio is (see Chapter 4)

$$B(\psi \to \gamma\eta') = (4.7 \pm 0.2(stat) \pm 0.7(sys)) \times 10^{-3}.$$

The agreement is surprisingly good.

Unfortunately, if the wave function at the origin for the η is extracted from its 2γ width, an extremely small value for $\Gamma(\psi \to \gamma\eta)$ is obtained. Presumably, one

or both of the assumptions (first-order perturbation theory or non-relativistic description of the η) is invalid. However, if one assumes that $R_\eta(0) = R_{\eta'}(0)$ (SU(3) invariance), then the result is

$$\frac{\Gamma(\psi \to \gamma\eta')}{\Gamma(\psi \to \gamma\eta)} \approx \left(\frac{\alpha_s(M_{\eta'})}{\alpha_s(M_\eta)}\right)^4 \cot^2\theta_{PS}\frac{M_\eta}{M_{\eta'}} = 5,$$

which agrees well with the data (see Chapter 4).

Finally, one would like to estimate the production of a radially excited pseudoscalar to see whether it is at all comparable to that of the ι. At the ι mass the partial width is

$$\frac{\Gamma(\psi \to \gamma + \iota(q\bar{q}_R))}{\Gamma(\psi \to \gamma + \eta')} = \frac{x_\iota}{x_{\eta'}}\left|\frac{H_{PS}(x_\iota)}{H_{PS}(x_{\eta'})}\right|^2 \frac{m_\iota}{m_{\eta'}}\left[\frac{R_\iota/m_\iota}{R_{\eta'}/m_{\eta'}}\right]^2$$
$$= 1.41\left[\frac{R_\iota/m_\iota}{R_{\eta'}/m_{\eta'}}\right]^2.$$

The wave function at the origin for a radially excited pseudoscalar is unknown. As a guess, one can simply use the fact that

$$\frac{\Gamma(\Upsilon' \to e^+e^-)}{\Gamma(\Upsilon \to e^+e^-)} \approx \frac{\Gamma(\psi' \to e^+e^-)}{\Gamma(\psi \to e^+e^-)} \approx 0.46$$

or

$$\frac{\Gamma(\phi' \to e^+e^-)}{\Gamma(\phi \to e^+e^-)} = 0.54 \pm 0.1.$$

From the latter value it is found that

$$r = \frac{\Gamma(\psi \to \gamma + \iota(q\bar{q})_R)}{\Gamma(\psi \to \gamma\eta')} \approx 0.76.$$

However, this result is obtained assuming that the value of α_s does not change between the η' and ι masses. If one uses the formula for α_s given above, then the ratio is reduced by a factor of two, $r = 0.38$, since the width depends on α_s^4.

The above calculation helps to make quantitative the expectation that the smaller value of the radial wave function of a radially excited pseudoscalar should lead to a suppression of its production relative to that of the η'. The result appears to confirm this to some extent, although the authors caution that, given the large theoretical uncertainties, the difference between the theoretical prediction of $r = 0.38 - 0.76$ and the experimental value of $r = 1.1$ is not very large. A more precise theoretical calculation would be of great interest.

The model also predicts the branching fractions for the production of the axial-vector mesons $D(1285)$ and $E(1420)$. The results are

$$B(\psi \to \gamma + \left\{ \begin{array}{c} D \\ E \end{array} \right\}) = \left\{ \begin{array}{c} 1.0 \\ 0.4 \end{array} \right\} \times 10^{-3}.$$

The prediction for the E is considerably less than the product branching fractions measured (see below) for the ι into $K\bar{K}\pi$, $B(\psi \to \gamma\iota)B(\iota \to K\bar{K}\pi) = 5.0 \times 10^{-3}$. However, the result indicates that there could be a small E signal in the mass region that might eventually be extracted with a partial wave analysis.

3.5 The Three-Body Spin-Parity Analysis Method

The spin-parity analysis of the ι presents some unusual difficulties because the correct description of the available two-body decay modes is not obvious. The fairly stringent upper limit on $\iota \to \delta\pi \to \eta\pi\pi$ suggests that something may be wrong either with the statement that the ι decays predominantly into $\delta\pi$ or with the statement that the δ decays both into $K\bar{K}$ and $\eta\pi$. In fact, the evidence for $\delta \to \eta\pi$ is far more convincing than that for $\delta \to K\bar{K}$. Perhaps the threshold enhancement in the $K\bar{K}$ system has a different origin than the $\eta\pi$ signal. For, in addition to the ι not appearing in $\eta\pi\pi$, the structure observed in $\psi \to \gamma(\delta\pi) \to \gamma(\eta\pi\pi)$ does not appear in $K\bar{K}\pi$. Another view is that the

ι does decay into $\delta\pi$, but the absence of a signal in $\eta\pi\pi$ is due to interference with $\iota \to \eta\epsilon \to \eta\pi\pi$ (46).

The spin-parity measurement presented here has two main advantages over the usual partial-wave analysis. These advantages come about because the measurement is based on the three-body helicity formalism, which is discussed in detail in Appendix A. First, the angular distributions that are calculated and the fits that are performed are independent of which two-body decays are present. The angles describe only the overall orientation of the three-body system. In other words, the quantities that describe the Dalitz plot do not enter. Second, because these angular distributions are always meaningful, regardless of any two-body decays, they provide direct visual evidence supporting the spin-parity assignment. Thus, one does not need to rely solely on the rather abstract calculation of the likelihoods for the different hypotheses; they complement the more convincing evidence obtained by simply looking at the angular distributions.

There are some disadvantages to the three-body formalism, which limit its applicability. First, in the presence of large backgrounds, the measured angular distributions will not be those of the decaying particle. Of course, this is a problem for any technique, but a partial-wave analysis can sometimes handle it by absorbing the background into a partial-wave with all distributions uniform. In the present analysis, however, the backgrounds are quite small, and there is no difficulty in applying the three-body technique. A second disadvantage is that high statistics are required, partly because the method does not use all the information that is in principle available. For example, if one knew that the ι decayed into $K^*\bar{K}$, then the angles of the π in the K^* rest frame could be used. In an analysis in which there is a single, clearly identified two-body decay

leading to the three-body final state, the usual two-body helicity formalism is clearly preferable.

The angles calculated in the three-body helicity analysis are shown in Fig. 3.6. Their definitions are:

$\theta_\iota =$ the polar angle of the $K\bar{K}\pi$ system in the lab-frame, measured with respect to the positron beam direction (z-axis)

$\beta =$ the polar angle of the normal to the ι decay plane in the $K\bar{K}\pi$ rest-frame, measured with respect to the momentum direction of the $K\bar{K}\pi$ system

$\alpha - \varphi_\iota =$ the azimuthal angle of the normal to the ι decay plane in the $K\bar{K}\pi$ rest-frame, measured with respect to the azimuthal angle of the ι production plane (the plane defined by the z-axis and the ι momentum direction in the lab-frame).

These definitions may need some clarification, particularly the last one. The lab-frame coordinate system (x, y, z) is defined in Section 2.1. As there is essentially no polarization of the beams, the x- and y-axes can be chosen arbitrarily. The coordinate system (x', y', z') in the ι rest frame is defined as follows: The z'-axis points along $\vec{p}_\iota$ (measured in the lab frame), so that the eigenvalue of $J_{z'}$ is equal to the ι helicity. In the ι rest-frame the momentum vectors of the three decay products sum to zero and therefore lie in a plane whose normal is $\hat{n}$. Then $\cos\beta = \hat{n} \cdot \hat{z}'$. The positions of the x' and y' axes are found by carrying the lab-frame axes through the rotation specified by the three Euler angles φ_ι, θ_ι, $-\varphi_\iota$. The last azimuthal angle, $-\varphi_\iota$, represents a choice of phase (see Appendix A). With this choice the ι production plane (formed by $\hat{p}_\iota$ and $\hat{z}$) has the same azimuth ($= \varphi_\iota$) in the ι rest-frame as in the lab-frame.

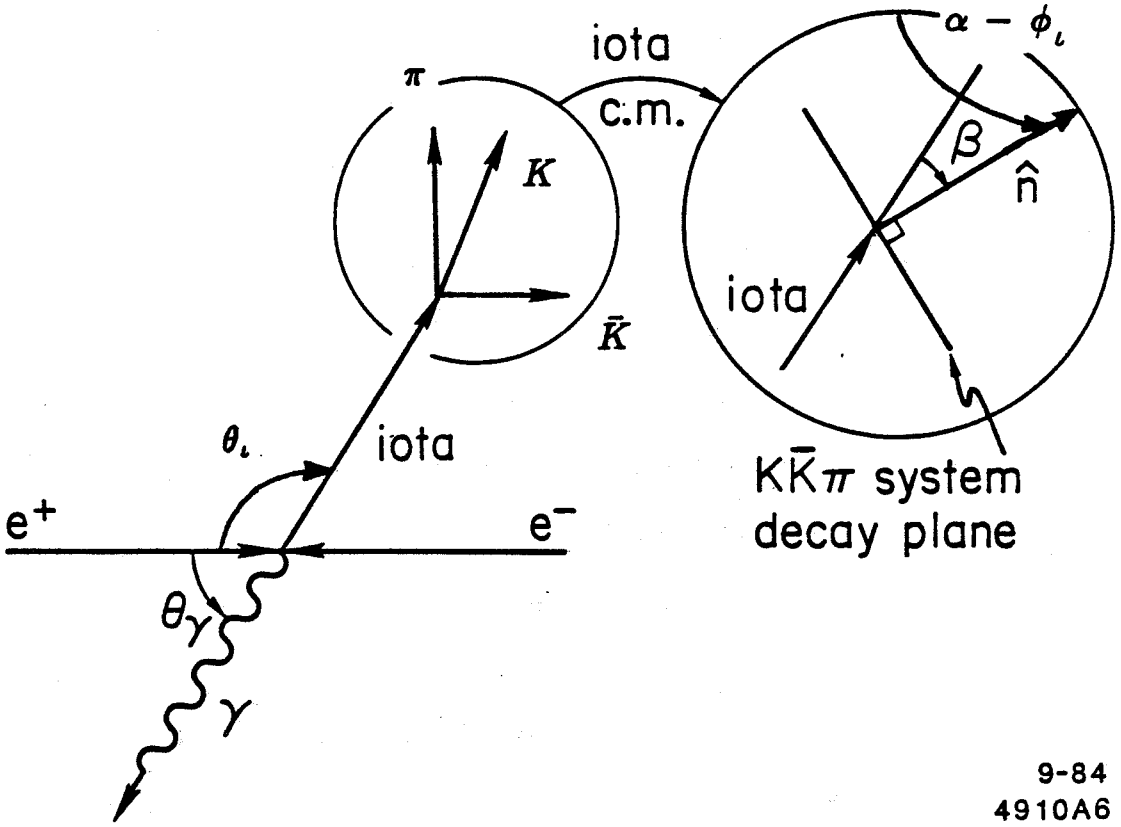

Figure 3.6. Angles used in the ι spin-parity analysis.

The difference $\alpha - \varphi_\iota$ between the azimuth of the decay plane normal and the production plane is the only physically meaningful function of α and φ_ι. The reader who is confused by the definitions of these azimuthal angles can take consolation in the fact that they have very little impact on the results of the fits.

The three-body helicity formalism predicts the following distributions:

$$\begin{aligned}
J^P = 0^- &\Rightarrow \frac{dN}{d\Omega} = (1+\cos^2\theta_\iota) \qquad \cos\beta = \text{ uniform} \\
J^P = 1^+ &\Rightarrow \frac{dN}{d\Omega} = \tfrac{1}{2}(1+\cos^2\theta_\iota)\sin^2\beta + \tfrac{1}{2}x^2\sin^2\theta_\iota(1+\cos^2\beta) \\
&\qquad + \tfrac{1}{4}x\sin 2\theta_\iota \sin 2\beta\cos(\alpha-\varphi_\iota) \\
J^P = 1^- &\Rightarrow \frac{dN}{d\Omega} = (1+\cos^2\theta_\iota)\cos^2\beta + x^2\sin^2\theta_\iota\sin^2\beta \\
&\qquad - \tfrac{1}{2}x\sin 2\theta_\iota\sin 2\beta\cos(\alpha-\varphi_\iota)
\end{aligned} \tag{3.2}$$

where x is the ratio of amplitudes for helicity 1 to helicity 0 and is assumed to be real (47).

The angular distributions given in Eq. (3.2) have the useful property that the marginal distributions of $\cos\beta$ and $\cos\theta_\iota$ are sufficient to distinguish $J = 0$ from $J = 1$. This property allows one to confirm the results of the maximum likelihood fits by a simple inspection of these distributions. For example, by integrating over $\cos\theta_\iota$ in the $J^P = 1^+$ distribution one obtains

$$\frac{dN}{d\cos\beta} = 2x^2 + (2-x^2)\sin^2\beta, \tag{3.3}$$

and by integrating over $\cos\beta$ one obtains

$$\frac{dN}{d\cos\theta_\iota} = 1 + 2x^2 + (1-2x^2)\cos^2\theta_\iota. \tag{3.4}$$

When $x^2 = 2$, the $J^P = 1^+$ $\cos\beta$ distribution becomes uniform and thus coincides with the $J^P = 0^-$ prediction. However, the $\cos\theta_\iota$ distribution for

$x^2 = 2$ is quite different from the $J^P = 0^-$ prediction of $1 + \cos^2\theta_\iota$:

$$\frac{dN}{d\cos\theta_\iota}(J^P = 1^+; \quad x^2 = 2) = 1 - 0.6\cos^2\theta_\iota. \tag{3.5}$$

This distribution is peaked at $\cos\theta_\iota = 0$, in contrast to $1 + \cos^2\theta_\iota$, which is peaked at $|\cos\theta_\iota| = 1$. Thus, there is no value of x^2 for which the $J = 0$ and $J = 1$ predictions for $\cos\theta_\iota$ and $\cos\beta$ both match.

One can verify that the $\cos\beta$ distribution is reasonably well measured by examining a decay for which this distribution is uniquely predicted. The decays $\psi \to \omega\eta$ and $\psi \to \omega\pi^0$, where $\omega \to \pi^+\pi^-\pi^0$, have this property. Here, β is the angle between the normal to the ω decay plane (formed by the three pions in the ω rest-frame) and the momentum vector of the ω. Although the ω is a spin-1 particle, helicity 0 is excluded by parity conservation in these Vector + Pseudoscalar decays. This leads to the prediction that $dN/d\cos\beta = \sin^2\beta$. Figure 3.7 shows the distribution of $\cos\beta$ separately for both $\omega\eta$ and $\omega\pi^0$ events. In both cases, clear agreement with the theoretical prediction is observed. Further checks of the $\cos\beta$ acceptance using the Monte Carlo will be discussed later.

Although the $\cos\beta$ distribution is well measured by the detector, the $\cos\theta_\iota$ distribution suffers from significant acceptance corrections. For large values of $|\cos\theta_\iota|$, it is more likely that one or more of the ι decay products will also have a large value of $|\cos\theta|$; at these angles there are fewer drift chamber hits along the track and the reconstruction efficiency is lower. However, the $\cos\theta_\iota$ distribution is sufficiently well measured – and the acceptance corrections are sufficiently well understood – that with a large number of events the spin 0 and spin 1 angular distributions can be distinguished.

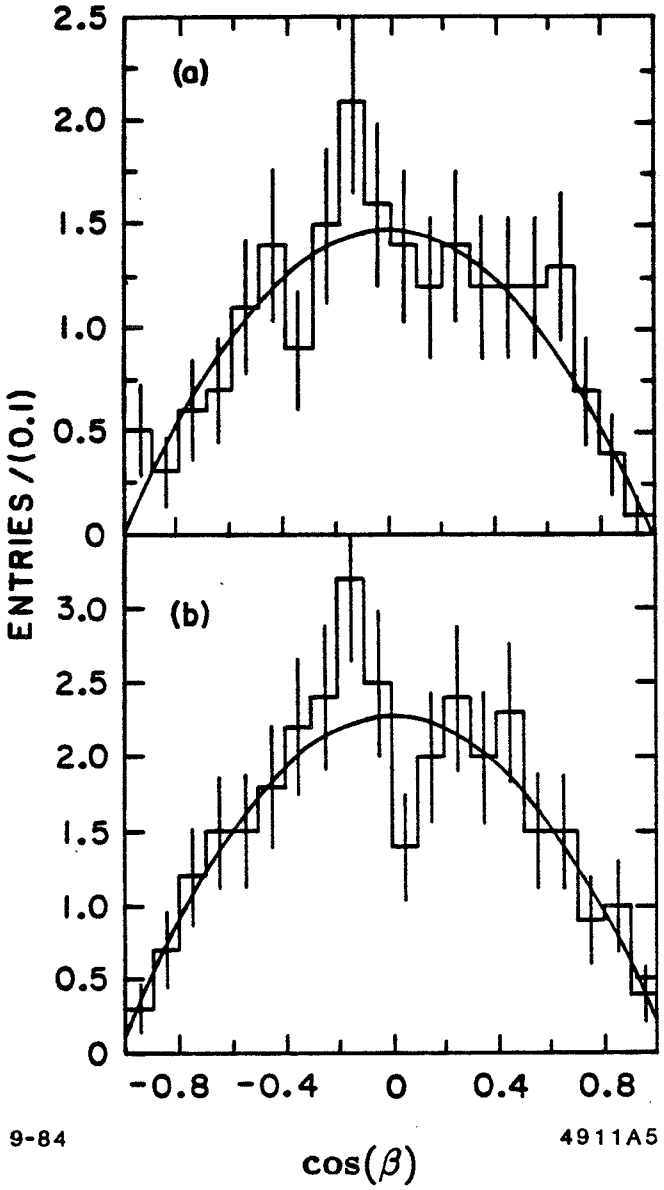

Figure 3.7. The distribution of $\cos\beta$ for $\psi \to \omega\eta$ and $\omega\pi^0$. Here β is the polar angle of the normal to the ω decay plane.

3.6 Fitting Procedure for $\iota \to K\bar{K}\pi$ Spin-Parity Analysis

The use of a maximum likelihood fitting procedure to incorporate acceptance corrections on an event-by-event basis is by now common practice. The technique has the virtue that all of the correlations among acceptance effects for different quantities are included; one is not just making one-dimensional acceptance corrections to measured distributions by averaging over all other kinematic quantities.

Let ν_e denote all of the kinematic quantities necessary to specify the configuration of an event e. The probability density for observing this event is then given by

$$p(e) = \frac{w(\nu_e)\epsilon(\nu_e)}{\left[\int d\nu w(\nu)\epsilon(\nu)\right]}$$

where $w(\nu_e)$ is the probability density to produce the configuration ν_e and $\epsilon(\nu_e)$ is the detection efficiency for the configuration. The integral in the denominator is required to normalize the probability density to one, regardless of the values of any parameters appearing in $w(\nu)$. The probability density for observing the sequence of events $e_1, \ldots, e_N$ with configurations $\nu_{e_1}, \ldots, \nu_{e_N}$ is the product of the corresponding $p(e)$'s:

$$P(e_1, \ldots, e_N) = \prod_{e=e_1}^{e_N} \frac{w(\nu_e)\epsilon(\nu_e)}{\int d\nu w(\nu)\epsilon(\nu)}.$$

It is convenient to work with (natural) log P rather than P. Thus,

$$\log P(e_1, \ldots, e_N) = \sum_{e=e_1}^{e_N} \log\left[\frac{w(\nu_e)}{\int d\nu w(\nu)\epsilon(\nu)}\right] + \sum_{e=e_1}^{e_N} \log \epsilon(\nu_e).$$

In most cases of interest one can write $w(\nu_e)$ as a sum with the unknown coefficients λ_α:

$$w(\nu) = \sum_\alpha \lambda_\alpha w_\alpha(\nu).$$

For example, the λ_α might be helicity or multipole amplitudes. The normalization integral can then be written

$$\begin{aligned}\int d\nu w(\nu)\epsilon(\nu) &= \sum_\alpha \lambda_\alpha \int d\nu w_\alpha(\nu)\epsilon(\nu) \\ &= \lambda_\alpha I_\alpha\end{aligned}$$

and

$$\log P(e_1, \ldots, e_N) = \sum_e \log\left[\frac{w(\nu_e)}{\sum_\alpha \lambda_\alpha I_\alpha}\right] + \sum_e \log \epsilon(\nu_e).$$

According to the maximum likelihood method the most likely values of λ_α are those that maximize $P(e_1, \ldots, e_N)$. The second term on the right hand side, the sum over $\log\epsilon(\nu_e)$, is independent of the λ_α. Thus, for the purpose of determining the values of λ_α, this term can be ignored. Furthermore, if one wishes to compute the relative likelihood for two hypotheses H_1 and H_2, with corresponding predictions $w(\nu;\ H_1)$ and $w(\nu;\ H_2)$, the $\epsilon(\nu_e)$'s divide out so that one has

$$\frac{P(e_1, \ldots, e_N;\ H_1)}{P(e_1, \ldots, e_N;\ H_2)} = \frac{\prod_e \left[w(\nu_e;\ H_1) \Big/ \int d\nu w(\nu;\ H_1)\epsilon(\nu)\right]}{\prod_e \left[w(\nu_e;\ H_2) \Big/ \int d\nu w(\nu;\ H_2)\epsilon(\nu)\right]}.$$

Remarkably, it is unnecessary to compute the acceptance $\epsilon(\nu_e)$ explicitly for each configuration ν_e, either for determining the λ_α or for comparing the likelihoods for different hypotheses. Only the acceptance integrals, I_α, which are fixed and independent of λ_α, need be calculated. They are obtained by generating Monte Carlo events according to phase space, weighting with the appropriate $w_\alpha(\nu)$, and summing over the Monte Carlo events.

It is important to determine the I_α with sufficient precision so that any resulting uncertainty in the ratios of likelihoods for different hypotheses is small compared to the true ratio. If $\Delta \log \mathcal{L} \sim 10$, one would like the uncertainty in

$\Delta \log \mathcal{L}$ to be $\lesssim 1$. In practice, this means that enough Monte Carlo events must be generated so that any statistical fluctuations in the resulting distributions are small. Consider a hypothesis that has no free parameters, such as the $J^P = 0^-$ angular distribution. If the uncertainty in I is δI, then the uncertainty in $\log P$ is

$$\delta(\log P) = \frac{\partial \log P}{\partial I}\delta I = \frac{-N}{I}\delta I$$

or

$$\frac{\delta I}{I} = -\frac{1}{N}\delta(\log P).$$

In the analysis of $\iota \to K_S^0 K^\pm \pi^\mp$ there are about 300 events; to reduce $\delta(\log P)$ below one, it is necessary to have $|\delta I/I| < 0.3\%$. Of course, in comparing likelihoods for different hypotheses there will be some cancellation of these errors; however, this calculation indicates that a surprising degree of precision can be required in the Monte Carlo evaluation of the efficiency integrals I_α.

For the spin analysis of $\iota \to K_S^0 K^\pm \pi^\mp$, a total of 1.2×10^5 Monte Carlo events were used to determine the efficiency integrals. As a check, the Monte Carlo events were divided into four subsamples of 4×10^4 events each, and the spin analysis was repeated with each subsample. The difference in the (natural) log likelihoods between $J = 0$ and $J = 1$ varied by only 1-3 among these fits.

3.7 ANALYSIS OF $\psi \to \gamma\iota$; $\iota \to K_S^0 K^\pm \pi^\mp$

Event selection

To reduce the data sample to a manageable size, events with four charged tracks are 4-C fit to the hypothesis $\psi \to \gamma K^\pm \pi^\mp \pi^+ \pi^-$. If there is more than one shower cluster in the event, the highest energy cluster is used in the fit; any fake photon produced in K decay would have an energy below 1.2 GeV, the

energy of the radiated photon. Photons near charged tracks are not excluded so that the angular distributions are biased as little as possible. No time-of-flight information is used at this stage to identify charged π's and K's. Instead, four fits are tried with each event, taking each particle in succession to be the K and the rest to be the π's. If any of the resulting 4-C fit χ^2's is less than 35, the event is saved for further analysis. This procedure reduces the data sample by about 95%. However, the requirement $\chi^2 < 35$ is extremely loose, and a large background remains that must be removed with more stringent cuts.

K^0_S Identification

The next step in the analysis is to search each event for K^0_S candidates. To do this, pairs of oppositely charged tracks are examined. Because of the fairly long K^0_S lifetime, some improvement in the mass resolution can be achieved by using the track parameters to calculate their crossing point, which is taken to be the vertex position of the K^0_S decay. The momentum vectors of the π^+ and π^- are then calculated at this decay vertex rather than at the distance of closest approach to the beam crossing position. These corrected momentum vectors have the same magnitude as the original vectors, but are rotated in the xy plane to account for the effect of the solenoidal magnetic field.

If there are two crossing points, both of which are within a reasonable distance (10 cm) of the origin, the one with the small z displacement is chosen. There can also be $\pi^+\pi^-$ pairs whose tracks, due to measurement errors, do not cross. In this case the distance of closest approach of the circles formed by the track projection in the $x-y$ plane is required to be less than 9 mm. The vertex position is taken to be halfway between the circles at their distance of closest approach.

Using the corrected momentum vectors and assuming pion masses, one can

calculate the mass of each pair. The pair with mass closest to the K^0_S mass is taken to be the K^0_S candidate; for the event to be considered further the $\pi^+\pi^-$ mass must be within 100 MeV of the K^0_S mass. This cut is very loose, as the mass resolution for the K^0_S is about 6 MeV (see below).

An interesting check is provided by the K^0_S proper lifetime distribution. The proper lifetime is given by

$$\tau = \frac{r}{\beta\gamma} = \frac{m_{K^0_S} r}{p} = \frac{m_{K^0_S} r_{xy}}{p_{xy}},$$

where r_{xy} is the transverse distance of the decay vertex and p_{xy} is the transverse momentum. This formula is useful because it depends only upon well measured transverse quantities and avoids use of the z-coordinate of the vertex. (The uncertainty in the z-position of the origin is $\sigma_z \sim 25$ mm, whereas $\sigma_x \sim 0.5$ mm and $\sigma_y \sim 0.05$ mm.) The K^0_S mass and lifetime distributions for events with $M(K^0_S K^{\pm}\pi^{\mp})$ in the ι mass region (1.34-1.58 GeV) are shown in Fig. 3.8a, b. The parameters obtained by fitting the $\pi\pi$ mass spectrum to a Gaussian plus a flat background are

$$M(K^0_S) = (497.0 \pm 0.3(stat)) \quad \text{MeV}$$
$$\sigma(K^0_S) = (6.0 \pm 0.3(stat)) \quad \text{MeV}$$

where $\sigma(K^0_S)$ is the experimental mass resolution. The lifetime distribution is fit to an exponential with the result

$$c\tau(K^0_S) = (2.3 \pm 0.2) \text{ cm.}$$

This is not quite in agreement with the known value of 2.675 ± 0.007 cm. However, it does agree well with the value 2.2 ± 0.2 cm obtained by analyzing Monte Carlo generated events, which shows that the acceptance effects are

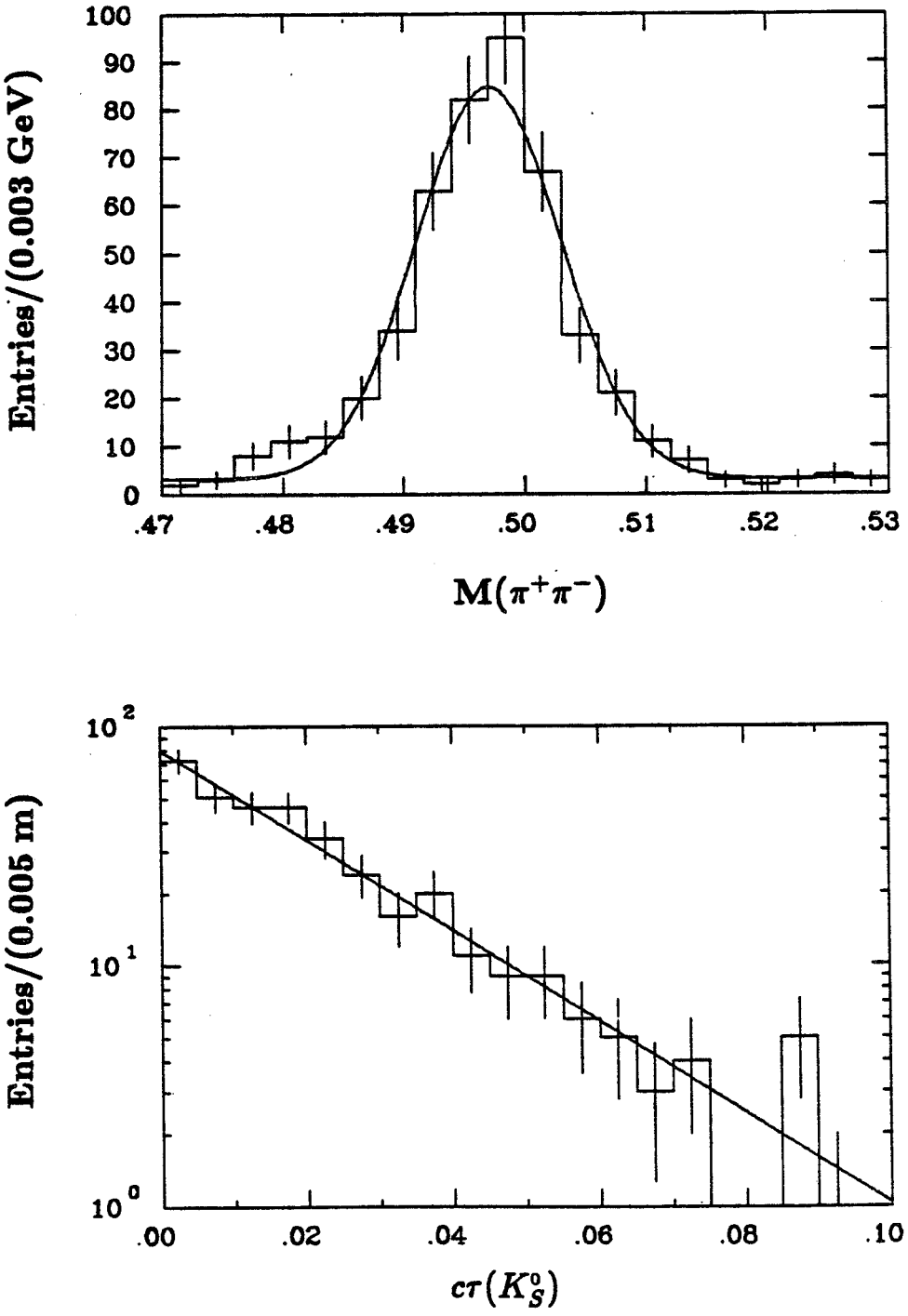

Figure 3.8. The K^0_S mass and lifetime distributions for the ι mass region.

reasonably well modeled. For the purposes of this analysis, it was considered unwarranted to rigorously measure the K^0_S lifetime; to do this would require a more sophisticated technique using a likelihood function to incorporate the acceptance corrections.

Charged Particle Identification

With the K^0_S's cleanly identified, one needs only to assign the correct particle identification to the other two charged tracks. Because the missing mass cannot be large if the event satisfies the initial selection procedure discussed above, there cannot be a missing K^0_L; from strangeness conservation one of the two recoiling charged tracks must be a kaon. Thus, only one of these tracks need be identified by time-of-flight in order to know the particle type of both. In practice, it is required that there be at least one charged track with a time-of-flight weight greater than 0.01 and a track with a non-zero kaon weight.

Breit-Wigner Fits and Branching Ratio

Figure 3.9a shows a scatterplot of $M(K^0_S K^{\pm})$ vs. $M(K^0_S K^{\pm}\pi^{\mp})$. There is a clear cluster of events in which the $K^0_S K^{\pm}$ mass is just above threshold and the $K^0_S K^{\pm}\pi^{\mp}$ mass is in the 1.4-1.5 GeV mass region. If one requires $M(K^0_S K^{\pm}\pi^{\mp})$ to be in the range 1.3-1.58 GeV, the associated M($K^0_S K^{\pm}$) distribution has a roughly triangular shape with a rapid falloff (Fig. 3.9b). The cut on $M(K^0_S K^{\pm}\pi^{\mp})$ restricts $M(K^0_S K^{\pm})$ to be less than 1.42 GeV; however, it is clear that there are very few events at the upper end of the $K^0_S K^{\pm}$ mass spectrum. For this reason, we impose the requirement $M(K^0_S K^{\pm}) < 1.32$ GeV. This cut removes some background above the ι mass region but has very little effect on the ι region itself. The cut used in the Crystal Ball analysis, $M(K^0_S K^{\pm}) < 1.125$ GeV, is much more stringent. (In the Mark III data, this cut removes $\sim 35\%$ of

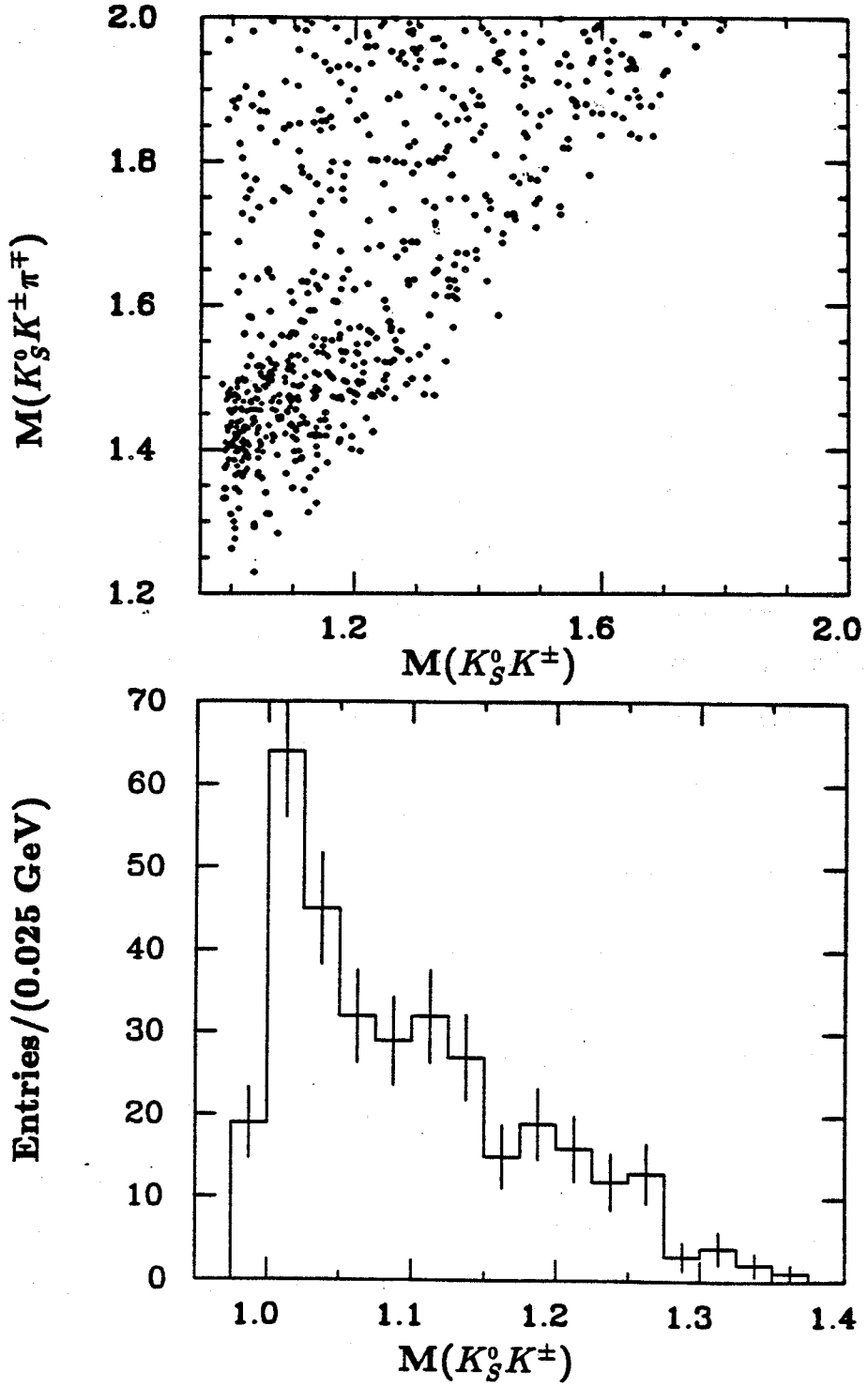

Figure 3.9. Correlation of the ι with low $K^0_S K^\pm$ mass. a) M($K^0_S K^\pm$) vs. M($K^0_S K^\pm \pi^\mp$) and b) M($K^0_S K^\pm$) after requiring M($K^0_S K^\pm \pi^\mp$) in the range $1.3 - 1.58$ GeV.

the events.)

For comparison, Figure 3.10 shows the $K^0_S K^\pm$ distributions that would result from ι decay into three-body $K\bar{K}\pi$ phase space and from decay into $\delta\pi$. Here the $\delta(980)$ line shape is assumed to be given by the Flatté parametrization discussed above. It should be emphasized, however, that this parametrization is based on very little data. The phase space projection is clearly not the correct desription of the measured M($K^0_S K^\pm$) distribution.

The main background in this channel is $\psi \to K^*(890)\bar{K}(1430) + c.c.$, which can produce the final state $K^0_S K^\pm \pi^\mp \pi^0$. The kaons tend to follow the direction of the original K^*'s, resulting in a high mass $K^0_S K^\pm$ system. The $K^0_S K^\pm$ mass cut helps to remove these events, which tend in any case to have $M(K^0_S K^\pm \pi^\mp)$ above the ι mass region. The large decay $\psi \to K^*(890)\bar{K} + c.c.$ does not produce a set of final state particles that can be confused with the signal. The decay $\psi \to \phi\pi^+\pi^-$, whose counterpart $\psi \to \phi\pi^0\pi^0$ feeds down into $\psi \to \gamma K^+ K^- \pi^0$, cannot produce both a K^0_S and a charged kaon.

After making the cut $M(K^0_S K^\pm) < 1.32$ GeV, one obtains the $K^0_S K^\pm \pi^\mp$ mass spectrum shown in Fig. 3.11. The mass resolution of 10 MeV, obtained from the Monte Carlo, is small compared with the observed width. The resonance parameters resulting from a fit to a Breit-Wigner folded with a Gaussian resolution function with a quadratic background shape are

$$M(\iota) = [1.456 \pm 0.005(stat) \pm 0.006(sys)] \text{ GeV}$$

$$\Gamma(\iota) = [0.095 \pm 0.010(stat) \pm 0.015(sys)] \text{ GeV}$$

The statistical errors are obtained from the likelihood function, and the systematic errors are obtained by trying fits with different cuts and different assumptions for the background shape.

The branching fraction is obtained with slightly more restrictive cuts that

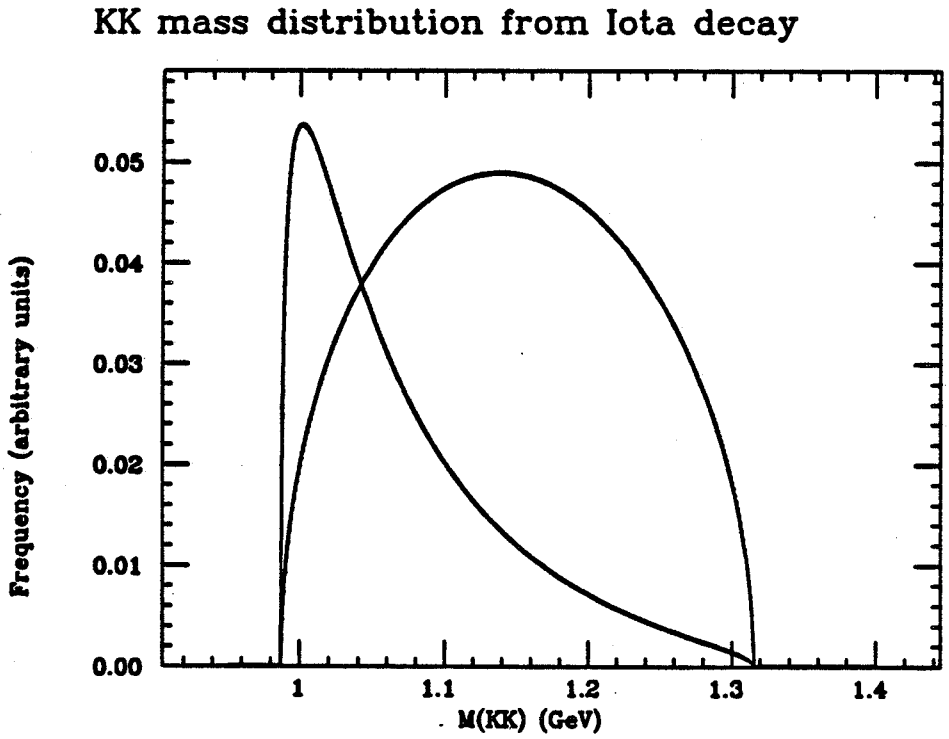

Figure 3.10. Studies of the $K^0_S K^{\pm}$ mass distribution. The curve peaked at threshold is the $\delta(980)$ and the broad curve is the projection of three-body phase space.

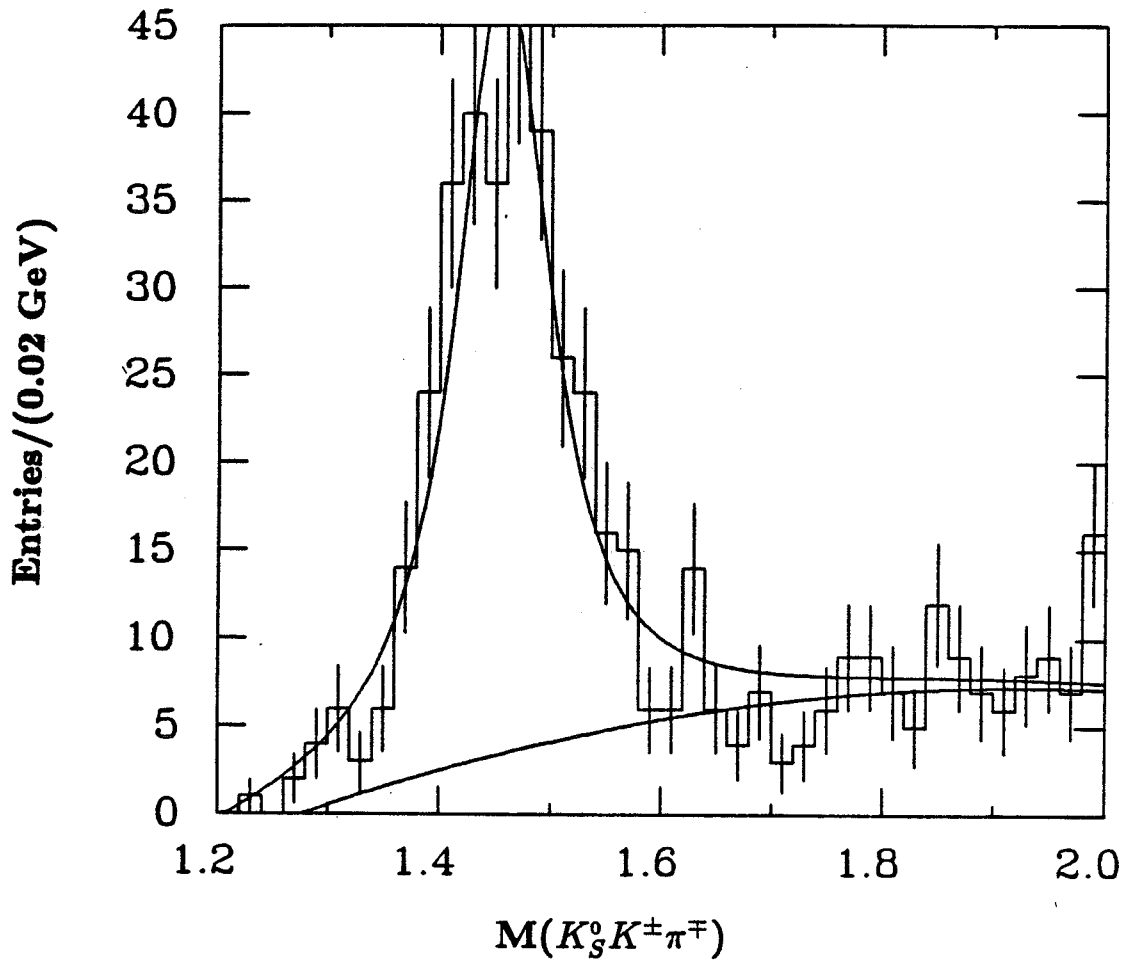

Figure 3.11. The ι signal in the $K^0_S K^\pm \pi^\mp$ mass spectrum.

require each charged track to pass through at least one stereo layer. In addition, the photon is required to be in the range $|\cos\theta| < 0.75$. The measured number of events is 340 ± 18, and with the efficiency of $(11.1 \pm 1.7)\%$ and $B(K^0_S \to \pi^+\pi^-)$=68.6%, one obtains

$$B(\psi \to \gamma\iota)B(\iota \to K\bar{K}\pi) = (5.0 \pm 0.3 \pm 0.8) \times 10^{-3}.$$

Here it is assumed that the isospin of the ι is zero, which implies

$$\frac{B(\iota \to K^0_S K^\pm \pi^\mp)}{B(\iota \to K\bar{K}\pi)} = \frac{1}{3}.$$

The isospin of the ι is discussed in a later section.

For comparison with the Crystal Ball results, one can temporarily make the so-called "δ-cut" and require $M(K^+K^-) < 1.125$ GeV. The resulting $K^0_S K^\pm \pi^\mp$ mass distribution is shown in Fig. 3.12. The parameters obtained from a Breit-Wigner fit are

$$M = [1.442 \pm 0.005(stat)] \text{ GeV}$$

$$\Gamma = [0.085 \pm 0.010(stat)] \text{ GeV}.$$

The mass agrees well with the Crystal Ball and Mark II values, but the width is still considerably larger.

Figure 3.13 shows the axial view of an event of the type $\psi \to \gamma\iota$ with $\iota \to K^0_S K^\pm \pi^\mp$. The tracks crossing near the origin are pions from the K^0_S, which has traveled some distance before decaying.

In modeling the efficiency for the ι, the resonance parameters are taken to be $M = 1.45$ GeV, $\Gamma = 0.095$ GeV, and the polar angle distribution of the photon is assumed to be $1 + \cos^2\theta$, corresponding to $J^P = 0^-$. The ι is then decayed into a broad $K^0_S K^\pm$ resonance below threshold. The ι decay and the decay of the $K^0_S K^\pm$ system are assumed to be isotropic. The values $M(K^0_S K^\pm) = 0.095$

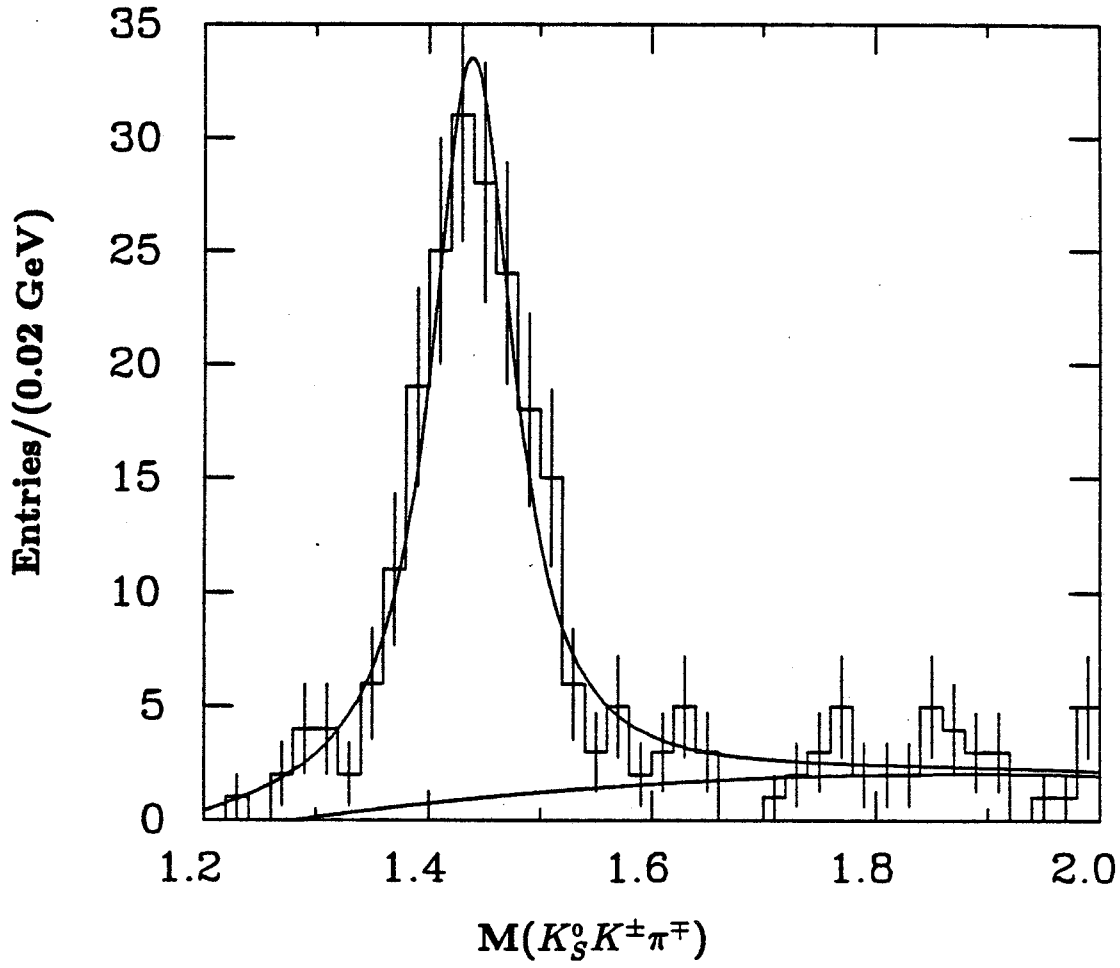

Figure 3.12. The ι signal after requiring $M(K^0_S K^\pm) < 1.125$ GeV.

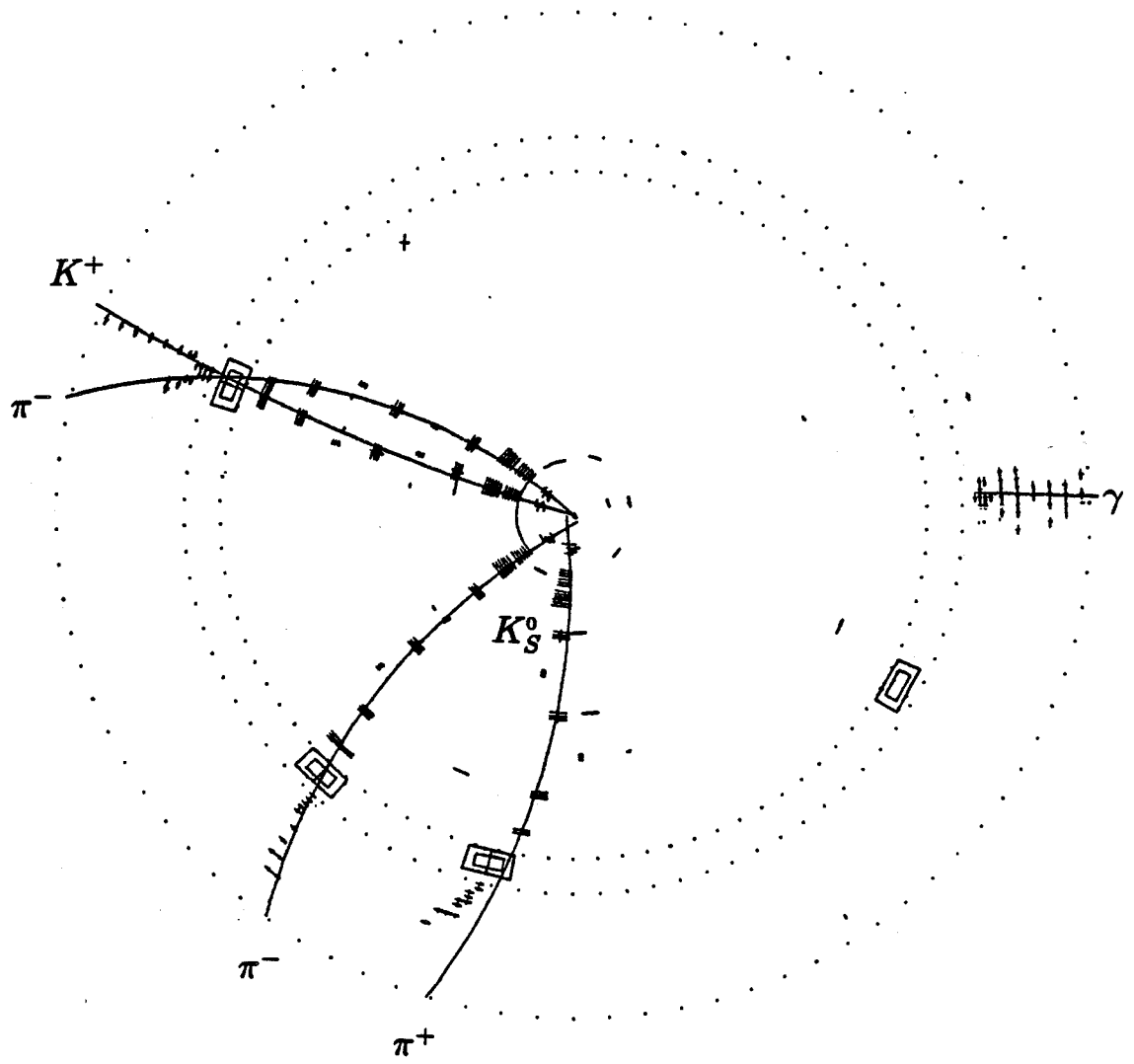

Figure 3.13. Radiative ψ decay to the ι. The 1.2 GeV photon is clearly visible in the shower counter; the tracks crossing near the origin are due to the $K^0_S \to \pi^+\pi^-$ decay.

GeV, $\Gamma = 0.100$ GeV are found to model the shape of the observed $K^0_S K^\pm$ mass distribution well, correctly reproducing the mean, median, and standard deviation. This check is not an argument that the ι actually decays via the δ; it is merely a procedure for ensuring that the Monte Carlo events used to obtain the detection efficiency model the data well. Because the $K^0_S K^\pm$ mass cut is so loose, the detection efficiency is not sensitive to the exact resonance parameters used to describe the $K^0_S K^\pm$ system. Values of $\Gamma(K^0_S K^\pm)$ from 0.075 GeV to 0.300 GeV were tried; the fraction of events with $M(K^0_S K^\pm) > 1.32$ GeV is typically less than 4%.

Angular Distributions and Maximum Likelihood Fits

We consider now the distributions of the ι polar angle (θ_ι) and the polar angle β of the normal to the ι decay plane. These distributions were shown above to discriminate between spin 0 and spin 1. As a check on the analysis procedure, Monte Carlo events were generated according to both spin 0 and spin 1 angular distributions and then passed through the analysis chain as if they were data. In all cases the maximum likelihood fitter, using MINUIT, strongly favored the correct hypothesis. The spin 1 distributions are governed by the parameter x, equal to the ratio of amplitudes for helicity 1 and helicity 0. Therefore, nine different values of x (0.2, 0.4, . . ., 1.8) were used. Figure 3.14 compares the measured values of x with the generated values and shows that they agree well. The line $x_{meas} = x_{gen}$ is shown for reference. The number of events generated in each case was approximately 5000. The good agreement shows not only that there are no gross errors in the analysis procedure, but also that the distributions are sufficiently well measured by the detector to extract the value of x with good precision. (The statistical errors are about the size of the diamonds representing the measurements.)

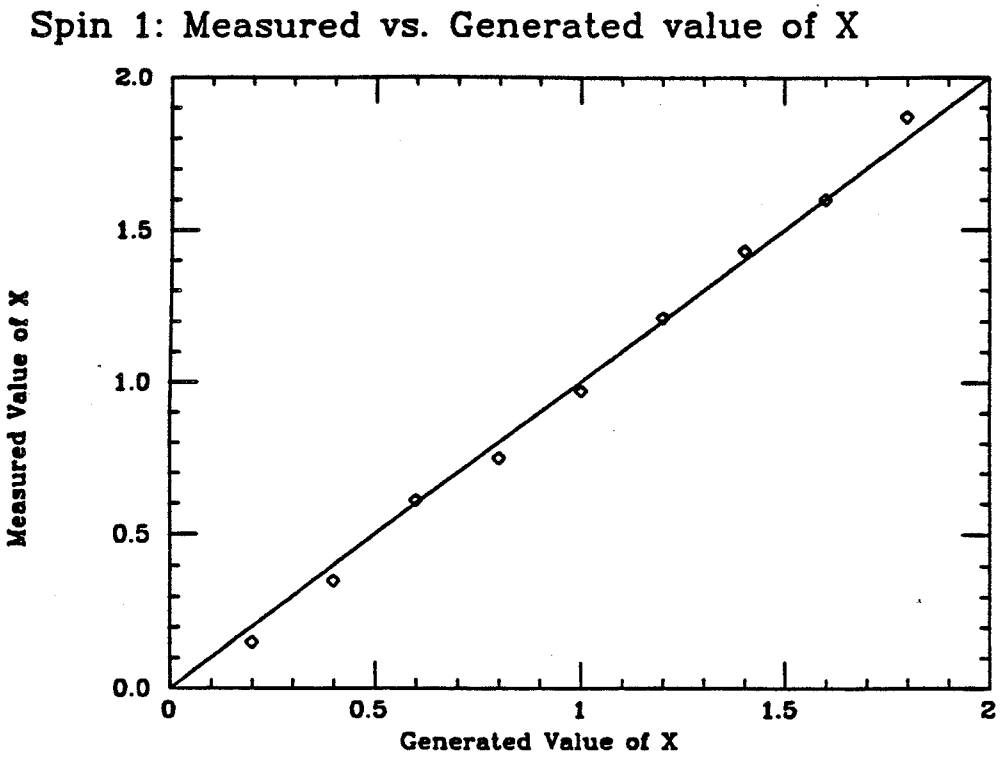

Figure 3.14. Monte Carlo check on the fitting procedure. The measured values of x agree well with the value of x governing the Monte Carlo generated $J^P = 1^+$ angular distribution.

The measured distribution of $\cos\beta$ is shown in Fig. 3.15a; the acceptance is shown in Fig. 3.15b. The $\cos\beta$ distribution agrees well with the uniform distribution predicted for spin 0. The acceptance (averaged over all other angles) is also quite flat for this angle. The fact that the measured $\cos\beta$ distributions for $\psi \to \omega\eta$ and $\omega\pi^0$ agree with the predictions also indicates that the acceptance is reasonably uniform.

The acceptance for $\cos\theta_\iota$ is very non-uniform. When the charged tracks recoiling against the photon have small polar angles and exit the detector through the endcaps, they have fewer drift chamber hits and at angles smaller than about 19°, no z information. The reconstruction efficiency is approximately uniform for $|\cos\theta| < 0.75$ but falls rapidly beyond this value. This geometric efficiency has been studied with $\psi \to \gamma\eta'$, $\eta' \to \gamma\rho^0$ events, and it is found that the agreement between data and Monte Carlo is quite good. Figure 3.16a shows the measured $\cos\theta_\iota$ distribution and Fig. 3.16b shows the acceptance after averaging over all other angles. Figures 3.17a and b show the $\cos\theta_\iota$ distribution after correcting for this average acceptance. In Fig. 3.17a, the (unique) spin 0 prediction is overplotted on the data; in Fig. 3.17b, the curve corresponding to spin 1 is shown. There is no unique spin 1 prediction, of course, but here x is set to the value that makes the $\cos\beta$ distribution uniform. Qualitatively, the data agree much better with the spin 0 prediction. The data do not show the dip at the extremes and the peak at the midpoint that would characterize spin 1^+.

The preceding argument is not meant to provide a quantitative comparison of the relative likelihoods for spin 0 and spin 1. It assumes that the $\cos\beta$ distribution is absolutely flat, perfectly constraining the spin 1 helicity amplitude ratio; it ignores any information present in the correlation between spin 0 and spin 1; and it uses only the average acceptance to correct the $\cos\theta_\iota$ distribution.

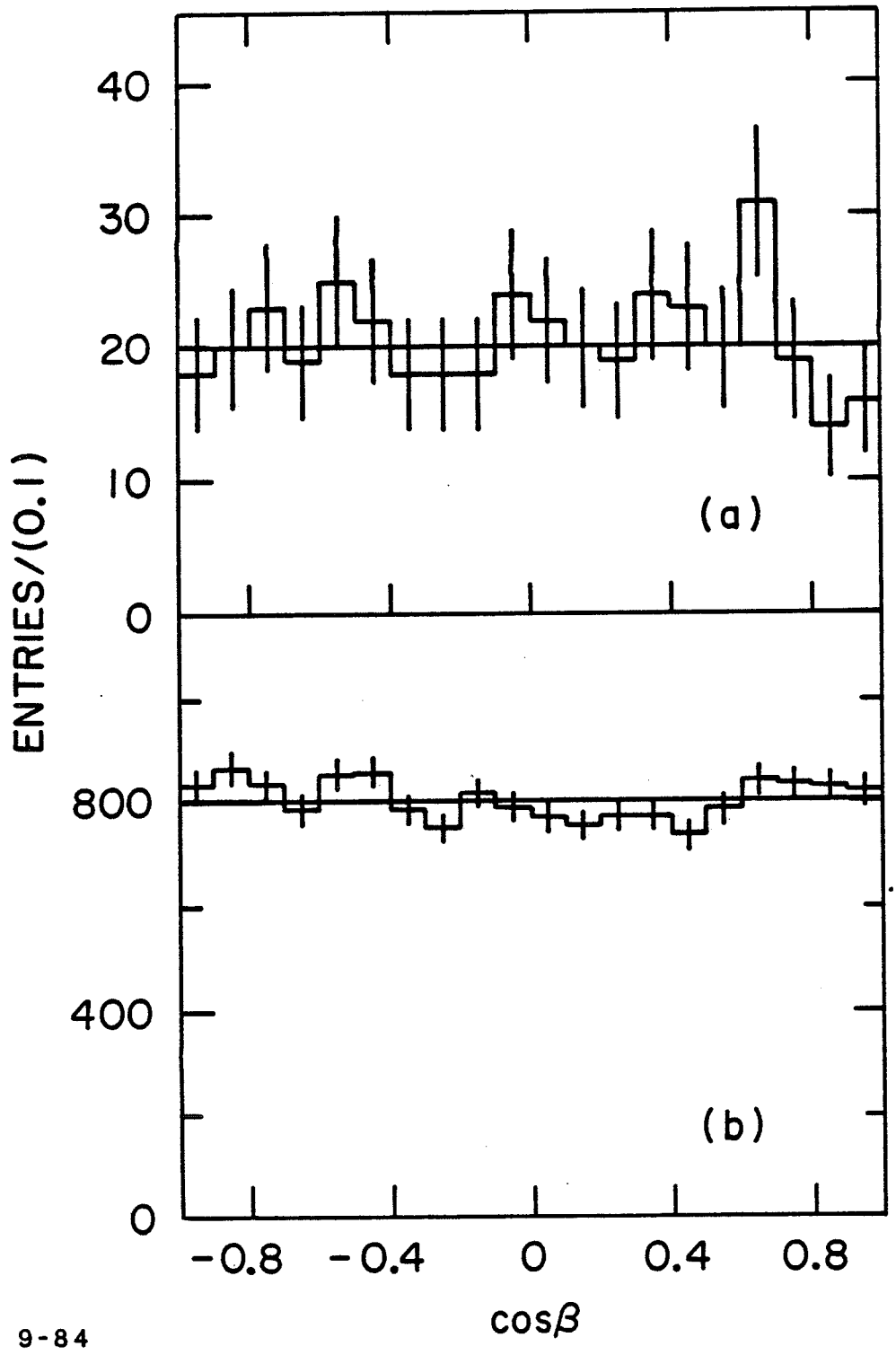

Figure 3.15. Distributions of $\cos\beta$ from $\iota \to K^0_S K^{\pm}\pi^{\mp}$. a) Data b) average acceptance from the Monte Carlo.

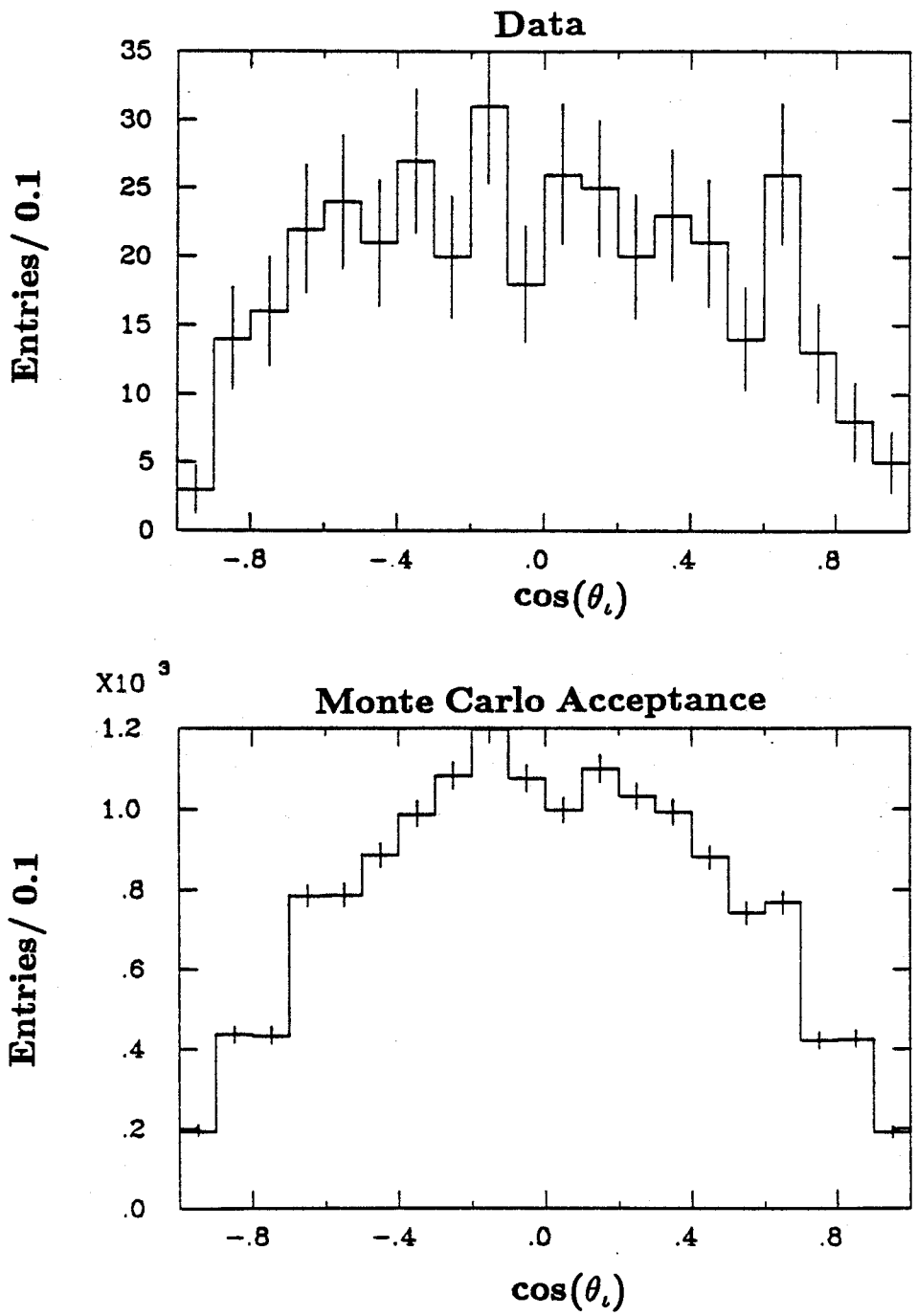

Figure 3.16. Distributions of $\cos\theta_\iota$ from $\iota \to K^0_S K^\pm \pi^\mp$. a) Data and b) average acceptance from the Monte Carlo.

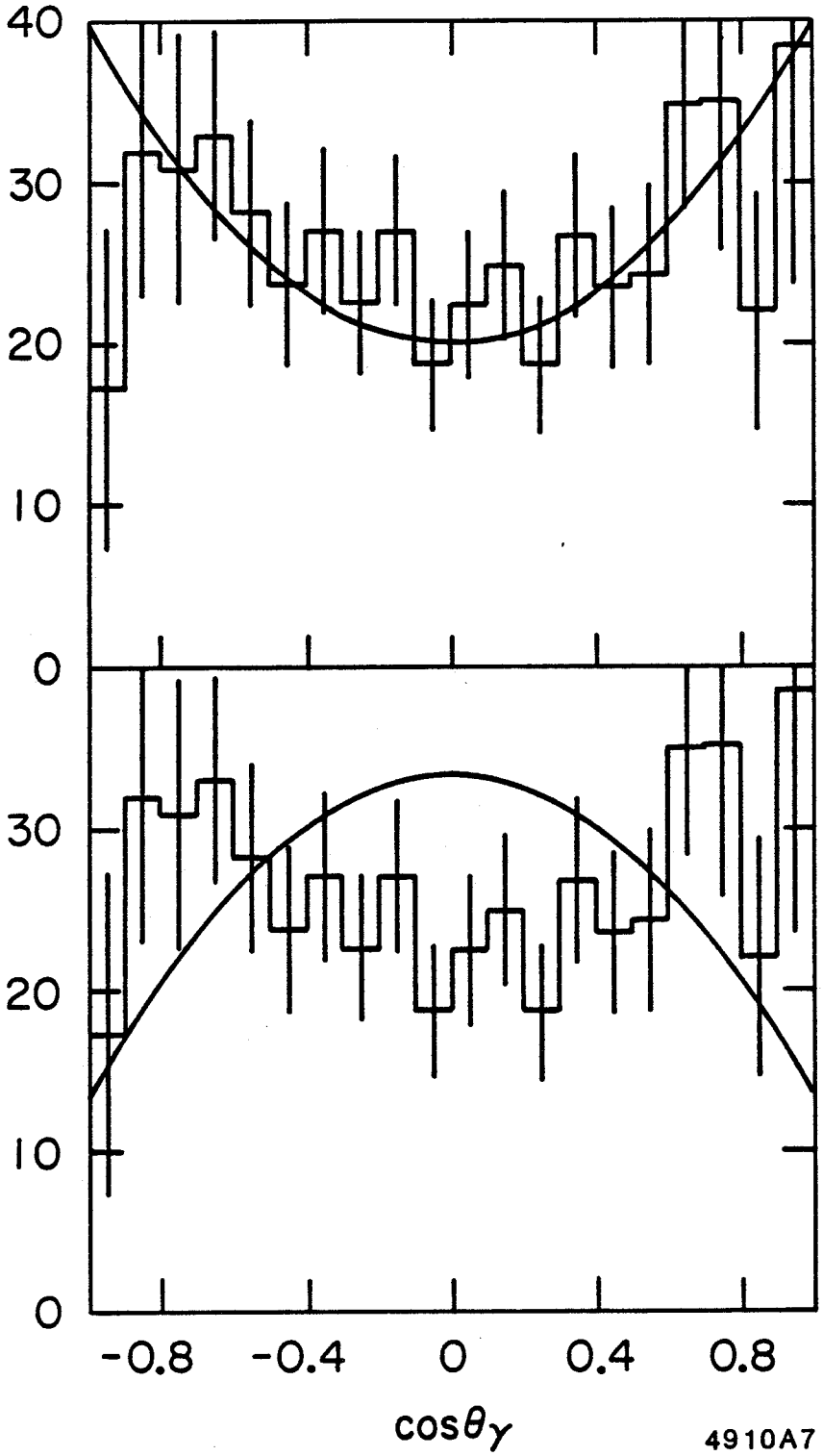

Figure 3.17. Distributions of $\cos\theta_\iota$ corrected for the average acceptance. a) With $J^P = 0^-$ prediction b) with the $J^P = 1^+$ prediction that makes $\cos\beta$ uniform.

It does show, however, where much of the power comes from in the maximum likelihood fits.

To get a feeling for what is happening in the fitting procedure, it is useful to consider a set of Monte Carlo generated histograms of the $\cos\beta$ and $\cos\theta_\iota$ distributions for a variety of hypotheses. The distributions can be compared directly with the non-acceptance corrected data. (The $\cos\beta$ acceptance correction, of course, is negligible.) Figure 3.18 shows the Monte Carlo $J^P = 0^-$ distributions and the $J^P = 1^+$ distributions for the value of x $(= 0.85 \pm 0.05)$ obtained from the best fit to the data.

By varying x, the fitter makes the best compromise between obtaining agreement with the data for both $\cos\beta$ and $\cos\theta_\iota$. The next set of figures (Figure 3.19, Figure 3.20, Figure 3.21, Figure 3.22, Figure 3.23) shows the variations of $\cos\beta$ and $\cos\theta_\iota$ as x is varied from 0.2 to 2.0 in steps of 0.2. For small values of x, the $\cos\theta_\iota$ distribution agrees reasonably well with the data, but the $\cos\beta$ distribution is far too peaked. As x is increased, $\cos\beta$ flattens out, but $\cos\theta_\iota$ becomes too peaked to match the data.

In presenting the three-body helicity formalism it was emphasized that this method permitted an analysis that is independent of which two-body decay modes are present – that is, the structure of the Dalitz plot. One slight qualification to this statement must be made. In obtaining the efficiency integrals from the Monte Carlo, one must choose some way to decay the ι. Conceivably, if the detection efficiency is sensitive to the decay mode, the efficiency integrals could change, affecting the final results. To investigate this question, the efficiency integrals were obtained in two ways. In the first method the ι was decayed according to the scheme discussed above for the branching ratio: the ι decays into "δ"π where the δ-like object has parameters $M = 0.950$

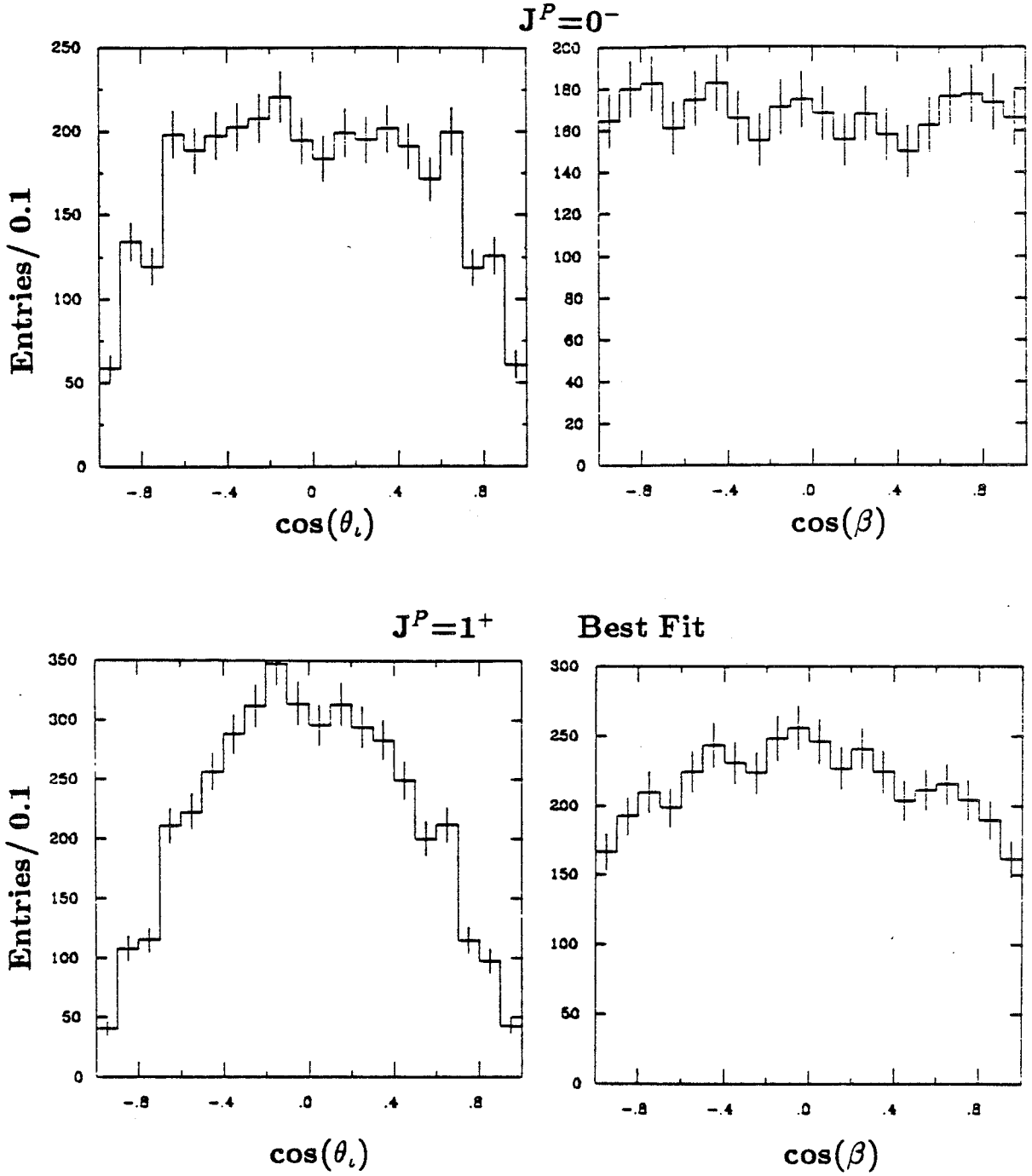

Figure 3.18. Monte Carlo angular distributions. a) The $J^P = 0^-$ distributions and b) the $J^P = 1^+$ distributions corresponding to the value of x (=0.85) obtained from the best fit to the data.

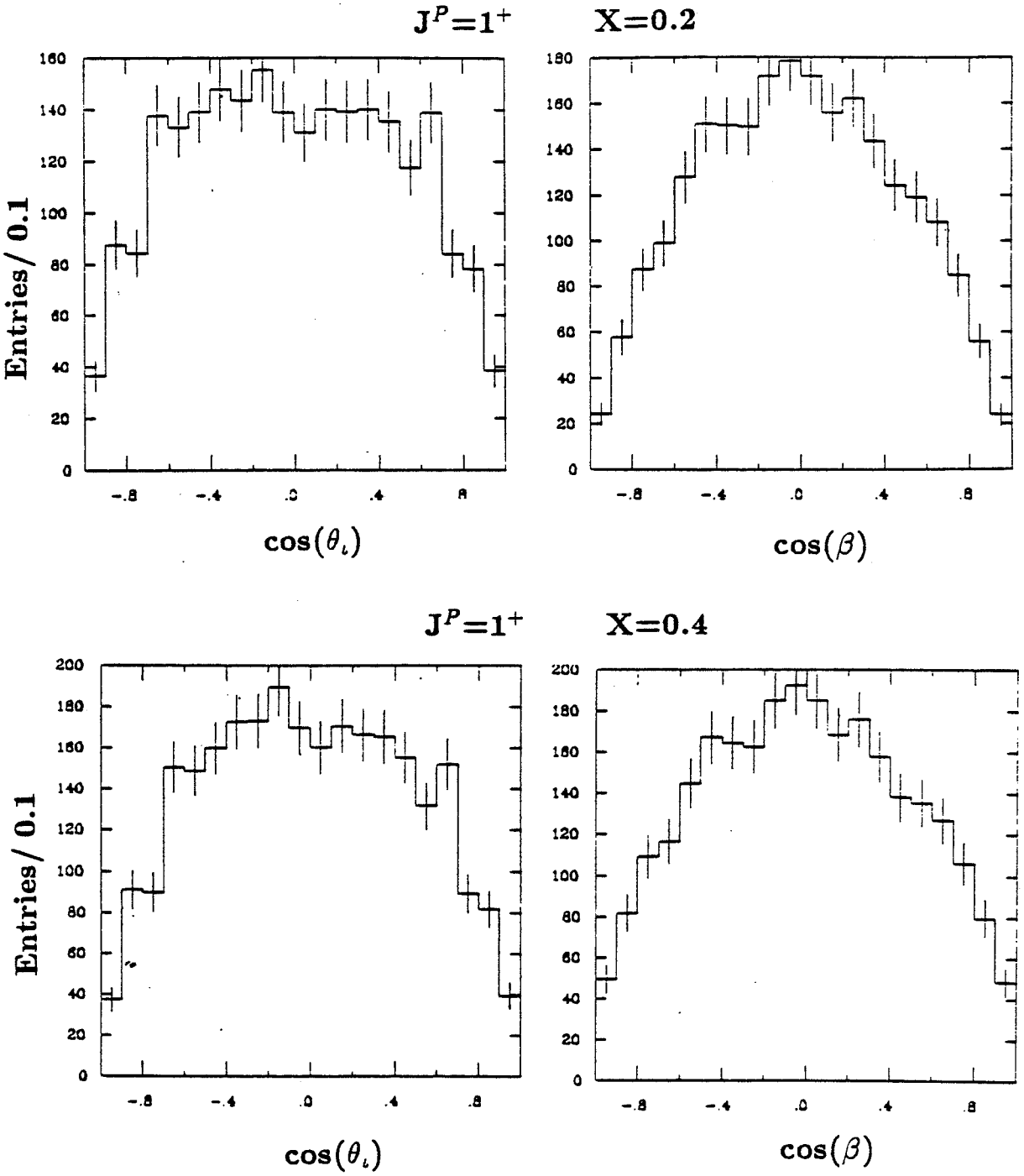

Figure 3.19. Monte Carlo $J^P = 1^+$, x=0.2, 0.4 distributions.

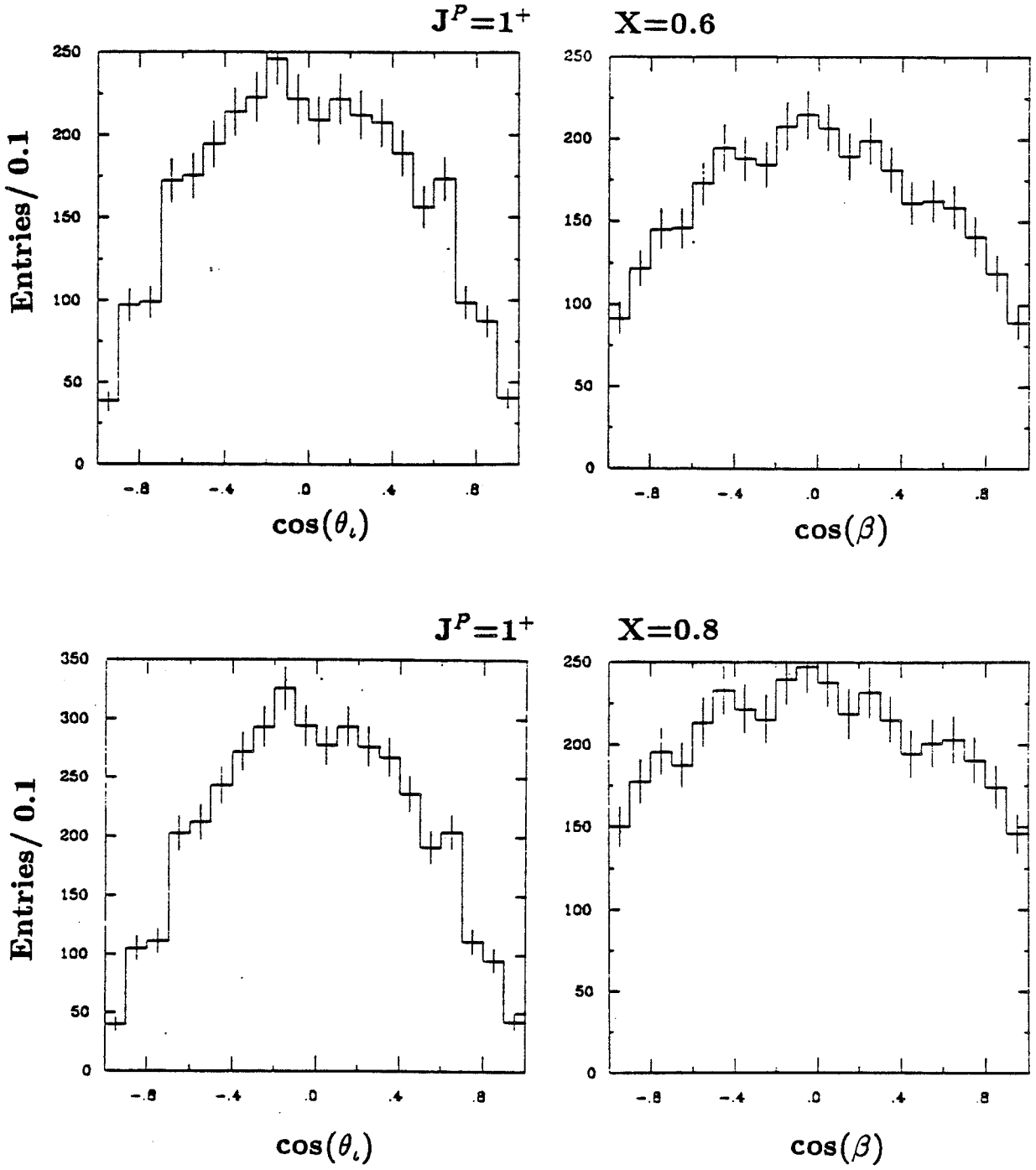

Figure 3.20. Monte Carlo $J^P = 1^+$, x=0.6, 0.8 distributions.

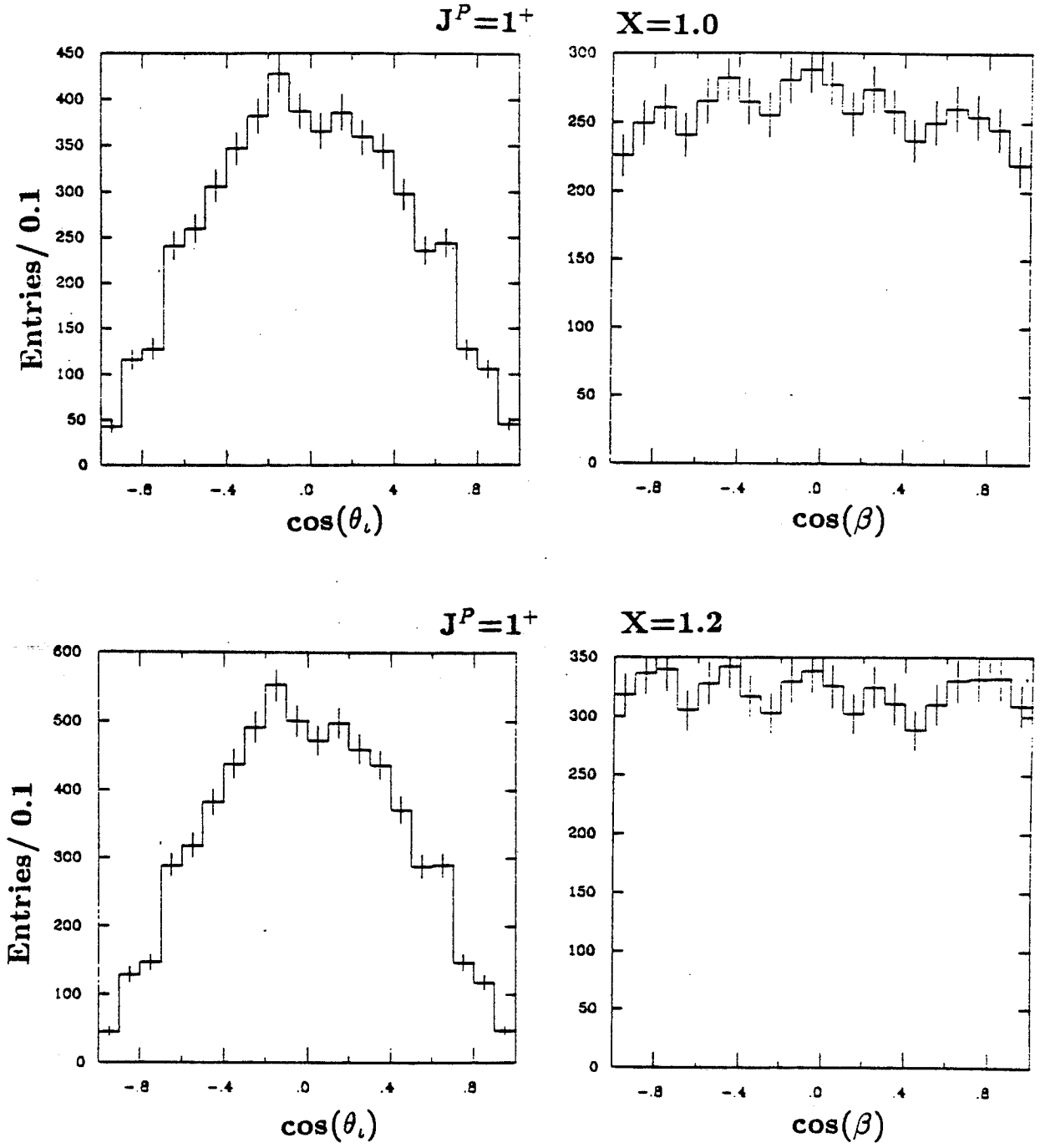

Figure 3.21. Monte Carlo $J^P = 1^+$, x=1.0, 1.2 distributions.

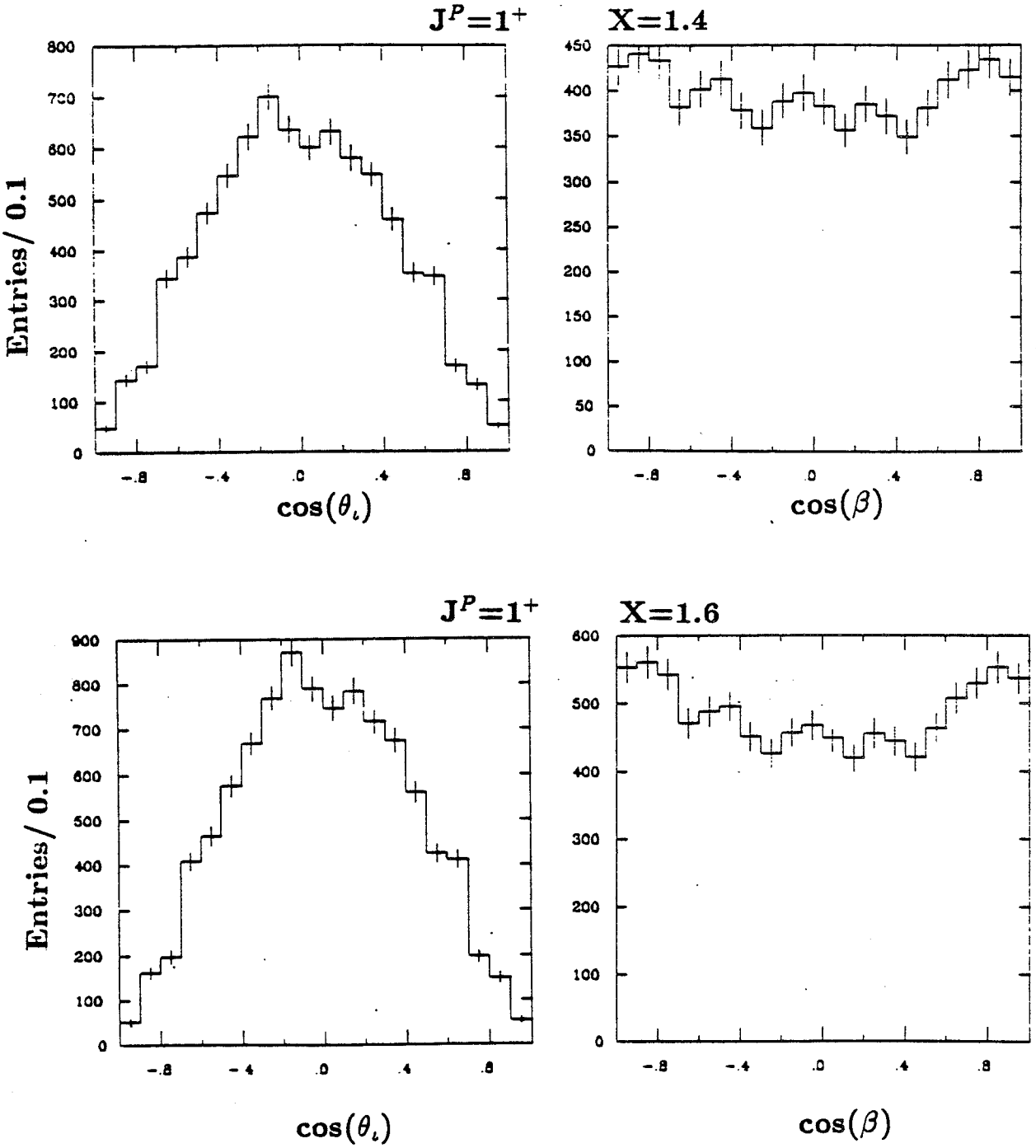

Figure 3.22. Monte Carlo $J^P = 1^+$, x=1.4, 1.6 distributions.

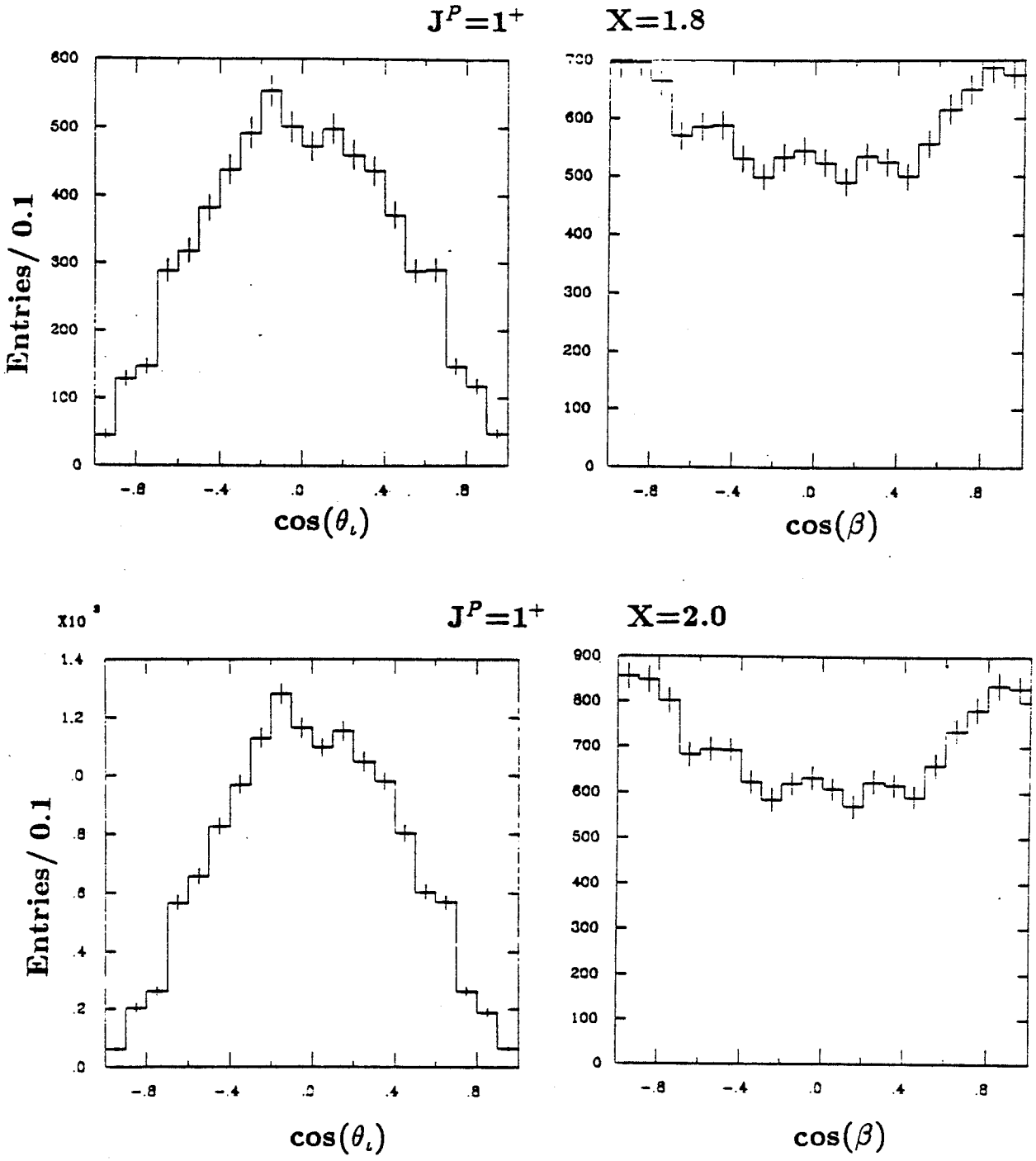

Figure 3.23. Monte Carlo $J^P = 1^+$, x=1.8, 2.0 distributions.

GeV and $\Gamma = 0.100$ GeV. As discussed above, this appears to model the $K^0_S K^{\pm}$ mass distribution quite well and probably provides the best estimate of the detection efficiency. The second method assumes that the ι decays solely via $K^* \bar{K} + c.c.$ This hypothesis is clearly incorrect, as will be seen later from the Dalitz plot. However, it does provide a measure of the worst case systematic errors that might be present in the efficiency integrals. It is found that the results are only slightly sensitive to the decay model; specifically, the difference in log likelihoods for spin 0 and spin 1 changes by only 1-2 when different decay models are used. This change is small compared to the difference in log likelihoods and therefore does not alter the conclusions.

For $J^P = 1^+$ the preferred value of x is 0.85 ± 0.05 and and for $J^P = 1^-$ the preferred value is -1.2 ± 0.1. The ratio of likelihoods is

$$\mathcal{L}(1^+)/\mathcal{L}(0^-) = \exp(-8) \sim 3 \times 10^{-4}$$
$$\mathcal{L}(1^-)/\mathcal{L}(0^-) = \exp(-14) \sim 8 \times 10^{-7}$$

In principle, one could argue that the spin 1 fit has an additional degree-of-freedom not present in the spin 0 hypothesis. This could be taken into account by subtracting 1 from the spin 1 log likelihoods, which would somewhat strengthen the conclusions. As the result is clear anyway, we adopt the more conservative approach and use the ratios quoted above. The likelihood function will be discussed in more detail in the analysis of $\iota \to K^+ K^- \pi^0$.

Dalitz Plot

Because the fitting procedure used to determine the ι spin was designed to

be as insensitive as possible to the details of which decay modes are present, it provides no information concerning this question. It would be surprising to observe $\iota \to K^*\bar{K} + c.c.$ because this decay is expected to be suppressed by G_V-parity. Apart from this theoretical prediction, the main interest in determining the fraction of ι decays to $K^*\bar{K} + c.c.$ is that all of the hadronic experiments find that the $K\bar{K}\pi$ Dalitz plot of the E is dominated by $K^*\bar{K}$. Thus, measuring $B(\iota \to K^*\bar{K})$ provides another means of distinguishing the ι from the E.

The Dalitz plot for $\iota \to K^0_S K^\pm \pi^\mp$ is shown in Figure 3.24. The measurement of its structure is not completely straightforward, because the K^* bands overlap in the δ region due to the limited phase space. We have therefore adopted the following procedure for obtaining a limit on $B(\iota \to K^*\bar{K} + c.c)$. Requiring $M(K^0_S K^\pm \pi^\mp)$ to be in the range 1.2-1.6 GeV, one counts the number of events in the Dalitz plot that are in the K^* bands but which are outside the region where the bands overlap. One then corrects this number for the fraction that would lie in these regions if the ι decayed solely into $K^*\bar{K}$.

Figure 3.25a shows the Dalitz plot for Monte Carlo $\iota(J^P = 0^-) \to K^*\bar{K}$ events. Angular momentum conservation requires the K^* helicity to be zero; this leads to a $\cos^2\theta$ distribution of the K^* decay products, which explains the node structure observed in the Dalitz plot. The bands constructively interfere in the overlap region. Figure 3.25b shows the Monte Carlo $K^\pm\pi^\mp$ mass spectrum after requiring $M^2(K^0_S\pi^\pm)$ to be in the range 0.44-0.55 GeV^2. The clear K^* peak is fit with a Breit-Wigner with mass and width fixed at the known values of the K^* plus a quadratic background. As there is no $\iota \to$ non $K^*\bar{K}$ background in the Monte Carlo, one expects the K^* Breit-Wigner to take up essentially all of the events. This is the case, with greater than 96% of the events in the distribution due to the K^* Breit-Wigner. In the analogous $K^0_S\pi^\pm$ mass spectrum, with

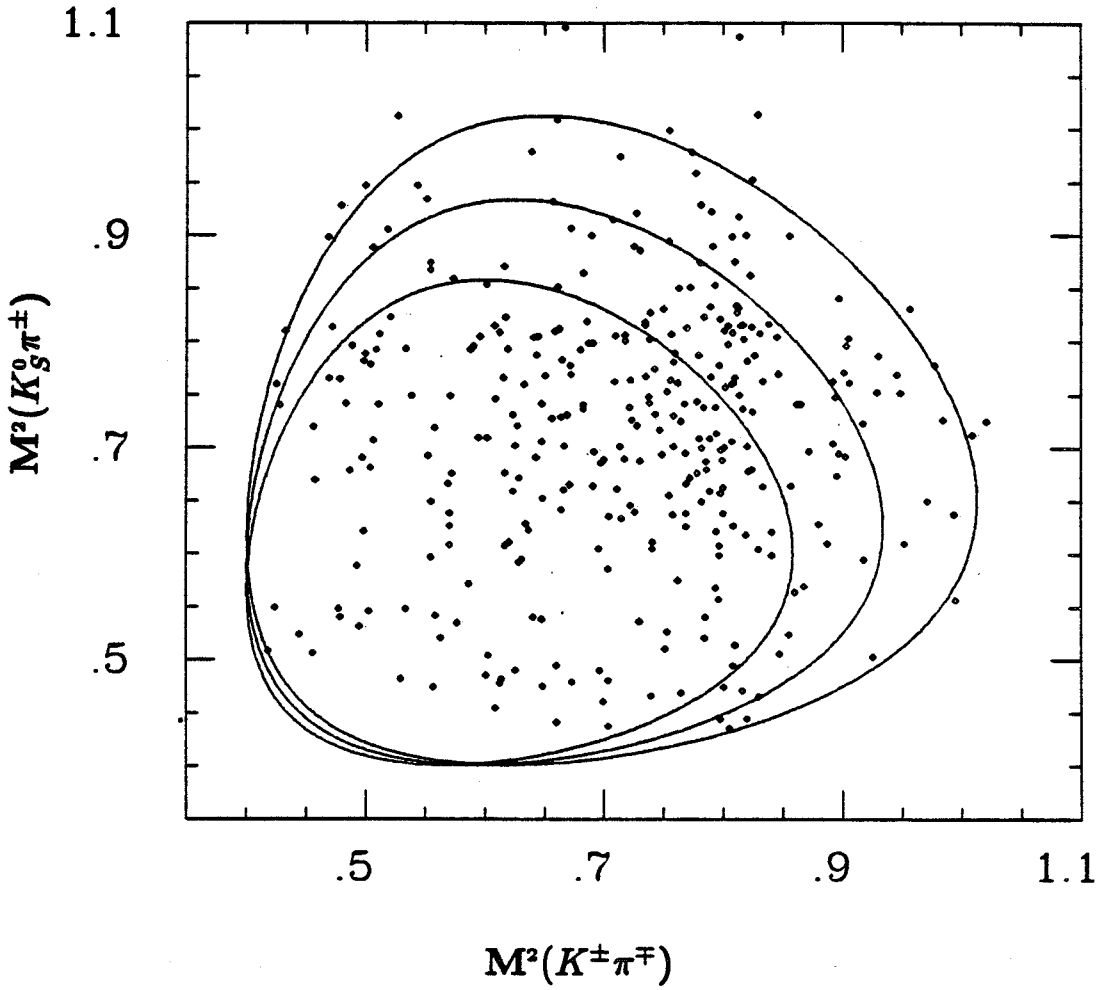

Figure 3.24. The Dalitz plot for $\iota \rightarrow K^0_S K^{\pm}\pi^{\mp}$. The boundary curves correspond to $M(K^0_S K^{\pm}\pi^{\mp}) = 1.42$, 1.46, and 1.50 GeV.

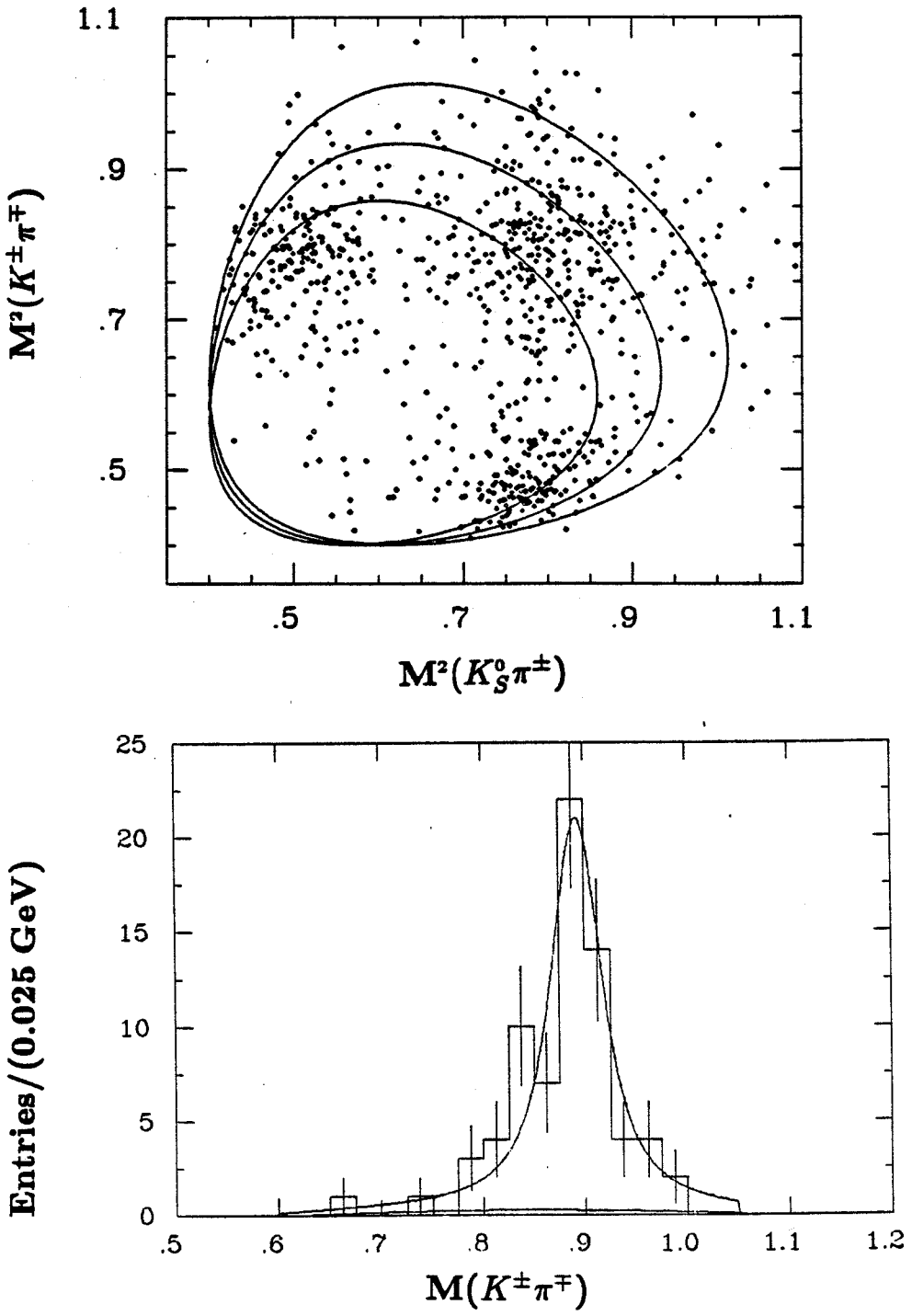

Figure 3.25. $\iota \to K^*\bar{K}$+c.c. Monte Carlo. a) Dalitz plot and b) M($K^{\pm}\pi^{\mp}$) for $M^2(K^0_S\pi^{\pm})$ in the range 0.44-0.55 GeV^2.

$M^2(K^0_S\pi^\pm)$ in the range 0.44-0.55 GeV^2, the fraction is 99%. Summing the number of events in the two regions, one finds that they constitute 29.2% of the total events in the Monte Carlo $\iota(J^P = 0^-) \to K^*\bar{K} + c.c.$ Dalitz plot.

We now apply the same procedure to the Dalitz plot associated with the ι mass region, 1.2-1.6 GeV. No $K^0_S K^\pm$ mass cut is made. Requiring $M^2(K^\pm\pi^\mp)$ to be in the range 0.44-0.54 GeV^2, one obtains the $K^0_S\pi^\pm$ mass distribution shown in Figure 3.26a. Again, the distribution is fit to a K^* Breit-Wigner plus a quadratic background. The curve corresponding to the 90% C.L. upper limit is shown in Fig. 3.26a; there are 19 events under the Breit-Wigner. Applying the same procedure to the $K^\pm\pi^\mp$ mass distribution leads to a 90% C.L. upper limit of 21 events (Fig. 3.26b). After summing these and dividing by the sampling fraction (29.2%) obtained above and by the number of ι events, one obtains

$$\frac{B(\iota \to K^*\bar{K} + c.c.)}{B(\iota \to K\bar{K}\pi)} < 0.35 \qquad 90\% \text{ C.L.}$$

Thus, the ι has a very different Dalitz plot from the $E(1420)$, for which $B(K^*K)/B(K\bar{K}\pi)$ is greater than 50% according to all experiments and 100% according to the experiment with the largest data sample.

3.8 Analysis of $\psi \to \gamma\iota$, $\iota \to K^+K^-\pi^0$

The analysis of the $K^+K^-\pi^0$ decay of the ι is performed in two steps. First, events with two charged tracks and at least three shower clusters are 4-C fit to the hypothesis $\psi \to 3\gamma K^+K^-$. No time-of-flight information is used at this point — the tracks are simply assigned kaon masses. Because there are often spurious photons due to kaon interactions in the shower counter or to kaon decays in flight, one cannot require that there be exactly three shower clusters. The difficulty is compounded by the soft energy spectrum of the photons from

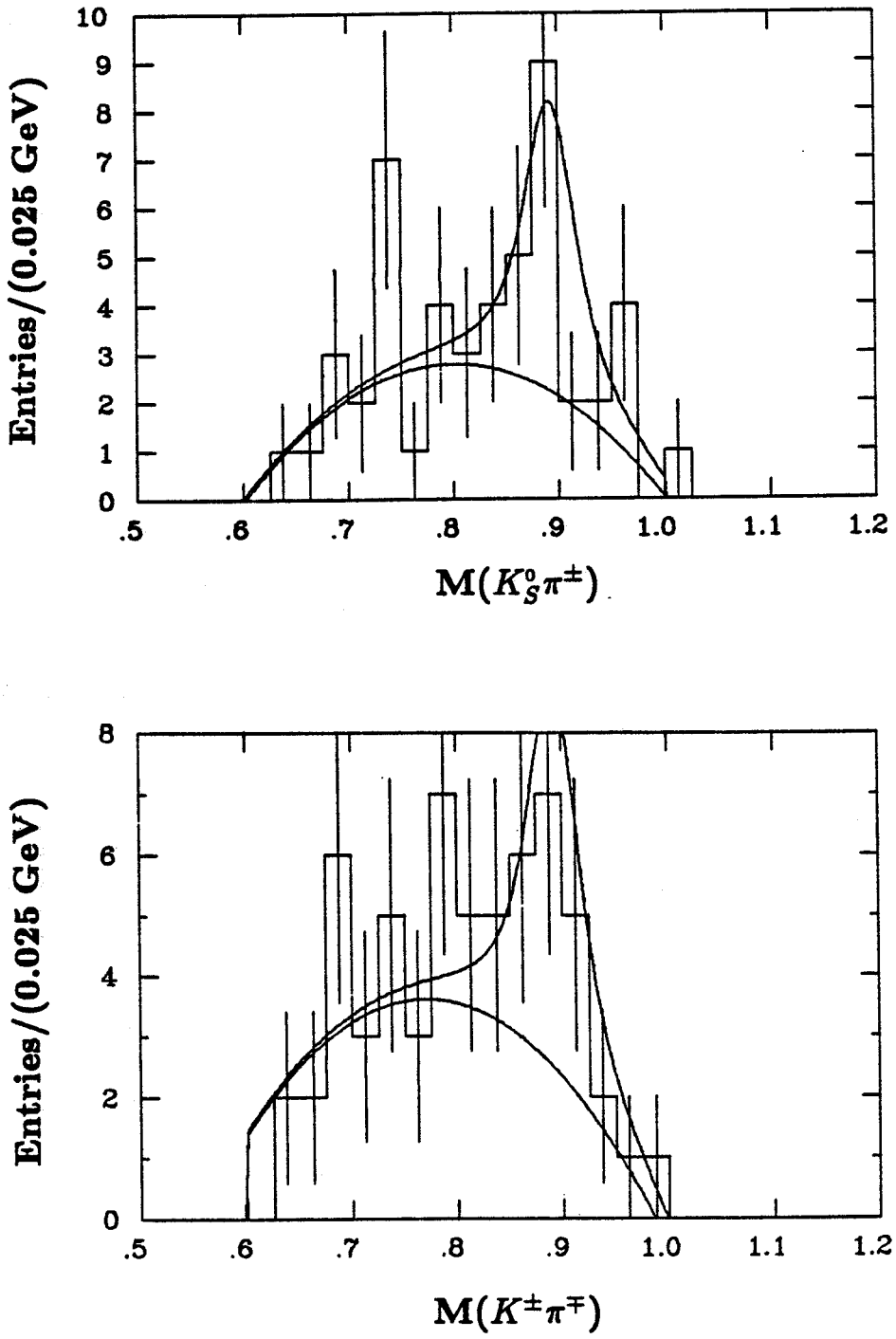

Figure 3.26. Setting the limit for $\iota \to K^*\bar{K} + c.c.$ a) M($K^0_S\pi^\pm$) for $M^2(K^\pm\pi^\mp)$ in the range 0.44-0.55 GeV^2. b) M($K^\pm\pi^\mp$) for $M^2(K^0_S\pi^\pm)$ in the range 0.44-0.55 GeV^2.

the π^0 decay. The spurious photons also typically have low energies, but in this channel they cannot be rejected on the basis of energy. For this reason, the following 4-C fits are done using the five highest energy photons:

$$\psi \to \gamma_1\gamma_2\gamma_3 K^+K^-$$

$$\psi \to \gamma_1\gamma_2\gamma_4 K^+K^-$$

$$\psi \to \gamma_1\gamma_2\gamma_5 K^+K^-$$

$$\psi \to \gamma_1\gamma_3\gamma_4 K^+K^-$$

where γ_1 has the highest energy. If any of the above fits has a $\chi^2 < 25$ and has at least one $\gamma_i\gamma_j$ combination with mass less than 0.35 GeV, the event is retained for further analysis. The cuts used in this procedure are extremely loose and are not sufficient to isolate a clean signal. Both the background rejection and the mass resolution can be improved by adding the π^0 mass constraint; the resulting mass resolution on the $K^+K^-\pi^0$ system at the ι mass is then $\sigma = 11$ MeV for the 5-C fit.

The 5-C fits are done using the same set of photon candidates as in the 4-C fits, but the two lower energy photons are constrained to the π^0 mass. The assumption that the highest energy γ is radiated by the ψ is in fact a very good one. Figure 3.27 shows the measured distributions of $E(\gamma_2)$ and $E(\gamma_3)$. The $E(\gamma_2)$ distribution cuts off around 0.6 GeV, substantially below the 1.2 GeV photon radiated by the ψ. Of course, the assumption that the highest energy photon is radiated by the ψ eventually ceases to be valid as the mass of the recoil system is increased.

The following cuts are then imposed:

1. $P_{\chi^2}(5C) > 0.1$.

2. Time-of-flight identification: at least one charged track must have a kaon

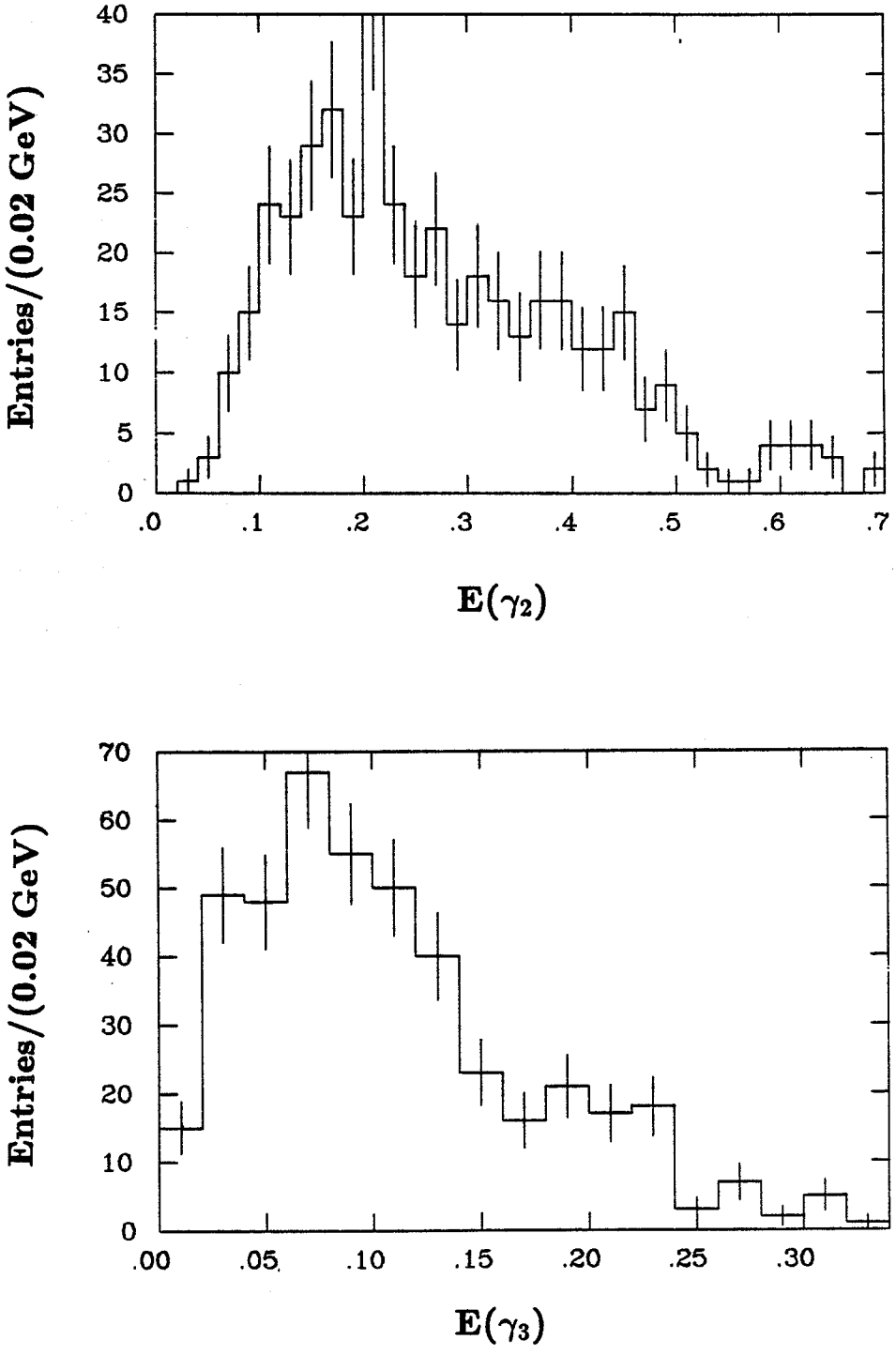

Figure 3.27. Measured distributions of $E(\gamma_2)$ and $E(\gamma_3)$ from $\iota \to K^+K^-\pi^0$.

weight greater than 0.011 (corresponding to $t_{meas} - t_{predicted}$ within 3σ). Events with pion weights larger than the kaon weights are excluded.

3. $E(\gamma_3) > 40$ MeV.

The last cut is required to ensure that the Monte Carlo adequately models the photon detection efficiency. A major concern in the analysis of this decay is the extremely high fraction of events with soft photons: approximately 50% have $E(\gamma_3)$ less than 100 MeV. Although the photon detection efficiency appears to be reasonably good in the 50-100 MeV range, correctly modeling this efficiency in the Monte Carlo is a nontrivial problem. In other decay modes discussed later, a shower generator based on crude shower phenomenology is used in the Monte Carlo. Because this generator does not adequately model the detection efficiency below 100 MeV, events are required to have photon energies above this value when branching fractions are obtained. In the decay $\iota \to K^+K^-\pi^0$, making such a cut would drastically reduce the number of events and, what is worse, bias the $\cos\beta$ distribution, because the energy of a photon in the lab frame is correlated with its production angle in the decay frame.

To improve the shower modeling, the EGS generator (48) was implemented and used for this analysis. Figure 3.28a shows the Monte Carlo generated distribution of $E(\gamma_3)$. In Fig. 3.28b, the observed $E(\gamma_3)$ distribution (from Fig. 3.27) has been divided by the Monte Carlo generated distribution bin-by-bin. If the two original distributions had the same shape, a flat distribution would result. (The relative normalization has no significance.) It is evident that while the agreement is fairly good above 40 MeV, the efficiency below 40 MeV is higher in the data than it is in the Monte Carlo. To some extent, this could be due to spurious low energy photons, which are not modeled by the Monte Carlo. In any case, the fraction of events with photons below 40 MeV is sufficiently

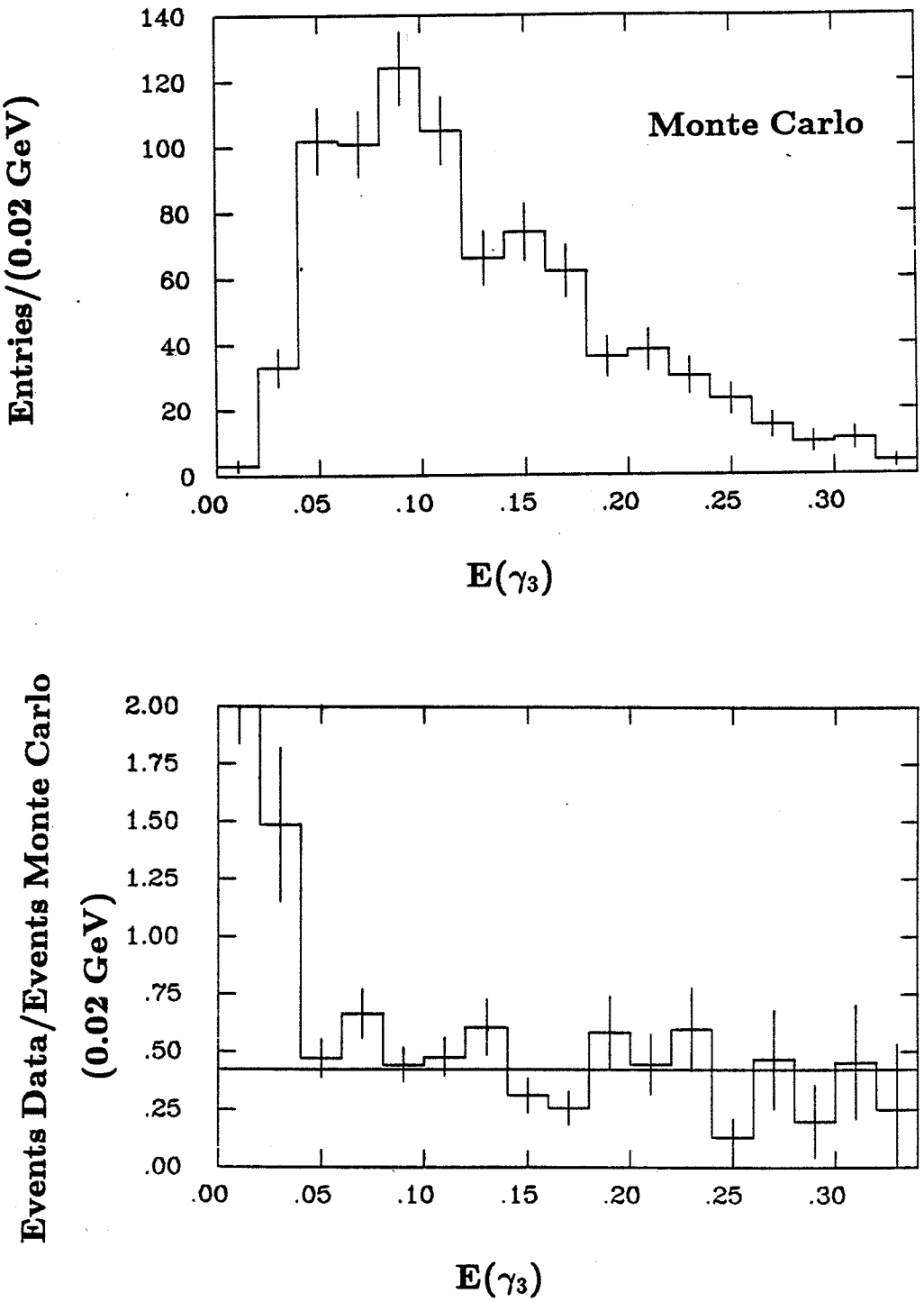

Figure 3.28. Study of soft photons from $\iota \to K^+K^-\pi^0$. a) The Monte Carlo distribution of $E(\gamma_3)$ and b) for each $E(\gamma_3)$ bin, the number of data events per Monte Carlo event.

small (15%) that the cut $E(\gamma_3) > 40$ MeV does not impair the analysis.

After making the three cuts listed above, one obtains the scatterplot of $M(K^+K^-\pi^0)$ vs $M(K^+K^-)$ shown in Fig. 3.29a. A clear ι signal is observed associated with low K^+K^- mass. The K^+K^- mass distribution for M($K^+K^-\pi^0$) in the range 1.3-1.55 GeV is shown in Fig. 3.29b. To reduce the background in the region above the ι it is useful to impose the loose requirement

$$M(K^+K^-) < 1.32 \text{ GeV}$$

as in the analysis of $\iota \to K^0_S K^\pm \pi^\mp$. The resulting $K^+K^-\pi^0$ mass distribution is shown in Fig. 3.30. A fit to a Breit-Wigner curve folded with a Gaussian resolution function plus a quadratic background yields the parameters

$$M(\iota) = (1.461 \pm 0.005) \text{ GeV}$$
$$\Gamma(\iota) = (0.101 \pm 0.010) \text{ GeV},$$

and the number of events in the Breit-Wigner is

$$N(\iota \to K^+K^-\pi^0) = 402 \pm 20.$$

Unlike the mode $\iota \to K^0_S K^\pm \pi^\mp$, here there is background from $\psi \to \phi + X$, especially $\psi \to \phi\pi^0\pi^0$, which is dominated by ϕS^*. In studying the angular distributions, the $K^+K^-\pi^0$ mass is required to be in the range 1.3-1.55 GeV. The signal-to-noise ratio for this mass region is very high, about 10:1. Furthermore, the angular distributions associated with the mass region just above the ι are roughly uniform.

The branching fraction for this signal is

$$B(\psi \to \gamma\iota)B(\iota \to K^+K^-\pi^0) = (8.2 \pm 0.4 \pm 1.4) \times 10^{-4}$$

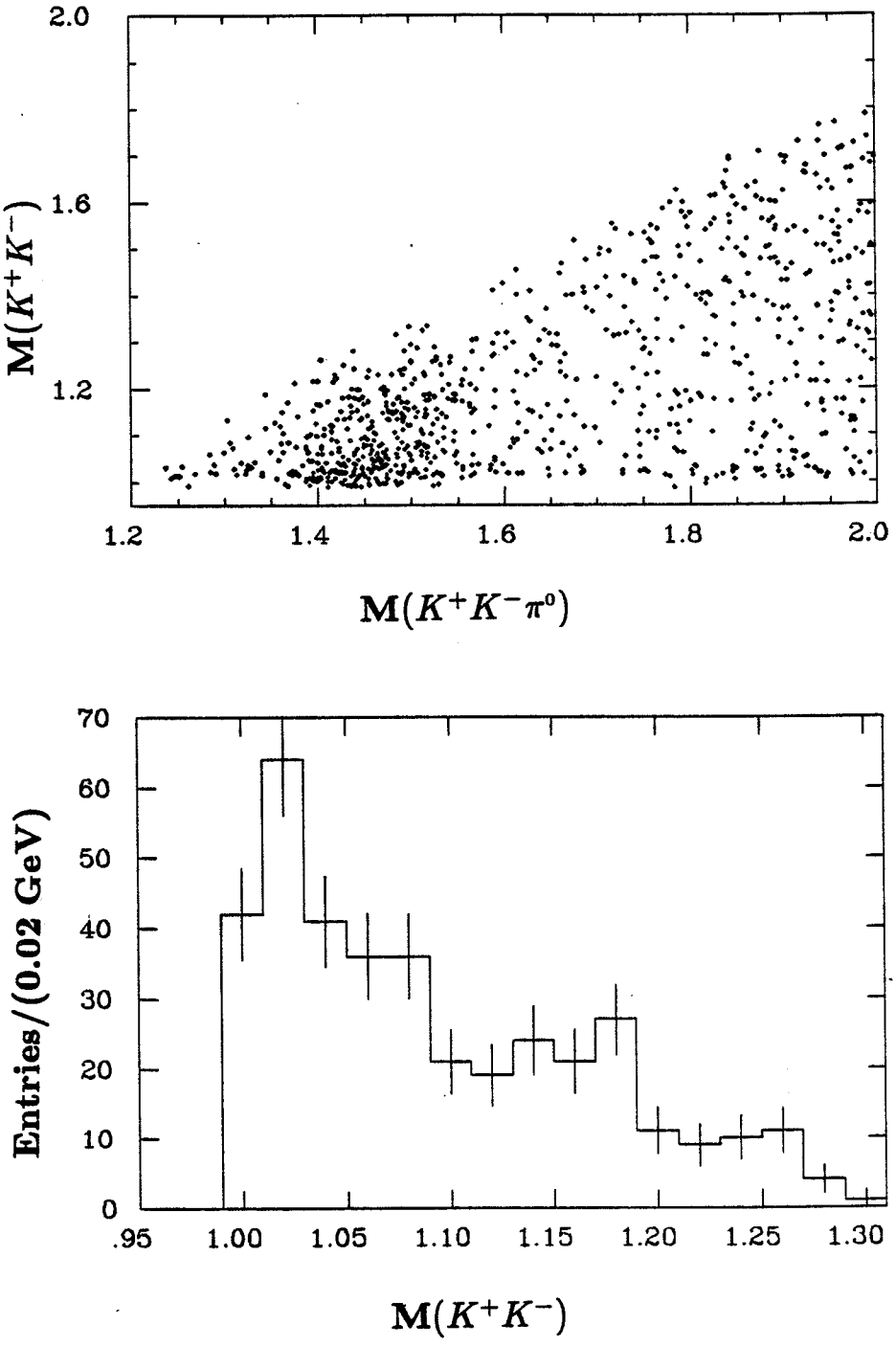

Figure 3.29. $K^+K^-\pi^0$ analysis. a) M($K^+K^-\pi^0$) vs. M(K^+K^-) and b) M(K^+K^-) after requiring M($K^+K^-\pi^0$) to be in the range 1.3-1.55 GeV.

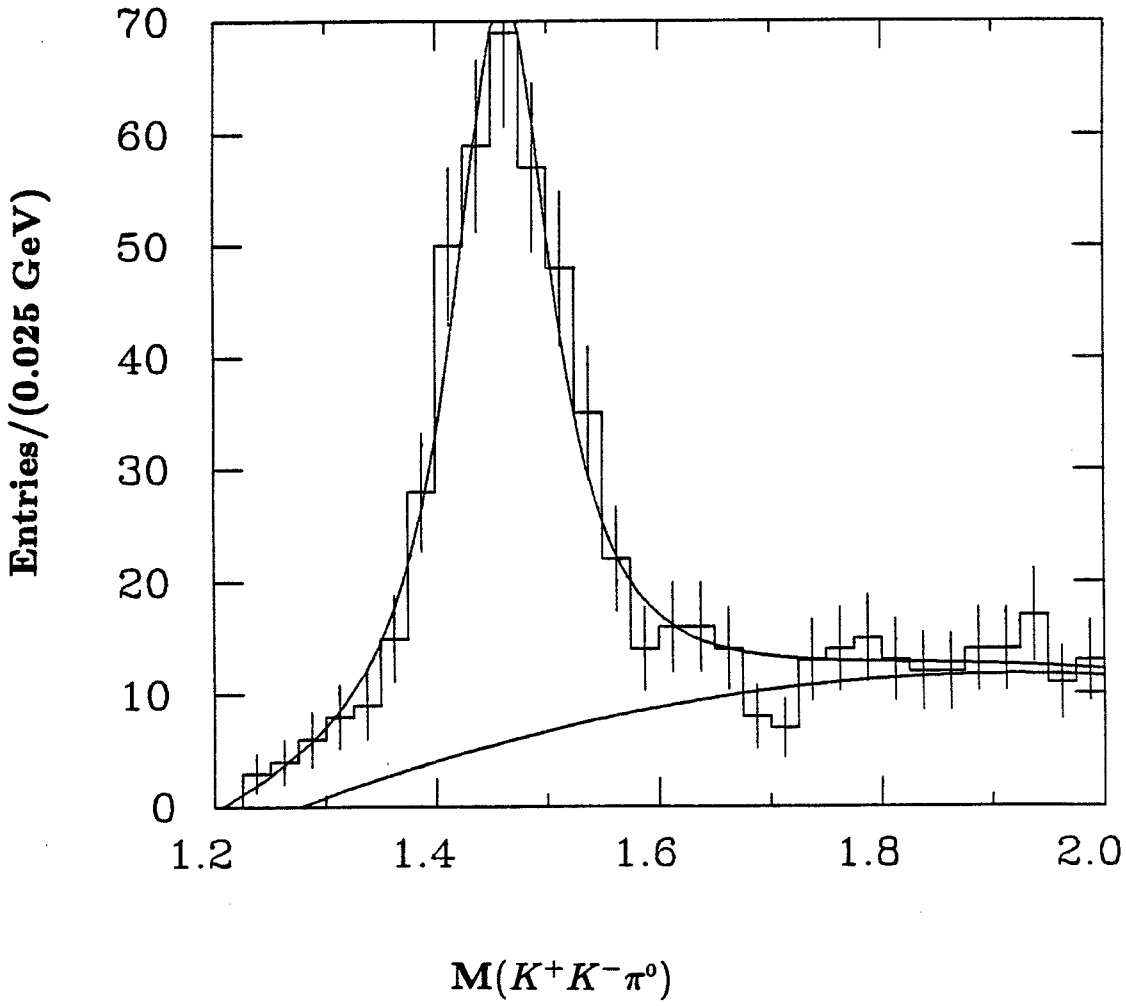

Figure 3.30. The ι signal in the $K^+K^-\pi^0$ mass distribution. The Breit-Wigner fit parameters are M(ι)=(1.461 $\pm$ 0.005) GeV and $\Gamma(\iota)$ = (0.101 $\pm$ 0.010) GeV, and the number of events is 402 $\pm$ 20.

or, correcting for the isospin factor of $\frac{1}{6}$,

$$B(\psi \to \gamma\iota)B(\iota \to K\bar{K}\pi) = (4.9 \pm 0.2 \pm 0.8) \times 10^{-3},$$

which agrees extremely well with the value obtained from the $K^0_S K^{\pm}\pi^{\mp}$ mode.

The spin analysis of this channel proceeds in exactly the same manner as that for $\iota \to K^0_S K^{\pm}\pi^{\mp}$. Figure 3.31 shows the measured $\cos\beta$ distribution and the Monte Carlo acceptance averaged over all other quantities. Both distributions are consistent with being uniform, although the Monte Carlo acceptance appears to dip slightly for small values of $|\cos\beta|$. This dip was much larger in the previous Monte Carlo, which had a very poor efficiency for low energy photons. Figure 3.32 shows the measured $\cos\theta_\iota$ distribution and the acceptance averaged over all other quantities. The acceptance is approximately uniform only in the narrow interval $|\cos\theta_\iota| < 0.5$. It does indicate, however, that the dip in the center of the $\cos\theta_\iota$ distribution is real. If one accepts that the $\cos\beta$ distribution is uniform, then if the ι had $J^P = 1^+$, the $\cos\theta_\iota$ distribution would have the form

$$\frac{dN}{d\cos\theta_\iota} = 1 - 0.6\cos^2\theta_\iota,$$

which peaks at the center.

A full maximum-likelihood fit, using the same procedure as for $\iota \to K^0_S K^{\pm}\pi^{\mp}$, provides quantitative confirmation that $J^P = 0^-$ is strongly preferred over $J^P = 1^+$. The $-\log(\textit{likelihood})$ function for the $J^P = 1^+$ fit is shown in Fig. 3.33. The presence of two minima is due to the fact that the angular distribution is quadratic in x (the ratio of helicity 1 to helicity 0 amplitudes) with a symmetry breaking linear term in x due to interference. The minimum is found at $x = 0.76 \pm 0.07$, corresponding to a positive natural log likelihood of -6.8. The log likelihood for $J^P = 0^-$ is found to be 10.6, giving a

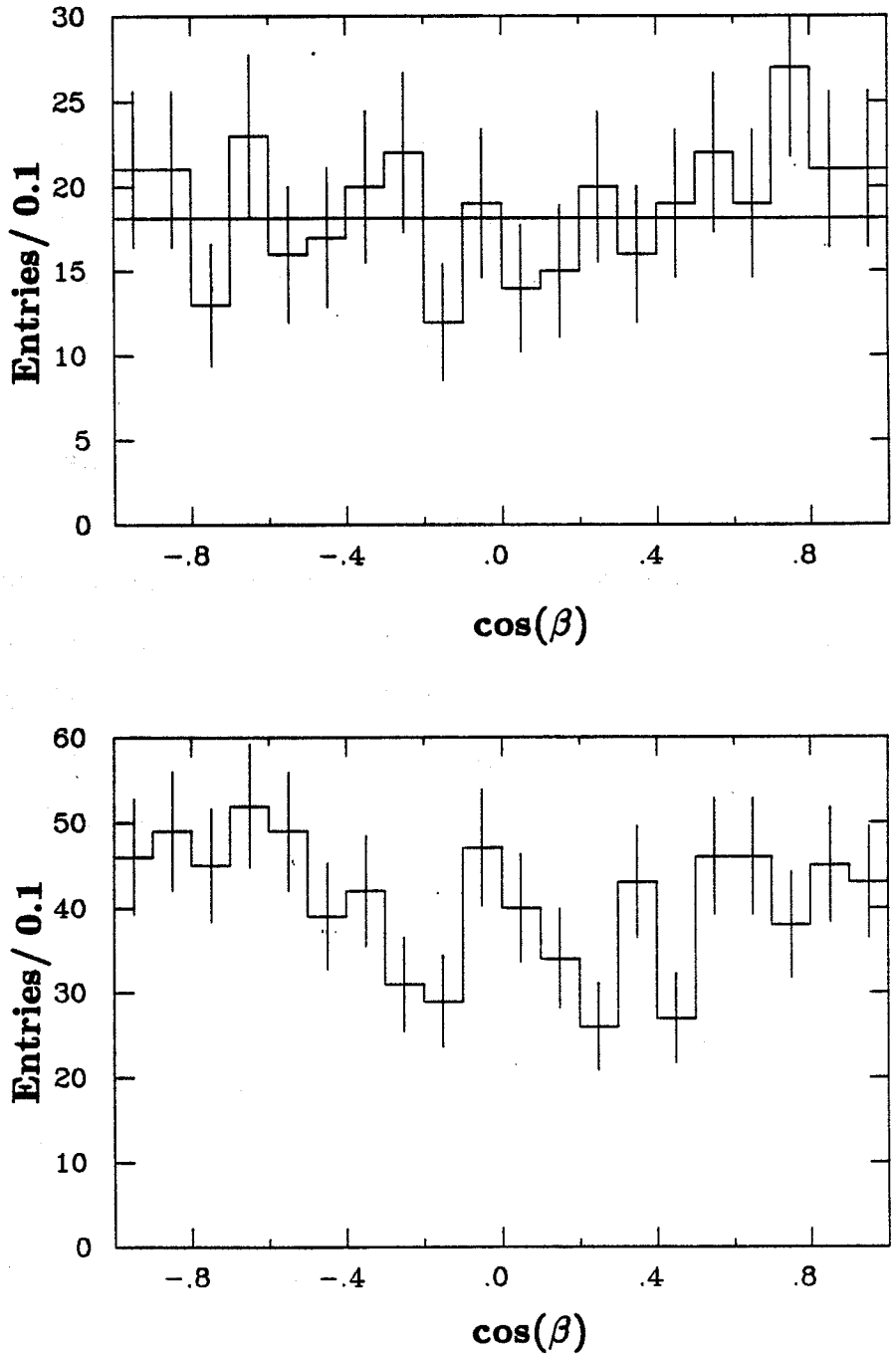

Figure 3.31. Study of $\cos\beta$. a) The measured $\cos\beta$ distribution and b) the average Monte Carlo acceptance.

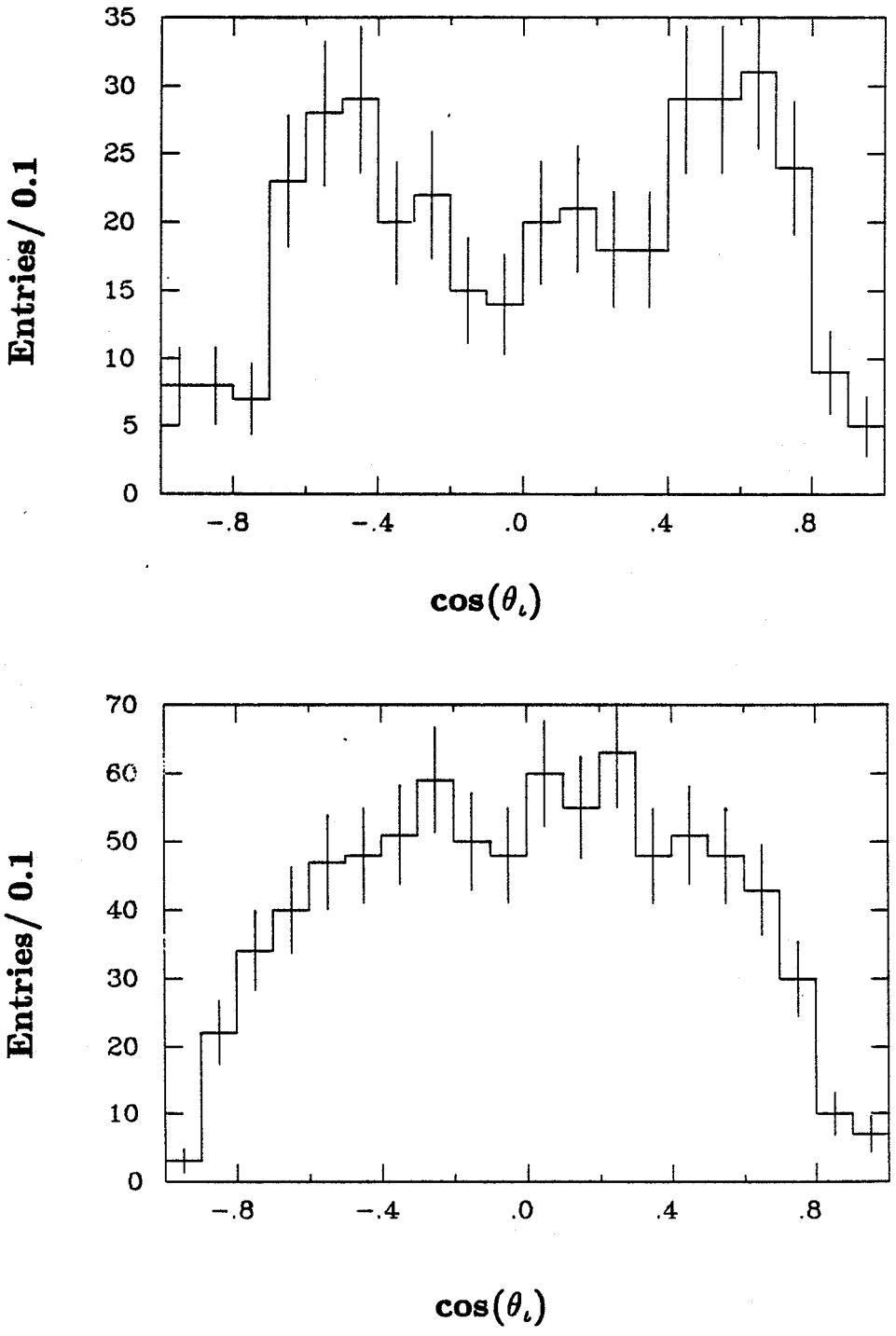

Figure 3.32. Study of $\cos\theta_\iota$. a) The measured $\cos\theta_\iota$ distribution and b) the average Monte Carlo acceptance.

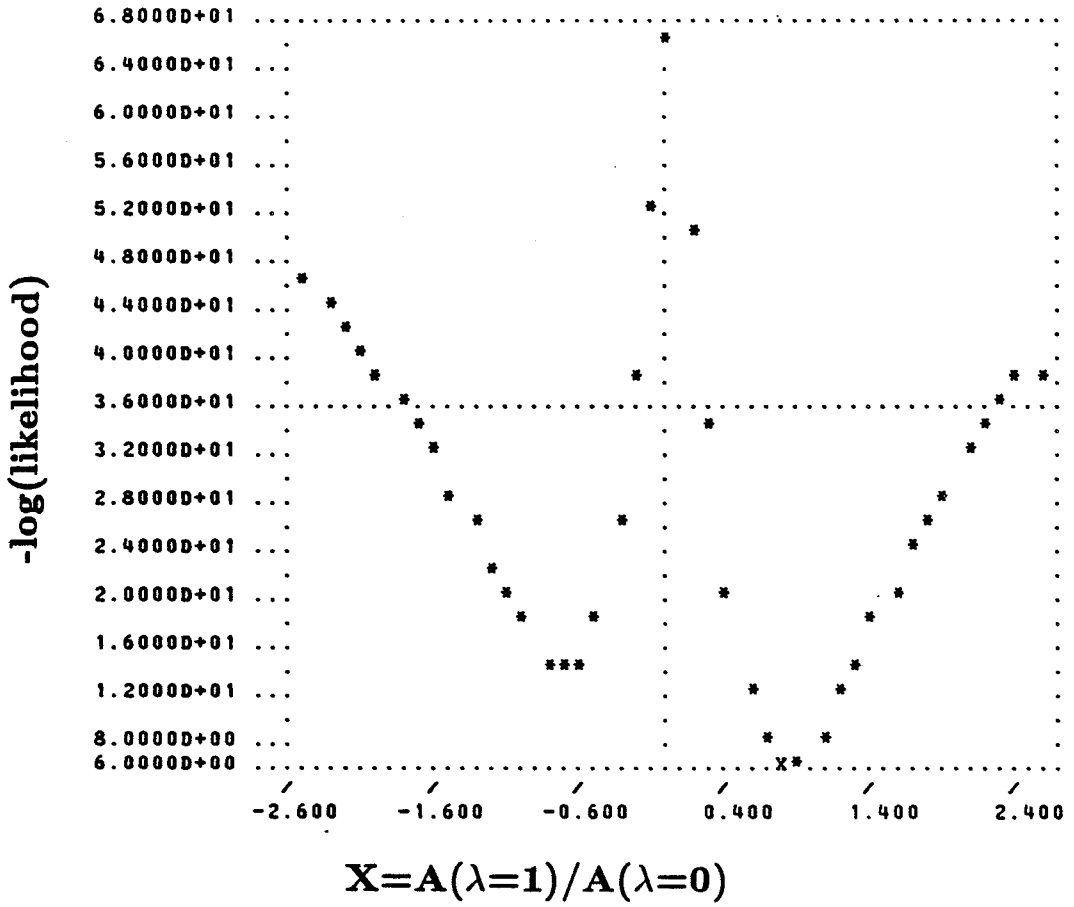

Figure 3.33. The $-\log(\textit{likelihood})$ function for $J^P = 1^+$. The presence of two minima is due to the fact the angular distribution is quadratic in x. The interference term in the angular distribution is linear in x and breaks the symmetry under $x \to -x$.

ratio of

$$\frac{\mathcal{L}(J^P = 1^+)}{\mathcal{L}(J^P = 0^-)} = e^{-17.4}.$$

The fit to the exotic quantum numbers $J^P = 1^-$ gives a log likelihood of -30 at $x = -1.1 \pm 0.1$. Thus, $J^P = 1^-$ is rejected with respect to $J^P = 0^-$ by an enormous factor. These results confirm the conclusions from the analysis of the $K^0_S K^\pm \pi^\mp$ channel. The values of x obtained here agree with those found in the $K^0_S K^\pm \pi^\mp$ analysis: $x(1^+) = 0.85 \pm 0.05$ and $x(1^-) = -1.2 \pm 0.1$.

3.9 Observation of $\iota \to K^0_S K^0_S \pi^0$

The ι has also been observed, although with rather poor statistics, in the channel $\iota \to K^0_S K^0_S \pi^0$ (49). The number of events (~ 50) is too small to permit a spin-parity analysis. The $K^0_S K^0_S \pi^0$ mass spectrum is shown if Fig. 3.34 and the branching fraction

$$B(\psi \to \gamma\iota) B(\iota \to K^0_S K^0_S \pi^0) = (3.0 \pm 1.3 \pm 1.5) \times 10^{-4}$$

is obtained. Correcting for the isospin factor $\frac{1}{12}$, one obtains

$$B(\psi \to \gamma\iota) B(\iota \to K^0_S K^0_S \pi^0) = (3.6 \pm 1.6 \pm 1.8) \times 10^{-3}.$$

3.10 Isospin Considerations

Because of its large production in radiative ψ decays, it is almost certain that the ι has isospin 0. If this is the case, one can predict

$$K^0_S K^\pm \pi^\mp : K^+ K^- \pi^0 : K^0_S K^0_S \pi^0 = \frac{1}{3} : \frac{1}{6} : \frac{1}{12} = 4 : 2 : 1.$$

The measured $K^+ K^- \pi^0$ and $K^0_S K^\pm \pi^\mp$ branching fractions are in very good agreement with this prediction. The $K^0_S K^0_S \pi^0$ measurement is also consistent within the rather large errors.

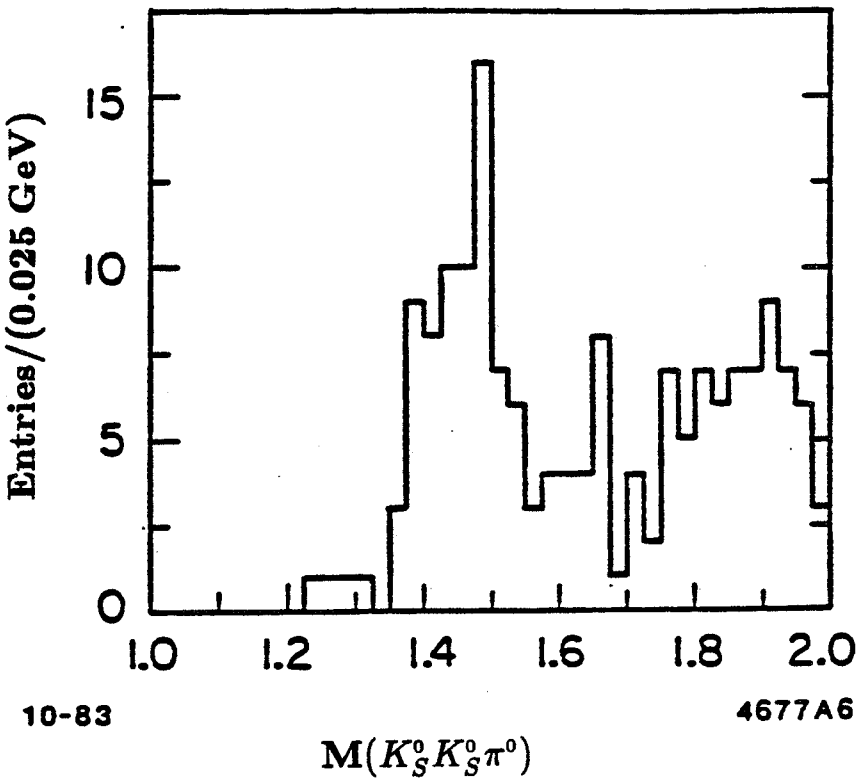

Figure 3.34. The ι signal in the $K^0_S K^0_S \pi^0$ mass spectrum.

If the ι is an isovector, one has

$$K^+K^-\pi^0 : K_S^0K_S^0\pi^0 = 2:1,$$

which is the same as for $I = 0$. The relative amounts of $K_S^0K^\pm\pi^\mp$ and $K^+K^-\pi^0$ are not uniquely predicted, but depend on the isospin of the $K\bar{K}$ system. If $\cos\alpha$ is the amplitude for the $K\bar{K}$ system to have $I = 0$ and $\sin\alpha$ the amplitude to have $I = 1$, then one has

$$K_S^0K^\pm\pi^\mp : K^+K^-\pi^0 : K_S^0K_S^0\pi^0 = \frac{1}{2}\sin^2\alpha : \frac{1}{2}\cos^2\alpha : \frac{1}{4}\cos^2\alpha.$$

If the $K\bar{K}$ system is in a pure isovector state (e.g., from $\delta \to K\bar{K}$) then there will be no $K^+K^-\pi^0$ production, which is obviously inconsistent with the data. However, for $\tan^2\alpha = 2$, the production is identical to that for $I = 0$.

Chapter 4. Study of the Double Radiative Decays $\psi \to \gamma + X; X \to \gamma +$ Vector

4.1 INTRODUCTION

The identification of the ι as a state with pseudoscalar quantum numbers considerably narrows the range of explanations for this particle. In particular, the existence of a complete nonet of low-mass pseudoscalars implies that the only conventional $q\bar{q}$ assignment for the ι is a radial excitation. Thus, a central question is whether there are characteristics that distinguish such a radially excited meson from a glueball. In fact, the problem is more subtle, because a glueball would almost certainly mix with $q\bar{q}$ pairs to some extent; the differences between such a state and a meson of the same mass and quantum numbers are not expected to be very great. Certainly, they are difficult to predict. In any case, the existence of a pseudoscalar glueball or hybrid requires the additional degrees of freedom provided by the gluons and would be unambiguously established if the two radially excited pseudoscalar mesons were discovered as well. Thus, an overpopulation of the $q\bar{q}$ nonets would provide compelling evidence for unconventional states. Unfortunately, such evidence does not yet exist.

In the absence of comprehensive knowledge of the meson spectrum, one can study other properties of glueball candidates, such as the pattern of their decay modes. Several theoretical papers have examined the question of whether a glueball can be expected to have substantial radiative width. Surprisingly, the answer appears to be yes, at least in the pseudoscalar sector. Of course, radiative decays of glueballs must be mediated by an intermediate state containing quarks or come about through the mixing of quarks into the glueball wave function. However, nearly all calculations indicate the presence of large mixing amplitudes

for the pseudoscalars. There is even some experimental evidence from hadronic ψ decays that the η' wave function is not saturated by quarks alone (50). In this chapter, the theoretical predictions are reviewed and the analysis of three decay channels is presented: $\psi \to \gamma X$; $X \to \gamma V$, where $V = \rho$, ϕ, and ω.

4.2 THEORETICAL PREDICTIONS

The results of several theoretical calculations are given in Table 4.1. In spite of large uncertainties, the agreement among the bag model predictions is surprisingly good. The largest uncertainty comes from estimating the mixing between the ι and the η and η'. The main elements of these calculations are briefly discussed below in order to demonstrate how a large glueball radiative width can arise. The term glueball will be used to describe not only pure gluonic states, but also states that are predominantly glue, with some admixture of $q\bar{q}$.

In the bag model calculation of Donoghue (54), two main results are obtained. First, it is found that in addition to processes that mix $q\bar{q}$ states (*e.g.*, η and η') into the glueball wave function (Fig. 4.1a, b), there are other diagrams (Fig. 4.1c, d) that can couple the gluons to quarks and contribute substantially to the radiative width. Second, in the nonrelativistic limit, the magnetic dipole transition of a radially excited pseudoscalar meson ($2s$) to the ground state vector ($1s$) vanishes due to orthogonality of the radial wave functions. In the relativistic case a strong suppression is still expected. Thus, a large radiative width might distinguish a glueball from radially excited quarkonium.

The amplitude for the decay is given by

$$M = \langle V(p')|j^{\mu}|P(p)\rangle. \tag{4.1}$$

where P and V represent the pseudoscalar and vector particle, respectively. The

Table 4.1. Theoretical Predictions for $\iota \to \gamma\rho^0$

Model	$\Gamma(\iota \to \gamma\rho^0)$ (MeV)
Pseudoscalar meson dominance + bag model; Iwao (51).	0.213 – 0.413
Bag model + η, η', glue mixing Carlson and Hansson (52).	0.43
Bag model $q\bar{q}$, $q\bar{q}g$ mixing; Barnes and Close (53).	$\lesssim 1.5$
Bag model with η, η', glue mixing and additional quark-glue coupling; Donoghue (54).	0.4 – 1.6
Pole model with input from $\psi \to \gamma\eta, \gamma\eta', \gamma\iota$; Palmer and Pinsky (55).	3.5
Effective Lagrangian incorporating chiral symmetry; Rosensweig(56).	2.5
ι, η, η', mixing via anomalous couplings; Senba and Tanimoto (57).	4.2

available four-vectors are p_α, $q_\beta = p'_\beta - p_\beta$, and S_ν, the polarization of V. The amplitude must therefore have the form

$$M = A\epsilon^{\mu\nu\alpha\beta} S_\nu(p') p_\alpha q_\beta, \tag{4.2}$$

implying a decay rate

$$\Gamma = \frac{A^2}{32\pi}\left[\left(\frac{m_P^2 - m_V^2}{m_P}\right)^3\right]. \tag{4.3}$$

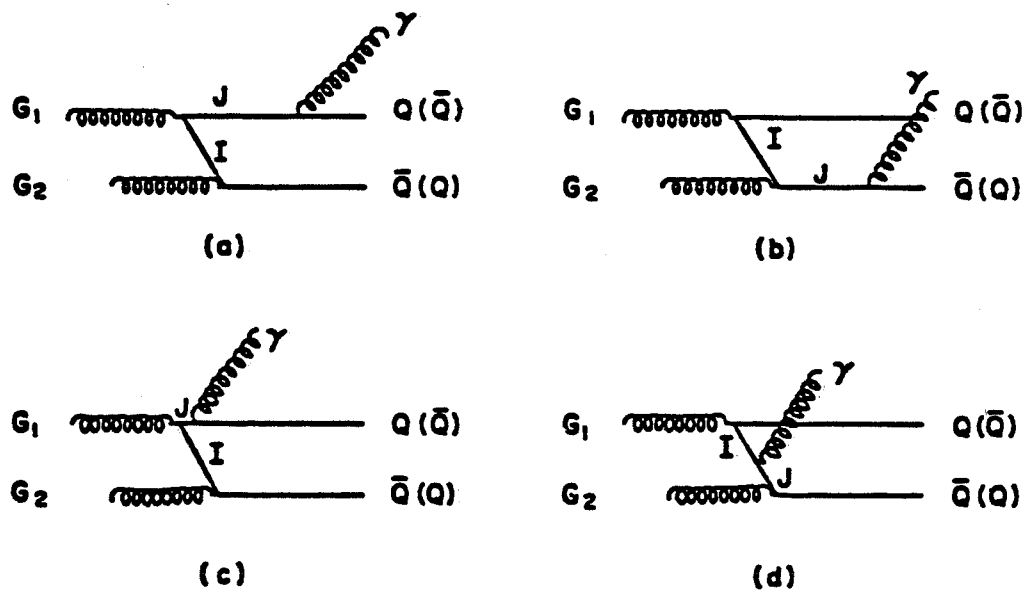

Figure 4.1. Time ordered diagrams for glueball radiative decay. The processes in a) and b) correspond to glueball-meson mixing, whereas those in c) and d) give an additional gluon-quark coupling. From Donoghue (54).

The two-body phase space is taken into account by the term in brackets ($\propto p^3$) and is 27 times larger for $\iota \to \rho^0\gamma$ than for $\eta' \to \rho^0\gamma$.

To calculate the amplitudes of the processes in Fig. 4.1a, b, it is first necessary to determine the mixing of the glueball with other particles. To first order in α_s,

$$|P\rangle = |G\rangle + \sum_I \frac{|I\rangle\langle I|H_{eff}|G\rangle}{E_G - E_I}. \tag{4.4}$$

The index I includes the η, η', and the radially excited pseudoscalar states: $(s\bar{s})_R$ and $\frac{1}{\sqrt{2}}(u\bar{u} + d\bar{d})_R$. The matrix elements of H_{eff} are calculated in the bag model and are on the order of (50-100)α_s MeV. The coefficient A in Eq. (4.2) and Eq. (4.3) is the matrix element of the magnetic dipole operator μ:

$$A = \langle V|\mu|P\rangle, \tag{4.5}$$

which is also calculated in the bag model. It is found that the amplitude for transition from the radially excited component of P, $(q\bar{q})_R$, is only about 5% of that for the $1s \to 1s$ transition, as expected from the nonrelativistic limit. The width can be related to $\Gamma(\eta' \to \rho\gamma)$ by dividing out $\langle V|\mu|\eta'\rangle$ in Eq. (4.5). Assuming that the ι is a glueball, Donoghue finds that the contributions from Fig. 4.1a, b are

$$\begin{aligned} \Gamma(\iota \to \rho^0\gamma) &= 0.23 - 0.94 \text{ MeV} \\ \Gamma(\iota \to \omega\gamma) &= \frac{1}{9}\Gamma(\iota \to \rho\gamma) \\ \Gamma(\iota \to \phi\gamma) &= 0.17 \times \Gamma(\iota \to \rho\gamma), \end{aligned} \tag{4.6}$$

depending on the value of α_s in the bag model. It turns out that the amplitudes in Fig. 4.1c, d are also large. The final estimate for the radiative width from all processes is

$$\Gamma(\iota \to \rho^0\gamma) = 0.4 - 1.6 \text{ MeV},$$

whereas for radially excited quarkonium the width is only

$$\Gamma(\iota_{q\bar{q}_R} \to \rho^0\gamma) \simeq 0.18 \text{ MeV}.$$

It is difficult to know how accurate these results are likely to be or whether they can be used on a quantitative basis to draw conclusions from an experimentally determined width. In particular, the relativistic $q\bar{q}$ model of Godfrey and Isgur (58), which has successfully predicted many features of the meson spectrum, indicates (59) that the partial width of the radially excited pseudoscalar is

$$\Gamma(\eta_R \to \rho^0\gamma) = 0.9 \pm 0.5 \text{ MeV}.$$

Apparently, one cannot draw an unambiguous conclusion from a large width into $\rho^0\gamma$.

The pole-model calculation of Palmer and Pinsky attempts to predict several ι decay modes, and will be discussed again later. The idea is simply to assume that if the ι is a pseudoscalar glueball, it will mediate the radiative decay of the ψ into pseudoscalars (Fig. 4.2a). Then the ratio of the amplitudes f_η and $f_{\eta'}$ for the η and η' to mix with the ι can be determined from $B(\psi \to \gamma\eta)/B(\psi \to \gamma\eta')$:

$$\frac{B(\psi \to \gamma\eta)}{B(\psi \to \gamma\eta')} = 1.2 \left(\frac{f_\eta}{f_{\eta'}}\right)^2 \left[\frac{m_\iota^2 - m_{\eta'}^2}{m_\iota^2 - m_\eta^2}\right]^2 .$$

The absolute magnitudes of f_η and $f_{\eta'}$ are determined from $B(\psi \to \gamma\eta')/B(\psi \to \gamma\iota)$. Unfortunately, the inclusive $\psi \to \gamma\iota$ branching ratio is unknown, and must be estimated. The ι decays are then assumed to be mediated by the η and η', as shown in Fig. 4.2b. A very large radiative width to $\rho\gamma$ is predicted: $\Gamma(\iota \to \rho^0\gamma) \sim 3.5$ MeV.

Barnes and Close (53) emphasize that additional information can be obtained by comparing the $\gamma\rho^0$ and $\gamma\phi$ mass distributions. If the $\gamma\rho^0$ signal is

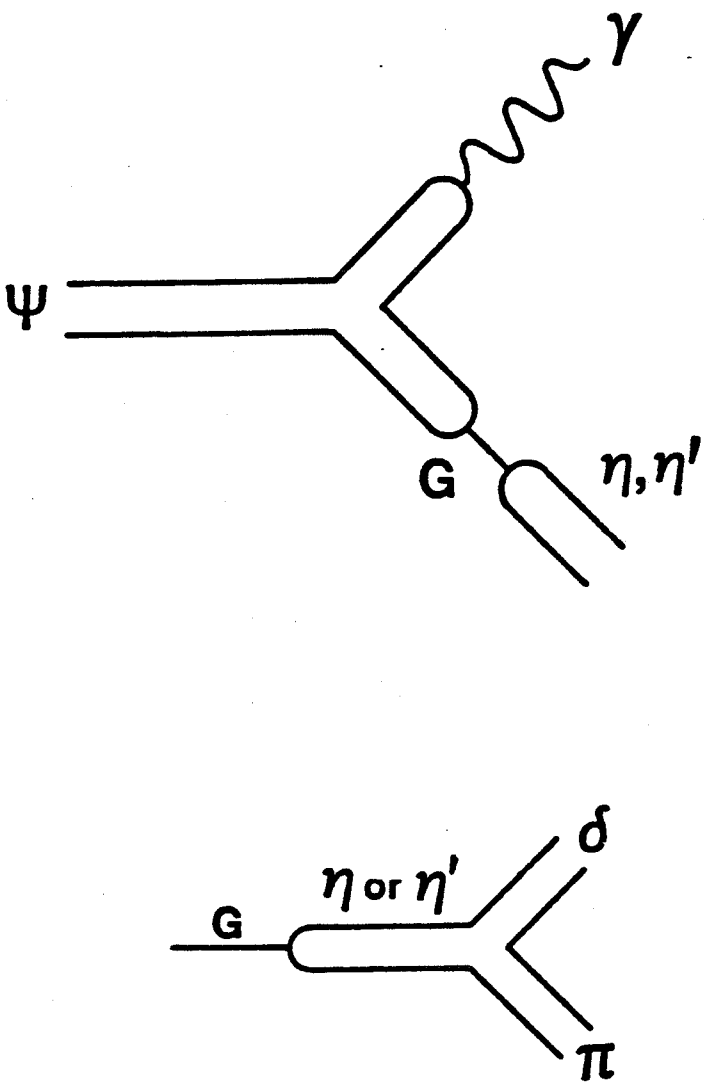

Figure 4.2. Pole model diagrams. a) Radiative ψ decay into pseudoscalars and b) ι decay. From Palmer and Pinsky(55).

due to a glueball, one expects to see a $\gamma\phi$ signal at the same mass, although at a much lower rate. For example, the standard perturbative picture of radiative ψ decay implies that

$$\psi \to \gamma \left[\gamma\rho^0 : \gamma\omega : \gamma\phi\right] = 9 : 1 : 2$$

if the $q\bar{q}$ pair is produced in a flavor independent manner.

On the other hand, if the $\gamma\rho^0$ signal is from the decay of a $q\bar{q}$ or $q\bar{q}g$ state with $q\bar{q} = \frac{1}{\sqrt{2}}(u\bar{u} + d\bar{d})$, then the $\gamma\phi$ mass distribution should have a peak about 300 MeV higher, from the $s\bar{s}$ or $s\bar{s}g$ partner. In general, the $q\bar{q}$ state will be a mixture of light and $s\bar{s}$ quarks, and there will be an orthogonal partner. Thus,

$$|\iota_1\rangle = \cos\beta|\Omega\rangle + \sin\beta|\Phi\rangle$$
$$|\iota_2\rangle = -\sin\beta|\Omega\rangle + \cos\beta|\Phi\rangle$$

where $\Phi \equiv s\bar{s}$ or $s\bar{s}g$ and $\Omega \equiv \frac{1}{\sqrt{2}}(u\bar{u} + d\bar{d})$ or $\frac{1}{\sqrt{2}}(u\bar{u} + d\bar{d})g$. Both states, $|\iota_1\rangle$ and $|\iota_2\rangle$, will decay into $\rho^0\gamma$ with relative amounts governed by the mixing angle β. Regardless of the value of β, the state that is mostly $s\bar{s}$ or $s\bar{s}g$ will decay into $\gamma\phi$ at a rate that is 2/9 of the rate that the light-quark state decays into $\rho^0\gamma$. Unfortunately, this prediction is difficult to test with the present statistics: given about 60 events in $\rho^0\gamma$ there should be only about 7 events in $\gamma\phi$; $\phi \to K^+K^-$ due to the factor of 0.5 from $B(\phi \to K^+K^-)$. The $P \to \gamma V$ decay width is also estimated by Barnes and Close. They find

$$\Gamma(\iota \to \rho^0\gamma) \leq 1.5 \text{ MeV}$$

if the ι is a hybrid state.

4.3 ANALYSIS OF $\psi \to \gamma X$; $X \to \gamma\rho^0$

Although the analysis of the $\gamma\gamma\pi^+\pi^-$ final state would appear to be straightforward, a great deal of care is required because of the large number of backgrounds. These arise not only from the $\gamma\gamma\pi^+\pi^-$ topology (*e.g.*, $\psi \to \rho\pi$), but also from the $3\gamma\pi^+\pi^-$ (*e.g.*, $\psi \to \gamma\eta\pi^+\pi^-$) and $4\gamma\pi^+\pi^-$ (*e.g.*, $\psi \to \rho^0\pi^0\pi^0$) final states. In the latter processes, it is nearly impossible to determine on an event-by-event basis whether one or more low-energy ($\lesssim$ 50 MeV) photons has been missed due to inefficiency. Therefore, one must study the relevant distributions for well-identified background events to be sure that they do not affect the measurement and/or interpretation of the signal.

Event Selection and Kinematic Fitting

The first step in the event selection is to kinematically fit events with two oppositely charged tracks to the hypothesis $\psi \to \gamma\gamma\pi^+\pi^-$. At this point no information from the time-of-flight counters is used; pion masses are simply assumed. Due to the presence of fake photons, which are additional clusters produced by the interactions of hadrons in the shower counter, one cannot require exactly two photons in the event. In selecting candidate photons it is desirable to try to exclude as many of these split-offs as possible. Two requirements are therefore imposed:

1. $\cos\theta_{\gamma q} < 0.95$, and

2. the shower must be at least two layers deep.

The angle $\theta_{\gamma q}$ is defined as the angle between the position vector of the photon and the position vector of the *nearest* charged track at the point the track enters the shower counter. The requirement that the photon shower be at least two layers deep has very little effect on the signal. Monte Carlo studies have shown

that $> 97\%$ of the photons γ_2 in the decay process $\psi \to \gamma_1\iota$; $\iota \to \gamma_2\rho^0$ have a lab-frame energy greater than 100 MeV. The loss of efficiency from the cut on $\cos\theta_{\gamma q}$ is modeled by the Monte Carlo. For pseudoscalar states (η', ι), such Monte Carlo simulations are quite reliable, because the angular correlations of all particles can be calculated exactly and do not depend on any unknown helicity amplitude ratios.

The photons satisfying these two cuts are then ordered according to energy, and each event is 4-C fit to the hypothesis $\psi \to \gamma\gamma\pi^+\pi^-$. If there are more than two photons, two fits are done using the first and second and then the first and third highest energy photons:

$$\gamma_1\gamma_2\pi^+\pi^-$$

$$\gamma_1\gamma_3\pi^+\pi^-.$$

The highest energy photon is always used because the photon radiated by the ψ has $E \sim 1.2$ GeV and would never be produced by a hadronic split-off.

Events with a 4-C fit $\chi^2 < 25$ are selected for further analysis. If both fits of an event have $\chi^2 < 25$, the fit with the better χ^2 determines which two photons are used.

The fake gammas are, in fact, a very minor problem in this channel. Because the real photons in the decay process usually have high energies, it is relatively easy to discriminate against fake photons with the 4-C fit. For example, in the analysis sample ($\chi^2 < 25$) only 2.6% of the events in the η' peak have fits to $\gamma_1\gamma_3\pi^+\pi^-$ with $P(\chi^2) \geq 0.04$, where

$$P(\chi^2) = \int_{\chi^2}^{\infty} p(\chi^2)\, d\chi^2$$

is the confidence level of the χ^2 from the 4-C fit (*i.e.*, the probability for χ^2 to

be worse than the value actually obtained). In the region $M(\gamma_2\rho^0) \sim 1.4$ GeV, about 1% of the events have better fits to $\gamma_1\gamma_3\pi^+\pi^-$ than to $\gamma_1\gamma_2\pi^+\pi^-$.

Distinguishability of the Photons

In the double radiative process $\psi \to \gamma X$; $X \to \gamma\rho^0$, the question arises as to whether the two photons can be distinguished. A Monte Carlo simulation has been used to verify that if $X = \iota$, the photon radiated by the ψ has a *higher* lab frame energy than the photon radiated by the ι in about 98% of the events. Thus, the mass of the recoil system is $M(\pi^+\pi^-\gamma_{low})$. In practice, the ability to distinguish between the two photons on the basis of energy is slightly worse because of the shower counter energy resolution. By using the fitted rather than the measured photon energies one can still correctly assign the photon in about 96% of the events. It is possible to estimate the error in $M(\pi^+\pi^-\gamma)$ that is made in the few events where ΔE is small and the wrong photon is used. The mass error is close to twice the photon energy difference.

The distribution of $M(\pi^+\pi^-\gamma_{low})$ for events selected with this procedure is shown in Fig. 4.3. A prominent η' signal is evident, as well as a broad background due to $\psi \to \rho\pi$.

Measurement of $\psi \to \gamma\eta'$

The large signal ($\sim$ 1000 events) from the process $\psi \to \gamma\eta'$; $\eta' \to \gamma\rho^0$ provides an extremely important calibration for the analysis of the ι mass region. Because nearly all of the background events under the η' can be removed with fairly simple and loose cuts, one can use the η' signal to check how accurately the distributions generated by the Monte Carlo reproduce the data. In addition, the branching ratios for $\psi \to \gamma\eta$ and $\psi \to \gamma\eta'$ are of some theoretical interest, especially in comparison with $\psi \to \gamma\iota$.

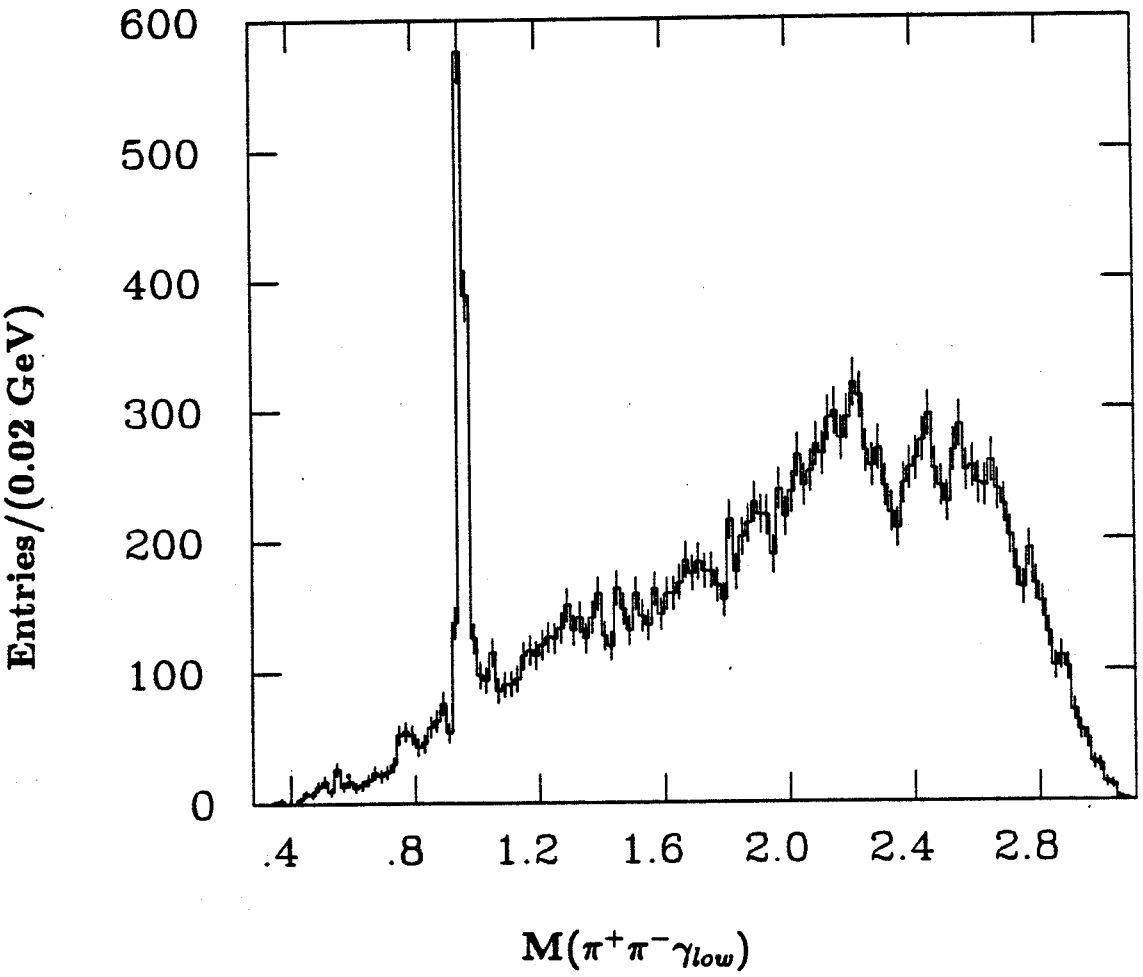

Figure 4.3. The distribution of $M(\pi^+\pi^-\gamma_{low})$ after requiring $\chi^2 < 25$ from the 4-C fit. A large η' signal is evident, as well as a broad background from $\psi \to \rho\pi$.

The cuts used to select events for the measurement of the branching ratios are:

1. $|\cos\theta| < 0.75$ for both photons and charge tracks.

2. $M(\gamma\gamma) \geq 0.2$ GeV.

3. $0.425 \leq M(\pi^+\pi^-) \leq 0.925$ GeV.

No cut is made on the 4-C fit χ^2 beyond the original very loose cut of $\chi^2 > 25$. The requirement that all tracks have momentum vectors in the polar angle region $|\cos\theta| < 0.75$ ensures that the charged tracks are well measured and that the photons are in the barrel shower counter. This avoids the crack between the barrel and the endcap, as well as the complicated geometrical acceptance of the endcap. For smaller signals, however, the endcaps are often used, and the charged tracks are only required to pass through at least one stereo layer of the drift chamber.

The second cut, $M(\gamma\gamma) \geq 0.2$ GeV, efficiently removes background from $\psi \rightarrow \rho\pi$ without seriously affecting the radiative signals. The effect of the cut is shown by Fig. 4.4a, which is a scatterplot of $M(\pi^+\pi^-\gamma_{low})$ vs. $M(\gamma\gamma)$. A dark π^0 band is evident. In the double radiative events the photons tend to be far apart and have a very broad mass distribution typically centered at about 1.5 GeV. The requirement $M(\gamma\gamma) \geq 0.2$ GeV removes only about 1% of the $\gamma\eta'$ events.

The final cut removes more background by requiring that $M(\pi^+\pi^-)$ be consistent with the ρ^0 mass. Because the phase space in the η' decay is limited, the ρ^0 line shape is not symmetric, but rather is skewed toward lower masses and cuts off sharply at the high end. The position of the cut is shown in Fig. 4.4b, a scatterplot of $M(\pi^+\pi^-)$ vs. $M(\pi^+\pi^-\gamma_{low})$. It should be noted that many of

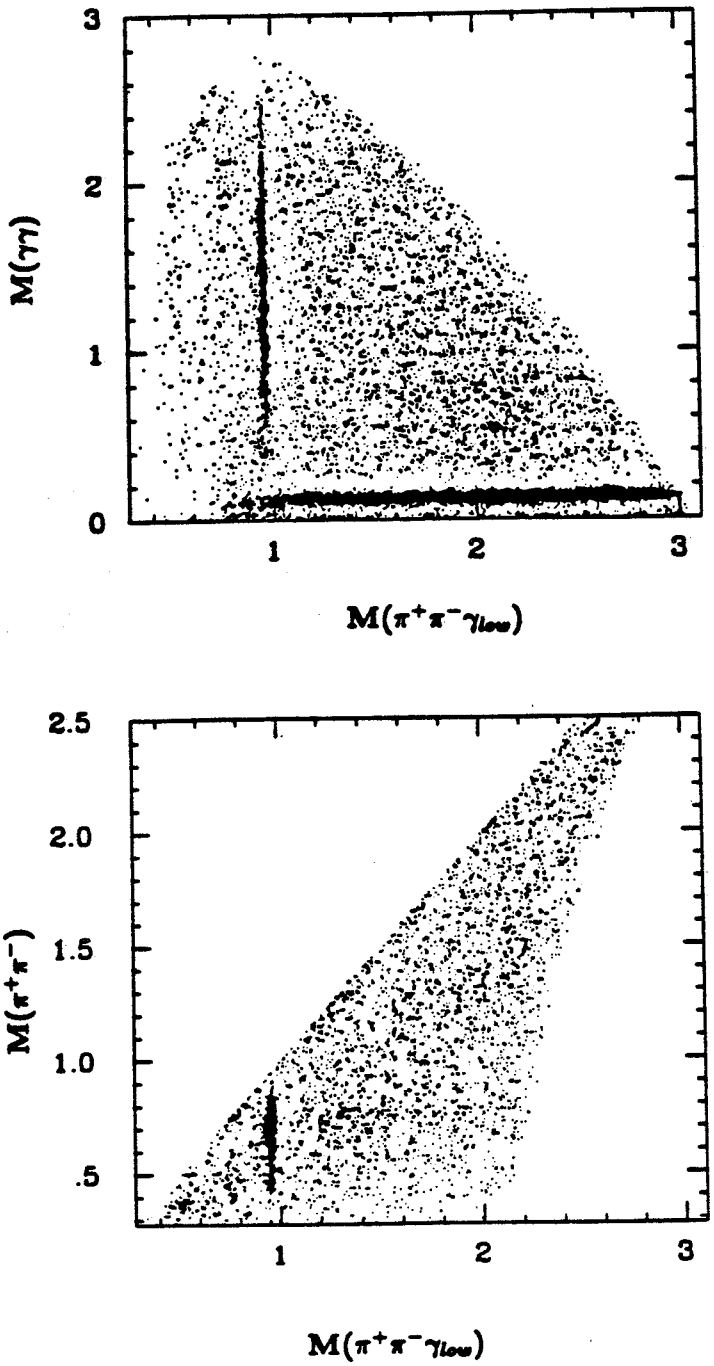

Figure 4.4. The effect of the $\gamma\gamma$ and $\pi^+\pi^-$ mass cuts. (a) Scatterplot of $M(\pi^+\pi^-\gamma_{low})$ vs. $M(\gamma\gamma)$, showing the positions of π^0 band, η' band, and $\gamma\gamma$ mass cut. (b) Scatterplot of $M(\pi^+\pi^-\gamma_{low})$ vs. $M(\pi^+\pi^-)$, showing the correlation between the η' and the ρ^0.

the events in the scatterplot are background because the χ^2 cut is so loose. A much cleaner scatterplot will be shown later.

The resulting $M(\pi^+\pi^-\gamma_{low})$ spectrum is shown in Fig. 4.5. The parameters obtained from a fit to a Gaussian line shape plus a quadratic background are

$$M(\eta') = 0.957 \pm 0.0005 \text{ GeV}$$

$$\sigma(\eta') = 0.009 \pm 0.0004 \text{ GeV}.$$

The good agreement with the known η' mass establishes that the mass scale is correct to within 1 MeV. The resolution of 9 MeV agrees with the value obtained from the Monte Carlo. Using the measured number of events, 631 ± 29 (1983 data), the efficiency determined from the Monte Carlo ($\epsilon = 0.248 \pm 0.025$), and the known value $B(\eta' \to \gamma\rho^0) = (30.0 \pm 1.6)\%$, one obtains

$$B(\psi \to \gamma\eta') = [4.7 \pm 0.2(stat) \pm 0.7(sys)] \times 10^{-3}.$$

The statistical uncertainty is obtained by adding in quadrature the uncertainties on the number of signal and background events. The systematic uncertainty is calculated by adding in quadrature the uncertainties in the efficiency, flux and $B(\eta' \to \gamma\rho^0)$. The above value is somewhat higher than the mean of the four Crystal Ball measurements in different modes (60):

$$B(\psi \to \gamma\eta') = [4.1 \pm 0.3(stat) \pm 0.5(sys)] \times 10^{-3},$$

although a more recent Crystal Ball measurement using only the $\gamma\rho^0$ mode finds (61)

$$B(\psi \to \gamma\eta') = [5.0 \pm 0.5(stat) \pm 0.6(sys)] \times 10^{-3}.$$

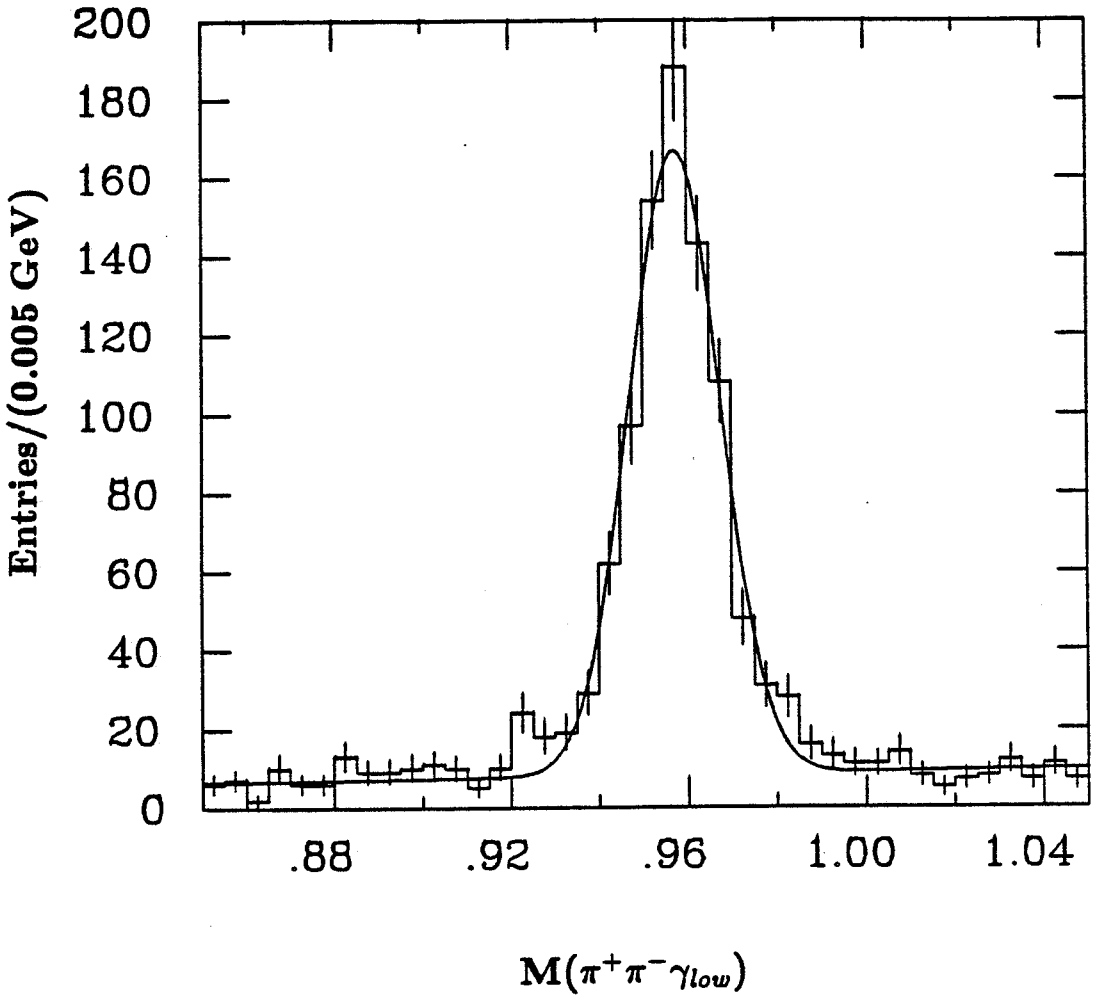

Figure 4.5. The M($\pi^+\pi^-\gamma_{low}$) distribution after removing $\rho\pi$ events.

Measurement of $\psi \to \gamma\eta$

The branching ratio for $\eta \to \gamma\pi^+\pi^-$ is only $(4.91 \pm 0.13)\%$, so one does not expect to see a strong η signal. The mass of the $\pi^+\pi^-$ system cannot be greater than the η mass, so a ρ^0 cut is not made. The complete set of cuts used is

1. Each charged track must pass through at least one stereo layer.
2. $|\cos\theta_\gamma| \leq 0.75$ for each photon.
3. $P(\chi^2) > 0.05$.
4. $M(\gamma\gamma) > 0.25$ GeV.
5. $E(\gamma) > 0.1$ GeV.

The cut $E(\gamma) > 0.1$ GeV is about 91% efficient; it is required because the Monte Carlo program does not adequately model the true photon detection efficiency for very low energy photons. The $M(\pi^+\pi^-\gamma_{low})$ mass spectrum in the range 0.44-0.63 GeV is shown in Fig. 4.6. The η signal contains 26 ± 6.4 events (1982 + 1983 data). Using the detection efficiency of $(21.6 \pm 3.2)\%$ and $B(\eta \to \gamma\pi^+\pi^-)$, one obtains

$$B(\psi \to \gamma\eta) = [9.1 \pm 2.2(stat) \pm 1.6(sys)] \times 10^{-4},$$

which agrees well with the Crystal Ball measurement (61) using $\eta \to \gamma\gamma$

$$B(\psi \to \gamma\eta) = [8.6 \pm 0.9] \times 10^{-4}.$$

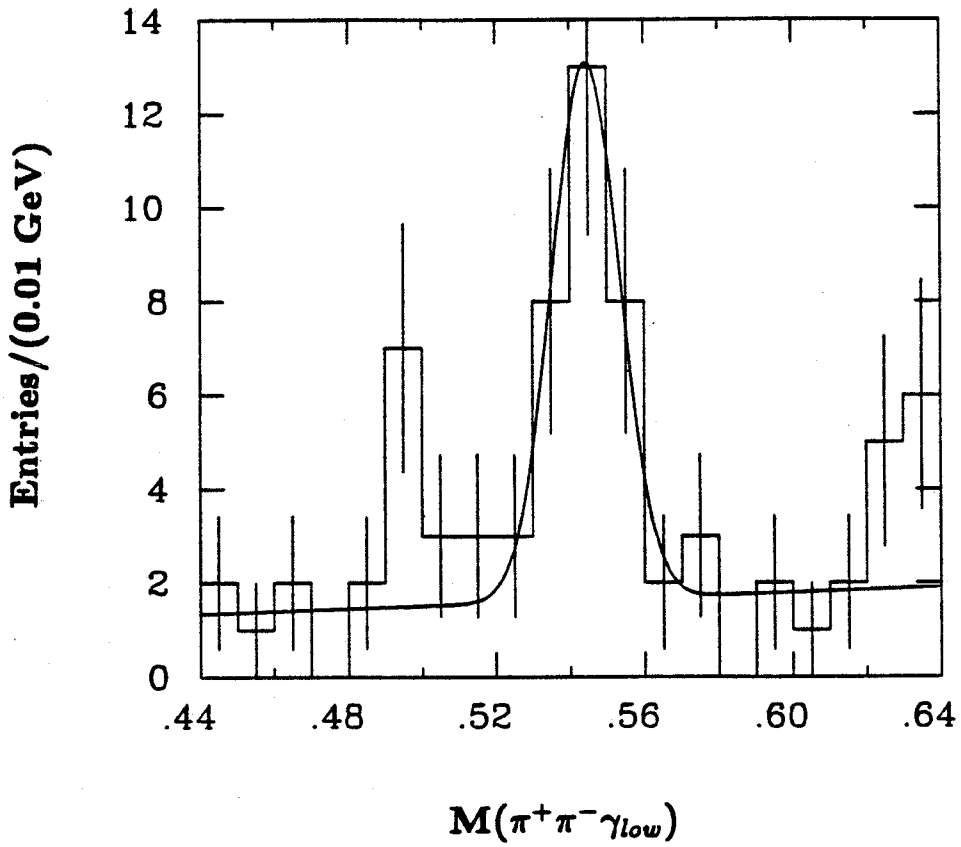

Figure 4.6. The $M(\pi^+\pi^-\gamma_{low})$ distribution in the 0.5 - 0.6 GeV region. The η signal is due to the process $\psi \rightarrow \gamma\eta$; $\eta \rightarrow \gamma\pi^+\pi^-$.

Table 4.2. Comparison of Efficiency of Stereo Layer Cut in Data and Monte Carlo for Events from $\psi \to \gamma\eta'$; $\eta' \to \gamma\rho^0$.

Stereo Layers	% of Tracks in Data	% of Tracks in Monte Carlo
no stereo	3	4
L4 only	10	9
L6 only	2	3
L4 and L6	85	84

Using the Mark III measurements for $\psi \to \gamma\eta$ and $\psi \to \gamma\eta'$ one finds

$$\frac{B(\psi \to \gamma\eta')}{B(\psi \to \gamma\eta)} = 5.2 \pm 1.3(stat) \pm 0.3(sys).$$

This value agrees well with the theoretical estimate (discussed in the preceding chapter) based on the first-order QCD diagram.

Study of the 1.4 GeV Mass Region

The study of the higher mass region in $M(\pi^+\pi^-\gamma_{low})$ is complicated by the presence of additional backgrounds. As a consequence, somewhat more stringent cuts are used. The first three cuts are

1. Each charged track must pass through at least one stereo layer.
2. $P(\chi^2) > 0.15$.
3. There must be only two shower clusters that are both (a) more than one layer deep and (b) outside of the $\cos\theta_{\gamma q} = 0.95$ cone of each charged track.

It is important to check that the efficiency for each of these cuts is reasonably well understood. One approach is to check that the effect of the cuts on Monte Carlo generated events and η' events is the same. Table 4.2 shows the fraction of

tracks with useful information in the stereo layers for both η' events and Monte Carlo events. The differences are very slight. Figure 4.7 compares the $P(\chi^2)$ distribution for the η' signal in the data and in the Monte Carlo; the events must have $\chi^2 < 25$. Both distributions have peaks at $P(\chi^2) \approx 0$ due to the fact that the underlying errors are not exactly Gaussian. In studying the data, one must take care to ensure that background events do not distort the $P(\chi^2)$ distribution. Although the signal-to-noise ratio is high at the η', the $P(\chi^2)$ distribution for the background is not uniform and contributes significantly to the peak at low $P(\chi^2)$. Thus, in making Fig. 4.7a, the $P(\chi^2)$ distributions for the sidebands 0.85-0.90 GeV and 1.02-1.07 GeV are subtracted from the $P(\chi^2)$ distribution associated with the η' signal region (0.91-1.01 GeV). The fraction of events with $P(\chi^2) > 0.15$ is 0.83 in the data and 0.80 in the Monte Carlo, a difference of about 4%. This agreement can be expected to apply to the 1.4 GeV mass region as well. The efficiency for the cut on the number of shower clusters (which excludes a region near the charged tracks) is found to be $(81 \pm 5)\%$ from $\psi \rightarrow \gamma\eta'$ events. This is quite similar to the value obtained from the Monte Carlo, although the agreement may be fortuitous, as the Monte Carlo does not model hadronic interactions in the shower counter. (One might expect rough agreement, however, because the cut ignores the regions near charged tracks, where most split-off clusters are found.)

Background from $\psi \rightarrow \rho^0\eta$

The hint of an η band in Fig. 4.4a is evidently due to another background process. To study this process further, it is useful to temporarily remove $\eta' \rightarrow \gamma\rho^0$ by excluding events with $M(\pi^+\pi^-\gamma_{low})$ in the range 0.8-1.1 GeV. The resulting scatterplot of $M(\pi^+\pi^-)$ vs. $M(\gamma\gamma)$ is shown in Fig. 4.8a. It is clear that most of the η's are correlated with $M(\pi^+\pi^-)$ at the ρ^0 mass, giving

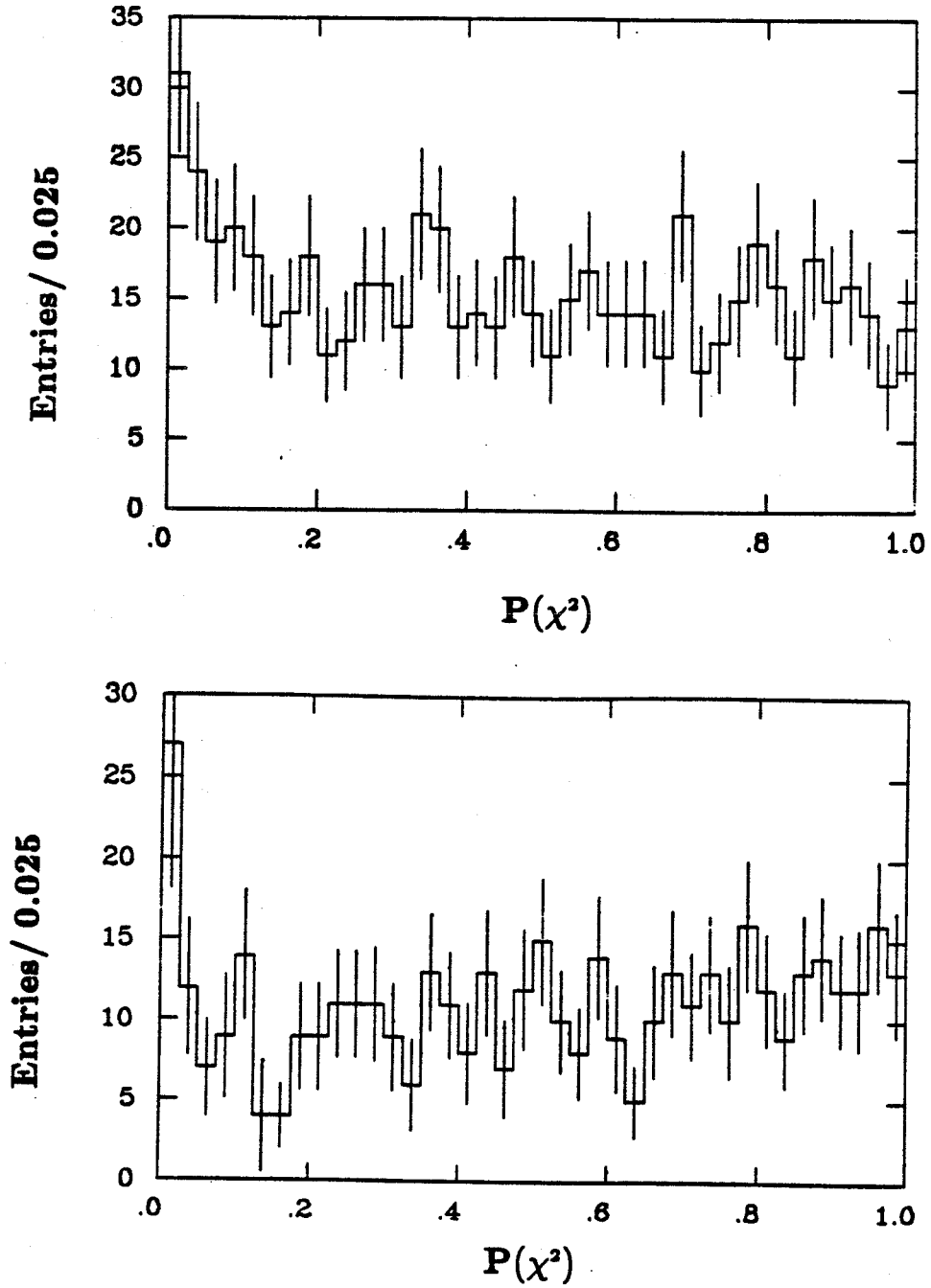

Figure 4.7. Comparison of the $P(\chi^2)$ distributions from $\psi \to \gamma\eta'$; $\eta' \to \gamma\rho^0$. (a) Monte Carlo (b) data.

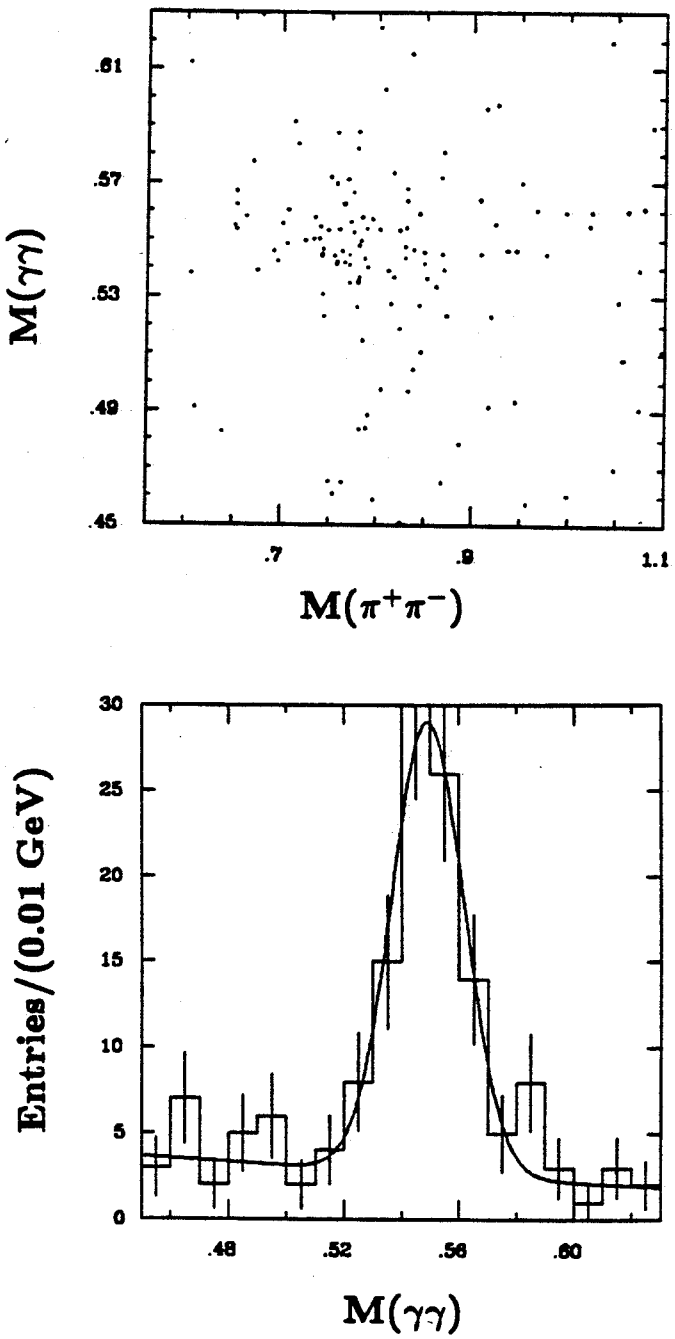

Figure 4.8. Evidence for $\psi \rightarrow \rho^0\eta$. a) M($\gamma\gamma$) vs. M($\pi^+\pi^-$), showing the correlation between the ρ^0 and the η. b) M($\gamma\gamma$) for M($\pi^+\pi^-$) $\leq$ 1.3 GeV, showing the η signal.

evidence for the previously unobserved isospin violating decay $\psi \to \rho^0\eta$.

The $M(\gamma\gamma)$ distribution for events with $M(\pi^+\pi^-) \leq 1.3$ GeV is shown in Fig. 4.8b. The mass obtained from a fit to a Gaussian is $M(\eta) = 0.549 \pm 0.005$ GeV, and the resolution is $\sigma = 0.017 \pm 0.005$ GeV. The $M(\pi^+\pi^-)$ distribution for events in the η region ($0.52 \leq M(\gamma\gamma) \leq 0.57$ GeV) is shown in Fig. 4.9a. The Breit-Wigner fit parameters are $M = 0.777 \pm 0.008$ GeV and $\Gamma = 0.082 \pm 0.029$ GeV. This width is 2.5σ lower than the true ρ^0 width. Further study of this channel has shown that the $\pi^+\pi^-$ signal is due to both ρ^0 and ω, and a fit allowing $\rho^0 - \omega$ interference gives a good description of the data. This analysis, along with the observation of other new vector-pseudoscalar channels, will be described in another publication (62). Here it is only necessary to understand the contribution of this signal to the background in the ι region. Figure 4.9b shows the distribution of $M(\pi^+\pi^-\gamma_{low})$ for $\rho\eta$ events. It is desirable to remove these events not only to improve the ratio of signal to noise, but also to ensure that any observed ρ^0 signal is due to radiative decay and not to a hadronic decay of the ψ. Both $\rho\pi$ and $\rho^0\eta$ events are removed by imposing the requirement that

$$M(\gamma\gamma) \geq 0.6 \text{ GeV}.$$

The mass region between the π^0 and η signals, 0.2–0.4 GeV, is also excluded because events in this region are still on the tail of the enormous π^0 peak. The effect of this cut on $\iota \to \gamma\rho^0$ events can be seen from the Monte Carlo generated $\gamma\gamma$ mass distribution (Fig. 4.10). The cut $M(\gamma\gamma) \geq 0.6$ GeV removes about 6.4% of the events.

Observation of a $\gamma\rho^0$ Signal Near 1.4 GeV

After making the cuts described above, the $M(\pi^+\pi^-)$ distribution is plotted against the $M(\pi^+\pi^-\gamma_{low})$ distribution (Fig. 4.11a). Three processes are evident

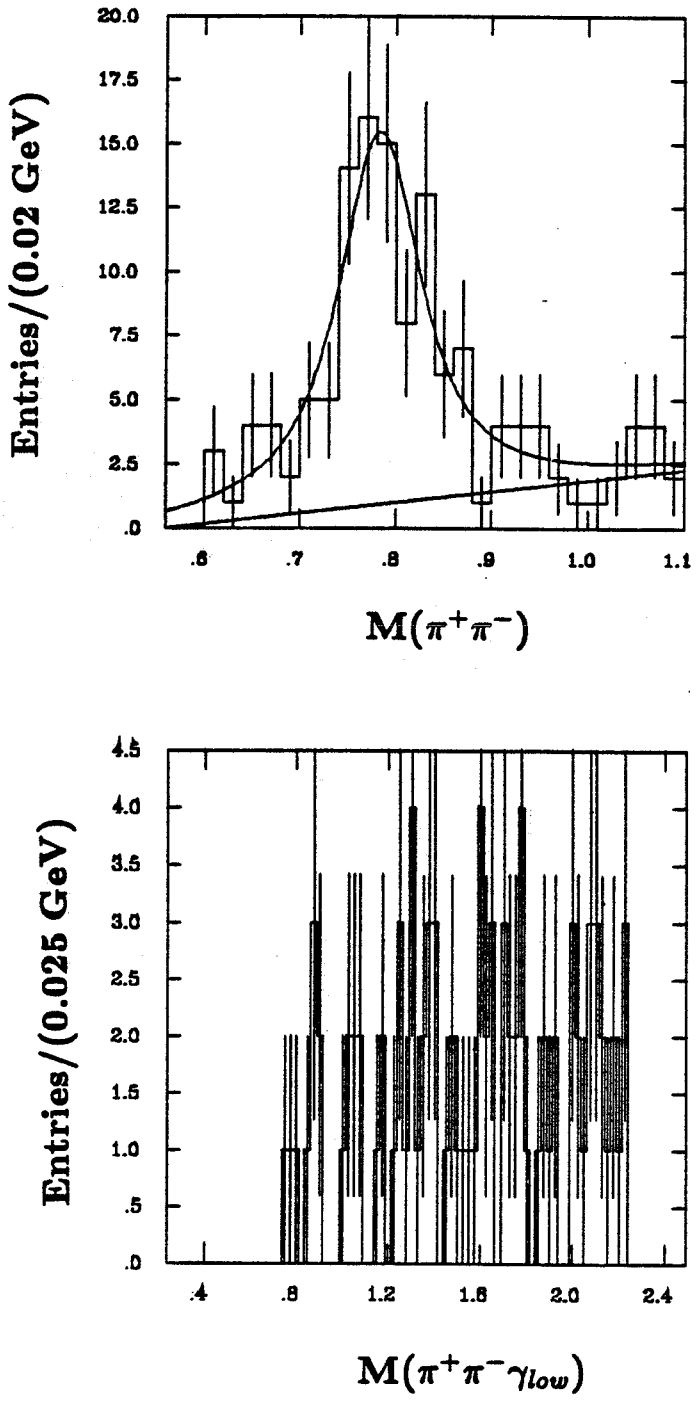

Figure 4.9. Study of $\psi \rightarrow \rho^0\eta$ background. a) The $M(\pi^+\pi^-)$ distribution for events in the η region and b) $M(\pi^+\pi^-\gamma_{low})$ for $\rho^0\eta$ events.

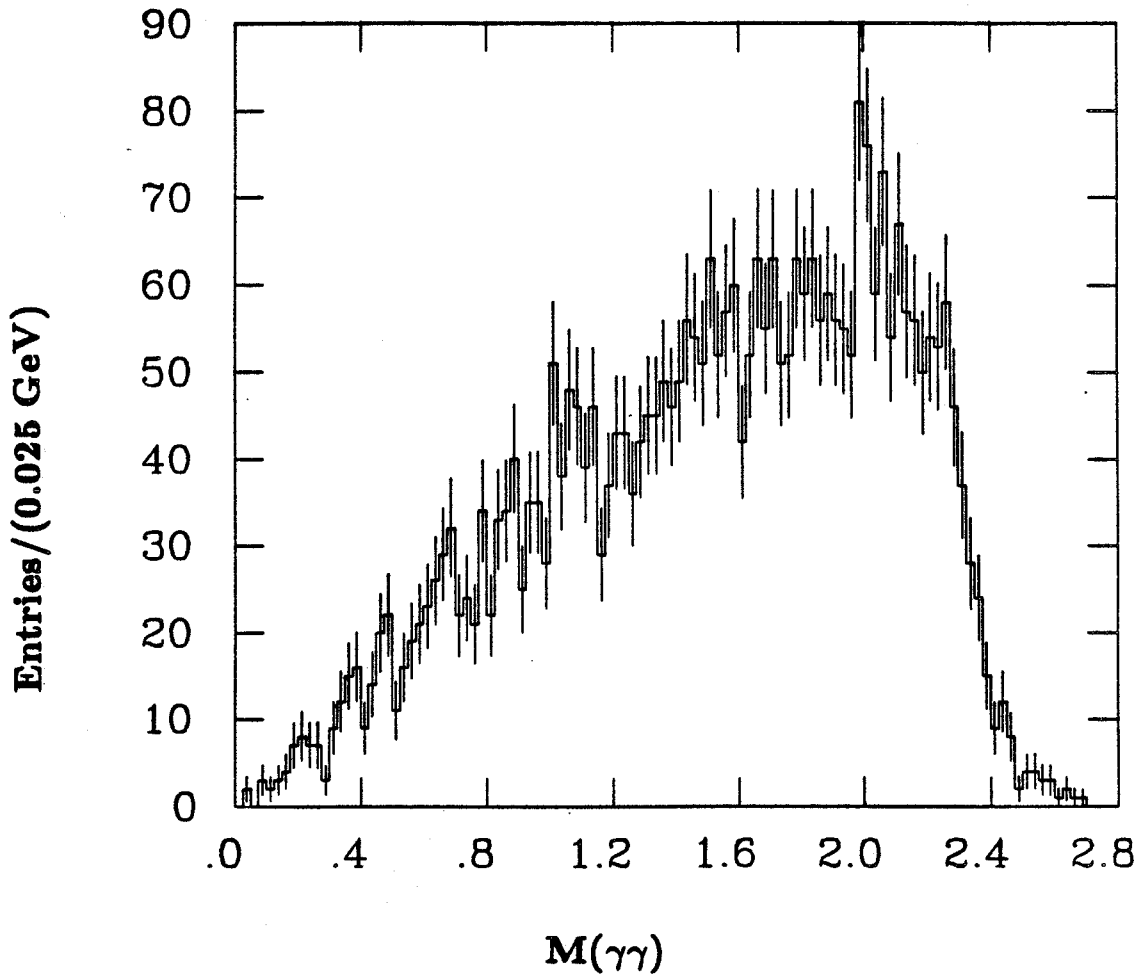

Figure 4.10. Monte Carlo generated $\gamma\gamma$ mass distribution for $\psi \rightarrow \gamma\iota$, $\iota \rightarrow \gamma\rho^0$. The cut $M(\gamma\gamma) \geq 0.6$ GeV removes about 6.4% of the events.

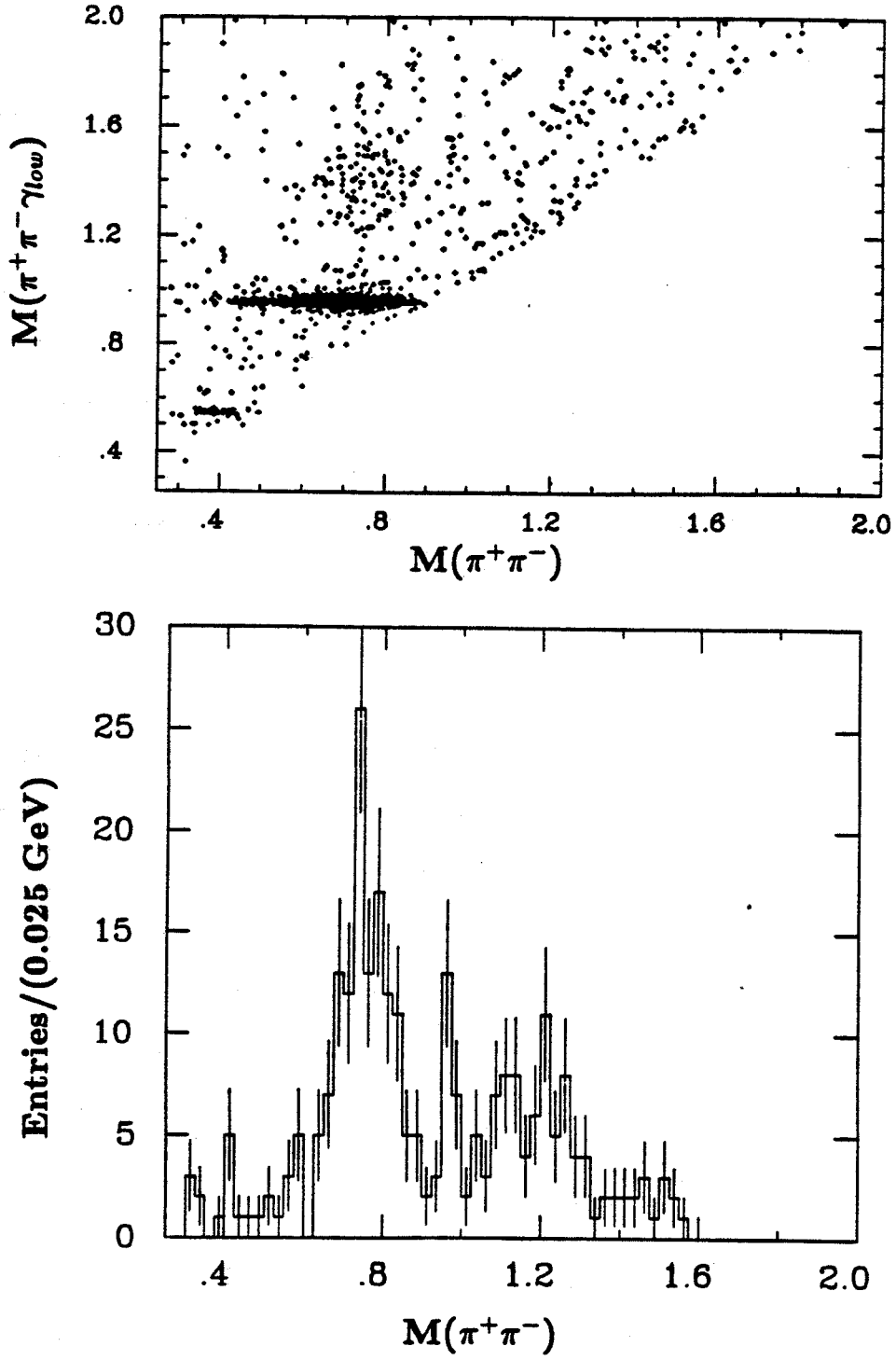

Figure 4.11. Evidence for a signal near 1.4 GeV. a) $M(\pi^+\pi^-\gamma_{low})$ vs. $M(\pi^+\pi^-)$, showing $\psi \to \gamma\eta$, $\psi \to \gamma\eta'$, and $\psi \to \gamma X(1.4)$. b) $M(\pi^+\pi^-)$ for events with $M(\pi^+\pi^-\gamma_{low})$ in the range 1.1–1.7 GeV.

from this plot. The lowest band is due to $\psi \to \gamma\eta$, $\eta \to \gamma\pi^+\pi^-$. Here the $\pi^+\pi^-$ mass is below the ρ^0 mass. The very dark band is due to the process $\psi \to \gamma\eta'$, $\eta' \to \gamma\rho^0$. Finally, there is a cluster of events that have a ρ^0 signal correlated with $M(\pi^+\pi^-\gamma_{low})$ in the 1.4 GeV region. To see this more clearly, it is useful to plot the $\pi^+\pi^-$ mass only for those events with $M(\pi^+\pi^-\gamma_{low})$ between 1.1 and 1.7 GeV (Fig. 4.11b). With the η' events excluded, one can see that there are still events with a ρ^0 remaining.

The presence of a ρ^0 is significant because all other known processes in which $\psi \to \gamma\gamma\rho^0$ have been removed with the $\gamma\gamma$ mass cut. The observation of a ρ^0 signal also narrows the range of potential backgrounds because C-invariance then requires an even number of photons:

$$C_\psi = -1 = C_{\rho^0}(-1)^{n_\gamma}.$$

If the signal is due to a background process in which photons are missed, there must be at least two such missing photons. Thus the processes $\psi \to \gamma\pi^0\pi^+\pi^-$ and $\psi \to \gamma\eta\pi^+\pi^-$ are not a serious problem.

Most of the additional structure in the $\pi^+\pi^-$ mass spectrum above the ρ^0 is due to the decay $\psi \to \omega\pi^+\pi^-$, including $\omega \to \gamma\pi^0$. This background will be discussed in more detail below. Figure 4.12a shows the distribution of $M(\pi^+\pi^-\gamma_{low})$ after requiring

$$0.5 \leq M(\pi^+\pi^-) \leq 0.9 \text{ GeV}.$$

There is evidence for a broad structure in the 1.4 GeV region.

Figure 4.12b shows the scatterplot of $E(\gamma_{high})$ vs. $E(\gamma_{low})$ for events with $M(\pi^+\pi^-\gamma_{low})$ in the range 1.1-1.6 GeV. Although the plot appears to provide evidence for a monochromatic photon, this is more or less an inevitable

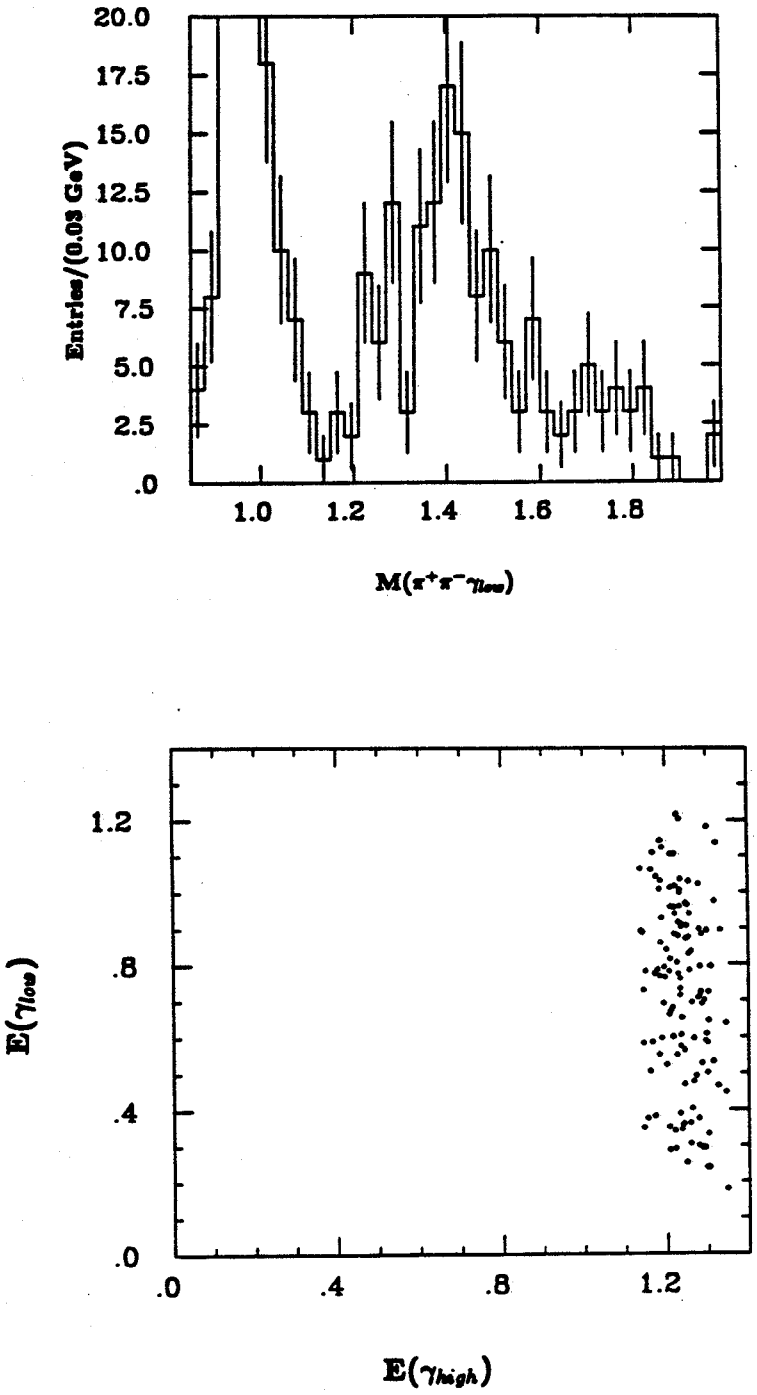

Figure 4.12. Distributions after requiring $0.5 \leq M(\pi^+\pi^-) \leq 0.9$ GeV. a) $M(\pi^+\pi^-\gamma_{low})$ and b) $E(\gamma_{high})$ vs. $E(\gamma_{low})$.

consequence of the 4-C fit: the band in $E(\gamma_{high})$ simply corresponds to the original cluster in $M(\pi^+\pi^-\gamma_{low})$. Because the measured photon energies have very large uncertainties, one cannot see a monochromatic photon in the measured photon energy spectrum.

Background from $\psi \to \omega\pi^+\pi^-$

Another background process has been identified by computing the neutral missing mass recoiling against the two charged pions. This decay process is

$$\psi \to \omega\pi^+\pi^- \qquad \omega \to \gamma\pi^0.$$

The product branching ratio for this decay (including $\psi \to \gamma f(1270)$) is $(0.68\%)(0.087) = 0.059\%$, which implies that there should be $\sim 1600\times$ efficiency such events in the data sample. If one of the photons from the π^0 is soft, these events will fit well to the hypothesis $\psi \to \gamma\gamma\pi^+\pi^-$. Most of the events can be removed by the $P(\chi^2) > 0.15$ cut (but not by a loose χ^2 cut, because the missing photon often has a very low energy) and by the ρ^0 cut. The missing mass distribution before the ρ^0 cut is shown in Fig. 4.13a. By requiring the missing mass to be greater than 1.0 GeV, one can remove these remaining $\omega\pi^+\pi^-$ events.

The missing mass cut cleans up somewhat the $M(\pi^+\pi^-)$ vs. $M(\pi^+\pi^-\gamma_{low})$ scatterplot (Fig. 4.14a) and the $\pi^+\pi^-$ mass spectrum (Fig. 4.14b). The only possibly significant structure besides the ρ^0 in the $\pi^+\pi^-$ mass spectrum is a cluster near 0.95 GeV. Because of the small number of events, it has proved extremely difficult to identify this background. The background under the ρ^0 itself appears to be very small. A fit to a Breit-Wigner line shape yields the parameters $M = 0.758 \pm 0.011$ GeV and $\Gamma = 0.141 \pm 0.025$ GeV, which are consistent within errors with the ρ^0 mass and width. Because the cut on the

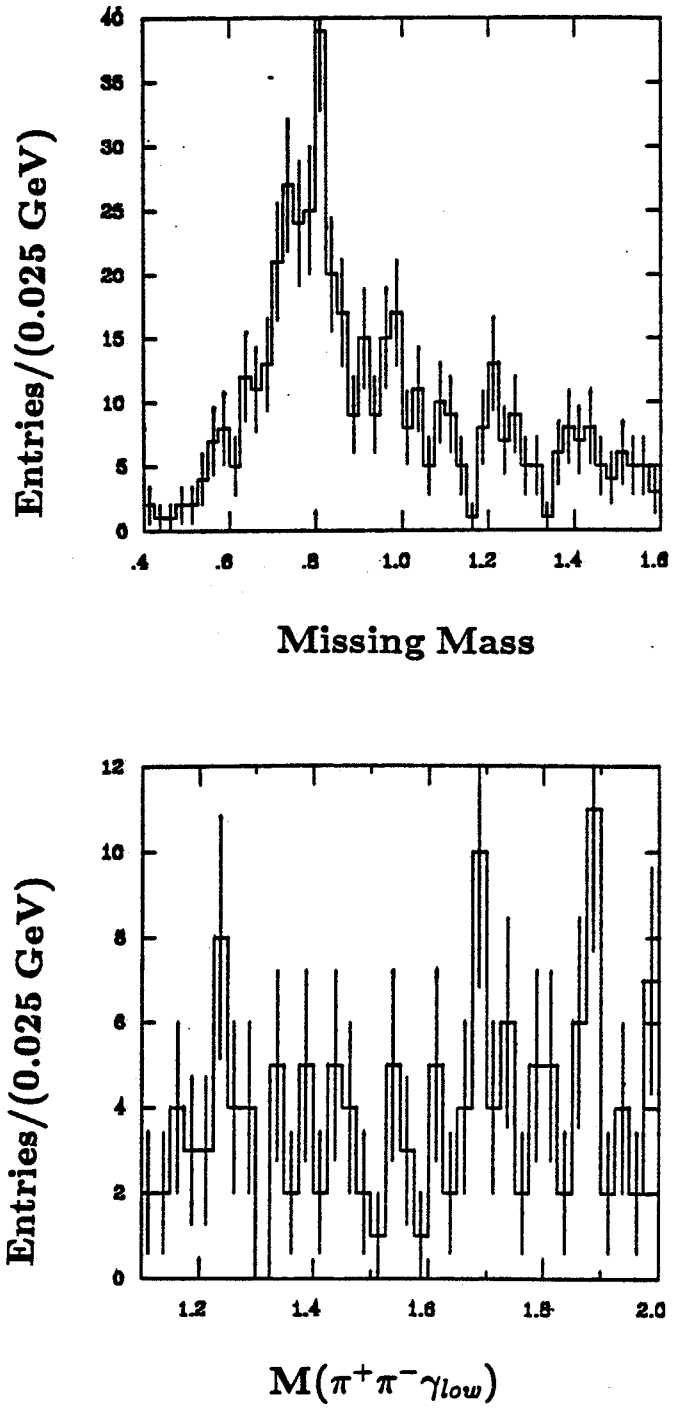

Figure 4.13. Background from $\psi \to \omega\pi^+\pi^-$, $\omega \to \gamma\pi^0$. a) The missing mass distribution before the ρ^0 cut and b) M($\pi^+\pi^-\gamma_{low}$) for $\omega\pi^+\pi^-$ events (no ρ^0 cut).

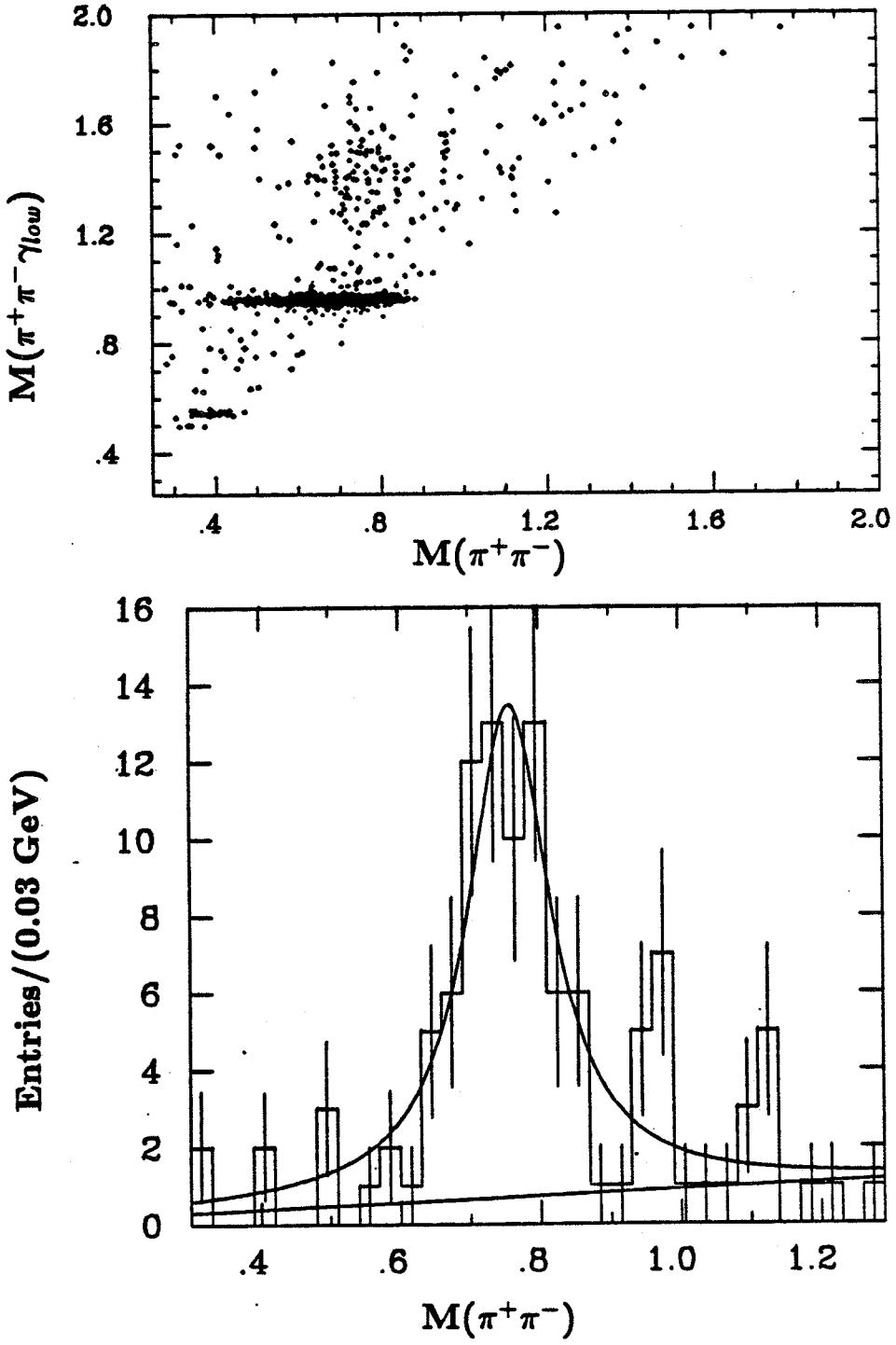

Figure 4.14. Distributions after requiring $M_{missing} > 1$ GeV. a) $M(\pi^+\pi^-)$ vs. $M(\pi^+\pi^-\gamma_{low})$ and b) $M(\pi^+\pi^-)$ for $M(\pi^+\pi^-\gamma_{low})$ in the 1.1–1.7 GeV region.

ρ^0 removes nearly all of the $\omega\pi^+\pi^-$ background, in the following sections the missing mass cut is not made.

It is interesting to know the distribution that the $\omega\pi^+\pi^-$ events would produce in the M($\pi^+\pi^-\gamma_{low}$) spectrum if they were not removed. In order to study this no ρ^0 cut is made, and the missing mass is required to be in the range 0.675–1.1 GeV. The distribution of M($\pi^+\pi^-\gamma_{low}$) shows no prominent structure in the 1.3 GeV mass region. (Fig. 4.13b).

Breit-Wigner Fit and Branching Ratio

To obtain the mass and width parameters, the signal is fit to a Breit-Wigner curve folded with a Gaussian resolution function (Fig. 4.15). The mass resolution at 1.44 GeV is determined from the Monte Carlo to be $\sigma = 11$ MeV.

The signal shown in Fig. 4.15 appears to have two components: a small one centered around 1.25 GeV and a large signal centered around 1.4 GeV. Because the lower mass signal appears in the $3\gamma\pi^+\pi^-$ control sample with approximately equal strength, it is unlikely to be background. It has not been possible to identify the specific decay producing this signal. For this reason, the Breit-Wigner parameters of the higher mass signal are obtained from a fit to the upper mass region (1.3-1.9 GeV) only. The results of this fit are

$$M(X) = 1.420 \pm 0.015 \pm 0.020 \text{ GeV}$$

$$\Gamma(X) = 0.133 \pm 0.055 \pm 0.030 \text{ GeV}.$$

To obtain the number of events due to the 1.4 GeV signal, the Breit-Wigner is simply extended into the rest of the mass region. This curve is shown in Fig. 4.15. The number of events (1982 + 1983 data) from this fit is 77 ± 15. The efficiency is found from the Monte Carlo to be $(35 \pm 4)\%$. This value does not include the efficiency for the requirement of two good gammas, which is found

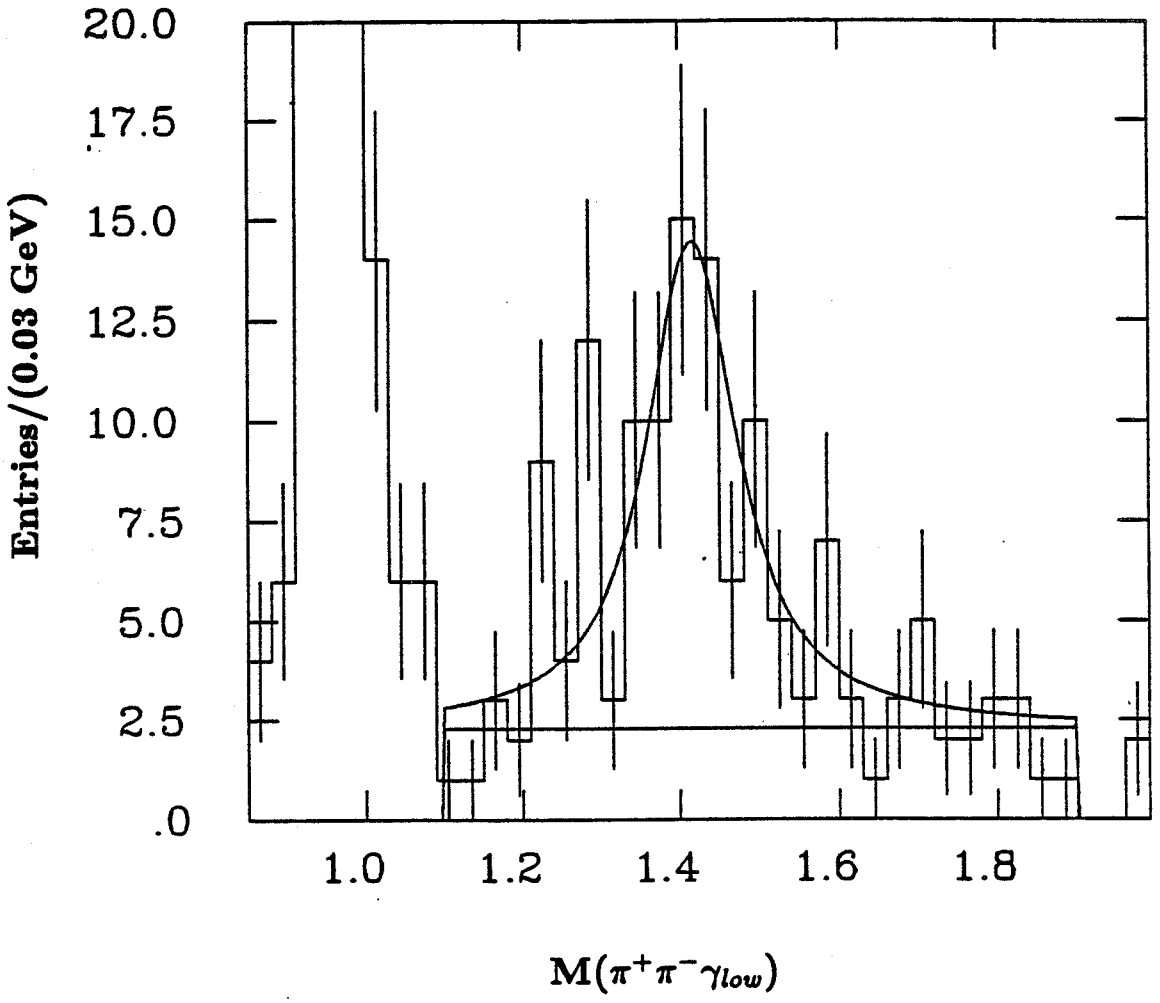

Figure 4.15. Breit-Wigner fit to $\gamma\rho^0$ signal. The parameters are obtained from a fit to the 1.3–1.9 GeV mass region.

to be $(81 \pm 5)\%$ from $\eta' \to \gamma\rho^0$ events. The product branching ratio is

$$B(\psi \to \gamma X)B(X \to \gamma\rho^0) = (1.0 \pm 0.2 \pm 0.2) \times 10^{-4}.$$

If one makes the identification $X = \iota$ then the partial radiative width to $\gamma\rho^0$, assuming $\Gamma = 95$ MeV and $B(\iota \to K\bar{K}\pi) \approx 1$, is

$$\Gamma(\iota \to \gamma\rho^0) = 1.9 \pm 0.7 \text{ MeV}.$$

Analysis of the Backgrounds

We now consider in more detail whether any decay process could be misidentified and produce the signal that is observed in the $\pi^+\pi^-\gamma_{low}$ mass spectrum. Such processes fall into three groups. First, we investigate the possibility that the charged particles are not pions. Second, we consider background processes with two charged pions and two photons that are not in a double radiative decay sequence. Finally, we look at processes with more than two photons that could feed down into $\gamma\gamma\pi^+\pi^-$.

To ensure that the charged particles are pions the following checks were performed:

1. The possibility that the events are double radiative Bhabhas, $e^+e^- \to e^+e^-\gamma\gamma$, is ruled out by computing the quantity $E_{shower}/|\vec{P}|$ for each charged track. The events have $E_{shower}/|\vec{P}| \ll 1$, in contrast to the expected value of 1 for $e^\pm$.

2. The possibility that the charged tracks are muons is ruled out in 40% of the events, which have at least one track with sufficiently high momentum for a muon to reach the muon counters. No hits are observed in the counters.

3. The possibility that the charged tracks are kaons is clearly excluded, except in the case of five events, through the use of time-of-flight information. These five events were already removed for the above fits and branching ratio determination.

The second class of backgrounds, those from $\psi \to \gamma\gamma\pi^+\pi^-$, fall into three categories:

1. Two-body decays $\psi \to \rho^0\pi^0$, $\rho^0\eta$, $X^\pm\pi^\mp$ (*e.g.*, $\rho^\pm\pi^\mp$),

2. Mismeasurement of $\psi \to \gamma\eta'$; $\eta' \to \rho^0$, or

3. A three-body decay $\psi \to \gamma\gamma\rho^0$

The two-body decays are easy to rule out because one of the pions or the ρ^0 must be monochromatic. Figure 4.16 shows the momentum spectra of the pions, and Fig. 4.17 shows the momentum spectrum of the ρ^0. There is no evidence of a narrow peak that would characterize two-body backgrounds.

The possibility that the signal results from a confusion between the photons from $\psi \to \gamma\eta'$; $\eta' \to \gamma\rho^0$ is interesting because there are over 1000 such events. However, the kinematic reflection of the η' when the wrong photon is selected to accompany the ρ^0 makes a substantial contribution to the $\pi^+\pi^-\gamma$ background only above 2 GeV, and the confusion between the photons is small anyway. In addition, Monte Carlo $\eta' \to \gamma\rho^0$ events do not show evidence of any structure in the 1.4 GeV region.

Finally, there is the unlikely possibility that the decay is actually a three-body mode ($\gamma\gamma\rho^0$). The $M(\pi^+\pi^-\gamma_{low})$ distribution for phase space events has been generated and shows no indication of any narrow structure.

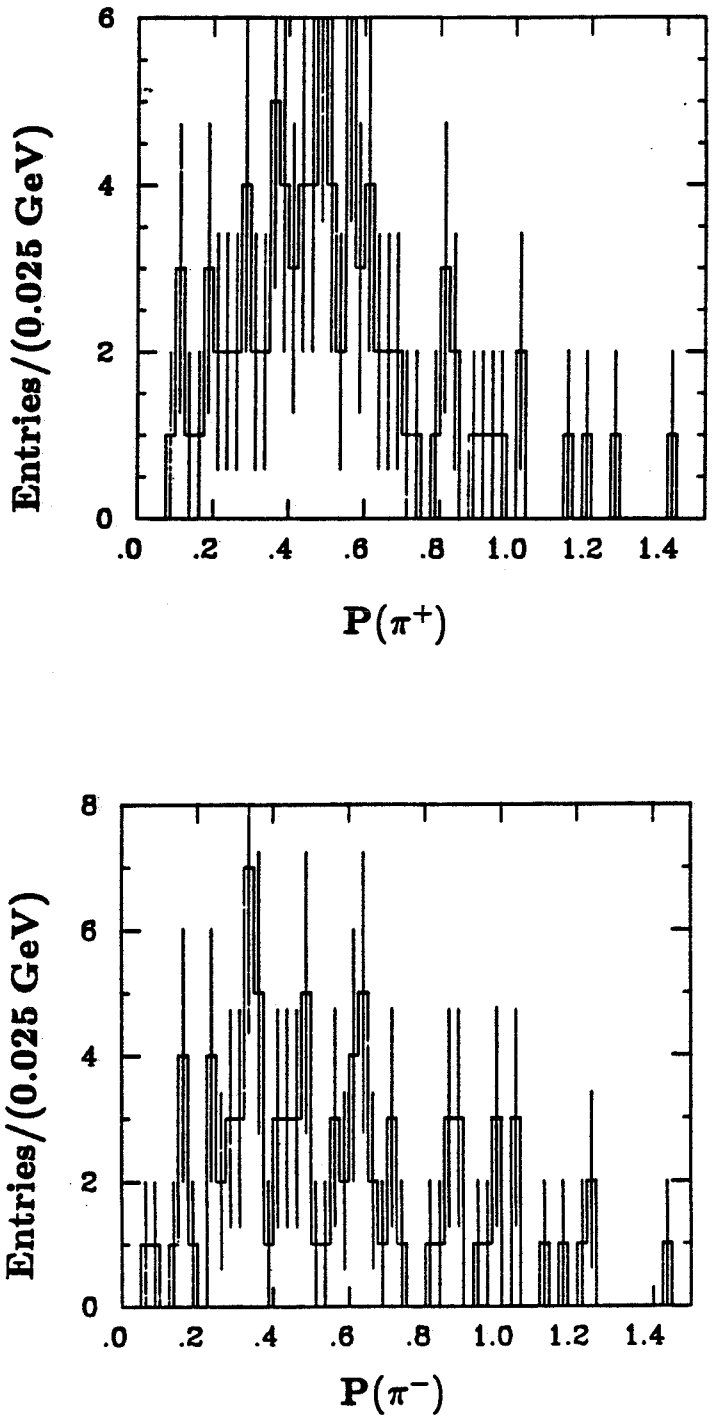

Figure 4.16. The momentum spectrum of the pions.

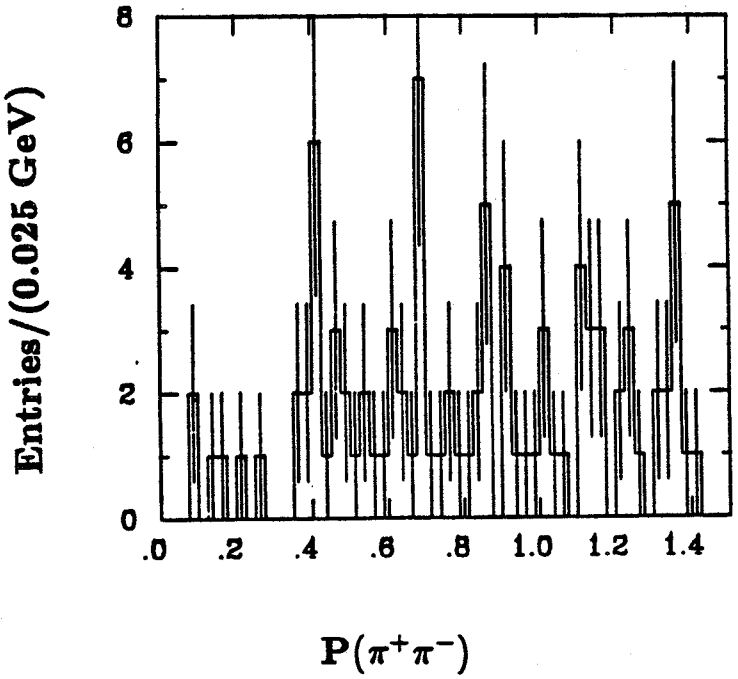

Figure 4.17. The momentum spectrum of the ρ^0.

Backgrounds from $\psi \to 3\gamma\pi^+\pi^-$ and $4\gamma\pi^+\pi^-$

The most difficult backgrounds are processes in which one or more photons are not detected, either because the photon energy is too low or because it is not within the detector solid angle. As noted above, the decay

$$\psi \to 3\gamma + \rho^0$$

is forbidden, because the right-hand side has even charge conjugation. Thus $3\gamma\pi^+\pi^-$ is a much less serious background than

$$\psi \to 4\gamma + \rho^0,$$

which is allowed. In particular, the hadronic decays to the final states $\rho^0\pi^0\pi^0$ and $\rho^0\pi^0\eta$ are quite large. Although many of these modes are electromagnetic (and violate isospin), they can have large branching ratios because the strong decays are OZI-suppressed. Table 4.3 summarizes the features of the $4\gamma\pi^+\pi^-$ backgrounds.

Backgrounds from $\psi \to 3\gamma\pi^+\pi^-$ will be considered first. These processes can contribute only to the extent that there is background under the ρ^0. Because the ρ^0 signal is very clean (Fig. 4.14), one can immediately conclude that there is very little background of this form ($\lesssim 6$ events). The most prominent signal in $3\gamma\pi^+\pi^-$, which is $\psi \to \gamma\eta'$; $\eta' \to \eta\pi^+\pi^-$, does not appear as a background under the ρ^0 because the dipion mass must be less than $M(\eta') - M(\eta) = 0.41$ GeV.

The background from $3\gamma\pi^+\pi^-$ was studied in two ways. First, the requirement that each event have two shower clusters was changed to a three cluster requirement. All other analysis cuts remained the same. The distribution of $M(\pi^+\pi^-\gamma_{low})$ for these events is shown in Fig. 4.18a. There is a large η'

Table 4.3. Backgrounds from $\psi \to 4\gamma + \rho^0$.

Background Process $\psi \to 4\gamma + \rho^0$	No. Events in Data Sample	Comments
$\psi \to (\pi^0 \text{ or } \eta) + X$;		
$X \to \rho^0\pi^0$		
$X = H(1190)$	–	$p(\rho^0) = 1.19$ GeV
$X = A_1(1270)$	0	forbidden: $C(\pi^0 A_1) = +1$
$X = \pi(1300)$	0	forbidden: $C(\pi^0\pi(1300)) = +1$
$X = A_2(1320)$	0	forbidden: $C(\pi^0 A_2) = +1$
$X = \omega(1670)$	–	should be suppressed: $l = 3$
$X = A_3(1678)$	0	forbidden: $C(\pi^0 A_3) = 0$
$\psi \to \rho^0 + X$;		
$X \to \pi^0\eta$		
$X = A_2(1300)$	$(1000 \pm 500) \times \epsilon$	$p(\rho^0) = 1.13$ GeV. No significant peak at this momentum
$X = \delta(980)$	–	$p(\rho^0) = 1.27$ GeV is beyond endpoint of measured momentum spectrum
$\psi \to \rho^0 + X$;		
$X \to \pi^0\pi^0$		
$X = S^*(975)$	–	$p(\rho^0) = 1.28$ GeV
$X = f(1270)$	–	$p(\rho^0) = 1.15$ GeV
$\psi \to (\pi^0 \text{ or } \eta) + X$; $X \to \rho^0\eta$	0	ψ is only particle with observed decay into $\rho^0\eta$
$\psi \to \rho^0\pi^0\pi^0$ 3-body	–	Checked with Monte Carlo (5000 events)
$\psi \to \rho^0\pi^0\eta$ 3-body	–	Checked with Monte Carlo (5000 events)

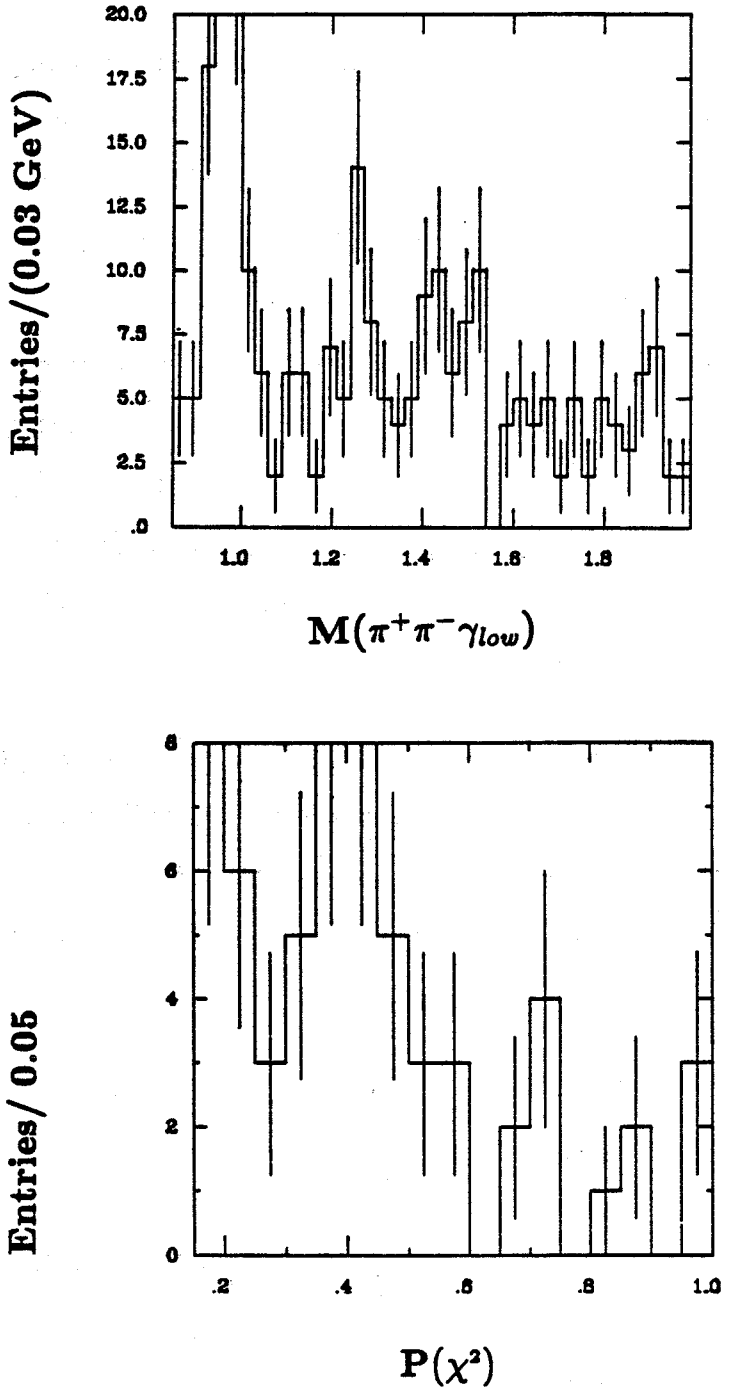

Figure 4.18. Study of the $3\gamma\pi^+\pi^-$ background. a) $M(\pi^+\pi^-\gamma_{low})$ for events with three shower clusters and b) $P(\chi^2)$ for events with $M(\pi^+\pi^-\gamma_{low})$ in the range 1.3–1.6 GeV.

signal! These events are not from $\psi \to \gamma\eta'$; $\eta' \to \eta\pi^+\pi^-$, but from $\psi \to \gamma\eta'$; $\eta' \to \gamma\rho^0$ events (a clear ρ^0 signal is present) that have a split-off cluster far from a charged track. These split-offs are often due to a low energy piece of a photon shower that appears topologically separate to the reconstruction code. From the η', one expects about 16% of the $X(1.4) \to \gamma\rho^0$ events to have three shower clusters and about 3% to have four. The spike near 1.3 GeV in Fig. 4.18a indicates that the shoulder in the two cluster events at the same mass is probably due to background. The number of excess events in the 1.4 GeV region in the three photon sample, however, is consistent with expectation. Figure 4.18b shows the $P(\chi^2)$ distribution for three cluster events with $M(\pi^+\pi^-\gamma_{low})$ in the range 1.3-1.6 GeV. In general, the events have low values of $P(\chi^2)$, indicating that many of them are background.

The second approach was to study events that had good 5-C fits to the hypothesis $\psi \to \gamma\eta\pi^+\pi^-$. These events have a high probability of having three photons. They were then refit to the hypothesis $\psi \to \gamma\gamma\pi^+\pi^-$. As expected, very few events in the 1.4 GeV region had a good χ^2 and no narrow structure was present.

The unambiguous presence of the ρ^0 signal shows that, in fact, the only *serious* and *dangerous* backgrounds that might *completely* produce the signal are $\psi \to \rho^0\pi^0\pi^0$ and $\psi \to \rho^0\pi^0\eta$, where two soft photons are lost. The possible decays leading to these final states are listed in Table 4.3. The $\pi^+\pi^-\gamma_{low}$ mass spectrum for events with four shower clusters away from charged tracks, but satisfying all other analysis cuts, is shown in Fig. 4.19a. There is no prominent structure in the 1.4 GeV region, although there is a considerable amount of smooth background. The $P(\chi^2)$ distribution from the $\gamma\gamma\pi^+\pi^-$ fit for events with $M(\pi^+\pi^-\gamma_{low})$ in the range 1.3-1.6 GeV is shown in Fig. 4.19b. The distribution

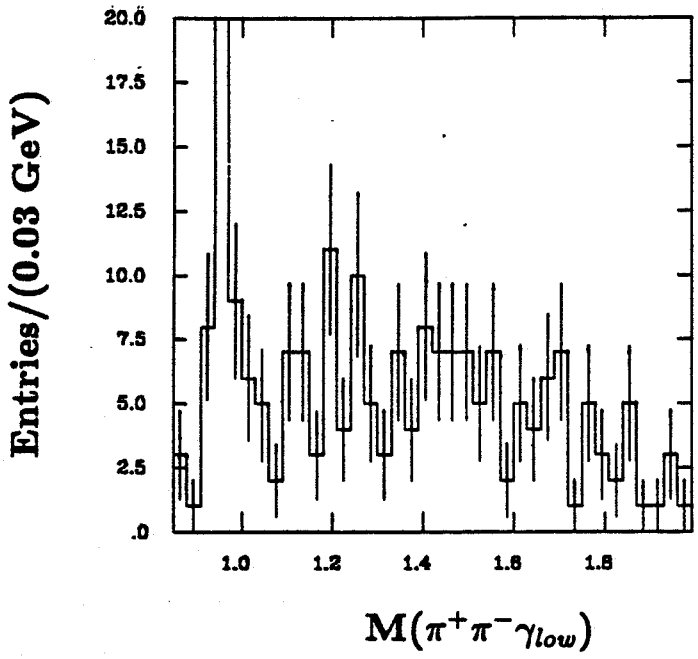

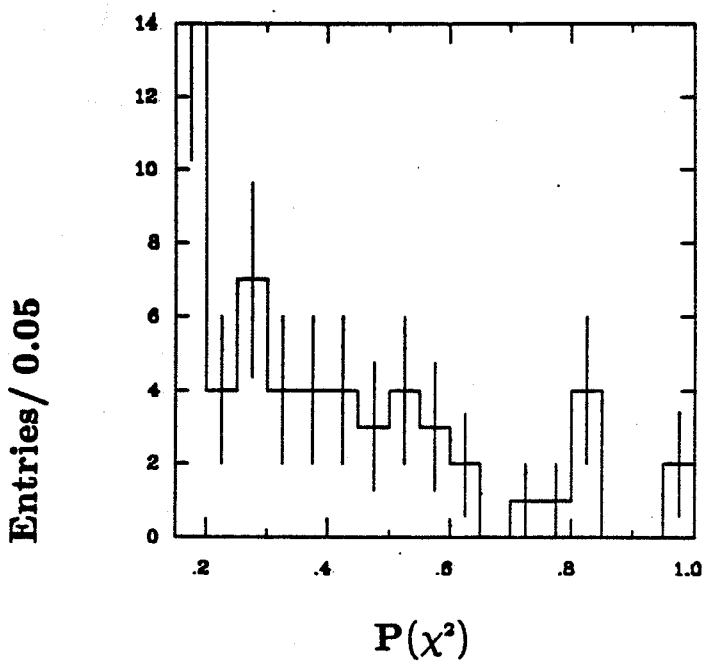

Figure 4.19. Study of the $4\gamma\pi^+\pi^-$ background. a) $M(\pi^+\pi^-\gamma_{low})$ for events with four shower clusters and b) $P(\chi^2)$ for events with $M(\pi^+\pi^-\gamma_{low})$ in the range 1.3–1.6 GeV.

is steeply falling, indicating that $\gamma\gamma\pi^+\pi^-$ is not the correct hypothesis. In contrast, the $P(\chi^2)$ distribution for the signal events (Fig. 4.20) is relatively flat and extends all the way out to $P(\chi^2) = 1$.

There are other useful checks that can be used to rule out backgrounds from $\psi \to 4\gamma\pi^+\pi^-$. First, many decay modes are forbidden by C-invariance (see Table 4.3). The presence of a ρ^0 is crucial for the use of this selection rule, as the analogous charged channels are allowed. A useful check for the presence of two-body decays of the form $\psi \to \rho^0 X$; $X \to (\eta\pi^0$ or $\pi^0\pi^0)$ is the ρ^0 momentum spectrum. This spectrum can be measured even if photons are lost. (In fact, the charged track momenta are not significantly changed by the 4-C fit to $\gamma\gamma\pi^+\pi^-$.) A potentially very serious background is $\psi \to \rho^0 A_2^0$; $A_2^0 \to \rho^0\eta$, but it can be largely excluded because it would produce a peak near the tail end of the momentum spectrum, whereas no such peak is observed (Fig. 4.17).

In addition to these checks, Monte Carlo $\rho^0\pi^0\pi^0$ and $\rho^0\eta\pi^0$ events were generated according to three-body phase space and fit to the hypothesis $\psi \to \gamma\gamma\pi^+\pi^-$ using the two highest energy photons. Both of these processes result in some events with $M(\pi^+\pi^-\gamma_{low})$ in the 1-2 GeV region. However, the mass distributions are broad, and most of the events fit very poorly to the $\gamma\gamma\pi^+\pi^-$ hypothesis. Applying the cuts used in the data analysis, even without the cut on the number of shower clusters, removes 99% of the $\rho^0\pi^0\eta$ events (Fig. 4.21). The $\rho^0\pi^0\pi^0$ events have somewhat better χ^2's than the $\rho^0\pi^0\eta$ events, and are more difficult to remove. The standard analysis cuts, without the cut on the number of shower clusters, remove 96% of this background. The $M(\pi^+\pi^-\gamma_{low})$ distribution for the remaining events is shown in Fig. 4.22a. There is some background in the 1-2 GeV region, and it has a shape very similar to that observed in the data. If one were to require only two shower clusters, as in

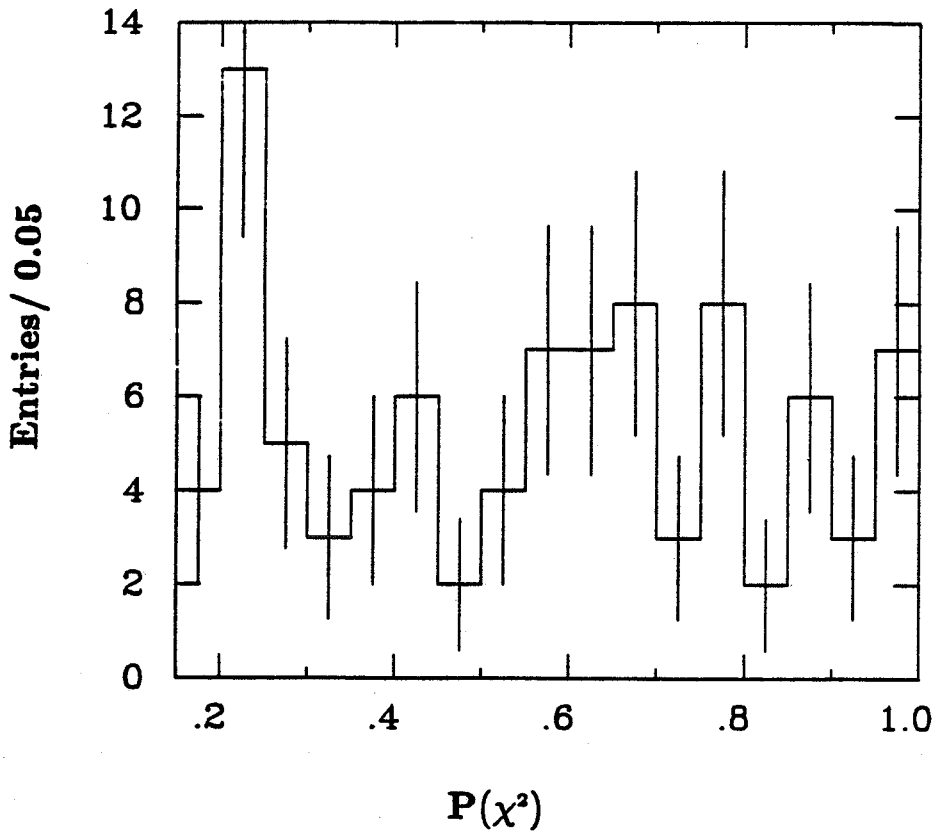

Figure 4.20. The $P(\chi^2)$ distibution for the signal events. The distribution is relatively flat and extends out to $P(\chi^2)$=1.

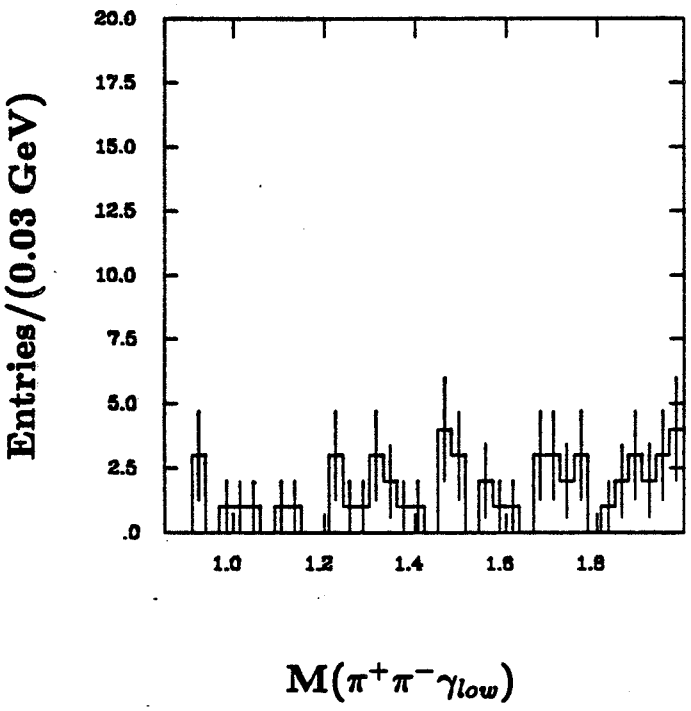

Figure 4.21. Background study. $M(\pi^+\pi^-\gamma_{low})$ distribution for Monte Carlo $\psi \rightarrow \rho^0\pi^0\eta$ events that pass all of the analysis cuts except for the two cluster requirement.

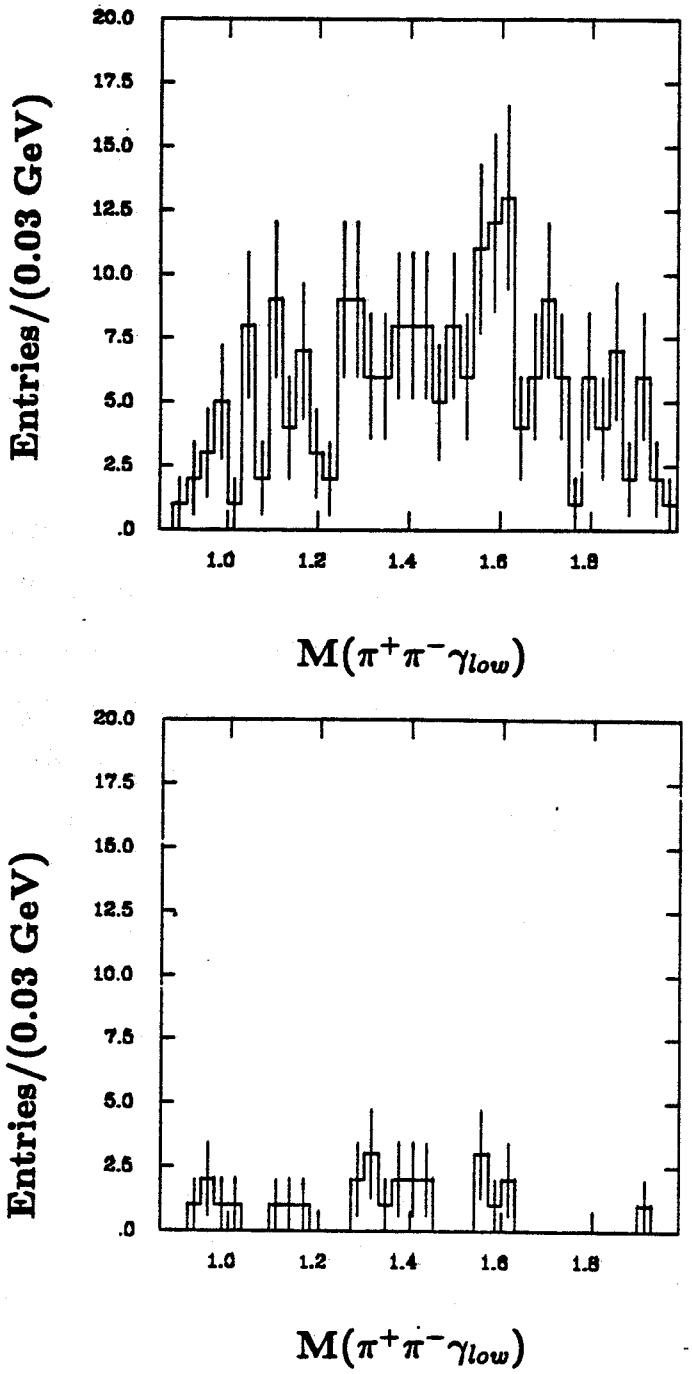

Figure 4.22. Background study. a) M($\pi^+\pi^-\gamma_{low}$) for Monte Carlo $\psi \to \rho^0\pi^0\pi^0$ events that pass all of the analysis cuts except for the two photon requirement. b) M($\pi^+\pi^-\gamma_{low}$) spectrum after requiring two photons.

the analysis of the data, only 27 events would survive in the 1-2 GeV region (Fig. 4.22b).

Because the branching ratios for these background processes have not been measured, one does not know the correct number of events to generate in the Monte Carlo program. The number generated (5000) was chosen quite conservatively, and corresponds to a branching ratio of about 0.2%. This is about half that of $\rho^0\pi^0$, a very large strong decay of the ψ.

Angular Distributions

Because the most obvious explanation for the signal (or perhaps just part of it) is the process $\psi \to \gamma\iota$; $\iota \to \gamma\rho^0$, it is important to investigate the decay angular distributions and determine whether they are consistent with $J^P = 0^-$. Using the two-body helicity formalism described in Appendix B, one can calculate the angular distributions for $\psi \to \gamma_1 X$; $X \to \gamma_2\rho^0$; $\rho^0 \to \pi^+\pi^-$ for $J^P(X) = 0^-$ and $J^P(X) = 1^+$. The following notation is used:

$\theta, \phi =$ the polar and azimuthal angles of X measured in the lab frame. The z-axis is defined by the positron beam (see Sec. 2.1).

$\theta_\rho, \phi_\rho =$ the polar and azimuthal angles of the ρ^0 in the X rest frame;

$\theta_\pi, \phi_\pi =$ the polar and azimuthal angles of the π^+ in the ρ^0 rest frame;

$x =$ $|A_1(X)/A_0(X)|$ = ratio of amplitudes for production of X in helicity one and helicity zero states;

$x_{\rho^0} =$ $|A_1(\rho^0)/A_0(\rho^0)|$ = ratio of amplitudes for production of ρ^0 in helicity one and helicity zero states.

For $J^P(X) = 0^-$, the angular distribution is predicted uniquely:

$$\frac{dN}{d\Omega} = (1 + \cos^2\theta)\sin^2\theta_\pi,$$

and the $\cos\theta_\rho$ distribution is uniform. This result can be understood intuitively. Because $J(X) = 0$, the angular momentum along the decay axis, $\mu = \lambda_{\rho^0} - \lambda_{\gamma_2}$, must be zero. But $\lambda_{\gamma_2} = \pm 1$ only, so $\lambda_{\rho^0} = 0$ is not allowed. Furthermore, the γ_2 helicities can be measured (in principle) in the final state, so the $\lambda_{\rho^0} = \pm 1$ amplitudes do not interfere.

The result for $J^P(X) = 1^+$ is quite complicated:

$$\begin{aligned}
\frac{dN}{d\Omega} = \tfrac{1}{2}x^2\sin^2\theta\Big\{&(1+\cos^2\theta_\rho)\cos^2\theta_\pi + x_\rho^2\sin^2\theta_\rho\sin^2\theta_\pi \\
&- \tfrac{1}{2}x_\rho\cos(\phi_\pi-\phi_\rho)\sin 2\theta_\rho\sin 2\theta_\pi\Big\} \\
+\tfrac{1}{2}(1+\cos^2\theta)\Big\{&\sin^2\theta_\rho\cos^2\theta_\pi + x_\rho^2\cos^2\theta_\rho\sin^2\theta_\pi \\
&+ \tfrac{1}{2}x_\rho\cos(\phi_\pi-\phi_\rho)\sin 2\theta_\rho\sin 2\theta_\pi\Big\} \\
+\tfrac{1}{8}x\sin 2\theta\Big\{&\cos(\phi_\rho-\phi)\sin 2\theta_\rho\left[\cos^2\theta_\pi - x_\rho^2\sin^2\theta_\pi\right] \\
&+ \tfrac{1}{2}x_\rho\sin 2\theta_\pi\Big[\cos(\phi_\pi-\phi)(\cos 2\theta_\rho + \cos\theta_\rho) \\
&+ \cos((\phi_\pi-\phi_\rho)-(\phi_\rho-\phi))(\cos 2\theta_\rho+\cos\theta_\rho)\Big]\Big\}.
\end{aligned}$$

There are two free parameters, x and x_ρ, both of which are assumed to be real. Consequently, two of the three polar angle distributions for $J^P = 1^+$ can always be made to match the distributions predicted for $J^P = 0^-$. This is unfortunate because only two of the distributions are well measured, $\cos\theta_\rho$ and $\cos\theta_\pi$, whereas $\cos\theta$ is measured very poorly (if at all) when the decay products of X go into the endcaps of the detector. Only with a large data sample is this distribution useful (see $\iota \to K\bar{K}\pi$).

In spite of the difficulty with $\cos\theta$, it is still possible to consider the question of whether the distributions are consistent with $J^P = 0^-$. Figure 4.23 compares

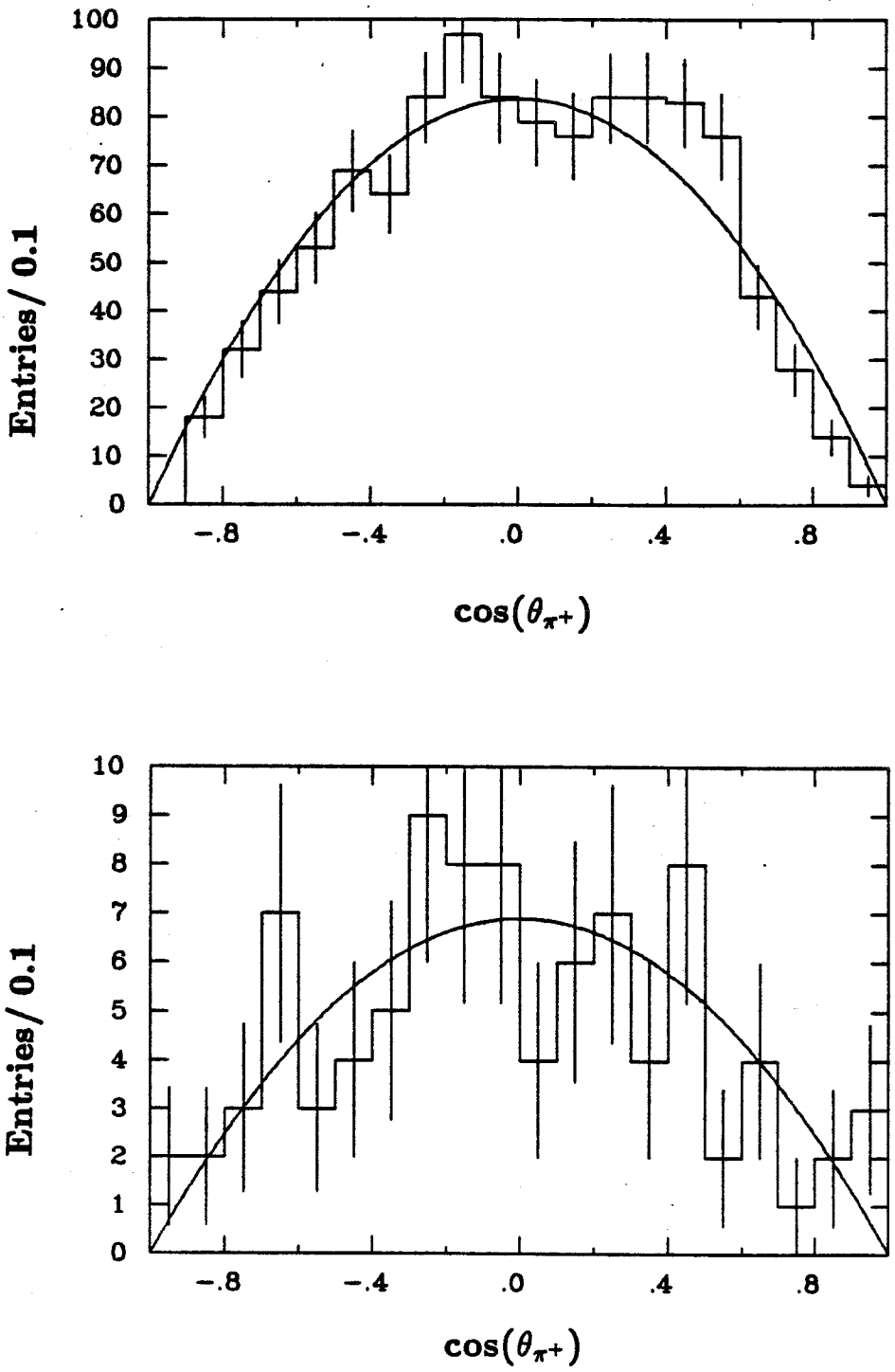

Figure 4.23. Study of the π^+ production angle, $\cos\theta_{\pi^+}$. a) η' events and b) events in the 1.3–1.5 GeV mass region. The distributions are fit to $N\sin^2\theta_{\pi^+}$.

the distribution of $\cos\theta_\pi$ for η' events and for events with $M(\pi^+\pi^-\gamma_{low})$ in the range 1.3-1.5 GeV. The $\cos\theta_\pi$ distribution has been fit to the function $N(1-\cos^2\theta_\pi)$ and shows fairly good agreement with the 0^- prediction of $\sin^2\theta_\pi$.

The $\cos\theta_\rho$ distribution should be uniform for $J^P = 0^-$. Although the distribution appears to be relatively flat, there is an excess of events with $\cos\theta_\rho < 0$ (Fig. 4.24)b. Part of this excess can be attributed to the fact that the cut $M(\gamma\gamma) > 0.6$ GeV biases the measurement of $\cos\theta_\rho$. For low values of $M(\gamma\gamma)$ the photon momenta are more closely aligned, and the ρ^0 momentum vector is therefore more aligned with the momentum vector of X. This configuration corresponds to $\cos\theta_\rho$ large. By studying this problem with Monte Carlo events it was found that the cut $M(\gamma\gamma) > 0.6$ GeV affects only the range of $\cos\theta_\rho$ from 0.9 to 1.0, that is, only the highest histogram bin. If one ignores this bin, then the probability that a uniform $\cos\theta_\rho$ distribution would lead to the measured asymmetry is only 1–2%. Whether this is an indication of a serious problem in the analysis or is just a statistical fluctuation is unclear. The photons are of sufficiently high energy that there can be no problem with efficiency, even though the asymmetry corresponds to the fact that in the E_{high} vs. E_{low} scatterplot the density of points becomes too low as E_{low} decreases.

It is possible to adjust the spin-one parameters x and x_ρ to produce a flat $\cos\theta_\rho$ distribution and a $1-\cos^2\theta_\pi$ distribution in $\cos\theta_\pi$. The $\cos\theta$ distribution, after integrating over azimuthal angles, is predicted to have the form

$$\frac{dN}{d\cos\theta} = 1 - 0.6\cos^2\theta$$

when $x = 2$ and $x_\rho^{-1} = 0$. This distribution has the opposite curvature from $J^P = 0^-$. Figure 4.25 shows the $\cos\theta$ distributions for the η' and for events in the 1.3–1.5 GeV region. Figure 4.26 shows the acceptance corrected

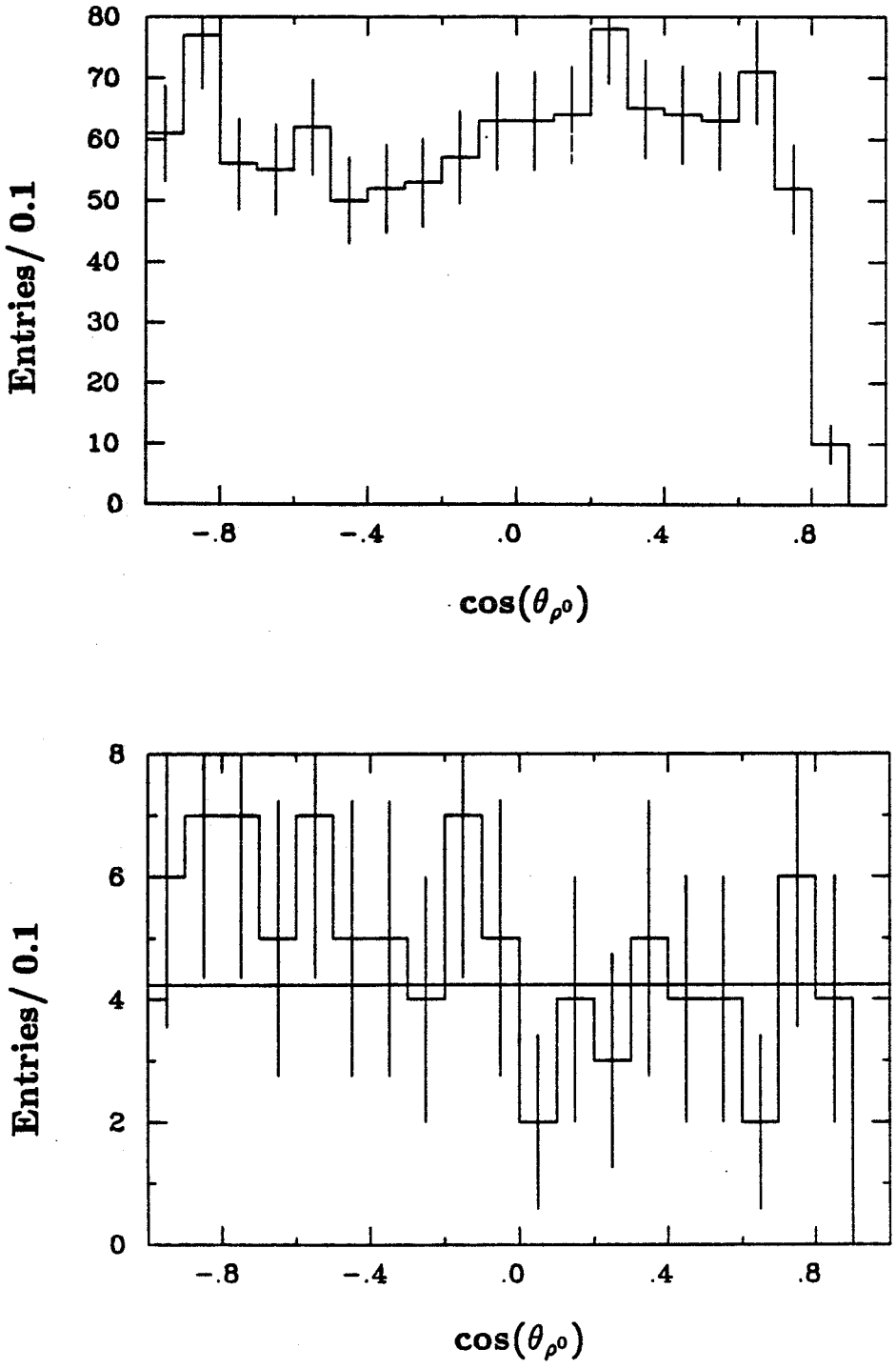

Figure 4.24. Study of the ρ^0 production polar angle distribution, $\cos\theta_{\rho 0}$. a) η' events and b) events in the 1.3–1.5 GeV mass region.

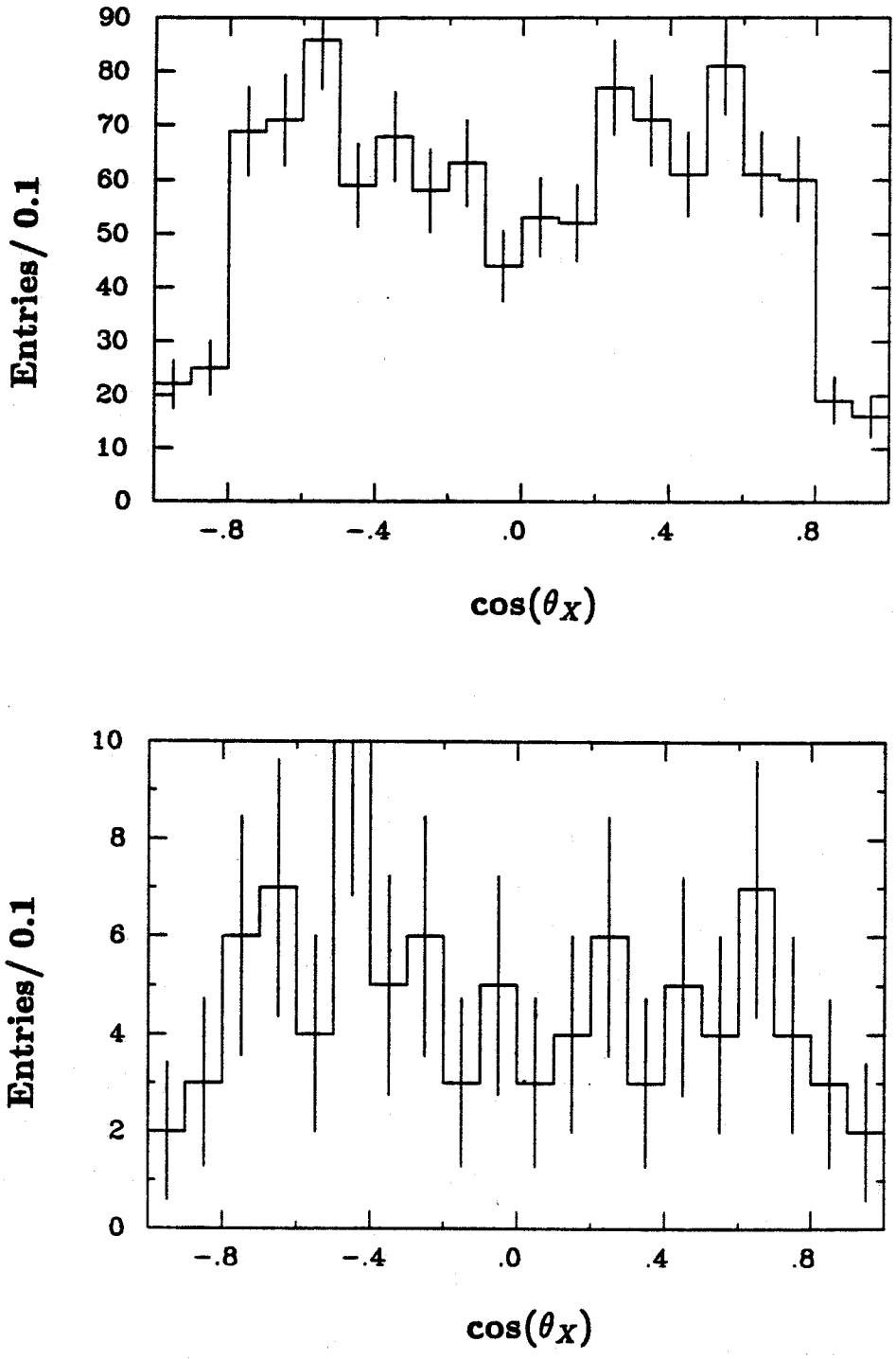

Figure 4.25. Production polar angle ($\cos\theta$) distributions. a) η' events and b) events in the 1.3–1.5 GeV mass region.

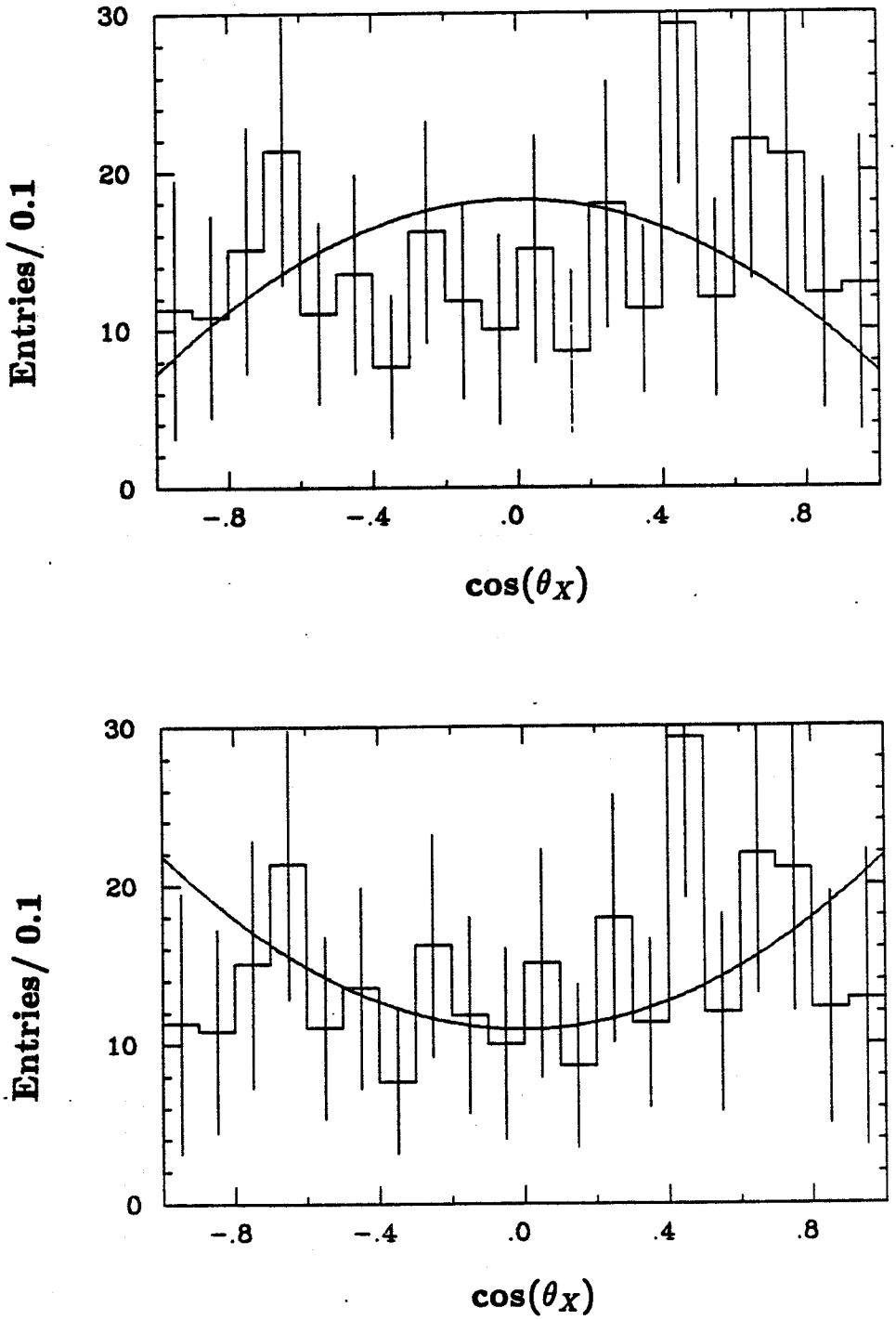

Figure 4.26. The acceptance corrected $\cos\theta$ distributions. a) The $J^P = 1^+$ prediction for which the $\cos\theta_{\rho^0}$ and $\cos\theta_\pi$ distributions agree with those of $J^P = 0^-$ b) $J^P = 0^-$ prediction.

$\cos\theta$ distributions for the 1.3–1.5 GeV region with fits to $\alpha(1+\cos^2\theta)$ and $\alpha'(1-0.6\cos^2\theta)$. The χ^2 per degree-of-freedom is 0.6 for the spin 0 prediction and 0.88 for the spin 1 prediction with x and x_ρ as stated above. Thus, the data are consistent with both spin 0 and spin 1, with spin 0 being slightly preferred.

Measurements by Other Experiments

Two other experiments have recently studied this decay process, the Crystal Ball, using data taken at SPEAR, and DM2, which is located at the DCI e^+e^- ring. The DM2 detector has a cylindrical design with a solenoidal magnet, and the $\gamma\gamma\rho^0$ analysis was based on 4.4×10^6 ψ's. The DM2 $\gamma\rho^0$ mass distribution is shown in Fig. 4.27a. There appears to be structure in the 1.4 GeV region, although no values for the mass, width, or branching ratio have yet been quoted.

The Crystal Ball has also observed (61) a signal near 1.4 GeV in this channel. Using a data sample of 2.2×10^6 ψ's, the $\gamma\rho^0$ mass spectrum shown in Fig. 4.27b is obtained. The signal has a shape similar to that observed by Mark III, with a shoulder at about 1.3 GeV. The total number of events in the signal is (61 ± 15) with an efficiency of $(14.3\pm1.7)\%$. A fit to a single Breit-Wigner yields:

$$M(X) = 1.390\pm0.025 \text{ GeV}$$
$$\Gamma(X) = 0.185^{+0.110}_{-0.080} \text{ GeV}$$
$$B(\psi\to\gamma X)B(X\to\gamma\rho^0) = (1.9\pm0.5\pm0.4)\times10^{-4}.$$

As in the Mark III analysis, the signal has been fit with combinations of $f+\iota$ or $\eta(1275)+\iota$, both of which give reasonably good fits.

The angular distributions obtained by the Crystal Ball are inconclusive. The

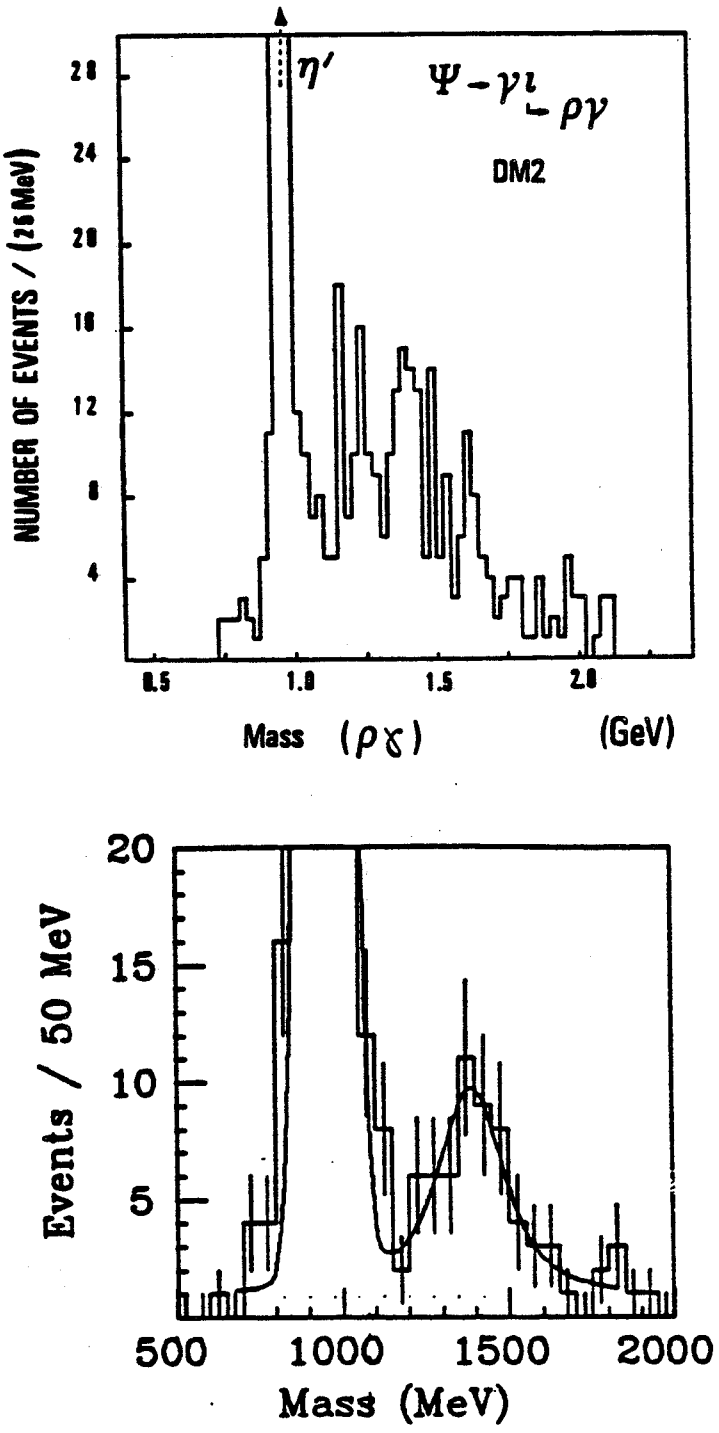

Figure 4.27. Results from other experiments. a) DM2 and b) Crystal Ball.

$\gamma\rho^0$ mass distribution is divided into three regions

$0.900 - 1.000$ GeV	η' region
$1.200 - 1.350$ GeV	X_{lo} region
$1.350 - 1.550$ GeV	X_{hi} region.

The distributions of $\cos\theta_{\gamma_2}(= -\cos\theta_\rho)$ and $\cos\theta_\pi$ for these three mass regions are shown in Fig. 4.28. It is found that the events in the X_{hi} region are consistent with a spin 0 interpretation, whereas those in the X_{lo} region are not. There is a potential difficulty with contamination from $\psi \to \gamma f(1270)$ events that have a split-off. These may contribute to the X_{lo} region to some extent. In the Mark III analysis the ρ^0 signal is clean (and the $\pi^+\pi^-$ mass resolution is very good), so there is no problem with this background.

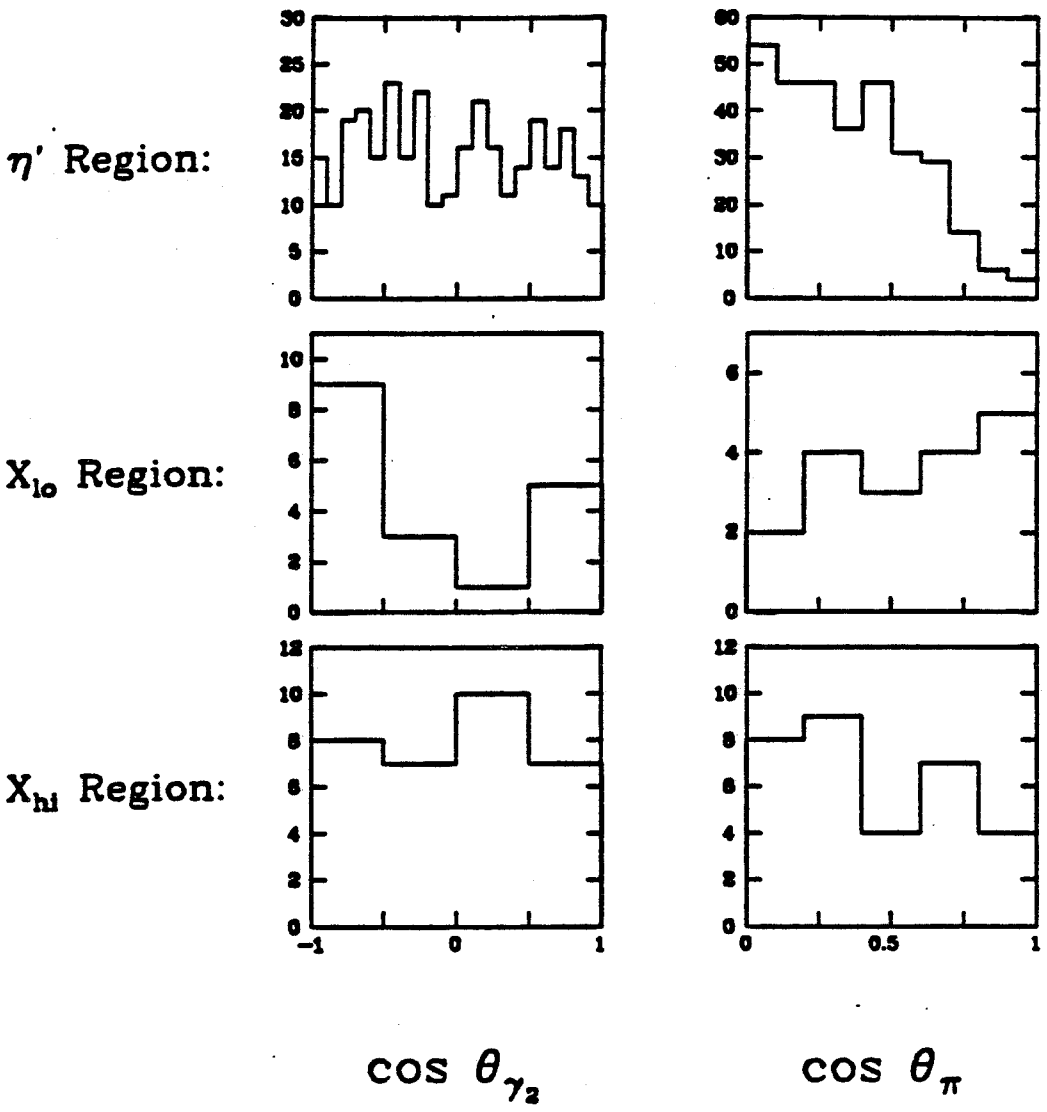

Figure 4.28. Angular distributions measured by the Crystal Ball. The three mass regions are η': 0.9–1.0 GeV, X_{low}: 1.20–1.35 GeV, and X_{hi}: 1.35–1.55 GeV.

4.4 ANALYSIS OF $\psi \to \gamma X$; $X \to \gamma\phi$

Event Selection and Fitting

Events with two oppositely charged tracks are 4-C fit to the hypothesis $\psi \to \gamma\gamma K^+K^-$. The selection procedure for photon candidates for these fits is the same as that used in the $\psi \to \gamma\gamma\pi^+\pi^-$ analysis: shower clusters within the $\cos\theta = 0.95$ cone of a charged track are ignored, as are clusters that have less than two layers. If there are more than two clusters, two kinematic fits are done, $\psi \to \gamma_1\gamma_2 K^+K^-$ and $\psi \to \gamma_1\gamma_3 K^+K^-$, where the gammas are ordered according to energy. Events with more than two clusters are allowed because there may be spurious photons due to kaon interactions in the shower counter or decays in flight. No time-of-flight information is used at this stage — kaon masses are assumed for the charged tracks. For the event to be considered further, the χ^2 for this fit must be less than 25. For events with two fits, the fit with the better χ^2 determines the selection of the candidate clusters.

To ensure that the momenta are well measured and that the acceptance is accurately modeled by the Monte Carlo, it is required that each charged track pass through at least one stereo layer and that the photons be within the solid angle range $|\cos\theta| \leq 0.75$. In this analysis only the 1983 data is used (1.8×10^6 ψ's).

Backgrounds from $\gamma\gamma K^+K^-$

The largest source of background in the $\gamma\gamma K^+K^-$ channel is the process $\psi \to K^{*\pm}K^{\mp}$; $K^{*\pm} \to K^{\pm}\pi^0$, which has a branching ratio of $(0.11 \pm 0.02)\%$. These events are easily removed by requiring $M(\gamma\gamma) \geq 0.2$ GeV. In addition, the charged kaons tend to be nearly back to back, so the K^+K^- system has a much higher mass than the ϕ.

In addition to $\psi \to K^*\bar{K}$, there is background from $\psi \to \phi\eta$. This signal is evident as a cluster of events in the scatterplot of $M(\gamma\gamma)$ vs. $M(K^+K^-)$ (Fig. 4.29a). The ϕ signal in the K^+K^- mass spectrum is shown in Fig. 4.29b, and the corresponding monochromatic peak in the K^+K^- momentum spectrum is shown in Fig. 4.30a. The central value of $p(K^+K^-) = 1.320 \pm 0.0005$ GeV agrees with the expectation for this two-body decay mode. The η signal is shown in Fig. 4.30b. The number of events in the signal is 64.5 ± 8.1; correcting for the detection efficiency $\epsilon = 0.265 \pm 0.03$ and taking into account $B(\phi \to K^+K^-) = 0.493 \pm 0.01$ and $B(\eta \to \gamma\gamma) = 0.390 \pm 0.008$, one obtains

$$B(\psi \to \phi\eta) = [0.070 \pm 0.009(stat) \pm 0.009(sys)] \times 10^{-2}.$$

The systematic uncertainty is obtained by adding in quadrature the 8% uncertainty on the flux, the 10% uncertainty on the Monte Carlo efficiency value, and the uncertainties on the ϕ and η branching ratios. The correct angular distributions were used in generating the Monte Carlo events. The above result can be compared to the *Review of Particle Properties* value of

$$B(\psi \to \phi\eta) = [0.10 \pm 0.06] \times 10^{-2}.$$

A convenient way to remove this signal with only a small loss of efficiency for $\psi \to \gamma\iota$; $\iota \to \gamma\phi$ is to exclude events with $M(\gamma\gamma)$ in the range 0.44-0.66 GeV.

Backgrounds from $\psi \to (n\gamma)K^+K^-$, $n = 3, 4$

The major background from $\psi \to (3\gamma)K^+K^-$ is

$$\psi \to \gamma_1\iota; \quad \iota \to K^+K^-\pi^0; \quad \pi^0 \to \gamma_2\gamma_3,$$

which is discussed in detail in Chapter 3. These events are difficult to discriminate against for two reasons:

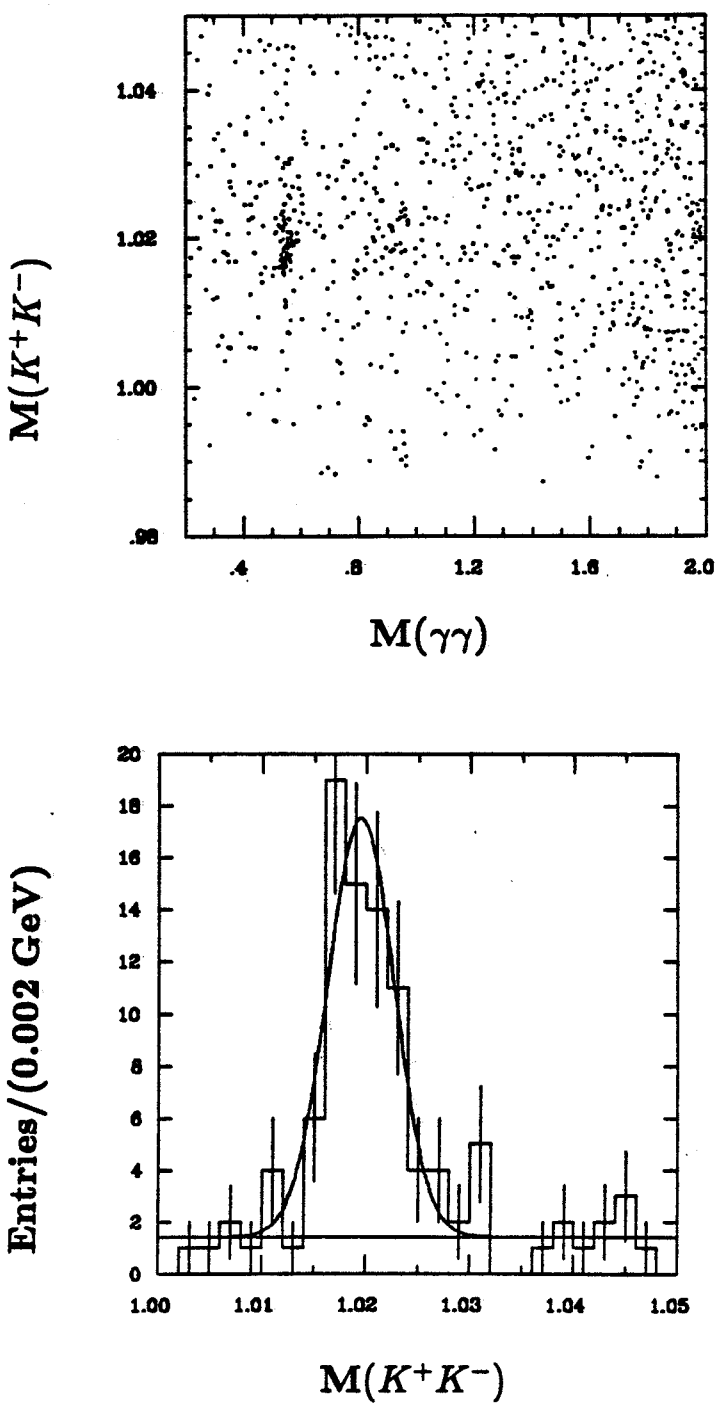

Figure 4.29. Evidence for $\psi \to \phi\eta$. a) M(K^+K^-) vs. M($\gamma\gamma$), showing the correlation between the ϕ and the η and b) the M(K^+K^-) distribution, showing the ϕ signal.

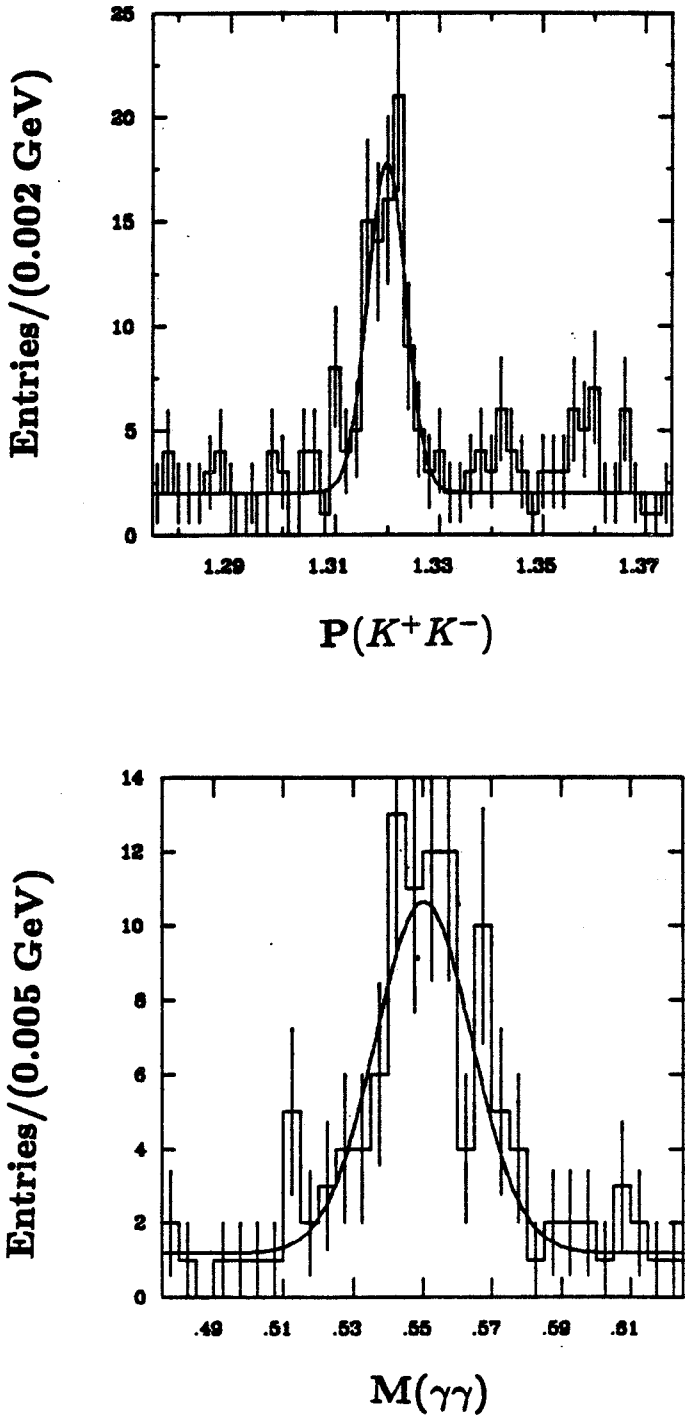

Figure 4.30. Analysis of $\psi \to \phi\eta$. a) The distribution of P(K^+K^-), showing a monochromatic peak and b) the M($\gamma\gamma$) distribution, showing an η signal.

1. If one of the photons $\gamma_2\gamma_3$ from the π^0 decay is soft (say, γ_3), then γ_2 will be energetic and $M(K^+K^-\gamma_2)$ will be at the ι mass.

2. The K^+K^- mass distribution from $\iota \to K^+K^-\pi^0$ peaks near K^+K^- threshold, which is very close to the ϕ mass.

Consequently, cutting around the ϕ does not completely remove these events, although it helps. In the present analysis, however, no $\iota \to \gamma\phi$ signal is observed, and an upper limit is set for this process. If this analysis is repeated in the future with a larger data set, and a small ι signal is observed in γK^+K^-, it must be thoroughly checked that there is an assigned ϕ signal at the correct mass and that the bump in the γK^+K^- mass spectrum is not just due to $\iota \to K^+K^-\pi^0$. (The first member of my examination committee who informs me that he has reached this point will be handsomely rewarded with a bottle of wine.) Most of these events can be removed by imposing a tighter χ^2 cut, which will be discussed below.

The last major background is due to $\psi \to \phi\pi^0\pi^0$, which is dominated by $\psi \to \phi S^*(975)$. The S^* is a narrow (Γ = 33 MeV), poorly understood scalar state. The signal shows up as a peak at 1.184 GeV in the K^+K^- momentum spectrum. (This is the only way to identify this process unless the events are refit to the correct hypothesis, $\psi \to 4\gamma K^+K^-$.) Figure 4.31a is a scatterplot of $P(K^+K^-)$ vs. $M(K^+K^-)$. In addition to a cluster corresponding to $\psi \to \phi\eta$, there is a small cluster near $p = 1.2$ GeV due to $\psi \to \phi S^*$. The ϕS^* events do not produce a peak in the $K^+K^-\gamma_{low}$ mass spectrum, although a few of them contribute to the broad background in the 1–2 GeV mass region.

Analysis Cuts

To analyze the $\iota \to \gamma\phi$ final state the following cuts are made:

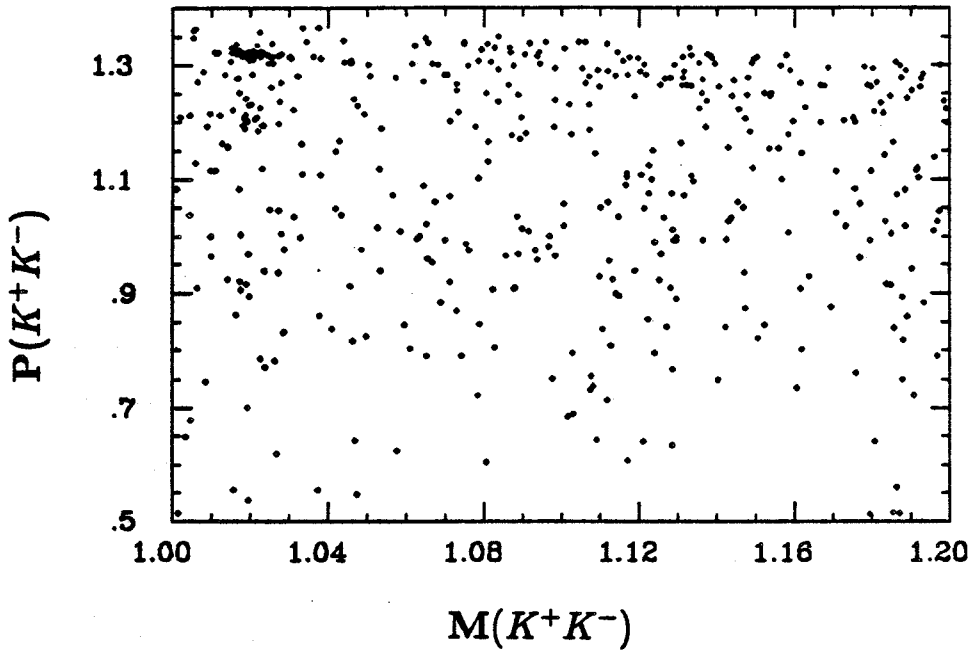

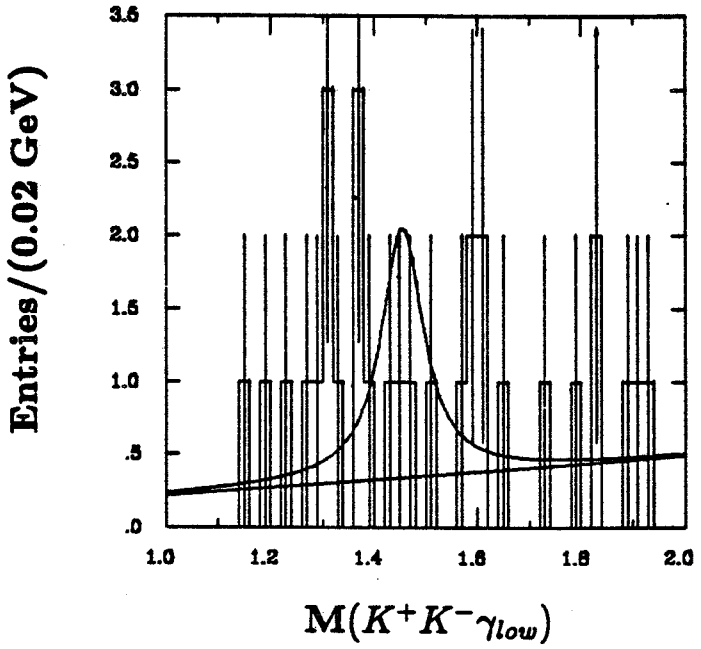

Figure 4.31. $\psi \to \gamma\gamma\phi$ analysis. a) The scatterplot of P(K^+K^-) vs. M(K^+K^-), showing clusters due to $\psi \to \phi\eta$ and $\psi \to \phi S^*$. b) The M($K^+K^-\gamma_{low}$) distribution, with a curve corresponding to the 90% confidence level upper limit for $\iota \to \gamma\phi$.

1. $P(\chi^2) > 0.05$.

2. At least one stereo layer per charged track.

3. $|\cos\theta| \leq 0.75$ for photons.

4. $M(\gamma\gamma) \geq 0.2$ GeV; $M(\gamma\gamma) \notin [0.44 - 0.66]$ GeV.

5. The time-of-flight K-weight for at least one charged track must be greater than 0.05.

No cut was made on the number of shower clusters allowed in an event. Such a cut would be dangerous because there can be additional photons due to K decays.

The final $K^+K^-\gamma_{low}$ mass distribution is shown in Fig. 4.31b. There is no ι signal, so an upper limit is set, using the following procedure. First, the mass region from 1.2-2 GeV is fit to a linear background plus a Gaussian-folded Breit-Wigner with the Mark III values for the ι mass and width. The folded mass resolution is determined with the Monte Carlo to be $\sigma = 8$ MeV. The area under the Breit-Wigner is then increased (allowing the background to vary) until the area under the likelihood function for area is 90% of the total area. The Breit-Wigner curve corresponding to this upper limit is shown in Fig. 4.31b and contains 12.3 events. The detection efficiency is found to be $\epsilon = 0.11$ from the Monte Carlo, which includes the correct angular distributions for all stages of the decay process. A comparison of the Monte Carlo and data χ^2 distributions for $\psi \to \phi\eta$, however, indicates that the Monte Carlo predicts too few events with large values of χ^2. The corrected efficiency, $\epsilon = 0.088$, is 20% lower than that found from the Monte Carlo. Taking into account $B(\phi \to K^+K^-)$ one obtains

$$B(\psi \to \gamma\iota)B(\iota \to \gamma\phi) < 1.6 \times 10^{-4} \qquad 90\% \text{ C.L.}$$

which is roughly comparable to the signal observed in $\gamma\rho^0$. Relative to $\iota \to K\bar{K}\pi$ this limit gives

$$\frac{B(\iota \to \gamma\phi)}{B(\iota \to K\bar{K}\pi)} < 3.1\% \qquad 90\% \text{ C.L.}$$

Although this is not a stringent upper limit, it shows that if the $\gamma\rho^0$ signal is due to the ι, then the quark content of the ι is not predominantly $s\bar{s}$.

4.5 ANALYSIS OF $\psi \to \gamma X;\ X \to \gamma\omega$

The decay sequence $\psi \to \gamma X;\ X \to \gamma\omega;\ \omega \to \pi^+\pi^-\pi^0$ produces four photons and two charged tracks in the final state. The efficiency is therefore not as high as it is for $\psi \to \gamma X;\ X \to \gamma\rho^0$, and one does not expect to be able to set a very stringent upper limit. However, an $\eta' \to \gamma\omega$ signal is observed, as well as two new hadronic decays, $\psi \to \omega\pi^0$ and $\psi \to \omega\eta$.

Event Selection and Fitting

Events with two oppositely charged tracks and at least four shower clusters are kinematically fit (4-C) to the hypothesis $\psi \to 4\gamma\pi^+\pi^-$. Candidate photons are selected with the same criteria as in the $\gamma\gamma\rho^0$ and $\gamma\gamma\phi$ analyses. If there are more than four such candidates, the clusters are ordered according to energy and two fits are done:

$$\psi \to \gamma_1\gamma_2\gamma_3\gamma_4\pi^+\pi^- \quad \text{and} \quad \psi \to \gamma_1\gamma_2\gamma_3\gamma_5\pi^+\pi^-.$$

The fit with the better χ^2 is chosen. Events with $P(\chi^2) < 0.1$ are excluded from further analysis. As before, each charged track is required to pass through at least one stereo layer.

Photon Combinatorics and Observation of an ω signal

The first step in the analysis is to determine which photons come from the sequence $\omega \to \pi^+\pi^-\pi^0;\ \pi^0 \to \gamma\gamma$. In the radiative decay $\psi \to \gamma P;\ P \to \gamma\omega$, where $P = \eta'$ or ι, the photon radiated by the ψ has the highest energy. In the background processes $\psi \to \omega\pi^0$ and $\omega\eta$, the recoiling π^0 or η has very high momentum (1.446 GeV/c or 1.394 GeV/c, respectively). Consequently, the decay of this high momentum π^0 or η nearly always produces the highest energy photon in the event. Thus, the most convenient scheme for organizing the six

Table 4.4. Convention for $\gamma\gamma$ combinations

	A	B
(1)	$\gamma_1\gamma_2$	$\gamma_3\gamma_4$
(2)	$\gamma_1\gamma_3$	$\gamma_2\gamma_4$
(3)	$\gamma_1\gamma_4$	$\gamma_2\gamma_3$

possible photon pairs is as shown in Table 4.4, where γ_1 is the highest energy photon and γ_4 is the lowest. The A combinations always include the highest energy photon, whereas the B combinations are complementary to them and nearly always contain the π^0 that is produced when the ω decays. Figure 4.32 shows the $\pi^+\pi^-\gamma\gamma$ mass distribution for both the A and B combinations. In making the distribution of $M(\pi^+\pi^-\gamma_i\gamma_j)$ it is required that $M(\gamma_i\gamma_j) \leq 0.2$ GeV; that is, because $\omega \to \pi^+\pi^-\pi^0$, consistency with a π^0 is required. There are only 24 ω's in the A combinations, but there are approximately 690 ω's in the B combinations (about 97% of the signal.)

Observation of $\psi \to \omega\eta$ and $\omega\pi^0$

Most of the events in the ω signal are not due to $\psi \to \gamma X$; $X \to \gamma\omega$, but rather are from hadronic ψ decays. This is seen from Fig. 4.33, which shows scatterplots of $M(\gamma_1\gamma_2)$ vs. $M(\pi^+\pi^-\gamma_3\gamma_4)$ and $M(\gamma_1\gamma_3)$ vs. $M(\pi^+\pi^-\gamma_2\gamma_4)$. There is a clear correlation between the ω signal and π^0 and η signals in the recoiling $\gamma\gamma$ combinations. The scatterplot of the other pair of combinations shows a similar correlation.

It is useful to narrow down the event sample by requiring that there be at least one $M(\pi^+\pi^-\gamma\gamma)$ combination consistent with the ω mass:

$$0.675 \leq M(\pi^+\pi^-\gamma_i\gamma_j) \leq 0.891 \quad \text{GeV (any B combination).}$$

The easiest way to remove the hadronic events is to exploit the fact that

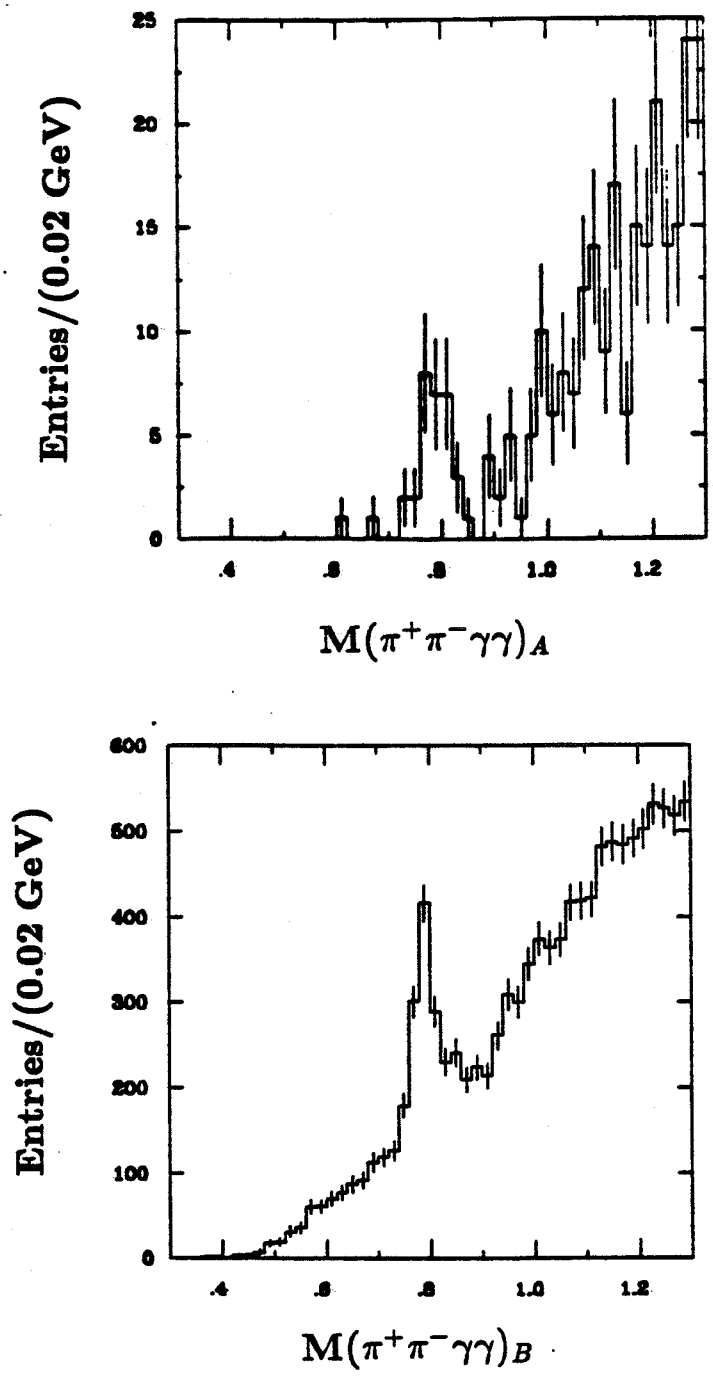

Figure 4.32. Observation of an ω signal. About 97% of the ω events are in the B combinations.

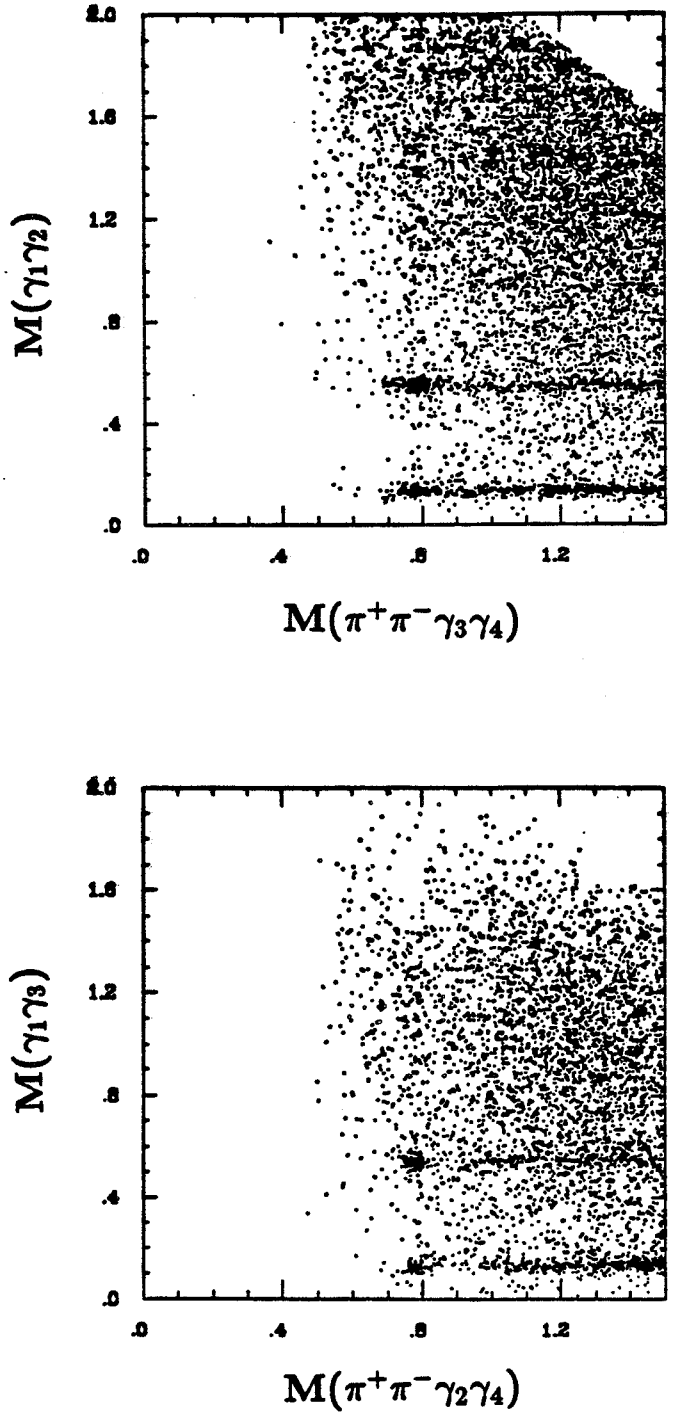

Figure 4.33. Correlation between $M(\gamma\gamma)$ and $M(\pi^+\pi^-\gamma\gamma)$. The clusters are due to the hadronic decays $\psi \to \omega\eta$ and $\psi \to \omega\pi^0$.

these are two-body decays with very high momenta. Figure 4.34 shows the momentum spectrum of the $(\gamma\gamma)_B\pi^+\pi^-$ combinations (which is the same as that for the $(\gamma\gamma)_A$ combinations) and the distribution of $M(\gamma\gamma)_A$. Two clear peaks corresponding to $\psi \rightarrow \omega\eta$ and $\omega\pi^0$ are observed. The number of events is determined by fitting the spectrum to two Gaussian-folded Breit-Wigners plus a linear background. The Breit-Wigner widths are fixed at 2 MeV, reflecting the width of the ω:

$$\delta p \approx \delta\left[E(1+\tfrac{1}{2}(\frac{m}{E})^2\right] \approx \delta E$$

and

$$\delta E = \delta\left[\frac{m_\psi^2 + m_P^2 - m_\omega^2}{2m_\psi}\right] = \frac{-m_\omega}{m_\psi}\delta m_\omega,$$

where m_P is the mass of the recoiling pseudoscalar. These fits yield the mean momenta and the number of events in the two modes

$$P = 1.395 \pm 0.001 \text{ GeV} \quad N(\omega\eta) = 321 \pm 21$$

$$P = 1.444 \pm 0.001 \text{ GeV} \quad N(\omega\pi^0) = 206 \pm 15.$$

Detailed checks have been performed to show that the Monte Carlo correctly models the small fraction of ω's in the B combinations. It has also been verified that the combinatorial background in the momentum spectrum is small and approximately uniformly distributed; it is therefore absorbed by the background term in the fit. The Monte Carlo events were generated using the correct angular distributions, including the effect of the ω spin polarization and the matrix element for ω decay.

One difficulty in obtaining the efficiency for these decay modes is the large fraction of events with low energy photons. It has been determined that the Monte Carlo FAKSHR generator does not correctly model the photon detection efficiency below about 100 MeV. (The EGS program was not installed in the

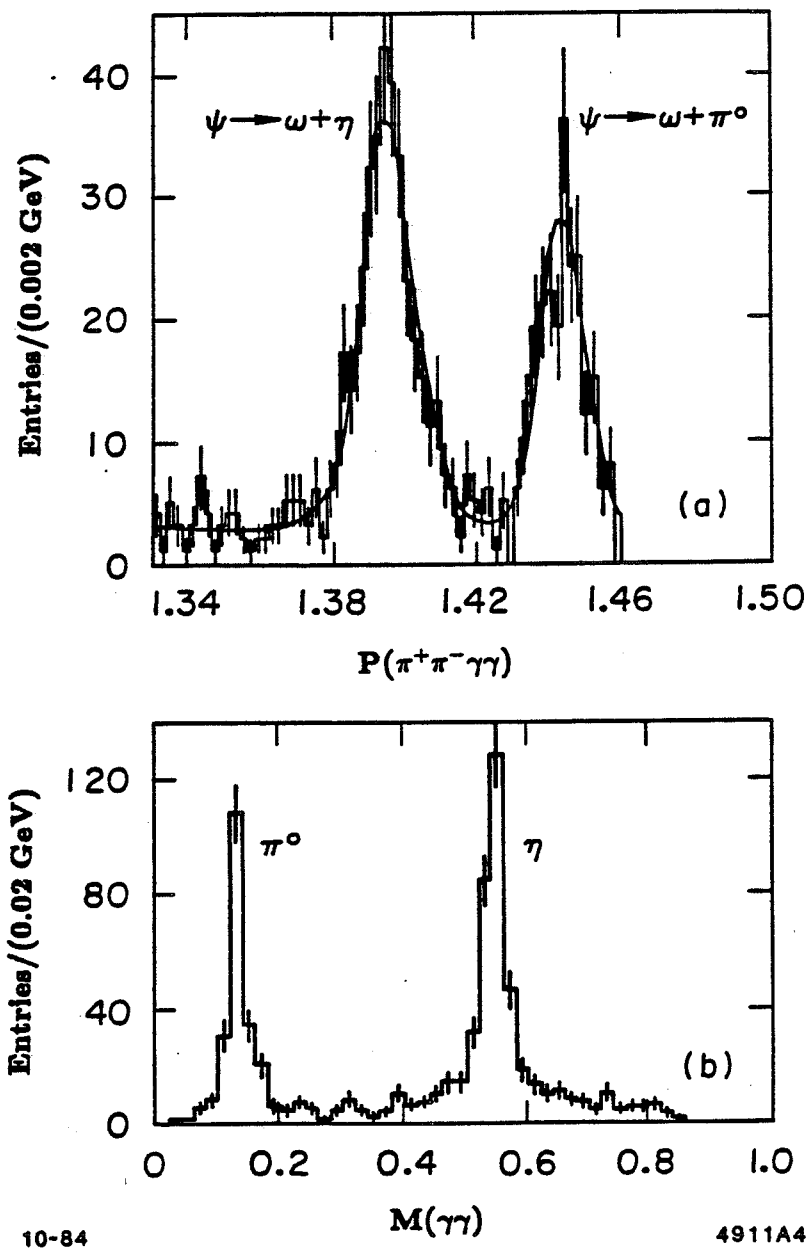

Figure 4.34. Evidence for $\psi \rightarrow \omega\eta$ and $\psi \rightarrow \omega\pi^0$. a) The $P(\pi^+\pi^-\gamma\gamma)_B$ distribution, showing monochromatic peaks for the two-body decays. b) π^0 and η signals in the $M(\gamma\gamma)_A$ combinations.

Mark III Monte Carlo at the time this analysis was performed.) It is therefore necessary to exclude events with photon energies below 100 MeV, both in the data and in the Monte Carlo, for the purpose of obtaining the branching ratio. The number of events in each mode after this cut is

$$N(\omega\eta) = 158 \pm 13$$

$$N(\omega\pi^0) = 108 \pm 9.$$

The efficiencies are found to be

$$\epsilon(\omega\eta) = (13.0 \pm 2.0)\%$$

$$\epsilon(\omega\pi^0) = (10.0 \pm 1.5)\%$$

where the uncertainties, as usual, are estimated by varying different cuts in the Monte Carlo. The measured branching fractions are

$$B(\psi \to \omega\eta) = (1.9 \pm 0.2 \pm 0.3) \times 10^{-3}$$

$$B(\psi \to \omega\pi^0) = (0.67 \pm 0.06 \pm 0.11) \times 10^{-3}$$

It is quite difficult to check whether the Monte Carlo adequately models the tail of the χ^2 distribution in the channel. In the following section it is shown that the branching ratio for $\psi \to \gamma\eta'$; $\eta' \to \gamma\omega$ agrees with expectation within the fairly large statistical errors. This provides some check of the overall normalization of the analysis procedure for the $4\gamma\pi^+\pi^-$ final state.

Analysis Cuts for the Radiative Channel

To study the process $\psi \to \gamma + X$; $X \to \gamma + \omega$ it is useful to remove $\omega\eta$ and $\omega\pi^0$ events. This can be accomplished by requiring $P(\pi^+\pi^-\gamma_i\gamma_j) < 1.36$ GeV for each B combination. With the exception of one addition to be discussed below, the cuts used in this analysis are:

1. $P(\chi^2) > 0.1$.

2. $E(\gamma_i) > 0.1$ GeV

3. $p(\pi^+\pi^-\gamma_i\gamma_j) < 1.36$ GeV (each B combination).

4. $M(\pi^+\pi^-\gamma_i\gamma_j)$ in the range 0.675-0.891 GeV (for at least one B combination).

5. $M(\gamma_i\gamma_j) < 0.2$ GeV (for at least one B combination).

6. Time-of-flight K weight $\leq \pi$ weight for each charged track.

In the radiative channel the mass of the recoil system is $M(\pi^+\pi^-\gamma_2\gamma_3\gamma_4)$, because γ_1 is always the photon radiated by the ψ in η' and ι decays. The distribution of this recoil mass, with the cuts listed above, is shown in Fig. 4.35a. A small η' signal is present, as well as a large number of events in the 1-2 GeV region. Most of these are easily shown to be due to background by selecting events that have exactly four shower clusters (not counting those near charged tracks or with only one layer). The resulting recoil mass spectrum is shown in Fig. 4.35b and is very much cleaner. There is some loss of efficiency from the four photon cut; its efficiency is estimated to be $(74 \pm 10)\%$ by comparing the number of η' events before and after the cut. Using the number of η' events ($= 17$), the *Review of Particle Properties* values for $\eta' \to \gamma\omega$ and $\omega \to \pi^+\pi^-\pi^0$, the efficiency $\epsilon = (0.74)(0.086)$, one obtains

$$B(\psi \to \gamma\eta') = [5.9 \pm 1.4(stat) \pm 1.6(sys)] \times 10^{-3},$$

which is consistent within the statistical error with the measurement in the $\eta' \to \gamma\rho^0$ mode. Although the above number is not useful as a measurement of $\psi \to \gamma\eta'$, it does serve as a calibration check for a somewhat difficult analysis.

To obtain an upper limit for $\psi \to \gamma\iota$; $\iota \to \gamma\omega$, the mass region $1.05 \leq M(\pi^+\pi^-\gamma_2\gamma_3\gamma_4) \leq 1.8$ GeV is fit to a flat background plus a Breit-Wigner.

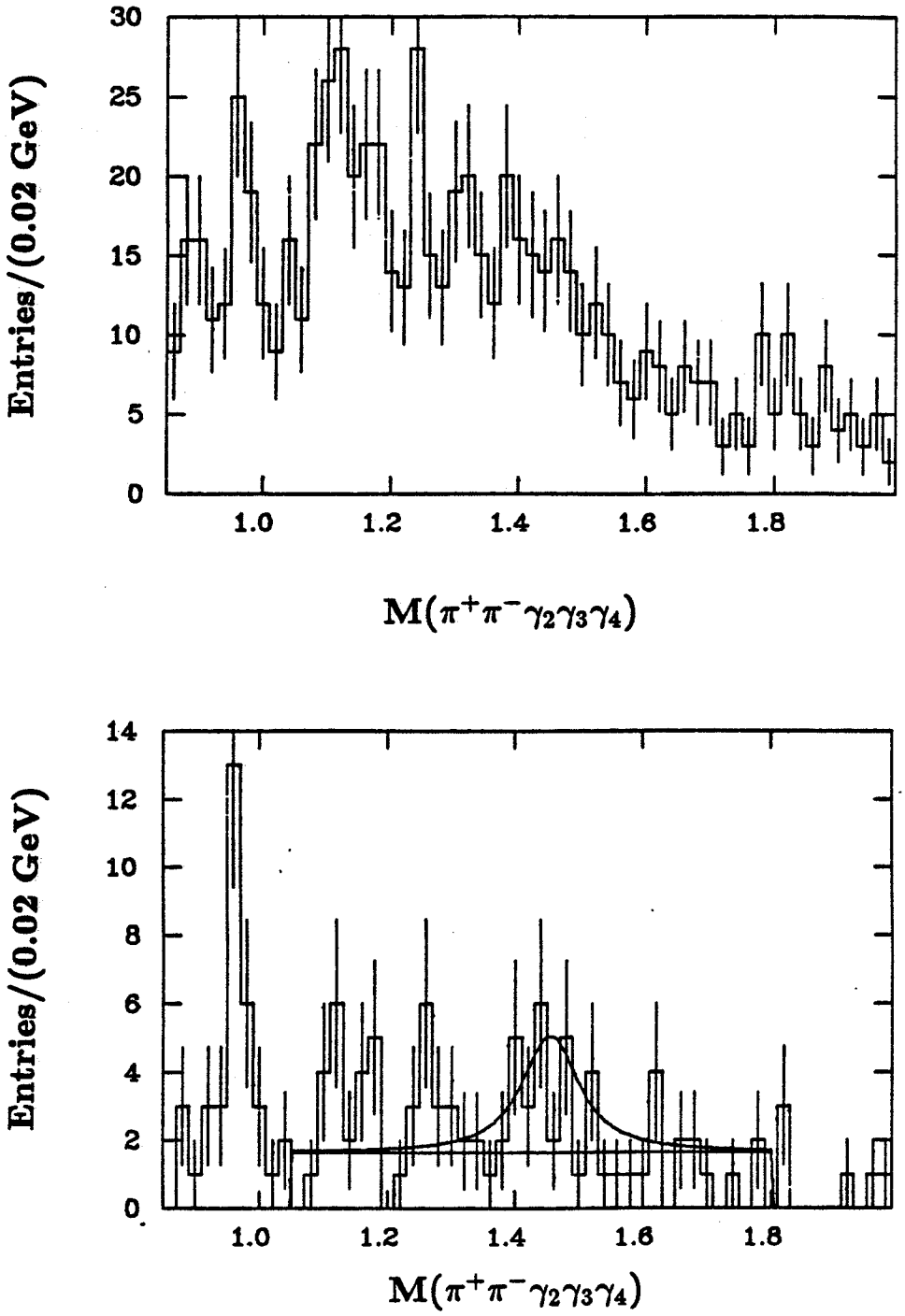

Figure 4.35. Study of $\psi \to \gamma(\gamma\omega)$. a) Distribution of $M(\pi^+\pi^-\gamma_1\gamma_2\gamma_3)$ without four shower cluster requirement. b) The distribution after requiring four shower clusters. A small η' signal is evident. The curve represents the 90% C.L. upper limit for $\psi \to \gamma\iota$, $\iota \to \gamma\rho^0$.

The Mark III values for the ι mass and width (M = 1.455 GeV, Γ = 0.095 GeV) are used. A Gaussian mass resolution of σ = 16 MeV, obtained from the Monte Carlo, is folded with the Breit-Wigner. Figure 4.35b shows the curve corresponding to the 90% C.L. upper limit. The number of events under the Breit-Wigner is 26; with an efficiency of 7.1% and the factor $B(\omega \to \pi^+\pi^-\pi^0)$ one obtains

$$B(\psi \to \gamma\iota)B(\iota \to \gamma\omega) < 2.3 \times 10^{-4} \quad \text{at 90\% C.L.}$$

or,

$$\frac{B(\iota \to \gamma\omega)}{B(\iota \to K\bar{K}\pi)} < 0.044 \quad \text{at 90\% C.L.}$$

Chapter 5. Limits on Other ι Decay Modes

The ι has sufficient mass to decay into several other multi-meson final states, including $\eta\pi\pi$, 4π, and $K\bar{K}\pi\pi$. Decays into an odd number of pions are forbidden by G-parity if the ι is an isosinglet, which is strongly implied by its large production in radiative ψ decay. The $\eta\pi\pi$ mode is of particular interest because a large branching fraction is expected from $SU(3)$ symmetry. If the ι decays via $\delta\pi$, as indicated by the Crystal Ball results, and one assumes that $SU(3)$ relates the $\eta\pi$ and $K\bar{K}$ couplings of the δ, then (55)

$$\frac{\Gamma(\iota \to \eta\pi\pi)}{\Gamma(\iota \to K\bar{K}\pi)} = \frac{4}{3}.$$

The very limited data on the δ indicate that

$$\frac{\Gamma(\delta \to \eta\pi)}{\Gamma(\delta \to K\bar{K})} = 0.25 - 1.3.$$

Using the Crystal Ball result

$$\frac{B(\iota \to \delta\pi)B(\delta \to K\bar{K})}{B(\iota \to K\bar{K}\pi)} > 0.75 \qquad 90\% \text{ C.L.}$$

and the Mark III measurement

$$B(\psi \to \gamma\iota)B(\iota \to K\bar{K}\pi) = 5.0 \times 10^{-3}$$

one can predict

$$B(\psi \to \gamma\iota)B(\iota \to \delta\pi)B(\delta \to \eta\pi) = (0.90 - 4.9) \times 10^{-3},$$

or

$$\frac{B(\iota \to \delta\pi)B(\delta \to \eta\pi)}{B(\iota \to K\bar{K}\pi)} = 0.19 - 0.98.$$

On the other hand, if one ignores the δ and rather assumes that $SU(3)$ governs the four-point amplitude for the ι coupling to three pseudoscalars, then the ratio is

$$\frac{\Gamma(\iota \to \eta\pi\pi)}{\Gamma(\iota \to K\bar{K}\pi)} = \frac{1}{3}.$$

Palmer and Pinsky (55) argue that $SU(3)$ – based predictions are unreliable, and that in the context of their pole model

$$\frac{\Gamma(\iota \to \eta\pi\pi)}{\Gamma(\iota \to K\bar{K}\pi)} = 0.09.$$

In addition, they find

$$\frac{\Gamma(\iota \to \rho\pi\pi)}{\Gamma(\iota \to K\bar{K}\pi)} = 1.5.$$

Unfortunately, no ι signals have been observed by Mark III in $\eta\pi\pi$, 4π, or $K\bar{K}\pi\pi$, with the (significant) possible exception of $\iota \to \rho\rho$. The results in the $\rho\rho$ channel are difficult to interpret because the $\rho\rho$ threshold is ill defined and near the ι mass.

The $\eta\pi\pi$ Final State

A detailed discussion of Mark III results on the process $\psi \to \gamma\eta\pi\pi$ can be found in the references (63). The analysis uses an initial 4-C fit to the hypothesis $\psi \to 3\gamma\pi^+\pi^-$ followed by a 5-C fit to the hypothesis $\psi \to \gamma\eta\pi^+\pi^-$. A broad structure, which could well consist of two or more resonances, is observed in the 1.2-2.0 GeV mass region. Because it is difficult to untangle this structure, a very conservative approach to obtaining the ι upper limit was used in which a Breit-Wigner with the ι mass and width ($M = 1.460$ GeV, $\Gamma = 0.100$ GeV) was superimposed on the mass spectrum (Fig. 5.1a). The upper limit derived from this procedure is

$$B(\psi \to \gamma\iota)B(\iota \to \eta\pi^+\pi^-) < 8.8 \times 10^{-4} \qquad 90\% \text{ C.L.}$$

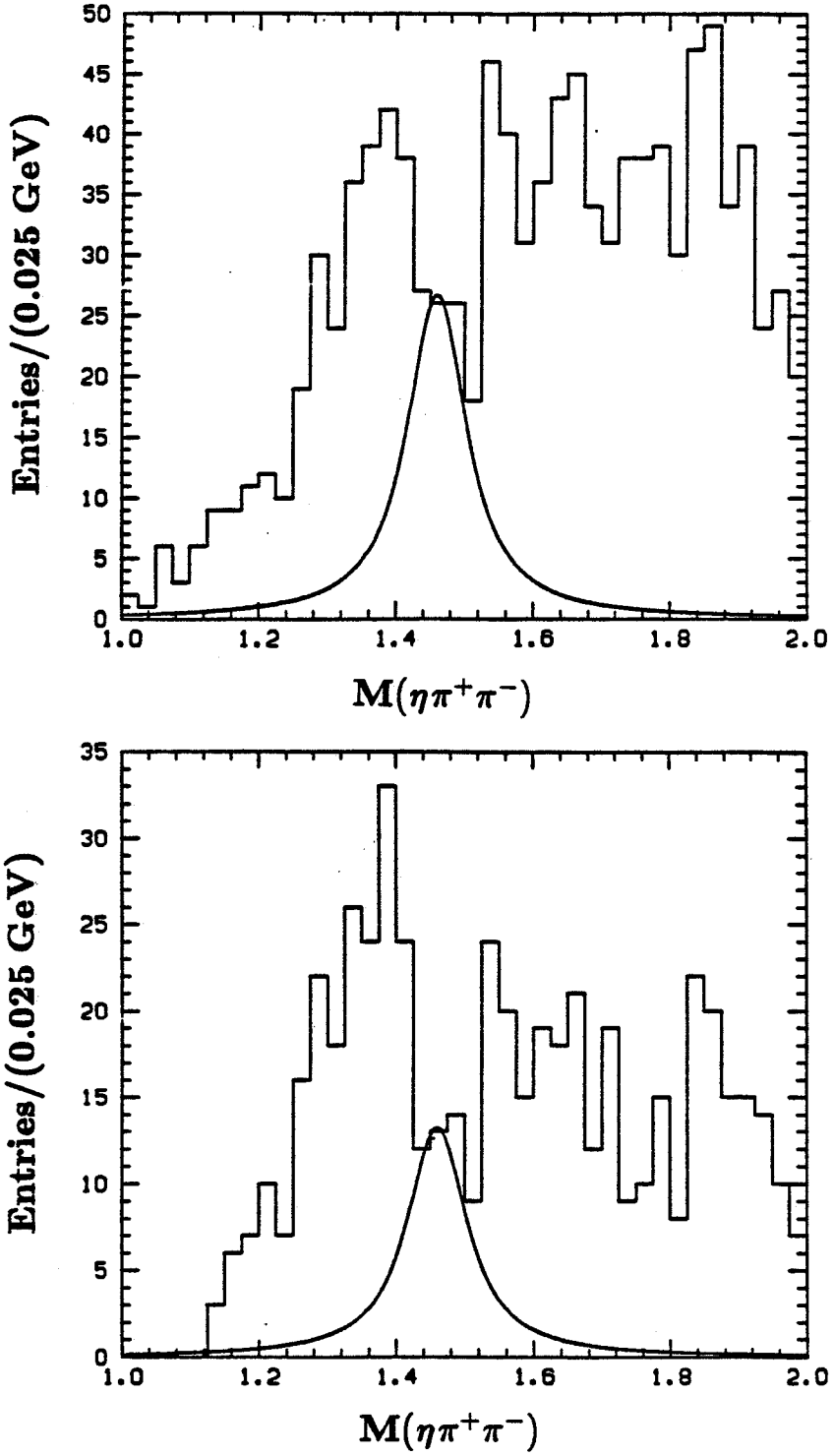

Figure 5.1. Analysis of the $\eta\pi^+\pi^-$ channel. The $\eta\pi^+\pi^-$ mass spectrum, with an ι Breit-Wigner superimposed. b) The $\eta\pi^+\pi^-$ mass spectrum after requiring an $\eta\pi$ mass consistent with the $\delta(980)$: $0.93 < M(\eta\pi^{\pm}) < 1.03$ GeV.

This implies

$$\frac{B(\iota \to \eta\pi\pi)}{B(\iota \to K\bar{K}\pi)} < 0.26$$

where the unobserved $\eta\pi^0\pi^0$ mode has been taken into account.

The additional requirement that either the $\eta\pi^+$ or $\eta\pi^-$ mass be consistent with the δ ($0.93 < M(\eta\pi) < 1.03$ GeV), yields the $\eta\pi\pi$ mass distribution shown in Fig. 5.1b. Using the same procedure to determine the upper limit, one obtains

$$B(\psi \to \gamma\iota)B(\iota \to \delta^{\pm}\pi^{\mp})B(\delta^{\pm} \to \eta\pi^{\pm}) < 4.6 \times 10^{-4} \qquad 90\% \text{ C.L.},$$

or

$$\frac{B(\iota \to \delta\pi)B(\delta \to \eta\pi)}{B(\iota \to K\bar{K}\pi)} < 0.14,$$

which contradicts the prediction based on the Crystal Ball measurement. The discrepancy could be due to the poor knowledge of $B(\delta \to \eta\pi)/B(\delta \to K\bar{K})$. However, the extremely conservative procedure used to obtain the ι upper limits indicates that one should be careful about invoking the δ to explain the $K\bar{K}$ threshold enhancement in $\iota \to K\bar{K}\pi$.

The $K\bar{K}\pi\pi$ Final State

The process $\psi \to \gamma K^+K^-\pi^+\pi^-$ will be discussed in detail elsewhere (64). The event selection procedure is based on a 4-C fit, although time-of-flight information is used to identify K's and π's. The resulting $K^+K^-\pi^+\pi^-$ mass spectrum is shown in Fig. 5.2. There are virtually no events around 1.4 GeV, and only one up to 1.6 GeV. Using the detection efficiency of 5% one obtains

$$B(\psi \to \gamma\iota)B(\iota \to K\bar{K}\pi\pi) < 2.2 \times 10^{-5},$$

a remarkably stringent limit.

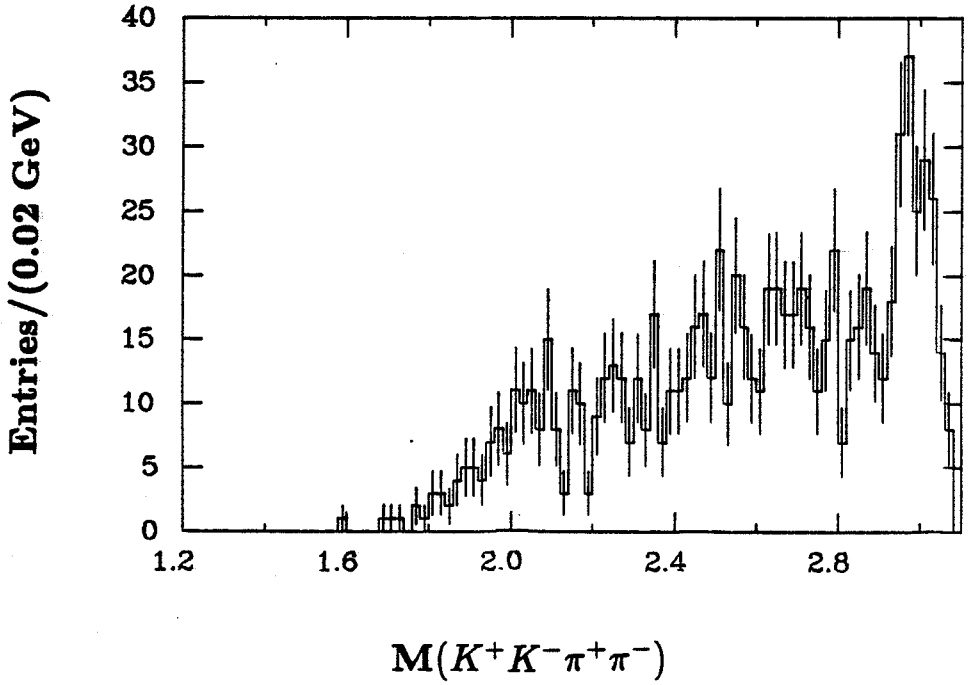

Figure 5.2. The $K^+K^-\pi^+\pi^-$ mass spectrum from the decay $\psi \rightarrow \gamma K^+K^-\pi^+\pi^-$. No ι signal is observed.

The 4π Final State

An extensive analysis of the process $\psi \to \gamma 4\pi$ has been performed (65) using the two isospin related channels, $\psi \to \gamma\pi^+\pi^-\pi^+\pi^-$ and $\psi \to \gamma\pi^+\pi^-\pi^0\pi^0$. The 4π mass distributions for these channels are shown in Fig. 5.3. Although there is a large, broad background from $\psi \to 5\pi$, clear structure is evident in the 1.4−1.9 GeV mass region. The separate partial wave contributions are extracted from a maximum likelihood fit that includes

1. $X \to \rho\rho$ with $J^P(X) = 0^+, 0^-, 1^+, 1^-, 2^+, 2^-$, and isotropic;

2. $X \to \rho\pi\pi$ with isotropic angular distributions;

3. $X \to 4\pi$ with isotropic angular distributions;

4. $X \to A_2\pi$.

It is nontrivial to separate the contributions from $\rho\rho$, $\rho\pi\pi$, and 4π because the large ρ width permits a π to participate in two $\pi\pi$ mass combinations consistent with the ρ mass. The amplitude must therefore be correctly symmetrized under π exchange.

The main result of this analysis is evidence for a pseudoscalar signal in the $\rho\rho$ channel. The signal is very broad, extending from about 1.4 to 1.9 GeV, and could well consist of more than one resonance. It is possible that the lower part of this structure is due to ι production. In fact, an $\iota \to \rho\rho$ branching fraction comparable to that of $\iota \to K\bar{K}\pi$ cannot be excluded. Such a result is expected (55) if $\iota \to \gamma\rho^0$ is large; it would also make ι decays more flavor symmetric. Taking events in the $\rho\rho$ $J^P = 0^-$ channel from $1.5 - 1.9$ GeV, one obtains

$$B(\psi \to \gamma X(0^-))B(X \to \rho\rho) = (2.3 \pm 0.9) \times 10^{-3}.$$

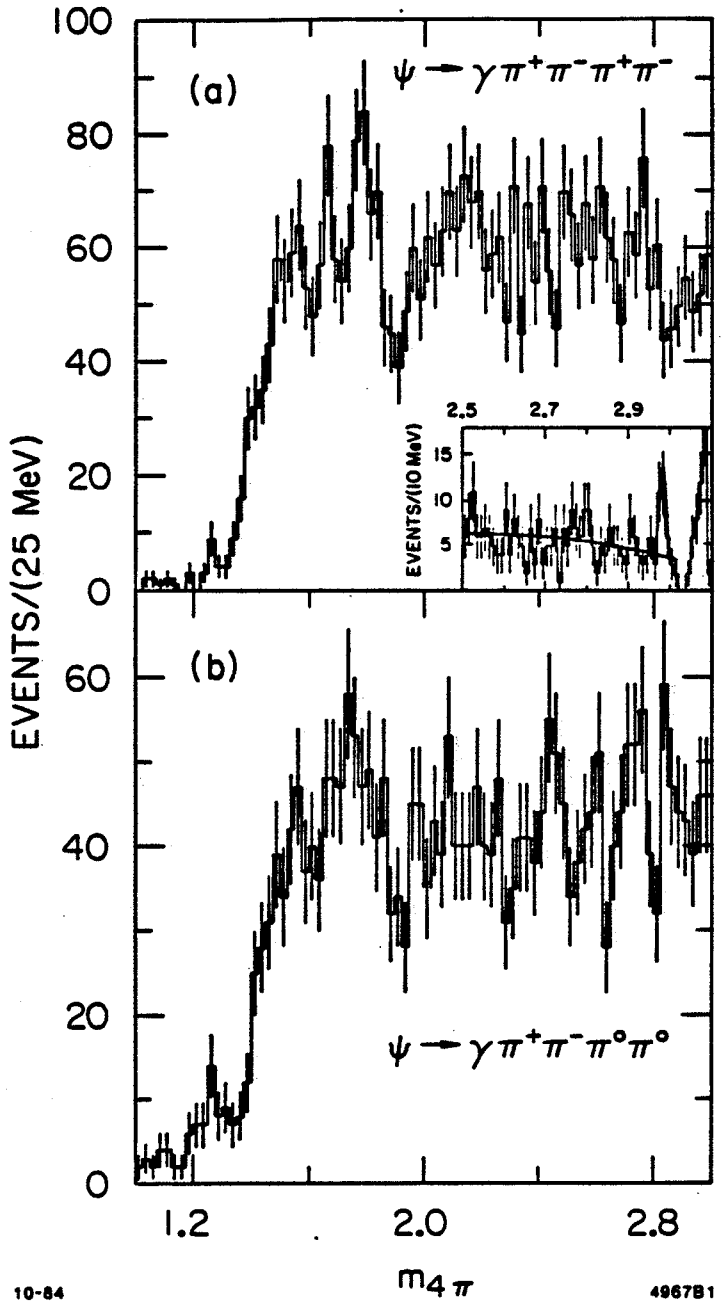

Figure 5.3. Distribution of M(4π) from $\psi \to \gamma 4\pi$.

From the multichannel likelihood fits one can obtain an upper limit for $\iota \to \rho\pi\pi$ ($\rho\rho$ and non-resonant 4π excluded):

$$B(\psi \to \gamma\iota)B(\iota \to \rho\pi\pi) < 9 \times 10^{-5} \qquad 90\% \text{ C.L.}$$

This upper limit may be somewhat sensitive to which other resonant channels are included in the fits to the $\gamma 4\pi$ events.

Chapter 6. Conclusions

The production, decay, and quantum numbers of the ι have been studied in radiative ψ decay. Using the processes $\psi \to \gamma\iota$; $\iota \to K^+K^-\pi^0$ and $\psi \to \gamma\iota$, $\iota \to K^0_S K^\pm\pi^\mp$, the spin-parity of the ι was investigated. Together, these channels contain about 760 ι's in the Mark III data. To avoid assumptions concerning the two-body decays – in particular, those involving the very poorly understood $\delta(890)$ – the three-body helicity formalism was used. This formalism allows one to predict the distribution of the ι production angles and the angles describing the orientation of the normal to the ι decay plane.

The maximum likelihood fits performed in these two channels indicate that $J^P = 0^-$ is strongly preferred over both $J^P = 1^+$ and $J^P = 1^-$. The source of the discriminating power of the three-body method is easy to identify, and visual examination of the relevant angular distributions provides clear support for the 0^- assignment. The use of this technique was made possible by the high signal-to-background ratio ($\sim 10:1$) in the ι mass region.

The ι mass and width obtained in the $K^0_S K^\pm\pi^\mp$ channel were found to be:

$$M(\iota) = (1.456 \pm 0.005 \pm 0.006)\ \text{GeV}$$
$$\Gamma(\iota) = (0.095 \pm 0.010 \pm 0.015)\ \text{GeV}.$$

These are consistent with the parameters obtained from the $K^+K^-\pi^0$ channel:

$$M(\iota) = (1.461 \pm 0.005 \pm 0.005)\ \text{GeV}$$
$$\Gamma(\iota) = (0.101 \pm 0.010 \pm 0.010)\ \text{GeV}.$$

It is possible that the difference in mass with respect to the Mark II and Crystal Ball experiments is due to the much less stringent $K\bar{K}$ mass cut used in the Mark III analysis. By making the $K\bar{K}$ mass cut identical to that made in the

Crystal Ball analysis, a downward shift in the central $K\bar{K}\pi$ mass was observed. However, there appears to be no clear justification for such a cut.

The very large radiative branching fraction of the ψ to the ι remains a source of mystery. Using the $K^0_S K^{\pm}\pi^{\mp}$ and $K^+K^-\pi^0$ channels, the following measurements were obtained:

$$B(\psi \to \gamma\iota)B(\iota \to K\bar{K}\pi) = (5.0 \pm 0.3 \pm 0.7) \times 10^{-3} \quad (K^0_S K^{\pm}\pi^{\mp})$$
$$B(\psi \to \gamma\iota)B(\iota \to K\bar{K}\pi) = (4.9 \pm 0.2 \pm 0.8) \times 10^{-3} \quad (K^+K^-\pi^0),$$

where isospin zero has been assumed. The good agreement shows that the relative sizes of the individual $K\bar{K}\pi$ branching fractions are consistent with the isoscalar predictions.

However, the Mark III value for $B(\psi \to \gamma\eta')$,

$$B(\psi \to \gamma\eta') = (4.7 \pm 0.2 \pm 0.7) \times 10^{-3},$$

which was obtained using $\eta' \to \gamma\rho^0$, is quite comparable. The branching fraction for $\psi \to \gamma\eta$ was measured to be

$$B(\psi \to \gamma\eta) = (9.1 \pm 2.2 \pm 1.6) \times 10^{-4},$$

using $\eta \to \gamma\pi^+\pi^-$, which implies

$$\frac{B(\psi \to \gamma\eta')}{B(\psi \to \gamma\eta)} = 5.2 \pm 1.3 \pm 0.3.$$

By studying the regions of the $K\bar{K}\pi$ Dalitz plot outside the area where $K^*\bar{K}$ and $\delta\pi$ would overlap, an upper limit on $\iota \to K^*\bar{K} + c.c.$ was obtained. The procedure does not depend on any description of the δ. The value is

$$\frac{B(\iota \to K^*\bar{K} + c.c.)}{B(\iota \to K\bar{K}\pi)} < 0.35 \qquad 90\% \text{ C.L.}$$

This measurement contrasts with that obtained for the $E(1420)$ in hadronic production experiments. The $E(1420)$ appears to decay predominantly, perhaps entirely, into $K^*\bar{K}$.

The pseudoscalar assignment for the ι implies that the only conventional $q\bar{q}$ assignment for this state is a radial excitation. The radially-excited pseudoscalar nonet is not well understood. The $\eta(1275)$ is a possible isoscalar candidate for this nonet, and the ι could be the other isoscalar member. Theoretical arguments indicate that the production of a radially-excited pseudoscalar at the rate observed for the ι is unexpected. However, these arguments are semi-quantitative at best; the only way to definitively settle this question is to find all members of the radially excited pseudoscalar nonet. An issue thought to have been settled that has now resurfaced is the spin-parity of the $E(1420)$. Two high statistics experiments have obtained contradictory results: $J^P = 0^-$ and $J^P = 1^+$. This inconsistency underscores the extreme difficulty of obtaining reliable spin-parity measurements where backgrounds are present.

The question of whether the ι decays into $\delta\pi$ is a very difficult one. Certainly the $K\bar{K}$ mass distribution peaks near threshold, but the very conservatively set upper limit

$$B(\psi \to \gamma\iota)B(\iota \to \delta^{\pm}\pi)B(\delta \to \eta\pi^{\pm}) < 4.6 \times 10^{-4} \qquad 90\% \text{ C.L.}$$

is inconsistent with the prediction based on the Crystal Ball measurement. Either the ι does not decay into $\delta\pi$, or $B(\delta \to \eta\pi)/B(\delta \to K\bar{K})$ is wrong, or $\iota \to \delta\pi \to \eta\pi\pi$ is suppressed for some reason, such as interference with $\iota \to E\eta$.

Upper limits for other channels accessible to the ι have been obtained. These

are:

$$B(\psi \to \gamma\iota)B(\iota \to K\bar{K}\pi\pi) < 2.2 \times 10^{-5} \quad 90\% \text{ C.L.}$$

$$B(\pi \to \gamma\iota)B(\iota \to \rho\pi\pi) < 9.0 \times 10^{-5} \quad 90\% \text{ C.L.}$$

A substantial part of the signal observed in the $\rho\rho$ 0^- channel could be the ι, but the high $\rho\rho$ threshold makes this difficult to establish. A branching fraction comparable to that for $\iota \to K\bar{K}\pi$ is not excluded.

To probe the quark content of the ι, the double radiative decays $\psi \to \gamma X$, $X \to \gamma +$ Vector were studied. An intriguing structure is observed in the $\gamma(\gamma\rho^0)$ channel with Breit-Wigner parameters

$$M(X) = (1.420 \pm 0.015 \pm 0.020) \text{ GeV}$$

$$\Gamma(X) = (0.133 \pm 0.055 \pm 0.030) \text{ GeV}$$

and product branching fraction

$$B(\psi \to \gamma + X)B(X \to \gamma\rho^0) = (1.0 \pm 0.2 \pm 0.2) \times 10^{-4}.$$

The measured angular distributions are consistent with pseudoscalar predictions. In particular, the distribution of the polar angle of the π in the ρ^0 rest frame is consistent with $\sin^2\theta$. Although both the Crystal Ball and DM2 experiments appear to confirm the observation of such a signal, the low value for the mass indicates that one should be cautious about associating the signal with the ι. It should be noted that the mass scale in this channel is verified to better than 1 MeV with the η' signal ($\sim$ 1000 events).

Investigation of the $\gamma(\gamma\omega)$ and $\gamma(\gamma\phi)$ final states revealed no structure in the 1.4 GeV region, although $\eta' \to \gamma\omega$ was observed at the expected rate. The following upper limits were obtained using the ι Breit-Wigner parameters from the $K\bar{K}\pi$ channels

$$B(\psi \to \gamma\iota)B(\iota \to \gamma\phi) < 1.6 \times 10^{-4} \quad 90\% \text{ C.L.}$$

$$B(\psi \to \gamma\iota)B(\iota \to \gamma\omega) < 2.3 \times 10^{-4} \quad 90\% \text{ C.L.}$$

Finally, several hadronic ψ decays were studied. The results are

$$B(\psi \to \phi\eta) = (0.70 \pm 0.09 \pm 0.09) \times 10^{-3}$$

$$B(\psi \to \omega\eta) = (1.9 \pm 0.2 \pm 0.3) \times 10^{-3}$$

$$B(\psi \to \omega\pi^0) = (0.67 \pm 0.06 \pm 0.11) \times 10^{-3}.$$

The isospin-violating decay $\psi \to \rho^0\eta$ was observed. The ρ^0 width was found to be too small, an effect attributed to interference with $\psi \to \omega\eta$.

If it definitely established that $\iota \to \gamma\rho^0$ is on the order of 1 MeV, then a significant $q\bar{q}$ component must be present in the ι wave function. According to the pseudoscalar mixing models, this would be a natural result of the strong mixing among the isoscalar mesons and a glueball. The η' would then be primarily $q\bar{q}$ with some gluonic component. An interesting test would be the measurement of $\psi \to \omega\iota$ relative to $\psi \to \omega\eta'$. Because the quarks in the two mesons are correlated by the production process–and the quark content of the ω is known– these decays would provide a means of probing the relative light-quark content of the ι and the η'. With a data sample of 10^7 ψ's, such a measurement should be possible.

Clear proof that a large $\iota \to \rho\rho$ signal is present would be another indication that the ι is not just a radially excited pseudoscalar. The ι production in radiative ψ decay would then be comparable to that of the η_c and much larger than that of any other state produced by the annihilation diagram.

Probably the most difficult approach to establishing the existence of glueballs is to identify two other light pseudoscalar mesons. If that goal were achieved, however, the ι would be excluded from the radially-excited nonet and would almost certainly be identified as a glueball.

Appendix A. The Three-Body Helicity Formalism

A.1 INTRODUCTION

This appendix describes the extension of the helicity formalism from two-body to three-body decays. The formalism was invented by Berman and Jacob (66), and the presentation here is intended to be a detailed elaboration, accessible to experimentalists, of the original paper. A basic knowledge of the two-body helicity formalism is assumed, although the main ideas should be clear without such knowledge. Another exposition of the three-body helicity formalism can be found in Chung (67). The three-body helicity formalism is useful because in the decay $a \rightarrow 1 + 2 + 3$, it is not always clear whether there are intermediate two-body states. For example, in the process $\psi \rightarrow \gamma\iota(1440)$, $\iota(1440) \rightarrow K\bar{K}\pi$, the $K\bar{K}$ mass spectrum peaks near threshold, suggesting $\iota \rightarrow \delta(980)\pi$. However, the $K\pi$ mass distributions overlap in the $K^*(890)$ region, so that one cannot easily rule out a K^*K component. Another difficulty is that the $\delta(890)$ is a very poorly understood state, and in fact may not even be a resonance. Although $\delta \rightarrow \eta\pi$ is observed, there appears to be little $\iota(1440) \rightarrow \eta\pi\pi$, leading one to question whether the $\iota(1440)$ does decay into $\delta\pi$.

It is therefore desirable to use a method that does not require knowledge of the intermediate two-body decays and uses only the properties of the entire three-body system. The first step is to construct three-particle CM states with definite total angular momentum j, projection m, and helicities λ_1, λ_2, λ_3. These states allow one to conveniently apply conservation of angular momentum to the decay process. In the construction of these states, it will be

evident that there is an additional rotationally invariant quantity: the angular momentum projection along the axis normal to the CM decay plane. It will then be possible to calculate the angular distribution of the normal to the CM decay plane, relative to the momentum direction of the decaying particle. The angular distribution is most conveniently expressed using the density matrix of the decaying particle. Finally, the consequences of parity conservation will be derived, and the angular distribution for $X(J^P = 1^{\pm})$ decaying into three pseudoscalars will be calculated.

A.2 CONSTRUCTION OF THREE-PARTICLE CM STATES

We will analyze the decay $\mathbf{a} \rightarrow 1 + 2 + 3$ in the rest frame of $\mathbf{a}$. Then

$$\begin{aligned} m_{\mathbf{a}} &= \omega_1 + \omega_2 + \omega_3 \\ 0 &= \vec{p}_1 + \vec{p}_2 + \vec{p}_3 \end{aligned} \tag{A1}$$

where ω_i is the energy of the i^{th} particle. The momentum conservation equation implies that the momentum vectors lie in a plane – the decay plane – and form a triangle (Fig. A.1a).

In the three particle rest frame, five variables are required to completely specify the kinematics of the state. (With known masses, there are nine momentum components, but there are four constraints from energy and momentum conservation.) These five variables can be taken to be any two energies (the position on the Dalitz plot) and the three Euler angles α, β, γ describing the orientation of the decay plane with respect to a fixed coordinate system.

The choice of the fixed coordinate system is usually based on physical considerations related to the production of the decaying particle. For example,

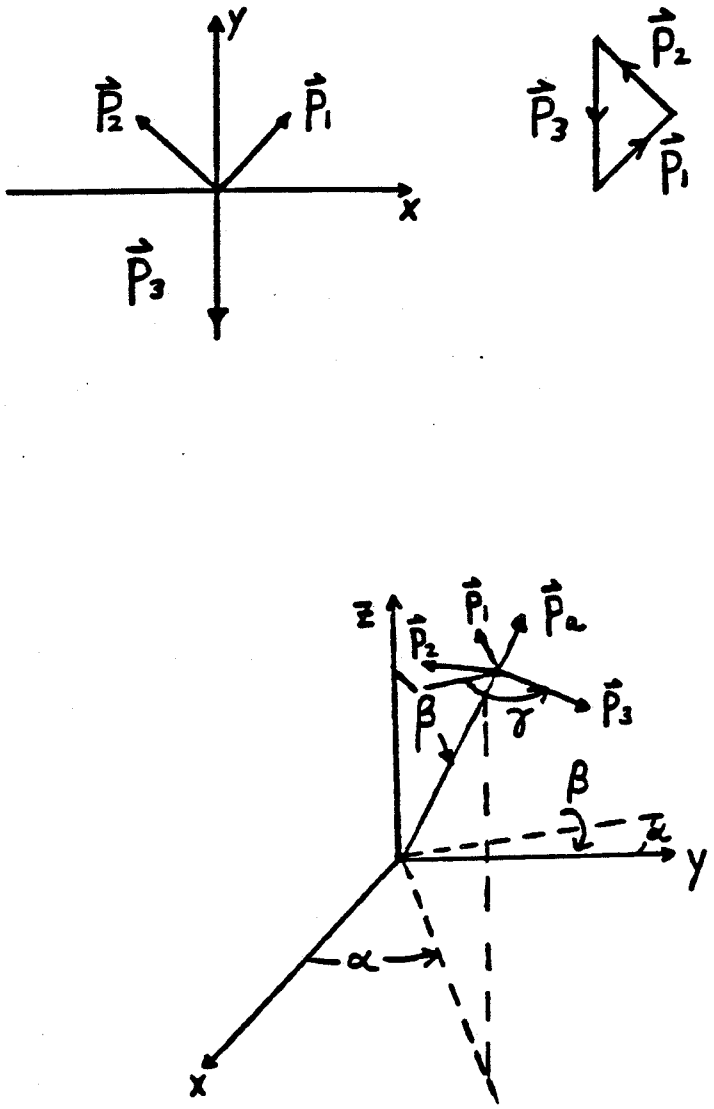

Figure A.1. Three-body decay. a) In the decay rest frame, the three momentum vectors form a plane. The reference configuration has $\alpha = \beta = \gamma = 0$. b) Euler angles specifying the decay plane orientation.

if a was produced in a previous decay with momentum $\vec{p}_a$, the z-axis in the rest frame of a is chosen to be aligned with $\vec{p}_a$. The angular momentum projection along z is then identical to the helicity λ_a. The definition of the x-axis in the a rest frame depends on the phase convention used to describe the decay that produced a. If a was produced by a two-body decay, and if the phase convention is that of Jacob and Wick (68) with the third Euler angle $\gamma = -\phi$, then the x-axis is such that the production plane of a is at the same azimuthal angle in the a rest frame as in the lab frame.

To refer the three particle states to the fixed coordinate system, we pick a reference state that by definition will have $\alpha = \beta = \gamma = 0$. A convenient choice for this state is one that lies in the x-y plane and that has the momentum of one of the particles, say $\vec{p}_3$, aligned with the –y axis (Fig. A.1a). If the three particles have helicities λ_1, λ_2, λ_3, then this three particle state can be described by a vector

$$|\omega_1, \lambda_1, \omega_2, \lambda_2, \omega_3, \lambda_3, \alpha = 0, \beta = 0, \gamma = 0\rangle.$$

Then any other state with the same energies $\omega_1, \omega_2, \omega_3$ and helicities $\lambda_1, \lambda_2, \lambda_3$ can be obtained by a rotation.

$$|\omega_1, \lambda_1, \omega_2, \lambda_2, \omega_3, \lambda_3, \alpha, \beta, \gamma\rangle = R(\alpha, \beta, \gamma)|\omega_1, \lambda_1, \omega_2, \lambda_2, \omega_3, \lambda_3, \alpha = 0, \beta = 0, \gamma = 0\rangle. \tag{A2}$$

The energies and the helicities are invariant under $R(\alpha, \beta, \gamma)$. Figure A.1b shows the Euler angles that specify the orientation of the decay plane.

We now construct the three-body states of definite angular momentum j, angular momentum projection m along the z-axis, helicities $\lambda_1, \lambda_2, \lambda_3$, and energies $\omega_1, \omega_2, \omega_3$. These quantum numbers, however, do not alone uniquely specify a three-body state. The angular momentum M quantized along the

normal $\hat{n}$ to the decay plane must be specified as well. The reason is that $\vec{J} \cdot \hat{n}$ commutes with all of the operators associated with the above quantum numbers. Because $\vec{J} \cdot \hat{n}$ is the generator of rotations about $\hat{n}$, it commutes with all of the rotationally invariant operators. But it is a scalar operator itself, so it commutes with J_z. Stated in other terms, if the system is rotated about the z-axis, the angular momentum along the normal to the decay plane is unchanged, because $\vec{J}$ and $\hat{n}$ rotate simultaneously.

Why isn't an analogous operator necessary in the two-body helicity formalism? In fact, such an operator could be defined: it is the angular momentum along the decay axis. But its eigenvalue is $\lambda = \lambda_1 - \lambda_2$, so it is not independent of λ_1 and λ_2, which are already specified. However, the quantum number M in the three-body formalism plays essentially the same role as $\lambda = \lambda_1 - \lambda_2$ in the two-body formalism.

The relation between the states with definite α, β, γ and those with definite j, m, M is easy to obtain. We will obtain the relation in two ways to illustrate the formalism. For convenience let $\Omega \equiv \omega_1, \omega_2, \omega_3$ and $\Lambda \equiv \lambda_1, \lambda_2, \lambda_3$. The goal is to find the coefficients in the equation

$$|\Lambda, \Omega, \alpha, \beta, \gamma\rangle = \sum_{j,m,M} c_{j,m,M}(\alpha, \beta, \gamma)|\Lambda, \Omega, j, m, M\rangle. \tag{A3}$$

Now consider the case $\alpha = \beta = \gamma = 0$. The z-axis is then aligned with the normal to the decay plane, so that $m = M$:

$$|\Lambda, \Omega, \alpha = 0, \beta = 0, \gamma = 0\rangle = \sum_{j,M} c_{j,M,M}(\alpha = 0, \beta = 0, \gamma = 0)|\Lambda, \Omega, j, M, M\rangle. \tag{A4}$$

We rotate back to the original state using Eq. (A2)

$$R(\alpha,\beta,\gamma)|\Lambda,\Omega,\alpha=0,\beta=0,\gamma=0\rangle = \sum_{j,M} c_{j,M,M}(\alpha=0,\beta=0,\gamma=0) \times R(\alpha,\beta,\gamma)|\Lambda,\Omega,j,M,M\rangle. \tag{A5}$$

The crucial point in this argument is that the states $|\Lambda,\Omega,j,m,M\rangle$ are angular momentum eigenstates, and therefore transform according to an irreducible representation of the rotation group. Note that for this to be true, all of the quantum numbers except for m must be rotationally invariant. Thus, the rotational invariance of M is essential to the argument. In general, the transformation is

$$R(\alpha,\beta,\gamma)|\Lambda,\Omega,j,m,M\rangle = \sum_{m'} D^{j}_{m'm}(\alpha,\beta,\gamma)|\Lambda,\Omega,j,m',M\rangle \tag{A6}$$

so that

$$R(\alpha,\beta,\gamma)|\Lambda,\Omega,\alpha=0,\beta=0,\gamma=0\rangle = \sum_{j,m,M} c_{j,M,M}(\alpha=0,\beta=0,\gamma=0) D^{j}_{mM}(\alpha,\beta,\gamma)|\Lambda,\Omega,j,m,M\rangle \tag{A7}$$

The coefficient $c_{j,m,M}(\alpha,\beta,\gamma)$ in Eq. (A3) can be read off from Eq. (A7):

$$c_{j,m,M}(\alpha,\beta,\gamma) = c_{j,M,M}(\alpha=0,\beta=0,\gamma=0) D^{j}_{mM}(\alpha,\beta,\gamma) \tag{A8}$$

and

$$|\Lambda,\Omega,\alpha,\beta,\gamma\rangle = \sum_{j,m,M} c_{j,M} D^{j}_{mM}(\alpha,\beta,\gamma)|\Lambda,\Omega,j,m,M\rangle \tag{A9}$$

where we have dropped the irrelevant labels on $c_{j,M}$. Equation (A9) can be inverted by using the orthogonality of the D–functions:

$$\int d\alpha\, d\cos\beta\, d\gamma \left[D^{j*}_{mn}(\alpha,\beta,\gamma) D^{j'}_{m'n'}(\alpha,\beta,\gamma)\right] = \frac{8\pi^2}{2j+1}\delta_{jj'}\delta_{mm'}\delta_{nn'}.$$

We can now express the states of definite total angular momentum in terms of states with definite α, β, γ:

$$|\Lambda, \Omega, j, m, M\rangle = \frac{1}{c_{j,M}} \cdot \frac{2j+1}{8\pi^2} \int d\alpha \, d\cos\beta \, d\gamma D^{j*}_{mM}(\alpha, \beta, \gamma) \times |\Lambda, \Omega, \alpha, \beta, \gamma\rangle. \tag{A10}$$

The coefficient multiplying the integral does not affect the form of the angular distributions and will be dropped.

We will now show the same result from a different point of view. We make the *definition*:

$$|\Omega, \Lambda, j, m, M\rangle = \int d\alpha d\cos\beta d\alpha D^{j*}_{mM}(\alpha, \beta, \gamma) |\Omega, \Lambda, \alpha, \beta, \gamma\rangle. \tag{A11}$$

We will show that the right-hand side transforms according to an irreducible representation of the rotation group, and hence is an eigenstate of angular momentum.

$$R(\alpha, \beta, \gamma)|\Omega, \Lambda, j, m, M\rangle = \int d\alpha' d\cos\beta' d\gamma' D^{j*}_{mM}(\alpha', \beta', \gamma') R(\alpha, \beta, \gamma) |\Omega, \Lambda, \alpha', \beta', \gamma'\rangle$$
$$= \int d\alpha' d\cos\beta' d\gamma' D^{j*}_{mM}(\alpha', \beta', \gamma') R(\alpha, \beta, \gamma) R(\alpha', \beta', \gamma') |\Omega, \Lambda, \alpha' = 0, \beta' = 0, \gamma' = 0\rangle. \tag{A12}$$

Because the set of rotation operators forms a group we can write

$$R(\alpha'', \beta'', \gamma'') = R(\alpha, \beta, \gamma) R(\alpha', \beta', \gamma')$$

and

$$D^{j*}_{mM}[R(\alpha', \beta', \gamma')] = D^{j*}_{mM}[R^{-1}(\alpha, \beta, \gamma) R(\alpha'', \beta'', \gamma'')]$$

$$= \sum_{M'} D^{j*}_{mM'}[R^{-1}(\alpha,\beta,\gamma)] D^{j*}_{M'M}[R(\alpha'',\beta'',\gamma'')]$$
$$= \sum_{M'} D^{j}_{M'm}[R(\alpha,\beta,\gamma)] D^{j*}_{M'M}[R(\alpha'',\beta'',\gamma'')] \quad \text{(A13)}$$

where the notation $D^j_{mM}[R(\alpha,\beta,\gamma)]$ means the D matrix element corresponding to the rotation $R(\alpha,\beta,\gamma)$, etc., and we have used

$$D^j_{mM'}[R^{-1}] = D^j_{mM'}[R^\dagger] = D^{j*}_{M'm}[R].$$

Because

$$d\alpha' d\cos\beta' d\gamma' = d\gamma'' d\cos\beta'' d\gamma'', \quad \text{(A14)}$$

we have

$$R(\alpha,\beta,\gamma)|\Omega,\Lambda,j,m,M\rangle = \int d\alpha'' d\cos\beta'' d\gamma'' \sum_{M'} D^j_{M'm}(\alpha,\beta,\gamma) D^{j*}_{M'M}(\alpha'',\beta'',\gamma'')$$
$$\times R(\alpha'',\beta'',\gamma'')|\Omega,\Lambda,\alpha''=0,\beta''=0,\gamma''=0\rangle$$
$$= \sum_{M'} D^j_{M'm}(\alpha,\beta,\gamma)|\Omega,\Lambda,j,M',M\rangle. \quad \text{(A15)}$$

Thus, $|\Omega\,\Lambda\,j\,m\,M\rangle$ transforms irreducibly under rotations and is an eigenstate of J^2 and J_z with eigenvalues j,m. The quantum number M is identified by considering the case $\alpha=\beta=\gamma=0$. Then in Eq. (A12) the D-function becomes

$$D^{j*}_{mM}(\alpha=0,\beta=0,\gamma=0) = \delta_{mM}.$$

Thus, when the normal to the decay plane and the z–axis are aligned, $M=m$. This implies that M is the angular momentum along $\hat{n}$.

A.3 DECAY ANGULAR DISTRIBUTION IN TERMS OF THE DENSITY MATRIX

Using Eq. (A12) we can now calculate the general form for the angular distribution of the decay plane. First, we introduce the density operator. Consider the amplitude for transition from the initial state $|I\rangle$ to the final state $|F\rangle$,

$$A(I \to F) = \langle F|U|I\rangle. \tag{A16}$$

If we don't know the initial state, but can give only the probability p_k that it is $|I_k\rangle$, then the transition probability, averaged over the possible initial states, is

$$\langle |A(I \to F)|^2\rangle = \sum_k p_k |\langle F|U|I_k\rangle|^2 = \sum_k p_k \langle F|U|I_k\rangle\langle I_k|U^\dagger|F\rangle. \tag{A17}$$

In general, the basis vectors convenient for expressing $|I_k\rangle$ will be different from those best suited for expressing $|F\rangle$. Here, the basis vectors for the $|I_k\rangle$ will be of the type $|E\,J\,M_k\rangle$, i.e., a single-particle state with mass E and angular momentum quantum numbers J, M_k. The states $|F\rangle$ will be three particle $|\Omega, \Lambda, \alpha, \beta, \gamma\rangle$ vectors and will be expressed in terms of the $|\Omega, \Lambda, j, m, M\rangle$ states. The quantization axis (z-axis) for m is the same as that for M_k. Let $|a\rangle, |b\rangle$ denote basis vectors for $|F\rangle$ and $|A\rangle, |B\rangle$ denote basis vectors for $|I_k\rangle$. Then Eq. (A17) becomes, after inserting complete sets of these basis vectors,

$$\langle |A(I \to F)|^2\rangle = \sum_{a,b,A,B} \langle F|a\rangle\langle a|U|A\rangle\langle A| \sum_k p_k |I_k\rangle\langle I_k|B\rangle\langle B|U^\dagger|b\rangle\langle b|F\rangle. \tag{A18}$$

The operator

$$\rho = \sum_k p_k |I_k\rangle\langle I_k| \tag{A19}$$

is referred to as the density operator. It is simply the sum of the projection operators for the possible initial states, weighted by their probabilities. Translating Eq. (A18) into the language of a three-body decay we find

$$\langle |A(I \to F)|^2 \rangle = \sum_{\substack{\text{indices on} \\ \text{intermediate states}}} \langle \Omega_F \Lambda_F \alpha, \beta, \gamma | \Omega' \Lambda' j' m' M' \rangle \langle \Omega' \Lambda' j' m' M' | U | E\, J\, \mathcal{M} \rangle \langle E\, J\, \mathcal{M}|$$
$$\times \left[\sum_k p_k |I_k\rangle\langle I_k| \right] |E' J' \mathcal{M}'\rangle \langle E' J' \mathcal{M}' | U^\dagger | \Omega'' \Lambda'' j'' m'' M'' \rangle$$
$$\times \langle \Omega'' \Lambda'' j'' m'' M'' | \Omega_F \Lambda_F \alpha, \beta, \gamma \rangle. \tag{A20}$$

To evaluate this expression, we use

$$\begin{aligned}
\langle \Omega_F \Lambda_F \alpha, \beta, \gamma | \Omega' \Lambda' j' m' M' \rangle &= D^{j'*}_{m' M'}(\alpha, \beta, \gamma) \delta_{\Omega_F \Omega'} \delta_{\Lambda_F \Lambda'} \\
\langle \Omega' \Lambda' j' m' M' | U | E\, J\, \mathcal{M} \rangle &= \mathcal{F}(\Omega', \Lambda', M', E) \delta_{m' \mathcal{M}} \delta_{j' J} \\
\langle E\, J\, \mathcal{M}| \left[\sum_k p_k |I_k\rangle\langle I_k| \right] |E' J' \mathcal{M}'\rangle &= \rho_{\mathcal{M}\mathcal{M}'} \delta_{J J_I} \delta_{J_I J'} \delta_{E E_I} \delta_{E_I E'} \\
\langle E' J' \mathcal{M}' | U^\dagger | \Omega'' \Lambda'' j'' m'' M'' \rangle &= \mathcal{F}^*(\Omega'', \Lambda'', M'', E') \delta_{J' j''} \delta_{\mathcal{M}' m''} \\
\langle \Omega'' \Lambda'' j'' m'' M'' | \Omega_F \Lambda_F \alpha, \beta, \gamma \rangle &= D^{j''}_{m'' M''}(\alpha, \beta, \gamma) \delta_{\Omega'' \Omega_F} \delta_{\Lambda'' \Lambda_F}.
\end{aligned} \tag{A21}$$

The $\mathcal{F}$ functions give the coupling to the final state quantum numbers. They must, however, be functions only of rotationally invariant quantities, and thus do not depend on m' or m''. The δ functions accompanying the $\mathcal{F}$'s express the conservation of angular momentum. In the formula for the density matrix we have used the fact that the initial states $|I_k\rangle$ all have the same mass $= E_I$ and spin $= J_I$ but can have different values of J_z. Furthermore, J_z for the $|I_k\rangle$ states in general has a different quantization axis than that of the $|E\, J\, \mathcal{M}\rangle$ states. Thus, the density matrix has off–diagonal terms. For example, in the decay $\psi \to \gamma\iota(1440)$, the quantization axis for the $|I_k\rangle$ states is the beam axis, whereas that for the $|E\, J\, \mathcal{M}\rangle$ states is the $\iota(1440)$ momentum direction.

Substituting these expressions into Eq. (A20), we find

$$\begin{aligned}
&\langle|A(I\to F)|^2\rangle \\
&= \sum_{\substack{\text{indices on}\\ \text{intermediate states}}} D^{j'*}_{m'M'}(\alpha,\beta,\gamma)\delta_{\Omega_F\Omega'}\delta_{\Lambda_F\Lambda'}\mathcal{F}(\Omega',\Lambda',M',E)\delta_{m'm}\delta_{j'J}\rho_{MM'} \\
&\qquad \times \delta_{JJ_I}\delta_{J_IJ'}\delta_{EE_I}\delta_{E_IE'}\mathcal{F}^*(\Omega'',\Lambda'',M'',E')\delta_{J'j''}\delta_{M'm''}D^{j''}_{m''M''}(\alpha,\beta,\gamma) \\
&\qquad \times \delta_{\Omega''\Omega_F}\delta_{\Lambda''\Lambda_F} \\
&= \sum_{\substack{m',m''\\ M',M''}} D^{J_I*}_{m'M'}(\alpha,\beta,\gamma)D^{J_I}_{m''M''}(\alpha,\beta,\gamma)\rho_{m'm''} \\
&\qquad \times \mathcal{F}(\Omega_F,\Lambda_F,M',E_I)\mathcal{F}^*(\Omega_F,\Lambda_F,M'',E_I). \qquad \text{(A22)}
\end{aligned}$$

To obtain the angular distribution we integrate over the final state energies $\Omega_F \equiv \omega_1,\omega_2,\omega_3$. Because only two energies are independent, we have

$$\begin{aligned}
&\int d\omega_1 d\omega_2 \int d\gamma \langle|A(I\to F)|^2\rangle \\
&\qquad = \sum_{M,M'}\sum_{m,m'}\rho_{mm'}\int d\gamma D^{J_I*}_{mM}(\alpha,\beta,\gamma)D^{J_I}_{m'M'}(\alpha,\beta,\gamma)F_{MM'}
\end{aligned} \qquad \text{(A23)}$$

where

$$F_{MM'} = \int d\omega_1 d\omega_2 \mathcal{F}(\Omega_F,\Lambda_F,M)\mathcal{F}^*(\Omega_F,\Lambda_F,M').$$

Here we have suppressed E_I, because it is fixed at the mass of the decaying particle. The dummy suffixes have also been relabeled. The integral over $d\gamma$ conveniently removes interference between states of different M, because the γ dependence of the integrand is simply $e^{i(M-M')\gamma}$. Thus, the distribution in α and β can be written, relabeling J_I by j,

$$\boxed{\frac{dN}{d\Omega} = \sum_{m,m'}\rho_{mm'}\sum_{M} D^{j*}_{mM}(\alpha,\beta,0)D^{j}_{m'M}(\alpha,\beta,0)|R_M|^2} \qquad \text{(A24)}$$

where

$$|R_M|^2 = 2\pi \sum_{\lambda_1\lambda_2\lambda_3} \int d\omega_1 d\omega_2 \mathcal{F}|(\omega_1\lambda_1\omega_2\lambda_2\omega_3\lambda_3, M)|^2.$$

We now combine the terms with opposite values of M

$$\begin{aligned}
\frac{dN}{d\Omega} &= \sum_{m,m'} \rho_{mm'} \sum_{M\geq 0} \Big[D^{j*}_{mM}(\alpha,\beta,0) D^{j}_{m',M}(\alpha,\beta,0)|R_M|^2 \\
&\qquad + D^{j*}_{m,-M}(\alpha,\beta,0) D^{j}_{m',-M}(\alpha,\beta,0)|R_{-M}|^2 \Big] \\
&= \sum_{m,m'} \rho_{mm'} \sum_{M\geq 0} \Big[e^{i\alpha m} d^{j}_{mM}(\beta) e^{-i\alpha m'} d^{j}_{m'M}(\beta)|R_M|^2 \\
&\qquad + e^{i\alpha m} d^{j}_{m,-M}(\beta) e^{-i\alpha m'} d^{j}_{m',-M}(\beta)|R_{-M}|^2 \Big] \\
&= \sum_{M\geq 0} \sum_{m,m'} \rho_{mm'} e^{i\alpha(m-m')} \Big[d^{j}_{mM}(\beta) d^{j}_{m'M}(\beta)|R_M|^2 \\
&\qquad + d^{j}_{m,-M}(\beta) d^{j}_{m',-M}(\beta)|R_{-M}|^2 \Big]. \qquad \text{(A25)}
\end{aligned}$$

Now exploit the hermiticity of ρ,

$$\rho_{mm'} = \rho^*_{m'm},$$

or

$$\begin{aligned}
\mathcal{R}e\,\rho_{mm'} &= \mathcal{R}e\,\rho_{m'm} \\
\mathcal{I}m\,\rho_{mm'} &= -\mathcal{I}m\,\rho_{m'm}.
\end{aligned}$$

The last bracketed term in Eq. (A25) is symmetric under $m \leftrightarrow m'$, whereas

$$e^{i\alpha(m-m')} = \cos(m-m')\alpha + i\sin(m-m')\alpha$$

has mixed symmetry under $m \leftrightarrow m'$. Therefore

$$\frac{dN}{d\Omega} = \sum_{m,m'} \sum_{M\geq 0} (\mathcal{R}e\,\rho_{mm'} + i\mathcal{I}m\,\rho_{mm'})(\cos(m-m')\alpha + i\sin(m-m')\alpha)$$

$$\times \left[d^j_{mM}(\beta) d^j_{m'M}(\beta) |R_M|^2 + d^j_{m,-M}(\beta) d^j_{m',-M}(\beta) |R_{-M}|^2 \right]$$
$$= \sum_{m,m'} \sum_{M \geq 0} \left[\mathcal{R}e\, \rho_{mm'} \cos(m-m')\alpha - \mathcal{I}m\, \rho_{mm'} \sin(m-m')\alpha \right]$$
$$\times \left[d^j_{mM}(\beta) d^j_{m'M}(\beta) |R_M|^2 + d^j_{m,-M}(\beta) d^j_{m',-M}(\beta) |R_{-M}|^2 \right]. \tag{A26}$$

The term involving the d-functions can be written

$$\left[\cdots \right] = \left(d^j_{mM}(\beta) d^j_{m'M}(\beta) + d^j_{m,-M}(\beta) d^j_{m',-M}(\beta) \right) \left(\frac{|R_M|^2 + |R_{-M}|^2}{2} \right)$$
$$+ \left(d^j_{mM}(\beta) d^j_{m'M}(\beta) - d^j_{m,-M}(\beta) d^j_{m',-M}(\beta) \right) \left(\frac{|R_M|^2 - |R_{-M}|^2}{2} \right). \tag{A27}$$

Defining

$$Z^{jM+}_{mm'}(\beta) = d^j_{mM}(\beta) d^j_{m'M}(\beta) + d^j_{m,-M}(\beta) d^j_{m',-M}(\beta)$$
$$Z^{jM-}_{mm'}(\beta) = d^j_{mM}(\beta) d^j_{m'M}(\beta) - d^j_{m,-M}(\beta) d^j_{m',-M}(\beta)$$
$$R^+_M = \tfrac{1}{2}(|R_M|^2 + |R_{-M}|^2)$$
$$R^-_M = \tfrac{1}{2}(|R_M|^2 - |R_{-M}|^2) \tag{A28}$$

we have

$$\frac{dN}{d\Omega} = \sum_{m,m'} \sum_{M \geq 0} \left[\mathcal{R}e\, \rho_{mm'} \cos(m-m')\alpha - \mathcal{I}m\, \rho_{mm'} \sin(m-m')\alpha \right]$$
$$\times \left[Z^{jM+}_{mm'}(\beta) R^+_M + Z^{jM-}_{mm'}(\beta) R^-_M \right]. \tag{A29}$$

The final manipulation is to combine terms with opposite values of m, m'. Because

$$d^j_{mm'}(\beta) = (-1)^{m-m'} d_{-m,-m'}(\beta),$$

we have

$$\begin{aligned} Z^{jM\pm}_{-m,-m'}(\beta) =& d^j_{-mM}(\beta) d^j_{-m'M}(\beta) \pm d^j_{-m,-M}(\beta) d^j_{-m',-M}(\beta) \\ =& (-1)^{-(m+M)}(-1)^{-(m'+M)} d^j_{m,-M}(\beta) d^j_{m',-M}(\beta) \\ & \pm (-1)^{-m+M}(-1)^{-m'+M} d^j_{mM}(\beta) d^j_{m'M}(\beta) \\ =& \pm (-1)^{2M}(-1)^{-(m+m')} Z^{jM\pm}_{m,m'}(\beta). \end{aligned} \tag{A30}$$

There are two cases to consider:

Case 1

$$j = \text{ integer } \Rightarrow \quad \begin{cases} M = \text{ integer } \Rightarrow (-1)^{2M} = 1 \\ m, m' = \text{ integer } \Rightarrow (-1)^{-(m+m')} = (-1)^{m-m'} \end{cases}$$

Case 2

$$j = \tfrac{1}{2} \text{ integer } \Rightarrow \quad \begin{cases} M = \text{ half integer } \Rightarrow (-1)^{2M} = (-1) \\ m, m' = \text{ half integer } \Rightarrow (-1)^{m+m'} = (-1)(-1)^{m-m'}. \end{cases}$$

Thus, for Case 2 we have

$$(-1)^{2M}(-1)^{-(m+m')} = (-1)(-1)(-1)^{m-m'} = (-1)^{m-m'},$$

and for both cases we find the same result:

$$\left[Z^{jM\pm}_{mm'}(\beta) + Z^{jM\pm}_{-m,-m'}(\beta) \right] = \left[1 \pm (-1)^{m-m'} \right] Z^{jM\pm}_{mm'}(\beta). \tag{A31}$$

We can now combine terms with (m, m') and $(-m, -m')$:

$$\begin{aligned}\frac{dN}{d\Omega} = \tfrac{1}{2} \sum_{\substack{mm' \\ (all)}} \sum_{M \geq 0} \Big[& \cos(m-m')\alpha(\mathcal{R}e\,\rho_{mm'} + (-1)^{m-m'}\mathcal{R}e\,\rho_{-m,-m'}) \\ & - \sin(m-m')\alpha(\mathcal{I}m\,\rho_{mm'} - (-1)^{m-m'}\mathcal{I}m\,\rho_{-m,-m'})\Big] \\ & \times R^{+}_{M} Z^{jM+}_{mm'}(\beta) \\ + \Big[& \cos(m-m')\alpha(\mathcal{R}e\,\rho_{mm'} - (-1)^{m-m'}\mathcal{R}e\,\rho_{-m,-m'}) \\ & - \sin(m-m')\alpha(\mathcal{I}m\,\rho_{mm'} + (-1)^{m-m'}\mathcal{I}m\,\rho_{-m,-m'})\Big] \\ & \times R^{-}_{M} Z^{jM-}_{mm'}(\beta). \end{aligned} \tag{A32}$$

Note that the above sum is over all m, m', not just $m, m' \geq 0$. That is because the $m = m' = 0$ term appears twice in the above formula so all terms must appear twice and then be multiplied by the overall factor of $\frac{1}{2}$.

This is a formidable looking expression. In applying it to the case of spin 1 we will see how reasonably simple results emerge, especially when the density matrix has some zero elements or symmetry.

A.4 CONSEQUENCES OF PARITY CONSERVATION

We now consider the action of the parity operator on the angular momentum eigenstates. We have

$$\prod |\Omega,\Lambda,j,m,M\rangle = \int d\alpha d\cos\beta d\gamma D^{j*}_{mM}(\alpha,\beta,\gamma) R(\alpha,\beta,\gamma) \prod |\Omega,\Lambda,\alpha=0,\beta=0,\gamma=0\rangle \tag{A33}$$

where $[\prod, R(\alpha,\beta,\gamma)] = 0$ has been used. The ket on the RHS is the direct product of three one-particle plane wave helicity states

$$|\Omega,\Lambda,\alpha=0,\beta=0,\gamma=0\rangle = \text{const } |\vec{p}_1 s_1 \lambda_1\rangle |\vec{p}_2 s_2 \lambda_2\rangle |\vec{p}_3 s_3 \lambda_3\rangle \tag{A34}$$

where the momentum $\vec{p}_i$ of each particle lies in the xy plane. From Ref. (3), p. 24, we know that

$$\prod |\vec{p}_z, s, \lambda\rangle = \eta(-1)^{s-\lambda} e^{-i\pi J_y} |\vec{p}_z, s, -\lambda\rangle. \tag{A35}$$

However, the derivation can just as well be carried out for a state whose momentum vector lies in the xy plane, yielding

$$\prod |\vec{p}_i s_i \lambda_i\rangle = \eta_i(-1)^{s_i-\lambda_i} e^{-i\pi J_x} |\vec{p}_i, s_i, -\lambda_i\rangle \quad i=1,2,3. \tag{A36}$$

Aside from the phase factor $(-1)^{s_i-\lambda_i}$, this result is easily understood. The parity operator reverses the helicity, because $\lambda = \vec{s}\cdot\hat{p}$, and rotates the momentum by π about any axis normal to the momentum vector, thus reversing it. In the present case we choose the normal axis to be the z-axis, because it is the only one perpendicular to all three momentum vectors. The coefficient η_i is

the intrinsic parity of the particle. Using Eq. (A36) in Eq. (A33) we find

$$\prod |\Omega, \Lambda, j, m, M\rangle = \eta_1\eta_2\eta_3(-1)^{s_1+s_2+s_3-\lambda_1-\lambda_2-\lambda_3} \times \int d\alpha d\cos\beta d\gamma D^{j*}_{mM}(\alpha,\beta,\gamma) R(\alpha,\beta,\gamma) e^{-i\pi J_z} |\Omega, -\Lambda, \alpha=0, \beta=0, \gamma=0\rangle. \tag{A37}$$

But

$$\begin{aligned} R(\alpha,\beta,\gamma)e^{-i\pi J_z} &= e^{-i\alpha J_z} e^{-i\beta J_y} e^{-i\gamma J_z} e^{-i\pi J_z} \\ &= R(\alpha,\beta,\gamma+\pi). \end{aligned} \tag{A38}$$

We therefore perform a change of variables

$$\begin{aligned} \gamma' &= \gamma + \pi \\ d\gamma' &= d\gamma \\ D^{j*}_{mM}(\alpha,\beta,\gamma=\gamma'-\pi) &= e^{i\alpha m} d^j_{mM}(\beta) e^{i\gamma' M} e^{-i\pi M} = (-1)^M D^{j*}_{mM}(\alpha,\beta,\gamma'). \end{aligned} \tag{A39}$$

Thus

$$\prod |\Omega, \Lambda, j, m, M\rangle = \eta_1\eta_2\eta_3(-1)^{s_1+s_2+s_3-\lambda_1-\lambda_2-\lambda_3}(-1)^M |\Omega, -\Lambda, j, m, M\rangle. \tag{A40}$$

For a state consisting of three pseudoscalars this is

$$\prod |\Omega, \lambda_1=0, \lambda_2=0, \lambda_3=0, j, m, M\rangle = (-1)^{M+1} |\Omega, \lambda_1=0, \lambda_2=0, \lambda_3=0, j, m, M\rangle \tag{A41}$$

and is a state of definite parity. If the decaying particle has even (odd) parity then M, the angular momentum component along the normal to the decay plane, must be odd (even).

For a parity conserving interaction, in general, we have

$$\langle \Omega, \Lambda, j, m, M|U|E_I, J_I, M_I\rangle = \langle \Omega, \Lambda, j, m, M|\prod U \prod |E_I, J_I, M_I\rangle$$
$$= \eta_I\eta_1\eta_2\eta_3(-1)^M(-1)^{s_1+s_2+s_3-\lambda_1-\lambda_2-\lambda_3}\langle \Omega, -\Lambda, j, m, M|U|E_I, J_I, M_I\rangle. \tag{A42}$$

A.5 ANGULAR DISTRIBUTIONS FOR $X \to 3$ PSEUDOSCALARS

We have seen that for a decay into three pseudoscalars conservation of parity restricts the values of M. The table below gives the number of values of M that are allowed for different spin–parity combinations.

		J even	J odd
even parity	$\Rightarrow M$ odd	J	$J+1$
odd parity	$\Rightarrow M$ even	$J+1$	J

Thus, although there are $2J+1$ values of M, there are only J or $J+1$ independent decay amplitudes. We now work out $dN/d\Omega$ for $J^P = 1^\pm$ decaying into three pseudoscalars.

$$J^P = 1^-$$

$$P = \text{ odd } \Rightarrow M \text{ even } \Rightarrow M = 0 \text{ only}$$

$$R_{M^-} = \tfrac{1}{2}(|R_M|^2 - |R_{-M}|^2) = 0.$$

From Eq. (A32) we have

$$\begin{aligned}\frac{dN}{d\Omega} = \tfrac{1}{2}\sum_{m,m'} \Big[&\cos(m-m')\alpha(\mathcal{R}e\,\rho_{mm'} + (-1)^{m-m'}\mathcal{R}e\,\rho_{-m,-m'} \\ &- \sin(m-m')\alpha(\mathcal{I}m\,\rho_{mm'} - (-1)^{m-m'}\mathcal{I}m\,\rho_{-m,-m'})\Big] \\ &\times R_0^+ Z_{mm'}^{1,0+}(\beta).\end{aligned} \tag{A43}$$

Performing the sums, we have

$$\begin{aligned}\frac{dN}{d\Omega} = \tfrac{1}{2}R_0^+\Big\{&2\mathcal{R}e\,\rho_{00}Z_{00}^{1,0+}(\beta) + 2(\mathcal{R}e\,\rho_{11} + \mathcal{R}e\,\rho_{-1,-1})Z_{1,1}^{10+}(\beta) \\ &+ 4\Big[\cos\alpha(\mathcal{R}e\,\rho_{10} - \mathcal{R}e\,\rho_{-1,0}) - \sin\alpha(\mathcal{I}m\,\rho_{10} + \mathcal{I}m\,\rho_{-1,0})\Big]Z_{1,0}^{1,0+}(\beta)\end{aligned}$$

$$+2\Big[\cos 2\alpha(\mathcal{R}e\,\rho_{1,-1}+\mathcal{R}e\,\rho_{-1,1})-\sin 2\alpha(\mathcal{I}m\,\rho_{1,-1}-\mathcal{I}m\,\rho_{-1,1})\Big]Z^{1,0+}_{1,-1}(\beta)\Big\}. \tag{A44}$$

Using $\rho=\rho^{\dagger}$ we obtain

$$\begin{aligned}\frac{dN}{d\Omega}=R_0^+\Big\{&\mathcal{R}e\,\rho_{00}Z^{1,0+}_{0,0}(\beta)+(\mathcal{R}e\,\rho_{11}+\mathcal{R}e\,\rho_{-1,-1})Z^{10+}_{1,1}(\beta)\\&+2\Big[\cos\alpha(\mathcal{R}e\,\rho_{10}-\mathcal{R}e\,\rho_{-1,0})-\sin\alpha(\mathcal{I}m\,\rho_{10}+\mathcal{I}m\,\rho_{-1,0})\Big]Z^{1,0+}_{1,0}(\beta)\\&+2\Big[\cos 2\alpha\mathcal{R}e\,\rho_{1,-1}-\sin 2\alpha\mathcal{I}m\,\rho_{1,-1}\Big]Z^{1,0+}_{1,-1}(\beta)\Big\}.\end{aligned} \tag{A45}$$

Substituting for the Z-functions, one finds that the result for $1^-\to 3(0^-)$ is

$$\begin{aligned}\frac{dN}{d\Omega}=R_0^+\Big\{&(2\cos^2\beta)\rho_{00}+\sin^2\beta(\rho_{11}+\rho_{-1,-1})\\&-\sqrt{2}\sin 2\beta\Big[\cos\alpha(\mathcal{R}e\,\rho_{10}-\mathcal{R}e\,\rho_{-1,0})-\sin\alpha(\mathcal{I}m\,\rho_{10}+\mathcal{I}m\,\rho_{-1,0})\Big]\\&-2\sin^2\beta\Big[\cos 2\alpha\mathcal{R}e\,\rho_{1,-1}-\sin 2\alpha\mathcal{I}m\,\rho_{1,-1}\Big]\Big\}.\end{aligned} \tag{A46}$$

We now calculate the result for $J^P=1^+$ decaying into three pseudoscalars. The parity restriction is

$$P=\text{ even }\Rightarrow M=\text{ odd }\Rightarrow M=\pm 1,$$

so that

$$\begin{aligned}\frac{dN}{d\Omega}=\tfrac{1}{2}\sum_{m,m'}R_1^+\Big[&\cos(m-m')\alpha(\mathcal{R}e\,\rho_{mm'}+(-1)^{m-m'}\mathcal{R}e\,\rho_{-m,-m'})\\&-\sin(m-m')\alpha(\mathcal{I}m\,\rho_{mm'}-(-1)^{m-m'}\mathcal{I}m\,\rho_{-m,-m'})\Big]\times Z^{11+}_{m,m'}(\beta)\end{aligned}$$

$$+R_1^- \Big[\cos(m-m')\alpha(\mathcal{R}e\,\rho_{mm'} - (-1)^{m-m'}\mathcal{R}e\,\rho_{-m,-m'}) - \sin(m-m')\alpha(\mathcal{I}m\,\rho_{mm'} + (-1)^{m-m'}\mathcal{I}m\,\rho_{-m,-m'})\Big] Z^{11-}_{m,m'}(\beta). \tag{A47}$$

Summing over m and m', we have

$$\begin{aligned}\frac{dN}{d\Omega} = R_1^+ \Big\{ & (\rho_{11}+\rho_{-1,-1}) Z^{1,1+}_{1,1}(\beta) + \rho_{00} Z^{11+}_{00}(\beta) \\ & + 2\Big[\cos\alpha(\mathcal{R}e\,\rho_{10} - \mathcal{R}e\,\rho_{-1,0}) - \sin\alpha(\mathcal{I}m\,\rho_{10} + \mathcal{I}m\,\rho_{-1,0})\Big] Z^{1,1+}_{1,0}(\beta) \\ & + \Big[\cos 2\alpha(\mathcal{R}e\,\rho_{1,-1} + \mathcal{R}e\,\rho_{-1,1}) - \sin 2\alpha(\mathcal{I}m\,\rho_{1,-1} - \mathcal{I}m\,\rho_{-1,1})\Big] Z^{1,1+}_{1,-1}(\beta)\Big\} \\ +R_1^- \Big\{ & (\rho_{1,1}-\rho_{-1,-1}) Z^{1,1-}_{1,1}(\beta) + \\ & + 2\Big[\cos\alpha(\mathcal{R}e\,\rho_{10} + \mathcal{R}e\,\rho_{-1,0}) - \sin\alpha(\mathcal{I}m\,\rho_{10} - \mathcal{I}m\,\rho_{-1,0})\Big] Z^{1,1-}_{1,0}(\beta) \\ & + \Big[\cos 2\alpha(\mathcal{R}e\,\rho_{1,-1} - \mathcal{R}e\,\rho_{-1,1}) - \sin 2\alpha(\mathcal{I}m\,\rho_{1,-1} + \mathcal{I}m\,\rho_{-1,1})\Big] Z^{1,1-}_{1,-1}(\beta)\Big\}.\end{aligned} \tag{A48}$$

We again use the hermiticity of ρ to obtain

$$\begin{aligned}\frac{dN}{d\Omega} = R_1^+ \Big\{ & (\rho_{11}+\rho_{-1,-1}) Z^{1,1+}_{11}(\beta) + \rho_{00} Z^{1,1+}_{00}(\beta) \\ & + 2\Big[\cos\alpha(\mathcal{R}e\,\rho_{10} - \mathcal{R}e\,\rho_{-1,0}) - \sin\alpha(\mathcal{I}m\,\rho_{1,0} + \mathcal{I}m\,\rho_{-1,0})\Big] Z^{1,1+}_{1,0}(\beta) \\ & + 2\Big[\cos 2\alpha\mathcal{R}e\,\rho_{1,-1} - \sin 2\alpha\mathcal{I}m\,\rho_{1,-1}\Big] Z^{1,1+}_{1,-1}(\beta)\Big\} \\ +R_1^- \Big\{ & (\rho_{1,1}-\rho_{-1,-1}) Z^{11-}_{1,1}(\beta) \\ & + 2\Big[\cos\alpha(\mathcal{R}e\,\rho_{10} + \mathcal{R}e\,\rho_{-1,0}) - \sin\alpha(\mathcal{I}m\,\rho_{10} - \mathcal{I}m\,\rho_{-1,0})\Big] Z^{1,1-}_{1,0}(\beta)\Big\}.\end{aligned} \tag{A49}$$

After substituting the Z-functions, we obtain the final result for $1^+ \to 3(P)$ in

terms of the density matrix:

$$\begin{aligned}\frac{dN}{d\Omega} = R_1^+ \Big\{ & (\rho_{1,1} + \rho_{-1,-1})\tfrac{1}{2}(1+\cos^2\beta) + \rho_{00}\sin^2\beta \\ & + \sqrt{2}\cos\beta\sin\beta\Big[\cos\alpha(\mathcal{R}e\,\rho_{10} - \mathcal{R}e\,\rho_{-1,0}) - \sin\alpha(\mathcal{I}m\,\rho_{1,0} + \mathcal{I}m\,\rho_{-1,0})\Big] \\ & + \sin^2\beta\Big[\cos 2\alpha\mathcal{R}e\,\rho_{1,-1} - \sin 2\alpha\mathcal{I}m\,\rho_{1,-1}\Big]\Big\} \\ + R_1^- \Big\{ & (\rho_{1,1} - \rho_{-1,-1})\cos\beta \\ & + \sqrt{2}\sin\beta\Big[\cos\alpha(\mathcal{R}e\,\rho_{10} + \mathcal{R}e\,\rho_{-1,0}) - \sin\alpha(\mathcal{I}m\,\rho_{10} - \mathcal{I}m\,\rho_{-1,0})\Big]\Big\}. \end{aligned} \tag{A50}$$

The density matrix elements are calculated for radiative ψ decay and substituted into the above formulas in the following section.

A.6 DENSITY MATRIX FOR $\psi \to \gamma + X(J = 1)$

The three-body helicity formalism presented above uses the density matrix to keep track of the polarization of the decaying particle. The density matrix is just a bookkeeping device; it is not essential to the calculation. However, by exploiting the hermiticity of the density matrix, some simplifications of the formulas were achieved. We now give an example of the calculation of the density matrix for a spin-one particle X produced in the process $\psi \to \gamma + X$. To be more precise, we will calculate the density matrix for X when it is produced in the direction $\hat{n}(\theta, \phi)$ in the lab frame. Thus, the correlations between θ, ϕ and the three-body decay plane angles α, β of X are implicit in Eq. (A24).

For $\psi \to \gamma + X$, the final state (the system consisting of the photon and the particle X, before X decays) is given by the action of the propagator on the initial state:

$$|f_{M_\psi}\rangle = U|J_\psi, M_\psi\rangle. \tag{A51}$$

Here $|J_\psi, M_\psi\rangle$ is the state vector of the ψ, which has its spin projection M_ψ either aligned or antialigned with the e^+e^- beam axis. For unpolarized beams, each direction has probability $p(M_\psi = +1) = p(M_\psi = -1) = \frac{1}{2}$. The state vector of the ψ is not a coherent superposition of the $M_\psi = +1$ and $M_\psi = -1$ states. It is *either* $|J_\psi, M_\psi = +1\rangle$ or $|J_\psi, M_\psi = -1\rangle$. The density operator for the ψ is then

$$\rho(\psi) = \tfrac{1}{2} \sum_{M_\psi = \pm 1} |J_\psi, M_\psi\rangle\langle J_\psi, M_\psi| \tag{A52}$$

and the density operator for the $\gamma + X$ system is

$$\rho(\gamma + X) = \tfrac{1}{2} \sum_{M_\psi = \pm 1} |f_{M_\psi}\rangle\langle f_{M_\psi}|. \tag{A53}$$

We can express $|f_{M_\psi}\rangle$ in terms of the two-particle eigenstates of total angular

momentum and helicity

$$|f_{M_\psi}\rangle = \sum_{\lambda_X,\lambda_\gamma} |J,M,\lambda_X,\lambda_\gamma\rangle\langle J,M,\lambda_X,\lambda_\gamma|U|J_\psi,M_\psi\rangle$$
$$= \sum_{\lambda_X,\lambda_\gamma} |J,M,\lambda_X,\lambda_\gamma\rangle A_{\lambda_X,\lambda_\gamma} \tag{A54}$$

where $J = J_\psi$ and $M = M_\psi$ from angular momentum conservation. As we remarked above, it is necessary to calculate the density operator for X at $\hat{n}(\theta,\phi)$. We can obtain the density operator for the system $(\gamma+X)$ at $\hat{n}(\theta,\phi)$ by recalling that the amplitude for producing X,γ at $\hat{n}(\theta,\phi)$ with the helicities λ_X,λ_γ is

$$A(\hat{n}(\theta,\phi),M_\psi,\lambda_X,\lambda_\gamma) = \langle\hat{n}(\theta,\phi),\lambda_X,\lambda_\gamma|f_{M_\psi}\rangle$$
$$= D^{1*}_{M_\psi,\lambda_X-\lambda_\gamma}(\phi,\theta,-\phi)A_{\lambda_X,\lambda_\gamma} \tag{A55}$$

so that the density operator for the $\gamma + X$ system at $\hat{n}(\theta,\phi)$ is

$$\rho(\gamma+X;\hat{n}(\theta,\phi)) = \tfrac{1}{2}\sum_{M_\psi=\pm1}\Big[\sum_{\lambda_X,\lambda_\gamma} A(\hat{n}(\theta,\phi),M_\psi,\lambda_X,\lambda_\gamma)|\hat{n},\lambda_X,\lambda_\gamma\rangle\Big]$$
$$\times\Big[\sum_{\lambda'_X,\lambda'_\gamma} A^*(\hat{n}(\theta,\phi),M_\psi,\lambda'_X,\lambda'_\gamma)\langle\hat{n},\lambda'_X,\lambda'_\gamma|\Big]. \tag{A56}$$

To obtain the density operator for X at $\hat{n}(\theta,\phi)$, we take the partial trace with respect to λ_γ:

$$\rho(X;\hat{n}(\theta,\phi)) = \sum_{\lambda_\gamma}\langle\lambda_\gamma|\rho(\gamma+X;\hat{n}(\theta,\phi))|\lambda_\gamma\rangle$$
$$= \tfrac{1}{2}\sum_{M_\psi=\pm1}\sum_{\lambda_\gamma}\Big\{\Big[\sum_{\lambda_X} A(\hat{n},M_\psi,\lambda_X,\lambda_\gamma)|\hat{n},\lambda_X\rangle\Big]$$
$$\times\Big[\sum_{\lambda'_X} A^*(\hat{n},M_\psi,\lambda'_X,\lambda_\gamma)\langle\hat{n},\lambda'_X|\Big]\Big\}. \tag{A57}$$

Note that this forces $\lambda_\gamma = \lambda'_\gamma$. Substituting Eq. (A55) we have

$$\rho(X;\hat{n}(\theta,\phi)) = \frac{1}{2}\sum_{M_\psi=\pm1}\sum_{\lambda_\gamma}\Big\{\sum_{\lambda_X,\lambda'_X} D^{1*}_{M_\psi,\lambda_X-\lambda_\gamma}(\phi,\theta,-\phi)D^{1}_{M_\psi,\lambda'_X-\lambda_\gamma}(\phi,\theta,-\phi) \times A_{\lambda_X,\lambda_\gamma}A^*_{\lambda'_X,\lambda_\gamma}|\hat{n},\lambda_X\rangle\langle\hat{n},\lambda'_X|\Big\} \qquad \text{(A58)}$$

The density operator simply consists of all the terms of the angular distribution (probability densities) multiplied by the projection operators for the given quantum numbers. Interference terms, which have $\lambda_X \neq \lambda'_X$, arise when λ_γ does not uniquely specify λ_X. The partial trace just sums over λ_γ in the probability, which is appropriate because λ_γ is a quantity that can be measured in the final state. In contrast, if X decays into other particles, λ_X is a quantum number characterizing an intermediate state, and is therefore summed over in the amplitude that contribute to the density matrix.

Equation (A58) is valid for any radiative ψ decay. We now specialize to the case of $J(X) = 1$. Because $J_\psi = 1$, we have the restriction $|\lambda_X - \lambda_\gamma| \leq 1$. The allowed values of $\lambda_X, \lambda'_X, \lambda_\gamma$ are shown in the table below.

λ_X	0	0	1	−1	0	0	1	−1
λ'_X	0	0	0	0	1	−1	1	−1
λ_γ	1	−1	1	−1	1	−1	1	−1

In evaluating the density operator, we encounter terms with coefficients like $A_{-1,-1}\,A^*_{0,-1}$. Because parity conservation implies

$$A_{\lambda_X,\lambda_\gamma} = \eta_\psi\eta_X\eta_\gamma(-1)^{J_\psi-J_X-J_\gamma}A_{-\lambda_X,-\lambda_\gamma}$$

$$= \eta_X(-1)^{J_X} A_{-\lambda_X,-\lambda_\gamma}$$
$$= (\pm 1) A_{-\lambda_X,-\lambda_\gamma} \qquad \text{(A59)}$$

such terms can be rewritten, for example, as $A_{11}A^*_{01}$.

The density matrix $\rho_{\lambda_X,\lambda'_X}$ is just the matrix of coefficients of the terms in the density operator. The position in the matrix is given by the values of λ_X, λ'_X. For example,

$$\rho_{00} = \tfrac{1}{2} \sum_{M_\psi=\pm 1} \left(|D^1_{M_\psi,1}|^2 + |D^1_{M_\psi,-1}|^2 \right) |A_{01}|^2.$$

After a short calculation, we find that

$$\begin{pmatrix} \rho_{11} & \rho_{10} & \rho_{1,-1} \\ \rho_{01} & \rho_{00} & \rho_{0,-1} \\ \rho_{-11} & \rho_{-10} & \rho_{-1,-1} \end{pmatrix} =$$
$$\begin{pmatrix} \frac{1}{2}|A_{11}|^2 \sin^2\theta & \frac{1}{4\sqrt{2}} A_{11}A^*_{01} e^{-i\phi} \sin 2\theta & 0 \\ \rho^*_{10} & \frac{1}{2}|A_{01}|^2(1+\cos^2\theta) & -\frac{1}{4\sqrt{2}} A_{01}A^*_{11} e^{-i\phi} \sin 2\theta \\ 0 & \rho^*_{0,-1} & \frac{1}{2}|A_{11}|^2 \sin^2\theta \end{pmatrix} \qquad \text{(A60)}$$

Substituting the density matrix Eq. (A60) into Eq. (A46) yields the angular distribution for $\psi \to \gamma X$; $X \to 3(0^-)$ for $J^P(X) = 1^-$:

$$\frac{dN}{d\Omega} = R_0^+ \Big\{ |A_{01}|^2(1+\cos^2\theta)\cos^2\beta + |A_{11}|^2 \sin^2\theta \sin^2\beta$$
$$- \tfrac{1}{2} \mathcal{R}e\,(A^*_{01}A_{11}) \sin 2\theta \sin 2\beta \cos(\alpha - \phi) \Big\}. \qquad \text{(A61)}$$

If one integrates over $(\alpha - \phi)$, there is only one unknown parameter, $|A_{11}|^2/|A_{01}|^2$, that controls the angular distribution.

The angular distribution for $\psi \to \gamma X$; $X \to 3(0^-)$ when $J^P(X) = 1^+$ is obtained by substituting the appropriate density matrix terms into Eq. (A50):

$$\begin{aligned}\frac{dN}{d\Omega} =& R_1^+ \Big\{ \tfrac{1}{2}|A_{01}|^2(1+\cos^2\theta)\sin^2\beta + \tfrac{1}{2}|A_{11}|^2\sin^2\theta(1+\cos^2\beta) \\ &+ \tfrac{1}{4}\mathcal{R}e\,(A_{01}^* A_{11})\sin 2\theta \sin 2\beta \cos(\alpha-\phi)\Big\} \\ &- \tfrac{1}{2}R_1^- \Big\{ \mathcal{I}m(A_{01}^* A_{11})\sin 2\theta \sin\beta \sin(\alpha-\phi)\Big\}. \end{aligned} \tag{A62}$$

Again, if one integrates over $(\alpha - \phi)$ there is only one parameter, $|A_{11}|^2/|A_{01}|^2$, controlling the angular distribution. The angular distributions for $J^P(X) = 1^\pm$ differ significantly from each and from the distribution for $J^P(X) = 0^-$, which is uniform in $\cos\beta$ and has a $(1 + \cos^2\theta)$ dependence in the lab frame polar angle.

No one *knows* anything until its proved. And even then you may have a nagging doubt.

–Horace Rumpole

APPENDIX B:

An Experimenter's Guide to the Helicity Formalism

B.1 Introduction

This paper is a pedagogical guide to the helicity formalism, which is the preferred method for obtaining angular distributions in most relativistic scattering and decay processes. The first question that arises is: Why don't we use the spin-orbit formalism that was developed in non-relativistic quantum mechanics? After all, total angular momentum is always conserved, and one should still be able to obtain the total angular momentum operator simply by adding the orbital and spin angular momentum operators for the particles. The problem is that these operators are defined in reference frames that are not at rest with respect to one another. The orbital angular momentum operator is defined in the center of mass (CM) frame, whereas the spin operators are defined in the rest frames of the particles. This leads to some technical problems in describing the spin states which, however, can be overcome (70). The helicity formalism is well suited to relativistic problems because the helicity operator $h = \vec{S} \cdot \hat{p}$ is invariant under both rotations and boosts along $\hat{p}$. As a consequence, one can construct relativistic basis vectors that are either eigenstates of total angular momentum and helicity, or of linear momentum and helicity.

In preparing this paper the author relied on the original paper of Jacob and Wick (71), as well as treatments by Chung (72), Perl (73), Lifshitz and Pitaevskii (74), Martin and Spearman (75), and Jackson (76). The phase conventions are the same as those used by Jacob and Wick.

Before plunging into the details, it is useful to give a brief overview of the main ideas. Consider a decay process, $\alpha \rightarrow 1 + 2$, where α has spin J and spin-projection M along an arbitrarily defined z-axis. We choose the rest frame of α, in which its state vector is $|J,M\rangle$. The amplitude for the final state particles 1,2 to have momenta $\vec{p}_1 = \vec{p}_f$ and $\vec{p}_2 = -\vec{p}_f$ and helicities λ_1,λ_2 is

$$A = \langle \vec{p}_1 = \vec{p}_f, \lambda_1 \; ; \; \vec{p}_2 = -\vec{p}_f, \lambda_2 | U | JM \rangle \tag{B.1.1}$$

The final state is referred to as a two-particle plane-wave helicity state. Here U is the time-evolution operator that propagates the initial state through the interaction. Because particles 1,2 have equal and opposite momenta in the CM frame, we can characterize the final state by the direction $\hat{n}(\theta,\varphi)$ of the decay axis with respect to the z-axis (spin-quantization axis of α), by the magnitude p of either particle's momentum, and by the helicities λ_1,λ_2. Thus (suppressing p because it is fixed)

$$A = \langle \theta,\varphi,\lambda_1,\lambda_2 \; | U | JM \rangle \tag{B.1.2}$$

Because $|A|^2$ is the probability for the particles to emerge with polar angles θ,φ, if we can calculate (B.1.2), we have the angular distribution. Typically the experiment does not measure the helicities λ_1,λ_2, so they must be summed over.

The key idea in the helicity formalism is that rotational invariance of the helicities allows one to define a set of two-particle basis states $|j,m,\lambda_1,\lambda_2\rangle$ that have definite total angular momentum j, angular momentum projection m, and helicities λ_1,λ_2. We can then exploit conservation of angular momentum by inserting a complete set of these states into Eq. (B.1.2).

$$\begin{aligned} A &= \sum_{j,m} \langle \theta,\varphi,\lambda_1,\lambda_2 | j,m,\lambda_1,\lambda_2 \rangle\langle j,m,\lambda_1,\lambda_2 | U | JM \rangle \\ &= \sum_{jm} \langle \theta,\varphi,\lambda_1,\lambda_2 | j,m,\lambda_1,\lambda_2 \rangle \delta_{mM}\delta_{jJ} A_{\lambda_1\lambda_2} \\ &= \langle \theta,\varphi,\lambda_1,\lambda_2 | J,M,\lambda_1,\lambda_2 \rangle A_{\lambda_1\lambda_2} \end{aligned} \tag{B.1.3}$$

It will be shown that

$$A = \text{constant} \times D^{J*}_{M\lambda}(\varphi,\theta,-\varphi) A_{\lambda_1\lambda_2} \tag{B.1.4}$$

where $\lambda = \lambda_1 - \lambda_2$. This result has a simple interpretation. For a decaying particle α with spin

projection M along z, the decay amplitude is equal to the amplitude for its spin to have projection $\lambda = \lambda_1 - \lambda_2$ along the decay axis $\hat{n}(\theta,\varphi)$, multiplied a constant $A_{\lambda_1\lambda_2}$ giving the coupling to the final state helicities.

The plan of this paper is to derive some properties of rotation operators, to use them to construct the plane-wave and total angular momentum helicity states mentioned above, and then to calculate the scattering and decay angular distributions. Finally, parity and the treatment of identical particles in the helicity formalism are discussed.

B.2 Rotation Operators and the $D^J_{M'M}(\alpha\beta\gamma)$ Functions

In this section we derive several results that will be required for the development of the helicity formalism. Especially important are the $D^J_{M'M}(\alpha\beta\gamma)$ functions, which are matrix elements of the rotation operator $R(\alpha\beta\gamma)$ between angular momentum eigenstates.

B.2.1 The Rotation Operator $R(\alpha\beta\gamma)$

We adopt the active view of rotations in which the Cartesian coordinate axes xyz are fixed, and the physical system is rotated with respect to them. The rotation is specified by attaching another coordinate system XYZ to the physical system and measuring the Euler angles of XYZ with respect to the xyz axes. Referring to Fig. B.1, we see that an arbitrary rotation $R(\alpha\beta\gamma)$ can be constructed from 3 successive rotations: 1) a rotation about the z-axis by an angle α, taking Oy into Ou; 2) a rotation about the u-axis by an angle β, taking Oz into OZ; and finally, 3) a rotation about the Z-axis by γ, taking Ou into OY. The complete rotation is therefore

$$R(\alpha\beta\gamma) = R_Z(\gamma)R_u(\beta)R_z(\alpha) = e^{-i\gamma J_z}e^{-i\beta J_u}e^{-i\alpha J_z} \qquad \text{(B.2.1)}$$

where we have used the fact that a rotation about a given axis $\hat{n}$ is generated by the angular momentum operator $\vec{J}\cdot\hat{n}$. Equation (B.2.1) for the rotation operator is not very useful because it is not expressed in terms of rotations about the original coordinate axes xyz. To do this, recall

that if $|a\rangle$ is a state vector representing some physical system and Q is an observable, then under a rotation R of both the system and observable

$$|a\rangle \rightarrow |a'\rangle = R|a\rangle \tag{B.2.2}$$

and

$$\langle a|Q|a\rangle = \langle a'|Q'|a'\rangle = \langle a|R^{\dagger}Q'R|a\rangle$$

so that

$$Q' = RQR^{\dagger}$$

Applying this rule to the sequence of three rotations that make up $R(\alpha\beta\gamma)$ we have

$$J_u = R_z(\alpha)J_yR_z^{\dagger}(\alpha) \tag{B.2.3}$$

$$J_Z = [R_u(\beta)R_z(\alpha)]J_z[R_u(\beta)R_z(\alpha)]^{\dagger} = R_u(\beta)J_zR_u^{\dagger}(\beta)$$

Substituting these expressions into Eq. (B.2.1) gives

$$R(\alpha\beta\gamma) = \left[R_u(\beta)e^{-i\gamma J_z}R_u^{\dagger}(\beta)\right][R_u(\beta)][R_z(\alpha)]$$

$$= \left[(R_z(\alpha)e^{-i\beta J_y}R_z^{\dagger}(\alpha))e^{-i\gamma J_z}R_u^{\dagger}(\beta)\right][R_u(\beta)][R_z(\alpha)]$$

$$R(\alpha\beta\gamma) = e^{-i\alpha J_z}e^{-i\beta J_y}e^{-i\gamma J_z} \tag{B.2.4}$$

In deriving Eq. (B.2.4) we have exploited the unitarity of the rotation operators, so that, for example

$$\exp[-i\gamma J_Z] = \exp[-i\gamma(R_u(\beta)J_zR_u^{\dagger}(\beta))]$$

$$= R_u(\beta)\exp[-i\gamma J_z]R_u^{\dagger}(\beta) \tag{B.2.5}$$

The expression (B.2.4) is important because it expresses an arbitrary rotation specified by Euler angles (α,β,γ) in terms of rotations about the fixed axes xyz. It appears in almost every paper on the helicity formalism, and, as we will see, it is the origin of the $D^J_{M'M}(\alpha\beta\gamma)$ functions.

B.2.2 Representations of Rotation Operators

It is useful to evaluate explicit matrix representations of R. We will denote a matrix representation of the unitary operator R by $\underset{\sim}{R}$.

B.2.2.1 Rotation of Vectors

A 3×3 representation can be obtained by considering rotations of vectors. The effect of a rotation is to take the unit vectors $\hat{e}_1$, $\hat{e}_2$, $\hat{e}_3$ that point along Ox, Oy, and Oz, respectively, into three new unit vectors $\hat{E}_1$, $\hat{E}_2$, $\hat{E}_3$ that point along OX, OY, and OZ. Thus

$$\hat{E}_j = R[\hat{e}_j] \qquad j = 1,2,3 \tag{B.2.6}$$

Expressing $\hat{E}_j$ in terms of the $\hat{e}_j$ basis vectors we have

$$\hat{E}_j = \sum_{i=1}^{3} \hat{e}_i \underset{\sim}{R}_{ij} \tag{B.2.7}$$

To evaluate the matrix elements $\underset{\sim}{R}_{ij}$ we use orthogonality of the $\hat{e}_i$

$$\hat{e}_k \cdot \hat{E}_j = \sum_{i=1}^{3} \hat{e}_k \cdot \hat{e}_i \underset{\sim}{R}_{ij} = \underset{\sim}{R}_{kj} \tag{B.2.8}$$

$$\underset{\sim}{R}_{ij} = \hat{e}_i \cdot \hat{E}_j$$

One can calculate $\hat{e}_i \cdot \hat{E}_j$ in terms of the Euler angles ($\alpha\beta\gamma$).

Because we can write any vector $\vec{V} = V_j\hat{e}_j$, $\vec{V}$ transforms as

$$\vec{V} \rightarrow \vec{V}' = R[\vec{V}] = \sum_j V_j R[\hat{e}_j] = \sum_j V_j \hat{E}_j = \sum_{i,j} V_j \hat{e}_i \underset{\sim}{R}_{ij} \tag{B.2.9}$$

so that the components of $\vec{V}'$ expressed in the xyz coordinate system are

$$V_i' = \sum_j \underset{\sim}{R}_{ij} V_j \tag{B.2.10}$$

Note the difference between the rule for transforming a basis vector (Eq. B.2.7) and the rule for obtaining the new components of a vector (Eq. B.2.10): the indices on $\underset{\sim}{R}$ are interchanged with respect to the summing index.

B.2.2.2 Rotation of Angular Momentum Eigenstates

The angular momentum eigenstates $|jm\rangle$ transform irreducibly under rotations because $[R,J^2] = 0$. Thus, a representation is labeled by the total angular momentum j. The action of $R(\alpha\beta\gamma)$ on the basis state $|jm\rangle$ is

$$R(\alpha\beta\gamma)|jm\rangle = \sum_{m'=-j}^{j} D^j_{m'm}(\alpha\beta\gamma)|jm'\rangle \tag{B.2.11}$$

$$\langle jm''|R(\alpha\beta\gamma)|jm\rangle = \sum_{m'=-j}^{j} D^j_{m'm}(\alpha\beta\gamma)\langle jm''|jm'\rangle = D^j_{m''m}(\alpha\beta\gamma)$$

These equations are analogous to Eqs. (B.2.7) and (B.2.8). They express the rotated state in terms of the original basis vectors.

Now we use the expression (B.2.4) to calculate $D^j_{mm'}(\alpha\beta\gamma)$

$$D^j_{m'm}(\alpha\beta\gamma) = \langle jm'|e^{-i\alpha J_z}e^{-i\beta J_y}e^{-i\gamma J_z}|jm\rangle$$

Thus

$$D^j_{m'm}(\alpha\beta\gamma) = e^{-i\alpha m'}d^j_{m'm}(\beta)e^{-i\gamma m} \tag{B.2.12}$$

where

$$d^j_{m'm}(\beta) = \langle jm'|e^{-i\beta J_y}|jm\rangle$$

This matrix element is given by the Wigner formula

$$d^j_{m'm}(\beta) = \sum_n \left\{ \frac{(-1)^n [(j+m)!(j-m)!(j+m')!(j-m')!]^{1/2}}{(j-m'-n)!(j+m-n)!(n+m'-m)!n!} \right. \tag{B.2.13}$$

$$\left. \times (\cos\tfrac{1}{2}\beta)^{2j+m-m'-2n}(-\sin\tfrac{1}{2}\beta)^{m'-m+2n} \right\}$$

The sum includes all integers n for which all of the arguments of the factorials are positive. Although Eq. (B.2.13) is somewhat complicated, the $d^j_{m'm}(\beta)$ have many simple properties. Clearly these functions are real and from Eq. (B.2.13)

$$d^j_{m'm}(-\beta) = (-1)^{m'-m} d^j_{m'm}(\beta) \tag{B.2.14}$$

Also, $R^\dagger = R^{-1}$ implies $\langle jm|R|jm'\rangle = \langle jm'|R^{-1}|jm\rangle^*$ so that

$$\left[D^j_{mm'}(0,\beta,0)\right] = \langle jm|e^{-i\beta J_y}|jm'\rangle = \langle jm'|e^{i\beta J_y}|jm\rangle \tag{B.2.15}$$

$$= D^j_{m'm}(0,-\beta,0)$$

where we have used the reality of the $d^j_{m'm}(\beta)$ functions. Thus

$$d^j_{m'm}(-\beta) = d^j_{mm'}(\beta) \tag{B.2.16}$$

Using (B.2.14) and (B.2.16), we find that

$$d^j_{m'm}(\beta) = (-1)^{m'-m} d^j_{mm'}(\beta)$$

and from (B.2.16) we have

$$D^j_{m'm}(\alpha\beta\gamma) = e^{-im'\alpha} d^j_{m'm}(\beta) e^{-im\gamma} = e^{-im\gamma} d^j_{mm'}(-\beta) e^{-im'\alpha}$$

$$= D^j_{mm'}(\gamma,-\beta,\alpha) \tag{B.2.17}$$

From Eq. (B.2.13) we can calculate $d^j_{m'm}(\beta)$ for $\beta = \pi, 2\pi$.

$$d^j_{m'm}(\pi) = (-1)^{j-m}\,\delta_{m',-m}$$

$$d^j_{m'm}(2\pi) = (-1)^{2j}\,d^j_{m'm}(0) = (-1)^{2j}\,\delta_{m'm} \tag{B.2.18}$$

Finally, there is the extremely useful orthogonality relation

$$\int_0^{2\pi} d\alpha \int_0^{2\pi} d\gamma \int_0^{\pi} \sin\beta d\beta \left[D^{j*}_{mn}(\alpha\beta\gamma) D^{j'}_{m'n'}(\alpha\beta\gamma)\right] = \frac{8\pi^2}{2j+1}\,\delta_{mm'}\delta_{nn'}\delta_{jj'} \tag{B.2.19}$$

B.3 Plane-Wave Helicity States

B.3.1 One-Particle Plane-Wave Helicity States

The definition of one-particle plane-wave helicity states is intuitive. In the case of massive particles we begin with the rest state $|\vec{p} = O,s,\lambda\rangle$, which has spin s and spin projection λ along the z-axis. In the rest frame the spin projection and the helicity are equivalent. But when this state is rotated only the helicity $\lambda = \vec{s}\cdot\hat{p}$ remains invariant, and we will use it to label the state. Physically, the invariance is due to the fact that the quantization axis $\hat{p}$ rotates along with the spin $\vec{s}$ of the system.

To obtain the state $|\vec{p},s,\lambda\rangle$, we first rotate $|\vec{p} = 0,s,\lambda\rangle$ so that its quantization axis points along $\hat{p}(\theta,\varphi)$ and then apply a Lorentz boost along $\hat{p}(\theta,\varphi)$.

$$|\vec{p},s,\lambda\rangle = L(\vec{p})R(\alpha = \varphi,\beta = \theta,\gamma = -\varphi)|\vec{p} = 0,s,\lambda\rangle \tag{B.3.1}$$

The choice $\gamma = -\varphi$ is conventional (Jacob and Wick, Ref. (71)), and has no physical meaning. It is convenient because as $\theta \to 0$

$$R(\varphi,\theta,-\varphi)|\vec{p} = 0,s,\lambda\rangle = \sum_{M'} D^j_{M'\lambda}(\varphi,\theta = 0,-\varphi)|\vec{p} = 0,s,M'\rangle$$

$$= \sum_{M'} e^{-i\varphi M'} \delta_{M'\lambda} e^{i\varphi\lambda} |\vec{p} = 0, s, M'\rangle$$

$$= |\vec{p} = 0, s, \lambda\rangle \tag{B.3.2}$$

independently of φ. The notation $L(\vec{p})$ means: boost the rest-frame particle with velocity V along $\hat{p}(\theta,\varphi)$ such that its final momentum is $\vec{p}$.

This procedure is completely equivalent to one in which we first boost along the z-axis and then rotate to the $\hat{p}(\theta,\varphi)$ direction, because

$$|\vec{p}, s, \lambda\rangle = L(\vec{p}) R(\varphi,\theta,-\varphi) |\vec{p} = 0, s, \lambda\rangle$$

$$= R(\varphi,\theta,-\varphi)[R^{-1}(\varphi,\theta,-\varphi) L(\vec{p}) R(\varphi,\theta,-\varphi)] |\vec{p} = 0, s, \lambda\rangle$$

$$= R(\varphi,\theta,-\varphi) L(\vec{p}_z = p\hat{z}) |\vec{p} = 0, s, \lambda\rangle \tag{B.3.3}$$

where we have used

$$L(\vec{p}) = R(\varphi,\theta,-\varphi) L(\vec{p}_z = p\hat{z}) R^{-1}(\varphi,\theta,-\varphi)$$

There is one more phase question. To obtain the state $|-\vec{p}_z, s, \lambda\rangle$ we use Eq. (B.3.1) or Eq. (B.3.3) with $\theta = \pi$, but there is no unique choice for φ. The ambiguity can be removed by imposing the desirable condition

$$\lim_{-\vec{p}_z \to 0} |-\vec{p}_z, s, \lambda\rangle = \lim_{\vec{p}_z \to 0} |\vec{p}_z, s, -\lambda\rangle \tag{B.3.4}$$

Because (using Eq. (B.2.18))

$$e^{-i\pi J_y} |\vec{p} = 0, s, \lambda\rangle = \sum_{\lambda'} D^s_{\lambda'\lambda}(0,\pi,0) |\vec{p} = 0, s, \lambda'\rangle$$

$$= \sum_{\lambda'} (-1)^{s-\lambda} \delta_{\lambda',-\lambda} |\vec{p} = 0, s, \lambda'\rangle$$

$$= (-1)^{s-\lambda} \, |\vec{p} = 0,s,-\lambda\rangle \tag{B.3.5}$$

we have

$$(-1)^{s-\lambda} e^{-i\pi J_y} |\vec{p} = 0,s,\lambda\rangle = |\vec{p} = 0,s,-\lambda\rangle \tag{B.3.6}$$

Comparing with Eq. (B.3.4) we see that the definition is

$$|-\vec{p}_z,s,\lambda\rangle = (-1)^{s-\lambda} e^{-i\pi J_y} \, |\vec{p}_z,s,\lambda\rangle \tag{B.3.7}$$

Equations (B.3.6) and (B.3.7) will be important when we consider the action of the parity operator on helicity states.

Finally, we choose the Lorentz invariant normalization

$$\langle \vec{p}',s',\lambda' | \vec{p},s,\lambda\rangle = (2\pi)^3 \, 2E \, \delta^3(\vec{p}'-\vec{p}) \, \delta_{s's} \, \delta_{\lambda'\lambda} \tag{B.3.8}$$

There is no difficulty in treating photons in the helicity formalism. For massive states we can go to the rest frame and thereby obtain all the states $|\vec{p} = 0,s,\lambda\rangle$, $\lambda = -s,-s+1,...s$ by applying the angular momentum lowering operator $J_- = J_x - iJ_y$ to $|\vec{p} = 0,s,s\rangle$, but we cannot do this for photons. Instead, the photon helicity states $|\vec{p},\lambda = +1\rangle$ and $|\vec{p},\lambda = -1\rangle$ are related with the help of the parity operator. See Ref. (71) for details.

B.3.2 Two-Particle Plane-Wave Helicity States in the Center of Mass Frame

We now construct states that represent two particles that are in plane-wave states with momenta $\vec{p}_1$ and $\vec{p}_2$. They are simply the direct product states

$$|\vec{p}_1\lambda_1; \vec{p}_2\lambda_2\rangle \equiv |\vec{p}_1,s_1,\lambda_1\rangle \otimes |\vec{p}_2,s_2,\lambda_2\rangle \tag{B.3.9}$$

The spins s_1 and s_2 of the two particles are fixed and will be suppressed. The Lorentz invariant normalization is obvious from (B.3.8)

$$\langle \vec{p}'_1\lambda'_1;\vec{p}'_2\lambda'_2|\vec{p}_1\lambda_1;\vec{p}_2\lambda_2\rangle = (2\pi)^6 4E_1E_2\delta^3(\vec{p}'_1-\vec{p}_1)\delta^3(\vec{p}'_2-\vec{p}_2)\delta_{\lambda'_1\lambda_1}\delta_{\lambda'_2\lambda_2} \tag{B.3.10}$$

We now pick the CM frame, so that $\vec{p}_1 = -\vec{p}_2 = \vec{p}$. Because the particles are back to back, we can now specify the same two-particle state in terms of spherical coordinates p,θ,φ, where $p = |\vec{p}_1| = |\vec{p}_2|$ and (θ,φ) are the angles of $\hat{p}_1$. The state vector is written $|p\theta\varphi\lambda_1\lambda_2\rangle$. It is shown in Section B.8 that the normalization expressed in spherical coordinates is

$$\langle p'\theta'\varphi'\lambda'_1\lambda'_2|p\theta\varphi\lambda_1\lambda_2\rangle = (2\pi)^6\frac{4\sqrt{s}}{p}\,\delta^4(\mathbf{P}'^{\alpha}-\mathbf{P}^{\alpha})\delta(\cos\theta'-\cos\theta)\delta(\varphi'-\varphi)\times\delta_{\lambda'_1\lambda_1}\delta_{\lambda'_2\lambda_2} \tag{B.3.11}$$

where $\mathbf{P}^{\alpha} = \mathbf{P}_1^{\alpha} + \mathbf{P}_2^{\alpha}$ is the total 4-momentum in the CM frame

$$\mathbf{P}^{\alpha} = (E,0,0,0) \qquad E = E_1 + E_2 = \sqrt{p^2+m_1^2} + \sqrt{p^2+m_2^2} \tag{B.3.12}$$

In effect, we are making a change of variables from $\vec{p}_1$, $\vec{p}_2$ (6 variables = 3 + 3) to $\mathbf{P}^{\alpha}$, $\cos\theta,\varphi$ (6 variables = 4 + 2).

Because the two-particle CM plane-wave states are eigenstates of total four-momentum $\mathbf{P}^{\alpha}$, it is useful to factor out the eigenstate $|\mathbf{P}^{\alpha}\rangle$. From (B.3.11) we see that a convenient factorization is

$$|p\theta\varphi\lambda_1\lambda_2\rangle = (2\pi)^3\left[\frac{4\sqrt{s}}{p}\right]^{1/2}|\theta\varphi\lambda_1\lambda_2\rangle|\mathbf{P}^{\alpha}\rangle \tag{B.3.13}$$

The factorization has been chosen so that the normalization (B.3.11) is preserved if we define the normalization of $|\mathbf{P}^{\alpha}\rangle$ and $|\theta\varphi\lambda_1\lambda_2\rangle$ to be

$$\langle \mathbf{P}'^{\alpha}|\mathbf{P}^{\alpha}\rangle = \delta^4(\mathbf{P}'^{\alpha}-\mathbf{P}^{\alpha}) \tag{B.3.14}$$

$$\langle \theta'\varphi'\lambda'_1\lambda'_2|\theta\varphi\lambda_1\lambda_2\rangle = \delta(\cos\theta'-\cos\theta)\delta(\varphi'-\varphi)\delta_{\lambda'_1\lambda_1}\delta_{\lambda'_2\lambda_2} \tag{B.3.15}$$

We will see later that Eq. (B.3.14) is the source of the four-momentum conserving δ-function that

is always factored out of the (momentum conserving) S-matrix.

B.4 Construction of Two-Particle States with Definite Total Angular Momentum: The Two-Particle Spherical-Wave Helicity Basis

To apply conservation of angular momentum to the transition matrix element, it is necessary to use eigenstates of total angular momentum as the basis for our two-particle CM states. These new basis states will be denoted by $|p,J,M,\lambda_1,\lambda_2\rangle$. Here p is the magnitude of the momentum of either particle, J is the total angular momentum of the two-particle system, M is the eigenvalue of J_z, and λ_1,λ_2 are the helicities of the two particles.Note that p,J,λ_1,λ_2 are all invariant under rotations and thus can be specified simultaneously with M. It may seem strange that p appears in the definition of these states, since neither particle is in an eigenstate of $\vec{P}$. But recall that we are specifying the magnitude, not the direction, of $\vec{p}$. A more intuitive label would be the total center of mass energy

$$E = \sqrt{m_1^2 + p^2} + \sqrt{m_2^2 + p^2} \tag{B.4.1}$$

but the use of p is conventional.

Because the $|p,J,M,\lambda_1,\lambda_2\rangle$ states are eigenstates of total angular momentum, they transform irreducibly under rotations

$$|p,J,M,\lambda_1,\lambda_2\rangle \rightarrow \sum_{M'} D^J_{M'M}(\alpha\beta\gamma)|p,J,M',\lambda_1,\lambda_2\rangle \tag{B.4.2}$$

The two particle plane-wave states $|p,\theta,\varphi,\lambda_1,\lambda_2\rangle$, which we defined as the direct products of two one-particle plane-wave states, do not have definite J,M. Under rotations they transform according to a fully reducible representation $\underset{\sim}{R}$ of the rotation group. (To say that $\underset{\sim}{R}$ is fully reducible means that it can be decomposed into a direct sum over all irreducible representations specified by J,M. In less abstract terms, the matrix $\underset{\sim}{R}$ that rotates $|p,\theta,\varphi,\lambda_1,\lambda_2\rangle$ is a block diagonal

matrix. Each block is responsible for transforming the components of $|p,\theta,\varphi,\lambda_1,\lambda_2\rangle$ with a particular value of J. Of course, $\underset{\sim}{R}$ and $|p,\theta,\varphi,\lambda_1,\lambda_2\rangle$ are then both written in terms of the $|p,J,M,\lambda_1,\lambda_2\rangle$ basis.) What is the transformation between these two bases? We write the expansion

$$|p,\theta,\varphi,\lambda_1,\lambda_2\rangle = \sum_{J,M} c_{JM}(p,\theta,\varphi,\lambda_1,\lambda_2)|p,J,M,\lambda_1,\lambda_2\rangle \tag{B.4.3}$$

To determine the coefficients c_{JM} we use a trick: it is easy to evaluate them for $\theta = \varphi = 0$. This direction corresponds to the z-axis, along which M is quantized. We have

$$|p,\theta = 0,\varphi = 0,\lambda_1,\lambda_2\rangle = \sum_{JM} c_{JM}(p,\theta = 0,\varphi = 0,\lambda_1,\lambda_2)|p,J,M,\lambda_1,\lambda_2\rangle. \tag{B.4.4}$$

Physically, this vector represents two oppositely moving particles in plane-wave states with momenta $\vec{p}_1 = p\hat{z}, \vec{p}_2 = -p\hat{z}$ and with helicities λ_1,λ_2. As we have noted before, this type of state has no orbital angular momentum component along the direction $\hat{p}$, because $\vec{L} = \vec{r} \times \vec{p}$. Hence, $|p,\theta = 0,\varphi = 0,\lambda_1,\lambda_2\rangle$ is an eigenstate of J_z with eigenvalue $\lambda = \lambda_1 - \lambda_2$, and the only terms on the right-hand side of Eq. (B.4.4) are those with $M = \lambda$.

$$|p,\theta = 0,\varphi = 0,\lambda_1,\lambda_2\rangle = \sum_{J} c_{J\lambda}(p,\theta = 0,\varphi = 0,\lambda_1,\lambda_2)|p,J,\lambda,\lambda_1,\lambda_2\rangle \tag{B.4.5}$$

Now we rotate back to the original state

$$\begin{aligned}|p,\theta,\varphi,\lambda_1,\lambda_2\rangle &= R(\varphi,\theta,-\varphi)|p,\theta = 0,\varphi = 0,\lambda_1,\lambda_2\rangle \\ &= \sum_{J,M'} c_{J\lambda}(p,\theta = 0,\varphi = 0,\lambda_1,\lambda_2) D^J_{M'\lambda}(\varphi,\theta,-\varphi)|p,J,M',\lambda_1,\lambda_2\rangle \end{aligned} \tag{B.4.6}$$

Referring back to Eq. (B.4.3), we can read off the coefficients c_{JM}

$$c_{JM}(p,\theta,\varphi,\lambda_1,\lambda_2) = c_{J\lambda}(p,\theta = 0,\varphi = 0,\lambda_1,\lambda_2) D^J_{M\lambda}(\varphi,\theta,-\varphi) \tag{B.4.7}$$

The coefficients $c_J(p,\theta=0,\varphi=0,\lambda_1,\lambda_2)$ are determined up to phase by normalization. It is shown in the appendix that

$$|c_J|^2 = \frac{2J+1}{4\pi} \tag{B.4.8}$$

and we choose

$$c_J = \sqrt{\frac{2J+1}{4\pi}} \tag{B.4.9}$$

The transformation between the two-particle plane-wave helicity basis and the two-particle spherical-wave helicity basis is therefore

$$|p,\theta,\varphi,\lambda_1,\lambda_2\rangle = \sum_{J,M} \sqrt{\frac{2J+1}{4\pi}}\, D^J_{M\lambda}(\varphi,\theta,-\varphi)|p,J,M,\lambda_1,\lambda_2\rangle \tag{B.4.10}$$

As an example, take $\theta=\varphi=0$ and assume spinless particles, so that $\lambda_1=\lambda_2=0$. Then

$$|p,\theta=0,\varphi=0,0,0\rangle = \sum_{J,M} \sqrt{\frac{2J+1}{4\pi}}\, D^J_{M0}(0,0,0)|p,J,M,0,0\rangle$$

$$= \sum_J \sqrt{\frac{2J+1}{4\pi}}\, |p,J,0,0,0\rangle \tag{B.4.11}$$

Finally, we note that because the $|p,J,M,\lambda_1,\lambda_2\rangle$ states have total momentum $\vec{P}=0$, they are eigenstates of total four-momentum $\mathbf{P}^\alpha$. This is simply because we are working in the CM frame. It is therefore useful to factor out the $|\mathbf{P}^\alpha\rangle$ part of the vector as in Eq. (B.3.13).

$$|p,J,M,\lambda_1,\lambda_2\rangle = (2\pi)^3 \left[\frac{4\sqrt{s}}{p}\right]^{1/2} |J,M,\lambda_1,\lambda_2\rangle|\mathbf{P}^\alpha\rangle \tag{B.4.12}$$

Substituting (B.3.13) and (B.4.12) into the transformation equation (B.4.10), we find, because $|\mathbf{P}^\alpha\rangle$ is invariant under rotations,

$$|\theta,\varphi,\lambda_1,\lambda_2\rangle = \sum_{J,M} \sqrt{\frac{2J+1}{4\pi}}\, D^J_{M\lambda}(\varphi,\theta,-\varphi)|J,M,\lambda_1,\lambda_2\rangle \tag{B.4.13}$$

To invert Eq. (B.4.10) or Eq. (B.4.13) we use the orthogonality relation between the D^J functions, Eq. (B.2.19), with $\alpha = -\gamma$. Thus

$$|J,M,\lambda_1,\lambda_2\rangle = \sqrt{\frac{2J+1}{4\pi}} \int_0^{2\pi} d\varphi \int_{-1}^{1} d\cos\theta \left[D^{J*}_{M\lambda}(\varphi,\theta,-\varphi)|\theta,\varphi,\lambda_1,\lambda_2\rangle\right] \tag{B.4.14}$$

An especially useful form is the inner-product

$$\langle J,M,\lambda'_1,\lambda'_2|\theta,\varphi,\lambda_1,\lambda_2\rangle = \delta_{\lambda'_1\lambda_1}\delta_{\lambda'_2\lambda_2} \sqrt{\frac{2J+1}{4\pi}}\, D^J_{M\lambda}(\varphi,\theta,-\varphi) \tag{B.4.15}$$

where

$$\lambda = \lambda_1 - \lambda_2 \ .$$

B.5 Angular Distributions

B.5.1 Two-Body Scattering

We consider now the process $a + b \to c + d$ in the center of mass frame. Let the helicities of the particles be $\lambda_a,\lambda_b,\lambda_c,\lambda_d$. The initial state particles a,b have momenta $\vec{p}_a = p_i\hat{z}$ and $\vec{p}_b = -p_i\hat{z}$; the final state particles have momenta $\vec{p}_c = \vec{p}_f$ and $\vec{p}_d = -\vec{p}_f$. Thus, the initial and final two-particle plane-wave helicity states are:

$$|i\rangle = |p_i,\theta_i = 0,\varphi_i = 0,\lambda_a,\lambda_b\rangle = (2\pi)^3 \left[\frac{4\sqrt{s}}{p_i}\right]^{1/2} |\theta_i = 0,\varphi_i = 0,\lambda_a,\lambda_b\rangle|\mathbf{P}_i^{\alpha}\rangle$$

$$|f\rangle = |p_f,\theta_f,\varphi_f,\lambda_c,\lambda_d\rangle = (2\pi)^3 \left[\frac{4\sqrt{s}}{p_f}\right]^{1/2} |\theta_f,\varphi_f,\lambda_c,\lambda_d\rangle|\mathbf{P}_f^{\alpha}\rangle \tag{B.5.1}$$

The transition amplitude for scattering from $|i\rangle$ to $|f\rangle$ is

$$\langle f|T|i\rangle = (2\pi)^6 4\sqrt{\frac{s}{p_i p_f}}\langle \mathbf{P}_f^a|\langle\theta_f,\varphi_f,\lambda_c,\lambda_d|T|0,0,\lambda_a,\lambda_b\rangle|\mathbf{P}_i^a\rangle \tag{B.5.2}$$

Because T conserves energy; but may depend on it, we have

$$\langle f|T|i\rangle = (2\pi)^6 \langle \mathbf{P}_f^a|\mathbf{P}_i^a\rangle\, 4\sqrt{\frac{s}{p_i p_f}}\,\langle\theta_f,\varphi_f,\lambda_c,\lambda_d|T(s)|0,0,\lambda_a,\lambda_b\rangle$$

$$= (2\pi)^4\,\delta^4(\mathbf{P}_f^a - \mathbf{P}_i^a)(2\pi)^2\, 4\sqrt{\frac{s}{p_i p_f}}\,\langle\theta_f,\varphi_f,\lambda_c,\lambda_d|T(s)|0,0,\lambda_a,\lambda_b\rangle \tag{B.5.3}$$

It is conventional when defining the T-matrix to factor out the four-momentum conserving δ-function

$$S_{fi} = \delta_{fi} + i(2\pi)^4\,\delta^4(\mathbf{P}_f^a - \mathbf{P}_i^a)T_{fi} \tag{B.5.4}$$

We will write (ignoring the i)

$$\langle f|T|i\rangle = (2\pi)^2\, 4\sqrt{\frac{s}{p_f p_i}}\,\langle\theta_f,\varphi_f,\lambda_c,\lambda_d|T(s)|0,0,\lambda_a,\lambda_b\rangle \tag{B.5.5}$$

We can now exploit conservation of angular momentum by inserting complete sets of the two-particle spherical helicity states and using Eq. (B.4.15)

$$\langle f|T|i\rangle = (2\pi)^2\, 4\sqrt{\frac{s}{p_i p_f}}\sum_{JM}\sum_{J'M'}\langle\theta_f\varphi_f\lambda_c\lambda_d|JM\lambda_c\lambda_d\rangle$$

$$\times\,\langle JM\lambda_c\lambda_d|T(s)|J'M'\lambda_a\lambda_b\rangle\,\langle J'M'\lambda_a\lambda_b|\theta_i = 0,\varphi_i = 0,\lambda_a\lambda_b\rangle$$

$$= (2\pi)^2\, 4\sqrt{\frac{s}{p_i p_f}}\sum_{JMJ'M'}\left[\frac{2J+1}{4\pi}\right]^{1/2}\left[\frac{2J'+1}{4\pi}\right]^{1/2} D^{*J}_{M\lambda_f}(\varphi_f,\theta_f,-\varphi_f)$$

$$\times\,\delta_{JJ'}\delta_{MM'}\,\langle\lambda_c\lambda_d|T^J(s)|\lambda_a\lambda_b\rangle \times D^{J'}_{M'\lambda_i}(0,0,0)$$

$$\langle f|T|i\rangle = (2\pi)^2 4\sqrt{\frac{s}{p_i p_f}} \sum_J \left[\frac{2J+1}{4\pi}\right] D^{J*}_{\lambda_i,\lambda_f}(\varphi_f,\theta_f,-\varphi_f)\langle\lambda_c\lambda_d|T^J(s)|\ \ \lambda_a\lambda_b\rangle \tag{B.5.6}$$

where $\lambda_i = \lambda_a - \lambda_b$ and $\lambda_f = \lambda_c - \lambda_d$. Let

$$T_{\lambda_c\lambda_d;\lambda_a\lambda_b} = \langle\lambda_c\lambda_d|T^J(s)|\lambda_a\lambda_b\rangle \tag{B.5.7}$$

we have

$$\langle f|T|i\rangle = 4\pi\sqrt{\frac{s}{p_i p_f}} \sum_J (2J+1)e^{i[\lambda_i-\lambda_f]\varphi_f}\, d^J_{\lambda_i,\lambda_f}(\theta_f) T^J_{\lambda_c\lambda_d;\lambda_a\lambda_b}(s) \tag{B.5.8}$$

The probability for a transition to final state particles with direction θ_f,φ_f, as a function of θ_f,φ_f–the angular distribution–is given by

$$\frac{d\sigma}{d\Omega_f}(\theta_f,\varphi_f) = \alpha|\langle f|T|i\rangle|^2 \tag{B.5.9}$$

The overall constant α comes from phase space factors and can be ignored if one is calculating only the angular distribution.

B.5.2 Two-Body Decays and Sequential Two-Body Decays

We now obtain the decay angular distribution for $a \to 1 + 2$, where the decaying particle a has mass m_a, spin J, and spin projection M along an arbitrarily chosen z-axis. The final state particles 1,2 have helicities λ_1,λ_2 and momenta $\vec{p}_1 = \vec{p}_f$, $\vec{p}_1 = -\vec{p}_f$. As usual, we work in the CM frame (rest frame of particle a). From Eq. (B.3.13) the two-particle plane-wave helicity final state is

$$|f\rangle = |p_f\theta_f\varphi_f\lambda_1\lambda_2\rangle = (2\pi)^3\left[\frac{4m_a}{p_f}\right]^{1/2}|\theta_f\varphi_f\lambda_1\lambda_2\rangle|\mathbf{P}^a_f\rangle \tag{B.5.10}$$

Here θ_f,φ_f are the polar angles of $\vec{p}_f$. The amplitude for a to decay into the state $|f\rangle$ is

$$A(a \to f) = (2\pi)^3 \left[\frac{4m_a}{p_f}\right]^{1/2} \langle \theta_f \varphi_f \lambda_1 \lambda_2 | U | JM \rangle \tag{B.5.11}$$

where the momentum conserving δ-function has been suppressed. We will also ignore the constants in Eq. (B.5.11), as they have no effect on the angular distribution. To exploit conservation of angular momentum we insert the two-particle spherical helicity basis states $|J_f M_f \lambda_1 \lambda_2\rangle$ and use Eq. (B.4.15)

$$\begin{aligned} A(a \to f) &= \langle \theta_f \varphi_f \lambda_1 \lambda_2 | U | JM \rangle \\ &= \sum_{J_f, M_f} \langle \theta_f \varphi_f \lambda_1 \lambda_2 | J_f M_f \lambda_1 \lambda_2 \rangle \langle J_f M_f \lambda_1 \lambda_2 | U | JM \rangle \\ &= \sum_{J_f, M_f} \left[\frac{2J+1}{4\pi}\right]^{1/2} D^{J*}_{M_f \lambda}(\varphi_f, \theta_f, -\varphi_f)\, \delta_{J_f J} \delta_{M_f M} \langle \lambda_1 \lambda_2 | U | M \rangle \end{aligned} \tag{B.5.12}$$

The matrix element $\langle \lambda_1 \lambda_2 | U | M \rangle$ must be rotationally invariant, so it is more precise to write it as $A_{\lambda_1 \lambda_2}$ with no M dependence, The amplitude for $a \to f$ is therefore

$$A(a \to f) = \left[\frac{2J+1}{4\pi}\right]^{1/2} D^{J*}_{M\lambda}(\varphi_f, \theta_f, -\varphi_f) A_{\lambda_1 \lambda_2} \tag{B.5.13}$$

where $\lambda = \lambda_1 - \lambda_2$. The decay probability is, of course, $|A(a \to f)|^2$, and if the experiment does not measure the final state helicities λ_1, λ_2 they must be summed over. The angular distribution is

$$\frac{d\sigma}{d\Omega_f}(\theta_f, \varphi_f) = \sum_{\lambda_1, \lambda_2} \left| \left[\frac{2J+1}{4\pi}\right]^{1/2} D^{J*}_{M\lambda}(\varphi_f, \theta_f, -\varphi_f) A_{\lambda_1 \lambda_2} \right|^2 \tag{B.5.14}$$

The simplest example is the decay to two spinless particles. The angular distribution is

$$\frac{d\sigma}{d\Omega_f}(\theta_f, \varphi_f) = \frac{2J+1}{4\pi} |D^{J*}_{M0}(\varphi_f, \theta_f, -\varphi_f) A_{00}|^2$$

$$= |Y_J^M(\theta_f,\varphi_f)|^2 \, |A_{00}|^2 \tag{B.5.15}$$

because J must be an integer.

The helicity formalism is easily extended to treat sequential two-body decays. For example, the amplitude for the process

$$a \to 1 + 2$$

$$\quad\;\; \lfloor\!\to 3 + 4$$

where the decaying particle has spin J and the final state particles have helicities $\lambda_1,\lambda_2,\lambda_3,\lambda_4$ is, ignoring overall constants,

$$A(a \to f) = \sum_{\lambda_1} \langle \theta_3\varphi_3\lambda_3\lambda_4 | U(1) | s_1, M_1 = \lambda_1 \rangle \langle \theta_1\varphi_1\lambda_1\lambda_2 | U(a) | JM \rangle$$

$$A(a \to f) = \sum_{\lambda_1} D^{s_1 *}_{\lambda_1,\lambda_3-\lambda_4}(\varphi_3,\theta_3,-\varphi_3)\, D^{J*}_{M,\lambda_1-\lambda_2}(\varphi_1,\theta_1,-\varphi_1) B_{\lambda_3\lambda_4} A_{\lambda_1\lambda_2} \tag{B.5.16}$$

Here we have summed over the allowed helicities of the intermediate particle 1 because they cannot be measured. The angles θ_1,φ_1 are measured in the rest frame of particle a, whereas the angles θ_3,φ_3 are measured in the rest frame of particle 1. (However, φ_3 is the same in both frames.) The z-axis in the frame of particle a is the arbitrarily defined spin-quantization axis for M. The z'-axis in the rest frame of particle 1 is not arbitrary. It is the direction of $\vec{p}_1$ in the particle a rest frame, so that the spin projection along z' is $M_1 = \lambda_1$.

B.6 Parity

The spherical helicity states $|p,J,M,\lambda_1,\lambda_2\rangle$ are not eigenstates of parity. However, we can discover their transformation property by starting with the simpler single-particle plane-wave states from which they are constructed. By exploiting parity conservation in strong and EM interactions we can reduce the number of helicity amplitudes by approximately a factor of 2.

B.6.1 Action of the Parity Operator on Single-Particle Plane-Wave Helicity States

In the rest frame of a single particle state the action of the parity operator Π is simply to multiply the state by its parity eigenvalue η

$$\Pi|\vec{p}=O,s,\lambda\rangle=\eta|\vec{p}=O,s,\lambda\rangle \tag{B.6.1}$$

To find the action of Π on the state $|\vec{p}_z,s,\lambda\rangle$ we use the relations for parity transformed operators

$$L(\vec{p}_z)=\Pi L(-\vec{p}_z)\Pi \tag{B.6.2}$$

$$L(\vec{p}_z)=e^{-i\pi J_y}L(-\vec{p}_z)e^{i\pi J_y}$$

Thus

$$\begin{aligned}\Pi|\vec{p}_z,s,\lambda\rangle&=\Pi L(\vec{p}_z)|\vec{p}=0,s,\lambda\rangle=L(-\vec{p}_z)\Pi|\vec{p}=0,s,\lambda\rangle\\&=\eta\,L(-\vec{p}_z)|\vec{p}=0,s,\lambda\rangle\\&=\eta\,e^{i\pi J_y}L(\vec{p}_z)e^{-i\pi J_y}|\vec{p}=0,s,\lambda\rangle\end{aligned} \tag{B.6.3}$$

With Eq. (B.3.5) to calculate the action of $e^{-i\pi J_y}$ we find

$$\Pi|\vec{p}_z,s,\lambda\rangle=\eta(-1)^{s-\lambda}\,e^{i\pi J_y}|\vec{p}_z,s,-\lambda\rangle \tag{B.6.4}$$

To calculate the effect of parity on a particle with $\vec{p}_z=-p\hat{z}$ we can use Eq. (B.3.7) for $|-\vec{p}_z,s,\lambda\rangle$

in terms of $|\vec{p}_z,s,\lambda\rangle$

$$\Pi|-\vec{p}_z,s,\lambda\rangle = (-1)^{s-\lambda}\, e^{-i\pi J_y}\, \Pi|\vec{p}_z,s,\lambda\rangle \tag{B.6.5}$$

where we have used $[\Pi,R] = 0$ for any rotation operator R. After inserting our previous result Eq. (B.6.4) and using Eq. (B.3.7) with $\lambda \to -\lambda$, we find

$$\Pi|-\vec{p}_z,s,\lambda\rangle = \eta\ |\vec{p}_z,s,-\lambda\rangle = \eta(-1)^{s+\lambda}\, e^{i\pi J_y}|-\vec{p}_z,s,-\lambda\rangle \tag{B.6.6}$$

B.6.2 Action of the Parity Operator on Two-Particle CM Plane-Wave

Helicity States

Now consider the action of the parity operator on a CM plane-wave state representing two particles with momenta $\vec{p}_1 = p\hat{z}$ and $\vec{p}_2 = -p\hat{z}$.

$$\begin{aligned}\Pi|p,\theta = 0,\varphi = 0,\lambda_1,\lambda_2\rangle &= \Pi_1|\vec{p}_z,s_1,\lambda_1\rangle\Pi_2|-\vec{p}_z,s_2,\lambda_2\rangle \\ &= \eta_1\eta_2(-1)^{s_1+s_2-\lambda_1+\lambda_2}\, e^{i\pi J_y(1)}|\vec{p}_z,s_1,-\lambda_1\rangle\, e^{i\pi J_y(2)}|-\vec{p}_z,s_2,-\lambda_2\rangle \\ &= \eta_1\eta_2(-1)^{s_1+s_2-\lambda_1+\lambda_2}\, e^{i\pi J_y}|p,\theta = 0,\varphi = 0,-\lambda_1,-\lambda_2\rangle\end{aligned} \tag{B.6.7}$$

B.6.3 Action of the Parity Operator on Two-Particle CM Spherical

Helicity States

By substituting the spherical helicity state expansion Eq. (B.4.10) for the two-particle plane-wave states on both sides of (B.6.7) we find

$$\Pi\sum_{JM} c_J D^J_{M\lambda}(0,0,0)|p,J,M,\lambda_1,\lambda_2\rangle =$$

$$\eta_1\eta_2(-1)^{s_1+s_2-\lambda_1+\lambda_2}\, e^{i\pi J_y}\sum_{J,M} c_J D^J_{M,-\lambda}(0,0,0)|p,J,M,-\lambda_1,-\lambda_2\rangle \tag{B.6.8}$$

The sums over M are trivial, because

$$D^J_{M\lambda}(0,0,0) = \delta_{M\lambda}$$

To evaluate the right-hand side we use Eq. (B.2.14) and Eq. (B.2.18)

$$e^{i\pi J_y}|p,J,-\lambda,-\lambda_1,-\lambda_2\rangle = \sum_{M'} D^J_{M',-\lambda}(0,-\pi,0)|p,J,M',-\lambda_1,-\lambda_2\rangle$$

$$= (-1)^{J-\lambda}|p,J,\lambda,-\lambda_1,-\lambda_2\rangle \tag{B.6.9}$$

so Eq. (B.6.8) becomes

$$\sum_J c_J \Pi|p,J,\lambda,\lambda_1,\lambda_2\rangle = \eta_1\eta_2(-1)^{s_1+s_2-\lambda_1+\lambda_2}\sum_J c_J(-1)^{J-\lambda}|p,J,\lambda,-\lambda_1,-\lambda_2\rangle \tag{B.6.10}$$

This equation must hold term by term, because states with different J are orthogonal and the parity operator on the left-hand side does not change J. Thus

$$\Pi|p,J,\lambda,\lambda_1,\lambda_2\rangle = \eta_1\eta_2(-1)^{J-s_1-s_2}|p,J,\lambda,-\lambda_1,-\lambda_2\rangle \tag{B.6.11}$$

By applying the raising and lowering operators $J_\pm = J_x \pm iJ_y$ to both sides of Eq. (B.6.11) we can step M from $-J$ to J. Thus

$$\Pi|p,J,M,\lambda_1,\lambda_2\rangle = \eta_1\eta_2(-1)^{J-s_1-s_2}|p,J,M,-\lambda_1,-\lambda_2\rangle \tag{B.6.12}$$

This result is expected: parity changes the sign of the individual helicities, but M is unchanged.

B.6.4 Applications of Parity Conservation to Helicity Amplitudes

For strong and electromagnetic interactions the T-matrix commutes with Π, so for a scattering process $a + b \to c + d$

$$\langle\lambda_d,\lambda_d|T^J|\lambda_a,\lambda_b\rangle = \langle\lambda_c,\lambda_d|\Pi T^J\Pi|\lambda_a,\lambda_b\rangle$$

$$= \frac{\eta_c\eta_d}{\eta_a\eta_b}(-1)^{s_c+s_d-s_a-s_b}\langle-\lambda_c,-\lambda_d|T^J|-\lambda_a,-\lambda_b\rangle \tag{B.6.13}$$

where we have used Eq. (B.6.12) for both the initial and final states.

For the decay process $a \rightarrow 1 + 2$, we have

$$\langle \lambda_1,\lambda_2|U|a\rangle = \langle \lambda_1,\lambda_2|\Pi U \Pi|a\rangle = \eta_1\eta_2\eta_a(-1)^{s_1+s_2-J} \times \langle -\lambda_1,-\lambda_2|U|a\rangle \qquad \text{(B.6.14)}$$

Here J and η_a are the spin and parity of a. The relations (B.6.13) and (B.6.14) reduce the number of independent helicity amplitudes by about a factor of 2. The reader can show trivially that a pseudoscalar cannot decay into two pseudoscalars by a parity conserving interaction.

As an example, consider radiative ψ decay

$$\psi \rightarrow \gamma + X$$

$$\eta_\psi = -1,\ \eta_1 = -1,\ \eta_2 = \eta_X$$

$$J = 1,\ s_1 = 1,\ s_2 = s_X$$

$$\langle \lambda_\gamma,\lambda_X|U|\psi\rangle = \eta_X(-1)^{s_X}\langle -\lambda_\gamma,-\lambda_X|U|\psi\rangle$$

or

$$A_{\lambda_\gamma\lambda_x} = \eta_X(-1)^{s_X}A_{-\lambda_\gamma-\lambda_x} \qquad \text{(B.6.15)}$$

Figure B.2 shows the case $s_X = 2$.

B.6.5 Example: Angular Distribution for $\psi \rightarrow \gamma\eta'$; $\eta' \rightarrow \gamma\rho^\circ$; $\rho^\circ \rightarrow \pi^+\pi^-$

The sequence of two-body decays

$$\psi \rightarrow \gamma_1\, \eta'$$

$$\rightarrow \gamma_2\, \rho^\circ$$

$$\rightarrow \pi^+\pi^-$$

is shown in Fig. B.3. The object is to calculate the angular distribution of the final state particles,

which are γ_1, γ_2, π^+, π^-. Let the helicities of the particles be denoted by

ψ decay	η' decay	ρ° decay
$\lambda_{\eta'} = 0$	$\lambda_\rho = 0, \pm 1$	$\lambda_{\pi^+} = 0$
$\lambda_{\gamma_1} = \pm 1$	$\lambda_{\gamma_2} = \pm 1$	$\lambda_{\pi^-} = 0$

In e^+e^- interactions the ψ is produced with spin-projection $M = \pm 1$ along the beam axis (no $M = 0$!). This is a consequence of the QED interaction $e^+e^- \rightarrow$ virtual γ at energies large compared to the electron mass, where electrons couple to positrons of the opposite helicity only. It is therefore convenient to define the z-axis to be along the beam direction. With unpolarized beams there is no φ dependence and the origin of φ is arbitrary. The amplitude to produce the final state particles with given helicities and angles is

$$A(M,\lambda_{\gamma_1},\lambda_{\gamma_2}) = \sum_{\lambda_\rho} D^{*s(\psi)}_{M,\lambda_{\gamma_1}-\lambda_{\eta'}}(\varphi,\theta,-\varphi)\, A_{\lambda_{\gamma_1}\lambda_{\eta'}} \tag{B.6.16}$$

$$\times\, D^{*s(\eta')}_{-\lambda_{\gamma_1},\lambda_{\gamma_2}-\lambda_\rho}(\varphi',\theta',-\varphi')\, B_{\lambda_{\gamma_2}\lambda_\rho} \times D^{*s(\rho)}_{\lambda_\rho,\lambda_{\pi^+}-\lambda_{\pi^-}}(\varphi'',\theta'',-\varphi'')\, C_{\lambda_{\pi^+}\lambda_{\pi^-}}$$

It is conventional to define the z' and z'' axes by the momentum directions of γ_1 and γ_2. The spin projection of the ρ° along the z'' is therefore $-\lambda_\rho$. Because the η' has spin = 0, $\lambda_{\gamma_2} - \lambda_\rho = 0$ and the ρ° cannot have helicity 0. Mathematically, this follows from the constant $D^{*s(\eta')}$ term, for which $s(\eta') = 0$ forces both subscripts to be 0. Substituting the known values for the spins, we find

$$A(M,\lambda_{\gamma_1},\lambda_{\gamma_2}) = D^{*1}_{M,\lambda_{\gamma_1}}(\varphi,\theta,-\varphi) A_{\lambda_{\gamma_1}} B_{\lambda_{\gamma_2}\lambda_{\gamma_2}} D^{*1}_{-\lambda_{\gamma_2}0}(\varphi'',\theta'',-\varphi'')\, C_{00} \tag{B.6.17}$$

If the photon helicities are not measured, we must sum over final states after squaring the amplitude. The angular distribution is therefore

$$\frac{d^2\sigma}{d\cos\theta_{\gamma_1}\, d\cos\theta''_{\pi^-}} = \tfrac{1}{2} \sum_M \sum_{\lambda_{\gamma_1},\lambda_{\gamma_2}} |A(M,\lambda_{\gamma_1},\lambda_{\gamma_2})|^2 \tag{B.6.18}$$

where we have also averaged over the initial spin states of the ψ. We can ignore the helicity couplings A,B,C because they form one overall factor. This would not have been the case if γ_2 were replaced by a massive particle so that there was an additional coupling to helicity 0. In our example, however, we can relate all couplings in the sum with parity (Eq. (B.6.14)).

$$\begin{aligned} A_{\lambda_1} \equiv A_{\lambda_1,0} &= \eta_\psi \eta_\gamma \eta_{\eta'} (-1)^{s(\gamma)+s(\eta')-s(\psi)} A_{-\lambda_1,0} \\ &= (-1) A_{-\lambda_1,0} \\ B_{1,1} &= \eta_{\eta'} \eta_\gamma \eta_\rho (-1)^{s(\gamma)+s(\rho)-s(\eta')} B_{-1,-1} \\ &= (-1) B_{-1,-1} \end{aligned} \tag{B.6.19}$$

The factors of (-1) are irrelevant in the squared amplitudes. Thus,

$$\begin{aligned} \sum_{\lambda_{\gamma_1},\lambda_{\gamma_2}} |A(M,\lambda_{\gamma_1},\lambda_{\gamma_2})|^2 &= (|d^1_{M,1}(\theta)|^2 + |d^1_{M,-1}(\theta)|^2) \\ &\times (|d^1_{1,0}(\theta'')|^2 + |d^1_{-1,0}(\theta'')|^2 \end{aligned} \tag{B.6.20}$$

Because

$$d^1_{1,0}(\theta'') = d^1_{0,-1}(\theta'') = (-1) d^1_{-1,0}(\theta'') = \frac{-\sin\theta''}{\sqrt{2}} \tag{B.6.21}$$

the second factor in Eq. (B.6.20) is just $\sin^2\theta''$. Also

$$\left.\begin{aligned} d^1_{M,1} = d^1_{-1,-M} &= (-1)^{M-1} \quad d^1_{-M,-1} = d^1_{-M,-1} \\ d^1_{M,-1} = d^1_{1,-M} &= (-1)^{M+1} \quad d^1_{-M,1} = d^1_{-M,1} \end{aligned}\right\} \tag{B.6.22}$$

where we have used the simple properties of the d functions. From Eq. (B.6.22) it is clear that the results for $M = \pm 1$ will be the same. Thus

$$\frac{d^2\sigma}{d\cos\theta_{\gamma_1} d\cos\theta''_{\pi^-}} = \left[\left(\frac{1 + \cos\theta_{\gamma_1}}{2} \right)^2 + \left(\frac{1 - \cos\theta_{\gamma_1}}{2} \right)^2 \right] \sin^2\theta''_{\pi^-}$$

$$= (1 + \cos^2\theta_{\gamma_1}) \sin^2\theta''_{\pi^-} \qquad \text{(B.6.23)}$$

where we have ignored overall constants. It should be emphasized that the angles in this formula are measured in the rest frames of the decaying particles ψ and ρ°. An interesting feature of this result is that there is no azimuthal angle dependence of any kind. This is a consequence of the fact that there were no unmeasurable intermediate helicities to be summed over, and will not, in general, be the case. For example, in $\psi \to \gamma f(1270)$; $f \to \pi^+\pi^-$, the sums over f helicity in the amplitude produce φ' dependence in the angular distribution.

B.6.6 Example: Angular Distribution for $\psi \to$ Vector + Pseudoscalar

The process $e^+e^- \to \psi \to$ Vector + Pseudoscalar provides an example of a nontrivial azimuthal angular dependence. For convenience, we consider $\psi \to \rho^\circ\pi^\circ$; $\rho^\circ \to \pi^+\pi^-$, although there are many other examples ($\varphi\eta$, $\varphi\eta'$, $\omega\eta$, $\omega\eta'$, $\omega\pi^\circ$, ...).

It will be shown below that the $\lambda = 0$ amplitude of the ρ° vanishes by parity conservation, and interference between the $\lambda = +1$ and $\lambda = -1$ amplitudes produces a correlation between the production plane and the decay plane of the ρ°. The production plane is defined by the e^+e^- beam axis (the z-axis) and the ρ° momentum vector (the z'-axis); this plane lies at the azimuthal angle φ about the z-axis in the lab frame. The decay plane is defined by the momentum vector of the π^+ in the ρ° rest frame and the momentum vector of the ρ° in the lab frame. This plane lies at the angle φ' about the z'-axis in the ρ° rest frame. With the phase convention used in this paper, the production plane lies at the azimuthal angle φ in the ρ° rest frame as well as in the lab frame. This follows from the fact that the $x'y'z'$ coordinate axes are obtained from the xyz axes by a rotation with the Euler angles $\alpha = \varphi$, $\beta = \theta$, $\gamma = -\varphi$. Thus, the angle between the production plane and the decay plane, which is the only physically meaningful azimuthal angle, is given by $\Delta\varphi = \varphi' - \varphi$.

The calculation is straightforward. Parity conservation (Eq. B.6.14) provides a relation between the helicity amplitudes

$$A_{\lambda_\rho\lambda_\pi} = \eta_\psi\eta_\rho\eta_\pi(-1)^{J_\psi-J_\rho-J_\pi}A_{-\lambda_\rho-\lambda_\pi} = -A_{-\lambda_\rho-\lambda_\pi} \tag{B.6.24}$$

which implies that $A_{0,0}$ vanishes. The ρ° therefore has helicities $\lambda_\rho = \pm 1$ only. The corresponding amplitudes interfere because the helicities characterize an intermediate state and cannot be determined by any measurement of the final state pions. The ψ, as discussed in the previous example, is produced as an incoherent mixture of $M_\psi = \pm 1$. The decay angular distribution is therefore

$$\frac{dN}{d\Omega} = \sum_{M_\psi} \left| \sum_{\lambda_\rho} D^{*1}_{M_\psi,\lambda_\rho}(\varphi,\theta,-\varphi)A_{\lambda_\rho,0}\, D^{*1}_{\lambda_\rho,0}(\varphi',\theta',-\varphi') \right|^2 \tag{B.6.25}$$

where we have used $\lambda_\pi = 0$. By substituting the D functions, one finds (ignoring overall constants)

$$\frac{dN}{d\Omega} = \Big\{(1 + \cos^2\theta) + \sin^2\theta\cos2(\varphi' - \varphi)\Big\}\sin^2\theta' \tag{B.6.26}$$

As in the decay $\psi \to \gamma\eta'$; $\eta' \to \gamma\rho^\circ$, the absence of helicity zero for the ρ° results in a $\sin^2\theta'$ distribution of the pions in the ρ° rest frame. If one integrates over the azimuthal angle, the ρ° has a $(1 + \cos^2\theta)$ distribution relative to the beam axis.The azimuthal angular dependence is

$$\frac{dN}{d\cos\Delta\varphi} = \Big\{1 + \tfrac{1}{2}\cos2(\varphi' - \varphi)\Big\} \tag{B.6.27}$$

after integrating over the polar angles. Figure B.4 is a histogram of $\Delta\varphi = \varphi' - \varphi$ for $\psi \to \rho^\circ\pi^\circ$ events measured by the Mark III detector. The $\cos2(\varphi' - \varphi)$ dependence is clearly present, although there are dips in the distribution at $\psi = 0,\pi$, and 2π due to the detector acceptance. At these angles the ρ° production and decay planes are aligned, and the charged pions are more

likely to go into the ends of the detector (closer to the beam pipe) where the detection efficiency is low.

The correlation between $\cos\theta$ and $\Delta\varphi$ is shown in Fig. B.5. The acceptance is also poor when $|\cos\theta| \sim 1$, but the approximately uniform horizontal bands at $\Delta\varphi = 0$, π, and 2π are evident, and contrast with the strong horizontal density variation in the bands at $\Delta\varphi = \frac{\pi}{2}$ and $\frac{3\pi}{2}$.

B.7 Symmetrization of Helicity States for Identical Particles

In the helicity formalism is it easy to construct appropriately symmetrized states for the analysis of processes with identical particles. Let P_{12} denote the particle interchange operator, which swaps particles 1 and 2. The action of P_{12} on an identical two-particle plane-wave helicity state aligned along the z-axis is, because $s_1 = s_2 = s$,

$$P_{12}|p,\theta = 0,\varphi = 0,\lambda_1\lambda_2\rangle = P_{12}[|\vec{p}_z,s,\lambda_1,1\rangle|-\vec{p}_z,s,\lambda_2,2\rangle] \tag{B.7.1}$$

The particle labels 1,2 have been added to the one-particle helicity states to indicate which of the two states each particle is in. The quantum numbers λ_1,λ_2 refer to states, not particles. Interchanging the particles gives

$$\begin{aligned} P_{12}|p,\theta = 0,\varphi = 0,\lambda_1\lambda_2\rangle &= |\vec{p}_z,s,\lambda_1,2\rangle|-\vec{p}_z,s,\lambda_2,1\rangle \\ &= (-1)^{s-\lambda_1}\, e^{i\pi J_y(1)}|-\vec{p}_z,s,\lambda_1,2\rangle \\ &\quad \times (-1)^{s-\lambda_2}\, e^{-i\pi J_y(2)}|\vec{p}_z,s,\lambda_2,1\rangle \end{aligned} \tag{B.7.2}$$

Some care is required with half-integer spins, where

$$(-1)^{s-\lambda_1}(-1)^{s-\lambda_2} = (-1)^{2s+\lambda_1+\lambda_2} = (-1)(-1)^{\lambda_1+\lambda_2} = (-1)^{\lambda_2-\lambda_1} \tag{B.7.3}$$

The last expression is also valid for bosons. We note that

$$e^{-i\pi J_y} = e^{i\pi J_y}\, e^{-i2\pi J_y} = e^{i\pi J_y}\,(-1)^{2s} \tag{B.7.4}$$

which says that half-integer spin particles pick up a factor of (-1) when they are rotated by 2π. Using these results in Eq. (B.7.2) gives

$$\begin{aligned} P_{12}|p,\theta=0,\varphi=0,\lambda_1\lambda_2\rangle &= (-1)^{2s+\lambda_2-\lambda_1}\, e^{i\pi J_y}\, |-\vec{p}_z,s,\lambda_1,2\rangle|\vec{p}_z,s,\lambda_2,1\rangle \\ &= (-1)^{2s+\lambda_2-\lambda_1}\, e^{i\pi J_y}|p,\theta=0,\varphi=0,\lambda_2,\lambda_1\rangle \end{aligned} \tag{B.7.5}$$

where the ordering of the λ's in the state vector is now reversed from the LHS of Eq. (B.7.2).

We can quickly determine the action of P_{12} on spherical two-particle helicity states by comparing Eq. (B.7.5) with the action of the parity operator in Eq. (B.6.7). The only differences are that in the present case, $s_1 = s_2 = s$, there are no parity factors, and now the order of the helicities is reversed. Thus, we can read off the answer from Eq. (B.6.12)

$$P_{12}|p,J,M,\lambda_1\lambda_2\rangle = (-1)^{J-2s}|p,J,M,\lambda_2,\lambda_1\rangle \tag{B.7.6}$$

According to the spin-statistics theorem, states of identical bosons must be even under particle exchange, and states of identical fermions must be odd under particle exchange. Thus, the correctly summarized two-particle spherical helicity states are

$$\left[1 + (-1)^{2s}P_{12}\right]|p,J,M,\lambda_1,\lambda_2\rangle = |p,J,M,\lambda_1,\lambda_2\rangle + (-1)^J|p,J,M,\lambda_2,\lambda_1\rangle \tag{B.7.7}$$

The result is the same for bosons and fermions.

As a simple application, we will show that a massive spin-1 particle cannot decay into two photons. From Eq. (B.7.7), the correctly symmetrized two photon CM state is

$$|\Phi\rangle = |p,J=1,M,\lambda_1,\lambda_2\rangle - |p,J=1,M,\lambda_2,\lambda_1\rangle \tag{B.7.8}$$

But $|\lambda_1 - \lambda_2| \leqslant J = 1$ because there can be no orbital angular momentum about the decay axis

($\vec{L} = \vec{r} \times \vec{p}$). For photons, which have no zero helicity component, this implies that $\lambda_1 = \lambda_2$. The two states on the RHS of Eq. (B.7.8) are therefore identical and

$$|\Phi\rangle = 0. \tag{B.7.9}$$

B.8 Normalization of Two-Particle Plane Wave Helicity States

We now show how to normalize the two-particle plane-wave helicity states when they are labeled by $|p,\theta,\varphi,\lambda_1,\lambda_2\rangle$ (Eq. B.3.11). The normalization in the $\vec{p}_1,\vec{p}_2$ coordinates is (Eq. B.3.10)

$$\langle \vec{p}'_1,\lambda'_1;\vec{p}'_2,\lambda'_2|\vec{p}_1,\lambda_1;\vec{p}_2,\lambda_2\rangle = (2\pi)^6 4E_1E_2\delta^3(\vec{p}'_1 - \vec{p}_1)\delta^3(\vec{p}'_2 - \vec{p}_2)\delta_{\lambda'_1\lambda_1}\delta_{\lambda'_2\lambda_2} \tag{B.8.1}$$

We are assuming that all other labels describing internal quantum numbers such as charge, isospin, strangeness, etc. are identical, so that we don't need additional δ-functions on the right-hand side of Eq. (B.8.1). By specifying the state with spherical coordinates, we are making a change of variables from $\vec{p}_1,\vec{p}_2$ to $\vec{\mathbf{P}},p,\theta,\varphi$, where $\vec{\mathbf{P}}$ is the total momentum in the CM and $\vec{p}$ is the momentum of one of the particles. It is easily seen that

$$d^3p_1d^3p_2 = |\mathbf{J}|d^3\mathbf{P}d^3p = d^3\mathbf{P}d^3p = d^3\mathbf{P}p^2dpd^2\Omega \tag{B.8.2}$$

We can find the relation between dp and $d\mathbf{P}^\circ$ from

$$\sqrt{s} = \mathbf{P}^\circ = E_1 + E_2 = \sqrt{p^2 + m_1^2} + \sqrt{p^2 + m_2^2}$$

$$d\mathbf{P}^\circ = pdp\left(\frac{1}{\sqrt{p^2 + m_1^2}} + \frac{1}{\sqrt{p^2 + m_2^2}}\right) = \frac{(E_1 + E_2)pdp}{E_1E_2} = \frac{\sqrt{s}pdp}{E_1E_2}$$

Thus

$$d^3p_1d^3p_2 = d^3\mathbf{P}\left(d\mathbf{P}^\circ\,\frac{pE_1E_2}{\sqrt{s}}\right)d^2\Omega$$

$$= \frac{pE_1E_2}{\sqrt{s}}\, d^4\mathbf{P}d^2\Omega \tag{B.8.3}$$

This change of variables means that

$$\int d^3p_1 d^3p_2 \langle \vec{p}'_1,\lambda'_1;\vec{p}'_2,\lambda'_2|\vec{p}_1,\lambda_1;\vec{p}_2\lambda_2\rangle = \int d^4\mathbf{P}d^2\Omega \frac{pE_1E_2}{\sqrt{s}} \langle p',\theta',\lambda'_1,\lambda'_2|p,\theta,\varphi,\lambda_1,\lambda_2\rangle$$

Using Eq. (B.8.1), we see that

$$(2\pi)^6 4E_1E_2\delta_{\lambda'_1\lambda_1}\delta_{\lambda'_2\lambda_2} = \int d^4\mathbf{P}d^2\Omega \frac{pE_1E_2}{\sqrt{s}} \langle p',\theta',\lambda'_1,\lambda'_2,|p,\theta,\varphi,\lambda_1,\lambda_2\rangle \tag{B.8.4}$$

which implies

$$\langle p',\theta',\varphi',\lambda'_1,\lambda'_2|p,\theta,\varphi,\lambda_1,\lambda_2\rangle = (2\pi)^6 \frac{4\sqrt{s}}{p}\delta^4(\mathbf{P}'^{\alpha}-\mathbf{P}^{\alpha})\delta^2(\Omega'-\Omega)\delta_{\lambda'_1\lambda_1}\delta_{\lambda'_2\lambda_2} \tag{B.8.5}$$

This proves Eq. B.3.11. By definition

$$\langle J',M',\lambda'_1,\lambda'_2|J,M,\lambda_1,\lambda_2\rangle = \delta_{J'J}\delta_{M'M}\delta_{\lambda'_1\lambda_1}\delta_{\lambda'_2\lambda_2} \tag{B.8.6}$$

Using Eq. (B.4.14) with c_J unknown and Eq. (B.3.15) we have

$$\langle J',M',\lambda'_1,\lambda'_2|J,M,\lambda_1,\lambda_2\rangle = |c_J|^2 \int\int d^2\Omega d^2\Omega' D^{J}_{M',\lambda'}(\varphi',\theta',-\varphi')D^{J*}_{M,\lambda}(\varphi,\theta,-\varphi)$$

$$\times\, \delta^2(\Omega'-\Omega)\delta_{\lambda'_1\lambda_1}\delta_{\lambda'_2\lambda_2} \tag{B.8.7}$$

Performing the integral over $d^2\Omega'$ and using orthogonality of the D^J functions with $\alpha = -\gamma = \varphi$ (Eq. B.2.19) gives

$$\langle J',M',\lambda'_1,\lambda'_2|J,M,\lambda_1\lambda_2\rangle = \frac{4\pi}{2J+1}\, |c_J|^2\, \delta_{J'J}\delta_{M'M}\delta_{\lambda'_1\lambda_1}\delta_{\lambda'_2\lambda_2} \tag{B.8.8}$$

By comparing Eq. (B.8.8) with Eq. (B.8.6) we see that

$$|c_J|^2 = \frac{2J+1}{4\pi} \tag{B.8.9}$$

as claimed.

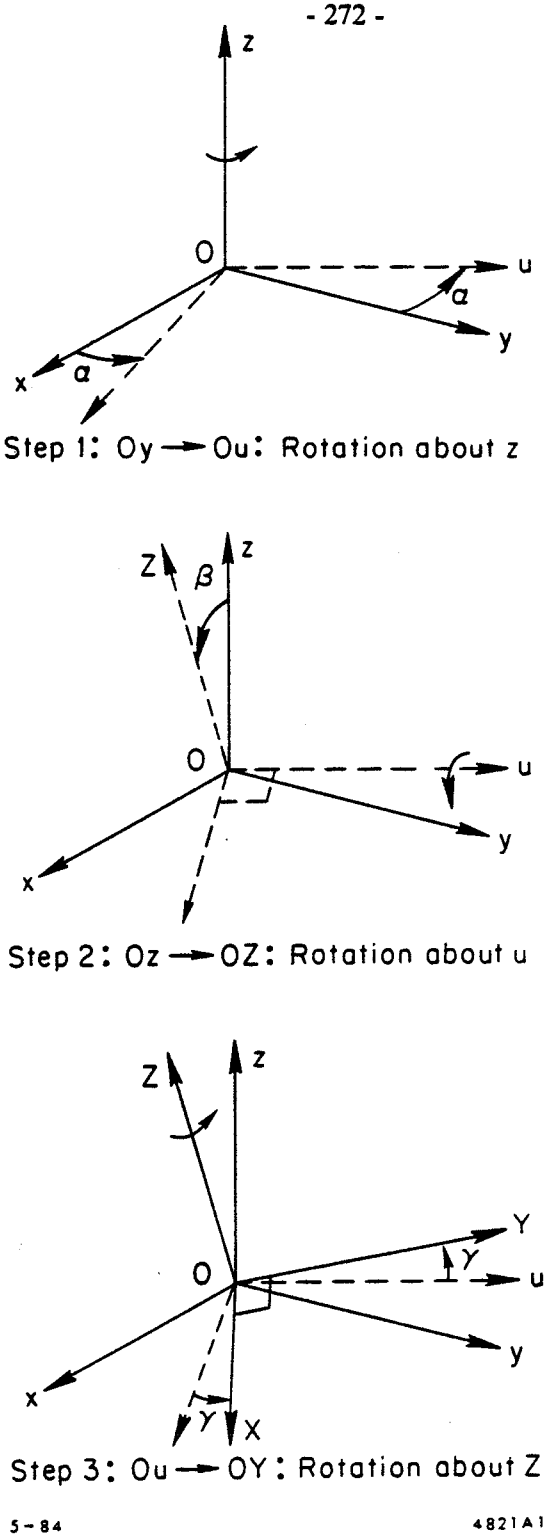

Figure B.1. Construction of an arbitrary rotation by three successive rotations parametrized by Euler angles α,β,γ.

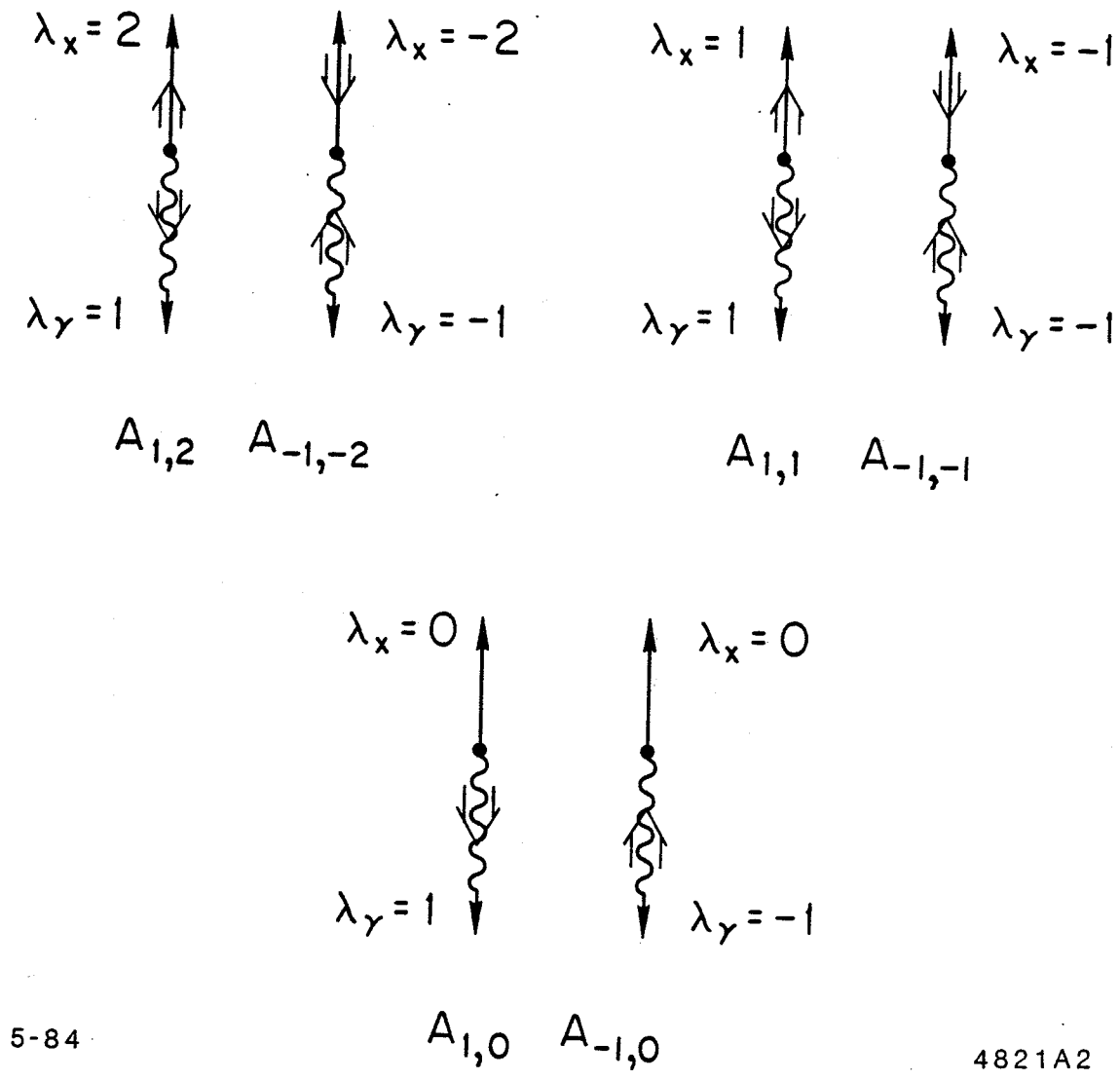

Figure B.2. Allowed decay processes $\psi \rightarrow \gamma X$, where X is a spin-2 particle. The two processes in each pair are related by parity because $\vec{s} \cdot \vec{p} \rightarrow \vec{s} \cdot (-\vec{p})$. The matrix elements $A_{\lambda_\gamma \lambda_x}$ and $A_{-\lambda_\gamma -\lambda_x}$ have a relative +(-) sign if the parity of X is even (odd). The photon is represented by a wavy line and spin projections are denoted by double arrows. Note that $|\lambda_\gamma - \lambda_X| \leqslant J = 1$ because there can be no orbital angular momentum about the decay axis ($\vec{L} = \vec{r} \times \vec{p}$). The $A_{i,j}$ are rotationally invariant.

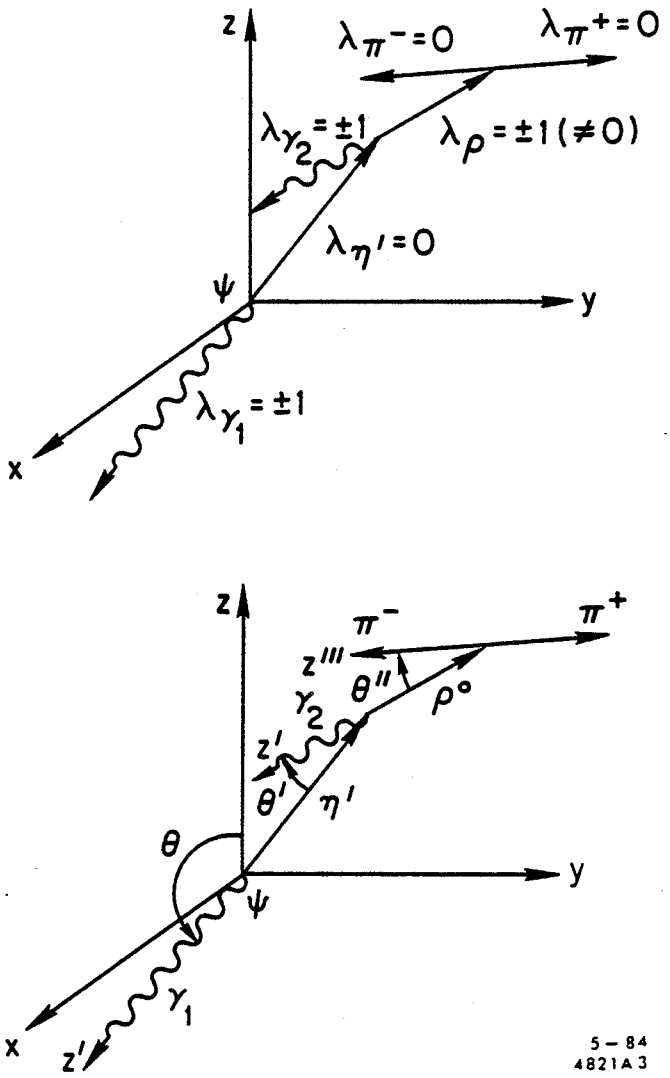

Figure B.3. Helicities and decay angle definitions for $\psi \to \gamma\eta'$; $\eta' \to \gamma\rho^\circ$; $\rho^\circ \to \pi^+\pi^-$. Each decay is viewed in the rest frame of the decaying particle.

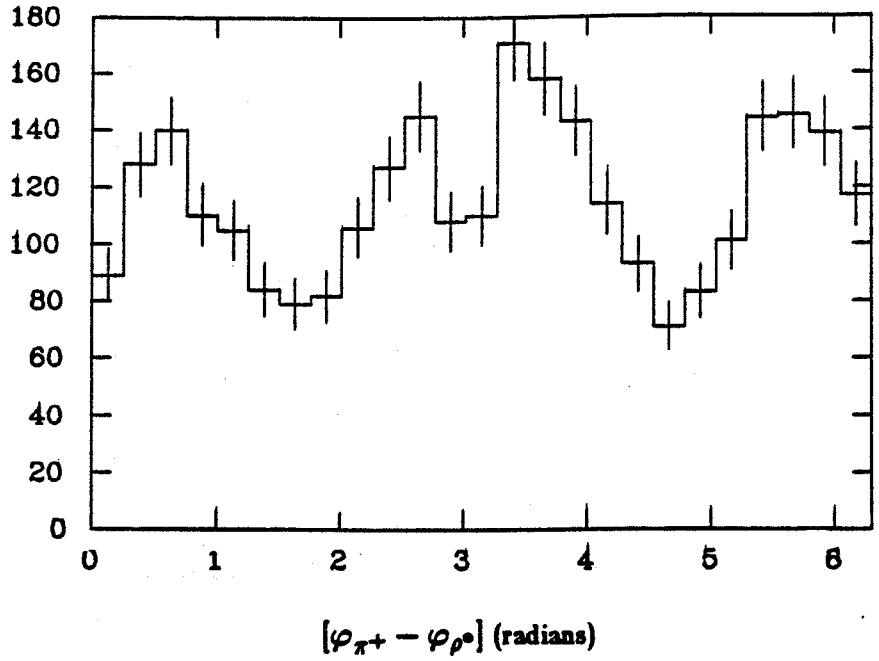

Figure B.4. Distribution of $\rho^{\circ}\pi^{\circ}$ events in $\Delta\varphi$. The $\cos 2\Delta\varphi$ dependence is due to interference between the $\lambda_{\rho} = \pm 1$ amplitudes.

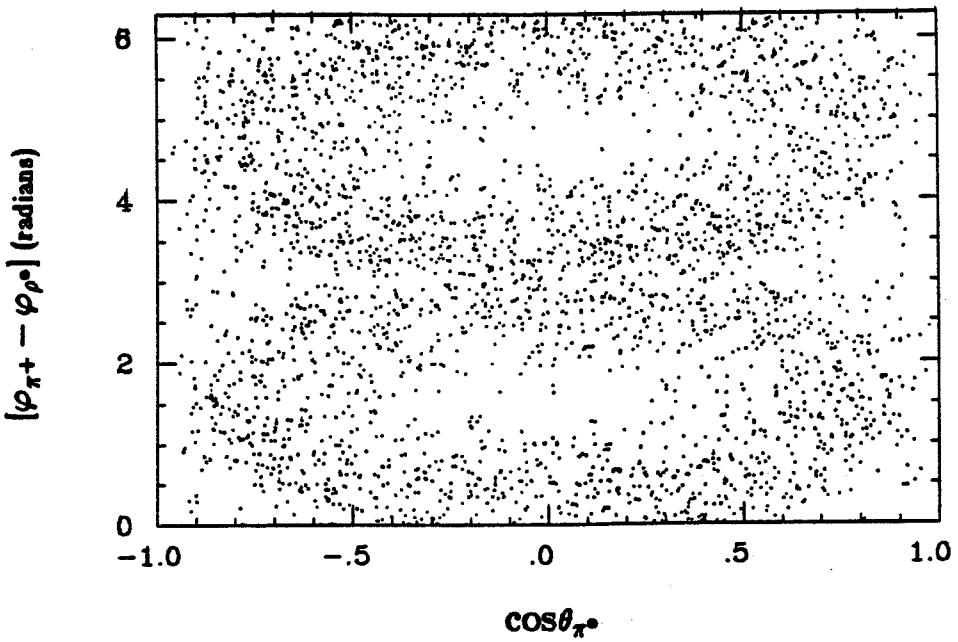

Figure B.5. Scatter plot of $\Delta\varphi$ vs. $\cos\theta$ for $\rho^0\pi^0$ events.

References

1. J.J. Aubert *et al.*, Phys. Rev. Lett. **33**, 1404 (1974); J.E. Augustin *et al.*, Phys. Rev. Lett. **33**, 1406 (1974).

2. S.L. Glashow, J. Iliopoulos, L. Maiani, Phys. Rev. **D2**, 1285 (1970); M.K. Gaillard and B.W. Lee, Phys. Rev. **D10**, 897 (1974); E.D. Commins and P.H. Bucksbaum, *Weak Interactions of Quarks and Leptons*, Cambridge University Press, Cambridge (1983), p. 249.

3. F. Halzen and A.D. Martin, *Quarks and Leptons: An Introductory Course in Modern Particle Physics*, John Wiley and Sons, New York (1984).

4. D.J. Gross and F. Wilczek, Phys. Rev. Lett. **304**, 1343 (1973); H.D. Politzer, Phys. Reports **14C**, 129 (1974).

5. T. Appelquist and H.D. Politzer, Phys. Rev. Lett. **34**, 43 (1975); T. Appelquist and H.D. Politzer, Phys. Rev. **D12**, 1404 (1975).

6. M. Chanowitz, Phys. Rev. **D12**, 918 (1975); T. Appelquist, R.M. Barnett, K. Lane, Ann. Rev. Nucl. Sci. **28**, 387 (1978).

7. S.J. Brodsky, G.P. LePage, P.B. Mackenzie, Phys. Rev. **D28**, 228 (1983).

8. For example: G. Bhanot, Phys. Lett. **101B**, 95 (1981); J.F. Donoghue, K. Johnson, B.A. Li, Phys. Lett. **99B**, 416 (1981); J. Coyne, P. Fishbane, S. Meshkov, Phys. Lett. **91B**, 259 (1980); T. Barnes, Z. Phys. **C10**, 275 (1981).

9. W.-S. Hou and A. Soni, Phys. Rev. D **29**, 101 (1984).

10. M. Chanowitz and S. Sharpe, Nucl. Phys. **B222**, 211 (1983); T. Barnes and F.E. Close, Nucl. Phys. **B224**, 241 (1983); F. Close, Rutherford Lab. preprint RL-82-041 (1982) and *Proceedings of the Conference on Unified Theories and Their Experimental Tests*, Venice (1982).

11. H.J. Lipkin, Phys. Lett. **109B**, 326 (1982).

12. M. Chanowitz and S. Sharpe, Phys. Lett. **123B**, 213 (1983).

13. A recent review is given by S.R. Sharpe in *High Energy e^+e^- Interactions (Vanderbilt, 1984)*, R.S. Panvini and G.B. Word, eds., AIP Conference Proceedings No. 121, New York (1984).

14. M. Chanowitz, in *Proceedings of the SLAC Summer Institute, 1981*, A. Mosher, ed., SLAC Report 245, Stanford (1982), p. 41, and and M. Chanowitz, Phys. Rev. Lett. **46**, 981 (1981).

15. J.D. Richman, in *High Energy e^+e^- Interactions (Vanderbilt, 1984)*, R.S. Panvini and G.B. Word, eds., AIP Conference Proceedings No. 121, New York (1984).

16. The numbers in this table are from the following sources: for $\gamma\pi^0$, $\gamma\eta\eta'$, C. Edwards, Caltech Ph.D. thesis, CALT-68-1165 (1985); for $\gamma\eta$, K. Konigsmann, *Proceedings of the XVII Rencontre de Moriond*, Les Arcs (1982) and SLAC-PUB-2910 (1982); for $\gamma\eta'$, $\gamma\iota$, this thesis; for $\gamma\eta\pi\pi$, R. Baltrusaitis, *et al.*, submitted to the *XXII Int. Conference on High Energy Physics*, Leipzig (1984); for $\gamma\rho\rho$ and $\gamma\omega\omega$, N. Wermes, *Proceedings of the XIX Rencontre de Moriond*, La Plagne (1984) and SLAC-PUB-3312 (1984); for γf, $\gamma f'$, $\gamma\theta$, $\gamma X(2.1)$, $\gamma\xi$, γS^*, K. Einsweiler, thesis, Stanford University, SLAC Report 272 (1984); for $\gamma\eta_c$ (inclusive), J. Gaiser, thesis,

Stanford University, SLAC Report 0255 (1982); for $\gamma p\bar{p}$, J.S. Brown, thesis, University of Washington (1984).

17. K. Einsweiler, thesis, Stanford University, SLAC Report 272 (1984).

18. N. Wermes, *Proceedings of the XIX Rencontre de Moriond*, La Plagne (1984), and SLAC-PUB-3312 (1984).

19. D.L. Scharre, *et al.*, Phys. Rev. **D23**, 43 (1981).

20. D. Bernstein *et al.*, SLAC-PUB-3222, submitted to Nucl. Instrum. Meth. (1983).

21. A. Seiden, *Proceedings of the XXII International Conference on High Energy Physics*, Leipzig (1984), and Santa Cruz Institute for Particle Physics preprint 84/27 (1984).

22. J. Roehrig *et al.*, SLAC-PUB-3199, submitted to Nucl. Instrum. Meth. (1983).

23. H. Kang, SLAC-PUB-2644 (1980).

24. D. Bernstein *et al.*, SLAC-PUB-2632 (1980).

25. J. S. Brown *et al.*, Nucl. Instrum. Meth. **221**, 503 (1984) and SLAC-PUB-3180 (1983).

26. W.B. Atwood, *Proceedings of the SLAC Summer Institute on Particle Physics, 1980*, A. Mosher, ed., SLAC Report 239, Stanford (1981).

27. W. Toki *et al.*, Nucl. Instrum. Meth. **219**, 479 (1984).

28. R. Fabrizio *et al.*, Santa Cruz Institute for Particle Physics preprint 83/23 (1984), submitted to Nucl. Instrum. Meth. (1984).

29. D. Bernstein and D. Hutchinson, IEEE Trans. on Nucl. Sci. **NS-29**, 294 (1982).

30. A. Spadafora, thesis, University of Illinois (1984).

31. J.J. Thaler, *et al.*, IEEE Trans. on Nucl. Sci., **NS-30**, 236 (1983).

32. J.J. Becker, *et al.*, SLAC-PUB-3442 (1984), submitted to Nucl. Instrum. Meth.

33. D.L. Scharre, *et al.*, Phys. Lett. **97B**, 329 (1980).

34. C. Edwards, *et al.*, Phys. Rev. Lett. **49**, 259 (1982).

35. DM2 Collaboration, *Proceedings of the XII International Conference on High Energy Physics*, Leipzig (1984).

36. P. Baillon, *et al.*, Il Nuovo Cimento, **A50**, 393 (1967).

37. P. Baillon, *et al.*, *Proceedings of the XXI International Conference on High Energy Physics*, Paris (1982).

38. C. Dionisi, *et al.*, Nucl. Phys. **B169**, 1 (1980).

39. T.A Armstrong, *et al.*, Phys. Lett. **146B**, 273 (1984).

40. S. U. Chung, private communication.

41. S. Flatté, Phys. Lett. **63B**, 224 (1976).

42. N. Törnquist, Phys. Rev. Lett. **49**, 624 (1982).

43. *Review of Particle Properties*, Rev. Mod. Phys. **56**, No. 2, Part II (April 1984).

44. A. Billoire, R. Lacaze, A. Morel, H. Navelet, Phys. Lett. **80B**, 381 (1979).

45. J.G. Kõrner, J.H. Kuhn, M. Krammer, H. Schneider, Nucl. Phys. **B29**, 115 (1983).

46. W.F. Palmer and S.S. Pinsky, Phys. Rev. **D27**, 2219 (1983).

47. By integrating over $\alpha - \varphi_\iota$, one could remove any possible dependence on the imaginary part of x. An analysis based on the integrated angular distributions was performed; the conclusions were identical to those presented below. In the Mark III analyses of $\psi \to \gamma f$, $\gamma f'$, and $\gamma\theta$, where the phases of the helicity amplitudes were not assumed to be relatively real, this was found to be the case.

48. R.L. Ford and W.R. Nelson, SLAC-210 (1978).

49. W. Toki, *Proceedings of the SLAC Summer Institute on Particle Physics, 1983*, A. Mosher, ed., SLAC Report 267, Stanford (1984).

50. J. Perrier, *Proceedings of the IV Physics in Collision Conference*, Santa Cruz (1984), and SLAC-PUB-3436 (1984).

51. S. Iwao, Nuovo Cim. Lett. **35**, 209 (1982).

52. C.E. Carlson and T.H. Hansson, Nucl. Phys. **B199**, 441 (1982). The phase space factor for the ι relative to the η' (=27) was omitted in this paper (C. Carlson, private communication to D. Hitlin).

53. T. Barnes and F.E. Close, Rutherford Lab. preprint RAL-84-055 (1984).

54. J.F. Donoghue, Phys. Rev. **D30**, 114 (1984).

55. W.F. Palmer and S.S. Pinsky, Phys. Rev. **D27**, 2219 (1983); W.F. Palmer, S.S. Pinsky, and C. Bender, Phys. Rev. **D30**, 1002 (1984).

56. C. Rosensweig, Syracuse preprint SU-4217-227 (1982).

57. K. Senba and M. Tanimoto, Nuovo Cimento Letters, **35**, 295 (1982).

58. S. Godfrey and N. Isgur, *Mesons with Chromodynamics*, Toronto preprint (1984).

59. See the remarks in Ref. (53).

60. K. Konigsmann, *Proceedings of the XVII Rencontre de Moriond: Workshop on New Spectroscopy*, Les Arcs (1982).

61. C. Edwards, thesis, California Institute of Technology, CALT-68-1165 (1984).

62. R. Baltrusaitis, *et al.*, to be submitted to Phys. Rev. D.

63. J. Becker, thesis, University of Illinois (1984).

64. M. Scarlatella, private communication.

65. N. Wermes, *Proceedings of the XIX Rencontre de Moriond*, La Plagne (1984), and SLAC-PUB-3312 (1984).

66. S. Berman and M. Jacob, Phys. Rev. **139**, B1023 (1965).

67. S. U. Chung, Cern Report 71-8 (1971).

68. M. Jacob and G. Wick, Ann. Phys. **7**, 404 (1959).

69. One should check, however, that acceptance effects do not affect the value of this integral.

70. A. McKerrel, Nuovo Cimento **34**, 1289 (1964).

71. M. Jacob and G.C. Wick, Ann. Phys. **7**, 404 (1959).

72. S.U. Chung, CERN Report 71-8 (1971).

73. M.L. Perl, *High Energy Hadron Physics*, Wiley, New York (1974).

74. E.M. Lifshitz and L.P. Piaevskii, *Relativistic Quantum Theory, Part 1*, Pergamon, Oxford (1974).

75. A.D. Martin and T.D. Spearman, *Elementary Particle Physics*, North Holland, Amsterdam (1970).

76. J.D. Jackson in *Les Houches Lectures in High Energy Physics, 1965*, C. DeWitt and M. Jacob, eds., Gordon and Breach, New York (1966).